ENGINEERED TRANSITION ZONE SYSTEMS FOR ENHANCED HEAT TRANSFER IN THERMO-ACTIVE FOUNDATIONS

A Dissertation
Presented to
The Academic Faculty

by

Fikret Atalay

In Partial Fulfillment
of the Requirements for the Degree
Doctor of Philosophy in the
School of Civil and Environmental Engineering

Georgia Institute of Technology
May 2019

ENGINEERED TRANSITION ZONE SYSTEMS FOR ENHANCED HEAT TRANSFER IN THERMO-ACTIVE FOUNDATIONS

Approved by:

Dr. J. David Frost, Advisor
School of Civil and Environmental Engineering
Georgia Institute of Technology

Dr. Sheng Dai
School of Civil and Environmental Engineering
Georgia Institute of Technology

Dr. Paul W. Mayne
School of Civil and Environmental Engineering
Georgia Institute of Technology

Dr. Marilyn A. Brown
School of Public Policy
Georgia Institute of Technology

Dr. Susan E. Burns
School of Civil and Environmental Engineering
Georgia Institute of Technology

Date Approved: [March 12, 2019]

ACKNOWLEDGEMENTS

First, I would like to acknowledge the guidance, support and encouragement of my doctoral advisor, Dr. J. David Frost. I would also like to thank Dr. Frost for his mentorship and for giving me the opportunities to travel, explore (matters both academic and non-academic), and grow as a person. I would also like to thank the members of my committee for their guidance and support, and extend my special thanks to both Dr. Jean-Michel Pereira and Dr. Anh-Minh Tang at École des Ponts – ParisTech, as well as Emmanuel De Laure and Marine Lemaire, for their time and assistance.

My gratitude extends to my parents, Aysel and Hasan Atalay, and my brother, Timur Atalay, for their patience and support. I would also like to thank my wife, Anne Atalay, for encouraging me over the years, for providing support and feedback, and finally for giving me a gentle nudge towards completing my dissertation. Without her, there is a good chance this dissertation would not exist. Additionally, I would like to thank my friends and colleagues at the Georgia Institute of Technology, as well as those outside the university. Your company was much appreciated on the long journey.

Last but not least, I would like to thank my bicycle for keeping me from becoming morbidly obese due to stress eating during my studies, my drum set for helping me relax, and our cat, Honey Badger, for always greeting me with her colorful and entertaining personality at the end of many long days.

TABLE OF CONTENTS

ACKNOWLEDGEMENTS iii

LIST OF TABLES vii

LIST OF FIGURES viii

SUMMARY xv

CHAPTER 1. Introduction 1
1.1 Thermo-Active Foundations: An Overview 1
1.2 Research Motivation 3
1.3 Research Scope & Outline 5

CHAPTER 2. Literature Review 11
2.1 Current State of Thermo-Active Foundations 11
2.1.1 Hydro-Mechanical Behaviour 11
2.1.2 Thermal Behaviour 18
2.1.3 Sustainability Considerations 21
2.2 Heat Transfer in Thermo-Active Foundations 23
2.2.1 Heat Transfer for Pipe Flow 24
2.2.2 Heat Transfer in Geomaterials 26
2.3 Thermal Conductivity of Geomaterials 29
2.3.1 Soil 29
2.3.2 Rock 35
2.4 Specific Heat Capacity of Geomaterials 36

CHAPTER 3. Index Properties and Mineralogical Composition of Piedmont Residual Soils 39
3.1 Methodology 40
3.2 Results & Discussion 45
3.2.1 X-Ray Diffraction 45
3.2.2 X-Ray Fluorescence 48
3.2.3 Quartz Content 49
3.3 Conclusions 53

CHAPTER 4. Thermal Properties of Piedmont Residual Soils From Laboratory Tests 55
4.1 Methodology 55
4.1.1 Test Apparatus and Sample Preparation 55
4.1.2 Thermal Properties Measurement 58
4.1.3 Development of Predictive Relationship 59

4.2 Results & Discussion 63
4.2.1 Thermal Conductivity 63
4.2.2 Specific Heat Capacity 73
4.3 Conclusions 77

CHAPTER 5. Estimating Thermal Conductivity From Cone Penetration Tests 78
5.1 Methodology 79
5.2 Results & Discussion 89
5.2.1 USCS Classification & Index Properties 89
5.2.2 SRCPTu Soundings – General 90
5.2.3 SRCPTu Soundings – Soil Behavior 94
5.2.4 Thermal Conductivity 98
5.3 Conclusions 103

CHAPTER 6. A Comparison Between Thermal Conductivity of Undisturbed Lab and Remolded Tube Samples 105
6.1 Methodology 106
6.2 Results & Discussion 108
6.3 Conclusions 112

CHAPTER 7. Engineered Transition Zone: Proof-of-Concept Via Numerical Modeling 114
7.1 Methodology 114
7.1.1 Engineered Transition Zone Concept 114
7.1.2 Numerical Model Validation 116
7.1.3 Parametric Study 128
7.2 Results & Discussion 132
7.2.1 Scenario #1 – Baseline Case 132
7.2.2 Scenario #2 – Baseline Case with ETZ 133
7.2.3 Scenario #3 – Helical Loop with ETZ 134
7.2.4 Scenario #4 – Helical Loop without ETZ 138
7.2.5 Summary of Parametric Study 139
7.2.6 Pile Temperature 142
7.2.7 Transient Operation 144
7.2.8 Drying Effects 149
7.3 Conclusions 152

CHAPTER 8. Laboratory Scale Chamber Testing 155
8.1 Methodology 155
8.1.1 Experimental Setup 155
8.1.2 Testing Program 160
8.2 Results & Discussion 161
8.3 Conclusions 168

CHAPTER 9. Public Policy Considerations **170**
9.1 Methodology **172**
9.1.1 Punctuated Equilibrium & Bass Diffusion Model 172
9.1.2 Longitudinal Data Analysis 175
9.2 Results & Discussion **176**
9.2.1 Bass Diffusion Model 176
9.2.2 Longitudinal Data Analysis 179
9.3 Conclusions **186**

CHAPTER 10. Conclusions and Future Work **187**

REFERENCES **192**

LIST OF TABLES

Table 2-1	– Summary of factors affecting soil thermal conductivity	29
Table 3-1	– Summary of index test results for Piedmont soils	41
Table 3-2	– Summary of XRF results for Piedmont soils	49
Table 3-3	– Summary of quartz content predictions for Piedmont soils	50
Table 5-1	– Summary of unit weight, moisture content and thermal conductivity at the Opelika NGES	83
Table 5-2	– Summary of index tests at the Opelika NGES	85
Table 5-3	– Relationship between electrical resistivity and thermal conductivity	99
Table 6-1	– Summary of index test results	107
Table 6-2	– Summary of measured thermal conductivity	110
Table 7-1	– Thermal properties for numerical model validation (from Cecinato and Loveridge, 2015)	119
Table 7-2	– Thermal properties for numerical model validation (from Nguyen, 2017)	124
Table 7-3	– Soil thermal properties for parametric study	130
Table 7-4	– Model extent for steady-state analyses	131
Table 7-5	– Thermal properties for hypothetical drying scenario	151
Table 8-1	– Relevant physical properties of Fontainebleau sand	158
Table 8-2	– Density and thermal properties for experimental program	159
Table 8-3	– Summary of lab scale model testing program	160
Table 8-4	– Summary of power extraction from lab scale model	166

LIST OF FIGURES

Figure 1-1	– Residential, commercial and total primary energy consumption in the U.S.	4
Figure 1-2	– Residential Sector delivered energy intensity, actual 2013 and estimated 2040 (million Btu per household per year)	4
Figure 1-3	– Commercial Sector delivered energy intensity, actual 2013 and estimated 2040 (million Btu per household per year)	4
Figure 1-4	– The Engineered Transition Zone (ETZ) concept – plan view	6
Figure 1-5	– Extent of Piedmont physiographic region (after Hack 1982), and approximate locations of the sampling locations and the Opelika test site	7
Figure 2-1	– Pile response to mechanical load only, no end restraint (from Bourne-Webb et al. 2013)	13
Figure 2-2	– Pile response to cooling, no end restraint	14
Figure 2-3	– Pile response to combined loading and cooling, no end restraint	14
Figure 2-4	– Pile response to heating, no end restraint	15
Figure 2-5	– Pile response to combined load and heating, no end restraint	15
Figure 2-6	– Pile response to combined load and heating, with base restraint	15
Figure 2-7	– Pile response to combined load and cooling, with base restraint	15
Figure 2-8	– Pile response to combined load and heating, with restraint on both ends	16
Figure 2-9	– Pile response to combined load and cooling, with restraint on both ends	16
Figure 2-10	– Primary heat transfer modes in a thermo-active foundation with fluid circulation pipe embedded in concrete and surrounded by geomaterial (not to scale)	24
Figure 3-1	– Grain size distribution results for Piedmont soils	41
Figure 3-2	– Fusion of flux and samples for XRF	42

Figure 3-3 – XRD scan data for sample JCS 45

Figure 3-4 – XRD scan data for sample SMS 46

Figure 3-5 – XRD scan data for sample ATLP 46

Figure 3-6 – XRD scan data for sample JCC 47

Figure 3-7 – XRD scan data for sample RUBY 47

Figure 3-8 – XRD scan data for sample TYRN 48

Figure 3-9 – Relationship between coarse fraction and quartz fraction for Piedmont soils 51

Figure 3-10 – Relationship between apparent quartz content and SiO_2 content from XRF tests for Piedmont soils 51

Figure 4-1 – Acrylic chamber (side view) for measurement of thermal properties (all measurements in millimeters, unless otherwise noted) 56

Figure 4-2 – (a) Sample conditions immediately after water injection (at three different saturation levels); (b) Sample conditions after a 6-hour period, showing the diffusion of the water column. 58

Figure 4-3 – Relationship between porosity and dry thermal conductivity for Piedmont residual soils 59

Figure 4-4 – Thermal conductivity vs. degree of saturation for the six Piedmont soil samples tested (two void ratios/densities and five different degrees of saturation 64

Figure 4-5 – Thermal conductivity vs. degree of saturation for the six Piedmont soil samples tested (two void ratios/densities and five different degrees of saturation 65

Figure 4-6 – Model calibration results for coarse Piedmont soils – wetting 66

Figure 4-7 – Model calibration results for fine Piedmont soils – wetting 67

Figure 4-8 – Relationship between predicted and measured thermal conductivity for Piedmont soils during wetting 68

Figure 4-9 – Model calibration results for coarse Piedmont soils – drying 69

Figure 4-10 – Model calibration results for fine Piedmont soils – drying 69

Figure 4-11 – Relationship between predicted and measured thermal conductivity for Piedmont soils during drying 70

Figure 4-12 – Kersten number (K_e) of coarse Piedmont soils during wetting and drying 71

Figure 4-13 – Kersten number (K_e) of fine Piedmont soils during wetting and drying 71

Figure 4-14 – Relationship between saturated thermal conductivity calculated from XRD results and measured from laboratory tests 72

Figure 4-15 – Relationship between predicted and measured specific heat for Piedmont soils during wetting 74

Figure 4-16 – Relationship between predicted and measured specific heat for Piedmont soils during drying 74

Figure 4-17 – Relationship between predicted and measured specific heat for Piedmont soils during drying (color coded by sample ID) 75

Figure 4-18 – Relationship between moisture content and specific heat for Piedmont soils – wetting phase 76

Figure 4-19 – Relationship between moisture content and specific heat for Piedmont soils – drying phase 76

Figure 5-1 – Opelika NGES and SRCPTu sounding and Shelby tube sample locations 80

Figure 5-2 – Sample testing and extraction sequence for determination of thermal and index properties of the Shelby Tube samples 82

Figure 5-3 – Summary of grain size distribution tests at the Opelika NGES 90

Figure 5-4 – Summary of SRCPTu soundings 91

Figure 5-5 – Electrical resistivity/conductivity of various geological materials (modified after Palacky, 1987). Clay and sand differ in conductivity by up to three orders of magnitude. 93

Figure 5-6 – Non-normalized SBT Charts for (a) SRCPTu-1, and (b) SRCPTu-2 94

Figure 5-7 – Normalized SBT Charts for (a) SRCPTu-1, and (b) SRCPTu-2 96

Figure 5-8 – Normalized Bq SBT Charts for (a) SRCPTu-1, and (b) SRCPTu-2 96

Figure 5-9 – Schneider et al. (2008) SBT Charts for (a) SRCPTu-1, and (b) SRCPTu-2 97

Figure 5-10 – Modified SBTn Charts for (a) SRCPTu-1, and (b) SRCPTu-2 97

Figure 5-11 – Variation of C_R with degree of saturation (S_r) and coarse content (F), from Sreedeep et al. (2005) 100

Figure 5-12 – Comparison of predicted and measured thermal conductivity based on electrical resistivity 101

Figure 5-13 – Comparison between predicted and measured soil unit weights 102

Figure 5-14 – Comparison between predicted and measured thermal conductivities 102

Figure 6-1 – Soil microstructure charts for sounding SRCPTu-1 and SRCPTu-2 109

Figure 6-2 – Comparison of thermal conductivity for remolded and Shelby tube samples 109

Figure 7-1 – (a) Engineered foundation system concept for enhanced heat transfer (plan view) (b) Pile tip extending below transition zone (left) or the same depth as the transition zone (right) 115

Figure 7-2 – (a) Typical configuration for a concrete pile in direct contact with soil, resulting in high impedance contrast at the interface; (b) ETZ concept to create transition zone between pile and soil for optimized heat transfer 116

Figure 7-3 – (a) Model pile geometry (b) Close-up of the pile top showing the single U-loop configuration for model validation using published results from Cecinato and Loveridge, 2015 117

Figure 7-4 – Thermal response test results (from Cecinato and Loveridge, 2015) 118

Figure 7-5 – Mesh size comparison 120

Figure 7-6 – (a) Model pile geometry (b) Meshed model for validation using TRT data from Cecinato and Loveridge, 2015 121

Figure 7-7 – COMSOL model validation results using TRT data from Cecinato and Loveridge, 2015 122

Figure 7-8	– (a) Model pile geometry (b) Close-up of the pile top showing the W-loop configuration for model validation using results from Nguyen, 2017	123
Figure 7-9	– Thermal response test results from Nguyen, 2017	123
Figure 7-10	– Regression analysis for approximation of inlet temperatures as a function of time	125
Figure 7-11	– (a) Model pile geometry (b) Meshed model for validation using published results from Nguyen, 2017	126
Figure 7-12	– COMSOL model validation results using data from Nguyen, 2017	127
Figure 7-13	– COMSOL simulation results for baseline case, Soils A – C	132
Figure 7-14	– Improvement ratios after introduction of ETZ for Soils A – C	133
Figure 7-15	– Pile configuration with ETZ and helical loop	135
Figure 7-16	– Improvement ratios for Scenario #3 relative to Scenario #1 for Soils A - C	136
Figure 7-17	– Improvement ratios for Scenario #3 relative to Scenario #2 for Soils A - C	136
Figure 7-18	– Power extracted for Scenario #3 for various helical loop lengths	137
Figure 7-19	– Improvement ratios for Scenario #4 relative to Scenario #1 for two helical loop	138
Figure 7-20	– Improvement ratios for Scenario #4 relative to Scenario #3 for two helical loop lengths	139
Figure 7-21	– Summary of power extraction for Scenarios #1 - #4	140
Figure 7-22	– Summary of improvement ratios for Scenarios #1 - #4	140
Figure 7-23	– Improvement in power for Scenario #2 (ETZ alone), Scenario #4 (helical loop alone), sum of Scenarios #2 and #4, and Scenario #3 (ETZ plus helical loop)	141
Figure 7-24	– Temperature along the pile face and pile center for baseline case (Scenario #1) and ETZ with tightly-spaced helical loops (Scenario #3-4)	143

Figure 7-25 – Transient simulation results for Scenario #1 and Scenario #3-4 145

Figure 7-26 – Outlet temperature response of energy pile (Scenario #1) operating under continuous and intermittent modes 147

Figure 7-27 – Outlet temperature response of energy pile (Scenario #3-4) operating under continuous and intermittent modes 147

Figure 7-28 – Power extracted from energy pile under continuous and intermittent modes (Scenario #1) 148

Figure 7-29 – Power extracted from energy pile under continuous and intermittent modes (Scenario #3-4) 148

Figure 7-30 – Thermal conductivity for hypothetical drying scenario 150

Figure 7-31 – Power extraction for hypothetical drying scenario 152

Figure 8-1 – Experimental setup for physical laboratory scale model (all dimensions in mm) 156

Figure 8-2 – Model pile (right) and 3D fluid circulation loop (left) used during laboratory scale model tests 158

Figure 8-3 – Temperature response for Trial 1 162

Figure 8-4 – Temperature response for Trial 3 162

Figure 8-5 – Temperature response for Trial 5 163

Figure 8-6 – Temperature response for Trial 6 163

Figure 8-7 – Recorded flow rates during heat injection 164

Figure 8-8 – Inlet and outlet temperature difference during heat injection 165

Figure 8-9 – Power extraction during heat injection 165

Figure 8-10 – Scale model pile surface temperature response 167

Figure 9-1 – Current state of deployment of renewable heating and cooling (REHC) technologies; from IEA (2007) 170

Figure 9-2 – S-shaped curves of diffusion (modified after Boushey, 2012) 173

Figure 9-3 – U.S. Census Regions 175

Figure 9-4 – Distribution of GSHP-related policies by year 177

Figure 9-5 – Distribution of GSHP shipment capacities by year 178

Figure 9-6 – Cumulative number of GHP-related policies (2000-2015) and Bass Diffusion Model (BDM) Results 178

Figure 9-7 – Cumulative rated capacity (in HVAC tons) of GSHP shipments (2002-2009) and Bass Diffusion Model (BDM) Results 179

Figure 9-8 – Distribution of GSHP-related policies by year for the four U.S. Census Regions 180

Figure 9-9 – Distribution of rated capacity of GSHP shipments by year for the four U.S. Census Regions 180

Figure 9-10 – Other factors with potential impacts on GSHP adoption for U.S. census regions 182

SUMMARY

In this study, results are presented from both a numerical model and a laboratory scale physical model to demonstrate the potential for improvement in thermal performance of shallow thermo-active foundations resulting from a novel concept termed the Engineered Transition Zone (ETZ). An ETZ provides a means to introduce a thermally optimized zone between the foundation and the surrounding geomaterials to reduce thermal resistance. It also allows decoupling of the structural portion of the foundation from the thermal portion, such that the length of each component can be selected individually to meet the specific structural and thermal needs. Additionally, it allows for various novel circulation pipe configurations to be used (for example, helical loops) to further enhance heat transfer due to increased pipe surface area available for heat transfer. Both the numerical and physical models show that there is a potential for significant improvement in thermal performance. Such improvements can make shallow thermo-active foundations, such as energy piles, a more feasible renewable and sustainable energy alternative for heating and cooling of buildings (provided that the ground energy balance can be equilibrated; that is, there is balance between heat extracted for heating and heat re-injected for cooling), particularly in areas where poor subsurface thermal properties might otherwise preclude their use.

The study also presents results from laboratory tests on Piedmont residual soils to demonstrate the importance of density, saturation, and texture on soil thermal properties, which in turn are critical to evaluating the performance of shallow thermo-active foundations in this physiographic region. In this regard, a predictive relationship was

developed for estimation of thermal conductivity (during both wetting and drying) for a given porosity and composition, and for moistures ranging from dry to full saturation for Piedmont residual soils. In addition, a predictive relationship was developed for estimation of specific heat capacity as a function of soil moisture content.

Using the predictive relationship obtained from the thermal property measurements on Piedmont soils, it was also shown that results from Seismic Piezocone Penetration Test (SCPTu) soundings and simple laboratory index tests (moisture content and percent fines) can be used to obtain a first-order estimate of thermal conductivity. In addition, the results from the thermal property measurements on Piedmont soils were used to provide a range of thermal properties that were subsequently used in the parametric study performed using the aforementioned numerical model.

This study also highlights some of the challenges associated with determination of thermal conductivity from field and laboratory tests. In the laboratory, while samples can be prepared under relatively controlled conditions, variances can still occur due to sample size and preparation, sensor size and accuracy, test method used, and other factors. In the field, there are natural variations in the ground conditions, and while a test such as a thermal response test (TRT) can capture a larger sensed volume (and hence better captures the natural vertical and lateral variation of soil properties), it is also subject to higher costs relative to laboratory testing, as well as variances resulting from the difference in the analytical models used to interpret the TRT results.

Lastly, this study presents some of the public policy challenges related to the adoption of shallow thermo-active foundations. A case study was performed looking at the

application of the punctuated equilibrium theory and policy diffusion to gain insight into ground source heat pump (GSHP) related policies in the U.S. between 2000 and 2015, as well as GSHP adoption rates between 2002 and 2009. Using the Bass Diffusion Model (BDM) and longitudinal data analysis, it is shown that that policies enacted at the federal level can act as a trigger and a signal for GSHP related policies to be enacted at the state level. Policy diffusion can in turn create awareness through signaling and information, leading to more widespread market adoption. In this case, the increase in GSHP adoption rates is observed to be more gradual, most likely because of higher initial costs relative to more conventional HVAC systems, as well as other market failures such as information asymmetry and split incentives between owners and building tenants. The longitudinal data analysis appears to confirm that the accumulation of GSHP related policies has an impact on GSHP adoption. Additionally, it highlights some of the other factors that may have contributed to higher adoption of GSHPs, such as increasing energy prices. These findings suggest that policy alternatives can be devised at the state and local levels to complement federal incentives, to help overcome market failures, and to encourage more widespread adoption of emerging energy efficient technologies such as shallow thermo-active foundations. Significantly improving the thermal performance of shallow thermo-active foundations through the use of an ETZ can also act to accelerate the rate of adoption of shallow thermo-active foundations by enabling the use of these systems in subsurface conditions that would otherwise preclude their use, and also by potentially reducing the payback period associated with these installations through the use of fewer but much higher performing elements.

CHAPTER 1. INTRODUCTION

1.1 Thermo-Active Foundations: An Overview

Thermo-active foundations are a variation of the traditional geotechnical foundation system, where the foundation is fitted with fluid-circulating tubes. The temperature characteristics of the ground, which typically remains at an approximately constant temperature below the upper few meters, are then utilized to enable the foundation to exchange heat energy with the ground in addition to providing vertical and/or lateral foundation support. During the winter, heat can be extracted from the ground to aid in heating, while during the summer heat can be injected into the ground to aid in cooling. Examples of thermo-active ground structures include heat exchanger piles, and energy walls such as retaining and basement walls (Brandl, 2006). The depths at which the energy transfer takes place when using thermo-active foundations are substantially less than those required for traditional deep geothermal systems, which can reduce the installation costs significantly (Arson et al., 2013). Further, shallow thermo-active foundations can aid in both heating and cooling, whereas deep geothermal systems are typically used only for heating purposes.

The transfer of heat is achieved via the use of a heat pump, which requires electricity to operate. However, a typical heat pump can move 3 to 5 times as much energy between the ground and the building than it consumes while doing so (Hughes, 2008). According to Hughes (2008), “if there were a market-driven reason to do so, the GHP industry could integrate the most advanced commercially available components into their heat pumps and

increase this multiplier effect to 6 – 8, and theoretically the multiplier could be as high as 14."

Because thermo-active foundation systems utilizing a ground source heat pump are more efficient than a traditional air heat pump due to the relatively constant temperature characteristics of the ground in comparison to relatively large fluctuations in ambient air temperatures, there is a potential for significant energy savings as well as a reduction in greenhouse emissions by using these systems as a renewable energy source, assuming the ground energy balance can be equilibrated; that is, there is balance between heat extracted for heating and heat re-injected for cooling (Arson et al., 2013). Achieving a ground energy balance also has implications on long-term performance of energy piles, in that unbalanced loads (i.e., unbalanced heat injection or heat extraction) can alter the ground temperature surrounding the thermo-active foundation and influence the thermal efficiency of the system (Olgun et al., 2015).

Studies on thermo-active foundations such as heat exchanger piles around the world have shown that when designed properly, these systems can meet a substantial portion of the heating and cooling demands of various commercial and institutional structures (airports, hospitals, office buildings, etc.), while also reducing carbon emissions (Himmler and Fisch, 2005, Desmedt and Hoes, 2006, Laloui et al., 2006, Pahud and Hubbuch, 2007, De Moel et al., 2010, Hemingway and Long, 2011). While the additional capital cost to install energy piles can be substantial (50 percent or more, compared to more conventional pile foundations), the simple payback periods are typically on the order of 5 and 10 years (Brandl, 2006, Desmedt and Hoes, 2006). This payback period would be expected to get shorter as market diffusion takes place, further technological advances are made, and

upfront costs are reduced. In addition, carefully crafted public policy options can help to speed up the adoption rates of thermo-active foundations.

1.2 Research Motivation

Historically, the design of thermo-active foundations has placed a significantly greater emphasis on the structural characteristics (i.e., the load carrying ability) in comparison to the heat transfer characteristics. While preventing structural or geotechnical failure of the pile is of utmost concern, the optimization of the heat transfer characteristics of thermo-active foundations to increase their efficiency and performance has equally significant implications with regards to sustainability and renewable energy.

Based on the Energy Information Administration (EIA)'s data, Figure 1-1 shows that residential and commercial buildings are responsible for approximately 40% of total energy consumption in the United States (EIA, 2018). Figure 1-2 and Figure 1-3 show that in 2013, heating, ventilation, and air conditioning (HVAC) and water heating accounted for about two-thirds of the total energy consumption in residential buildings, and about one-half in commercial buildings (EIA, 2015). While reductions in energy intensity due to increased energy efficiency and other factors are expected to result in reduced energy use in residential and commercial building over time, in aggregate these buildings will continue to use a large amount of energy for their HVAC needs in the near future, for which a majority of the generation will be from carbon-intensive fossil fuels (i.e., coal, natural gas and petroleum).

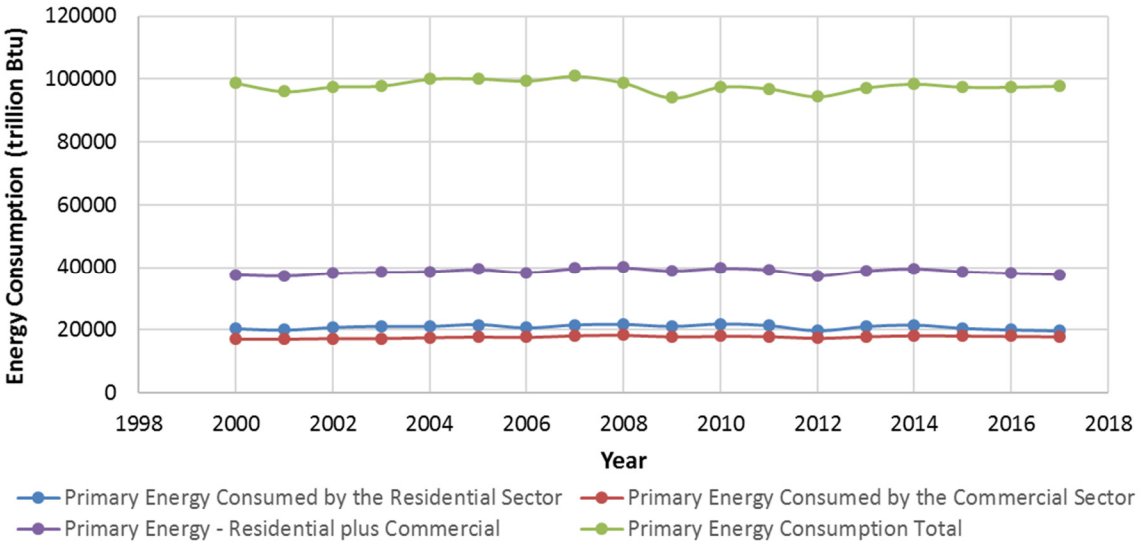

Figure 1-1 – Residential, commercial and total primary energy consumption in the U.S.

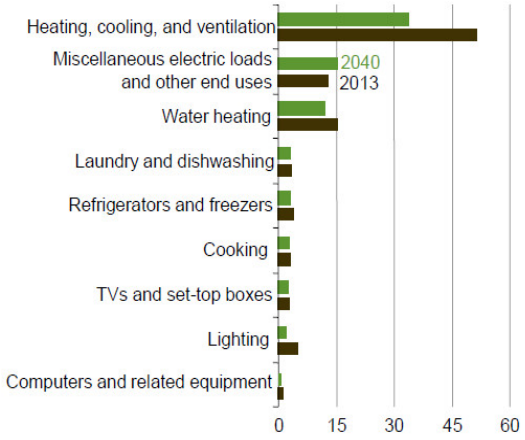

Figure 1-2 – Residential Sector delivered energy intensity, actual 2013 and estimated 2040 (million Btu per household per year)

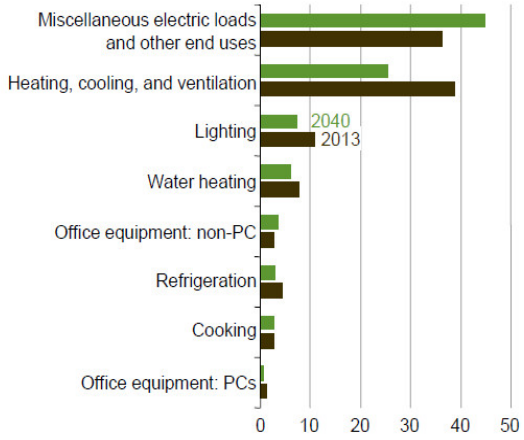

Figure 1-3 – Commercial Sector delivered energy intensity, actual 2013 and estimated 2040 (million Btu per household per year)

In this regard, optimization of the heat transfer characteristics of thermo-active foundations and their more widespread use can play an important role as sustainable, renewable energy sources to reduce HVAC-related energy use and carbon emissions, particularly in municipal, commercial and residential sectors. This study aims to assess the improvement in thermal performance of shallow thermo-active foundations using a novel concept termed the Engineered Transition Zone (ETZ), with a particular focus on the subsurface conditions encountered in the Piedmont physiographic region of the United States. The findings can be generalized to other regions as well.

1.3 Research Scope & Outline

This study focuses primarily on the heat exchange behavior of thermo-active foundations, or more specifically, the use of the ETZ concept to improve the thermal performance of these systems. The thermal performance of thermo-active foundations is strongly related to the thermal properties of the surrounding geomaterials; as such, this study also aims to improve the understanding of the thermal properties of geomaterials typically encountered in the Piedmont physiographic region, which includes Atlanta, Georgia and extends from central Alabama in the south to New Jersey.

The ETZ concept involves an in-situ manufactured zone, which surrounds the thermo-active foundation, and acts as a high diffusivity (i.e., low thermal impedance) interface between the foundation and the surrounding geomaterials (Figure 1-4).

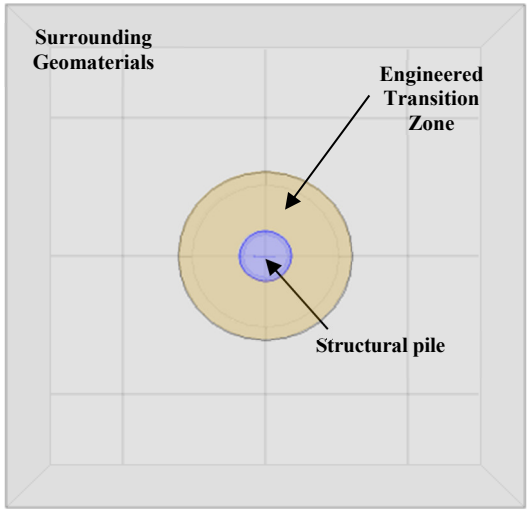

Figure 1-4 – The Engineered Transition Zone (ETZ) concept – plan view

The outline of the dissertation is as follows. A literature review is provided in Chapter 2, summarizing the current state of thermo-active foundations, a review of the fundamentals governing heat transfer for thermo-active foundations, and a review of the relevant thermal properties of geomaterials as they apply to these shallow heat exchangers.

In Chapter 3, results from a study on the mineralogical composition of Piedmont soil samples are presented and their impact on thermal properties are discussed. Soil samples were obtained from the exposed soil overburden section of several rock quarry locations around the state of Georgia. From the several locations sampled, six (6) samples were selected based on grain size distribution and Atterberg Limits test results. The soils that range from high plasticity silts to low plasticity clays and silty and clayey sands, represent the general conditions encountered in the Piedmont physiographic region. The approximate sample locations are shown on Figure 1-5 (note that two samples were selected from the Junction City Quarry location).

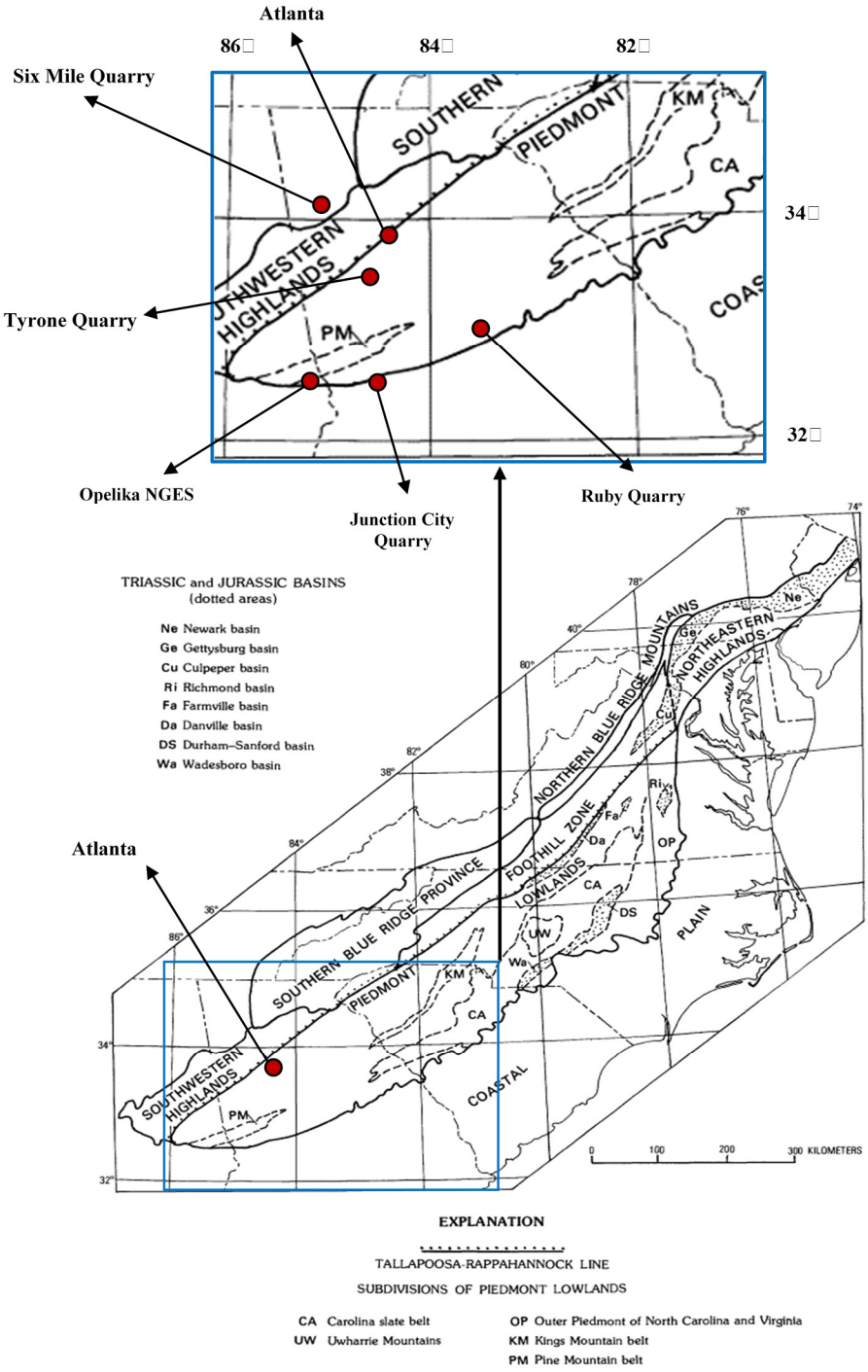

Figure 1-5 – Extent of Piedmont physiographic region (after Hack 1982), and approximate locations of the sampling locations and the Opelika test site

In Chapter 4, results from a study on the thermal conductivity and specific heat capacity of Piedmont soils is presented. The same six samples from the previous chapter were used for laboratory measurement of thermal conductivity and heat capacity under different density and saturation conditions. The saturated thermal conductivity measurements from the six samples were also used for comparison against saturated thermal conductivity calculated from X-day diffraction (XRD) test results as presented in Chapter 3.

Chapters 5 and 6 present results from a field exploration program conducted at the National Geotechnical Experimentation Site (NGES) in Opelika, Alabama, USA, which is located within the Piedmont physiographic region. The goal of the field exploration was to supplement the findings from the laboratory testing program in Chapter 4, and to evaluate whether or not thermal properties of Piedmont residual soils can be predicted using in-situ test results. Seismic cone penetration tests with resistivity measurements and undisturbed Shelby tube sampling were performed side by side at this site. The soil resistivity measurements were used to evaluate whether or not a relationship exists between the thermal conductivity and electrical resistivity of the site soils. The seismic cone penetration test results were used to evaluate the subsurface conditions and assess soil microstructure effects, while the Shelby tube samples were used to determine soil unit weight / density, grain size distribution and Atterberg Limits, moisture content, and to perform laboratory measurements of thermal conductivity of the tube samples. Additionally, the tube samples were remolded in the laboratory to their field density and saturation conditions, and their thermal conductivity measured again. A comparison was then performed between the thermal conductivity from the field tube samples and the remolded samples.

In Chapter 7, results from a proof-of-concept numerical model investigating the effect of the ETZ on thermal performance are shown. Numerical modeling was performed using COMSOL Multiphysics, a finite-element software package that allows the coupling of heat transfer for pipe flow (to simulate heat transfer due to the fluid circulation in a thermo-active foundation system) with heat transfer in solids (to simulate heat transfer due to conduction in the geomaterials surrounding a thermo-active foundation system). The numerical model was validated using two data sets, and a parametric study was performed to assess the level of thermal performance improvement that can be achieved by using an ETZ and helical fluid loop configurations compared to a more conventional system with U-shaped fluid circulation loops.

Chapter 8 presents results from a laboratory scale physical model which was used to evaluate the effect of the ETZ and a helical fluid loop configuration on thermal performance. An approximately 0.55 m diameter and 0.9 m tall aluminum chamber at École des Ponts – ParisTech was backfilled with Fontainebleau sand, and the system was instrumented to measure temperatures in the soil surrounding the scale model, as well as monitoring the fluid inlet and outlet temperatures for quantification of improvement in thermal performance.

In Chapter 9, a case study highlighting the public policy factors related to the adoption of ground-source heat pumps is presented. Ground-source heat pump adoption can be seen as a proxy to the shallow thermo-active foundations, in that both require a relatively large upfront cost with the return on investment occurring over a period of time. Data from the Database of State Incentives for Renewables & Efficiency (DSIRE) and other public sources of information such as Energy Information Administration (EIA), the

U.S. Census Bureau, and Bureau of Economic Analysis (BEA) were used to evaluate whether or not the number of ground source heat pump related policies have an impact on heat pump adoption.

Lastly, Chapter 10 presents the major conclusions and recommendations for future work.

CHAPTER 2. LITERATURE REVIEW

2.1 Current State of Thermo-Active Foundations

As will be discussed in the subsequent sections, current research focuses heavily on the thermo-mechanical and thermo-hydro-mechanical behavior; that is, changes in mechanical pile behavior (e.g., load transfer and capacity, induced strains and stresses, etc.) resulting from the induced thermal gradients and/or pore pressure changes in and around thermo-active foundations. In comparison, relatively little attention appears to be given to the heat exchange behavior of these systems. While preventing structural or geotechnical failure of a thermo-active foundation is of utmost concern, the optimization of the heat transfer characteristics of these systems to increase their efficiency and performance has equally significant implications with regard to sustainability and renewable energy. Further, while the idea of a foundation serving a dual role for both structural support and heat transfer is novel, it also implies that there are inherent compromises to satisfy both criteria simultaneously. In this regard, decoupling of the structural component of a thermo-active foundation from its heat exchange component with the utilization of the ETZ offers significant advantages in terms of thermal performance.

2.1.1 Hydro-Mechanical Behaviour

Research in the area of thermo-active foundations has focused heavily on the mechanical and hydro-mechanical behavior of energy piles; that is, changes in mechanical pile behavior (e.g., load transfer and capacity, induced strains and stresses, etc.) resulting from the induced thermal gradients and/or pore pressure changes in and around the energy

piles. More recently, some consideration has also been given to other thermo-active foundation types (basement walls, slabs, tunnels, etc.) (Bidarmaghz and Narsilio, 2018, Makasis et al., 2018).

Based on results from instrumented laboratory and in-situ test piles, as well as results from coupled numerical simulations, it has been shown that the pile expands/contracts in an elastic fashion about a null point. There is potential for tensile axial forces to develop during cooling as the pile contracts (and mechanical load is diminished towards the bottom of the pile) and significant compressive axial forces to develop during heating as the pile expands due to the uniform nature of thermal effects. The magnitude of these forces depend on the type of surrounding soil, the magnitude of the temperature change and the degree of pile end axial fixity (Brandl, 2006, Laloui et al., 2006, Bourne-Webb et al., 2009, Knellwolf et al., 2011, Amatya et al., 2012, Bourne-Webb et al., 2013, Mimouni and Laloui, 2014). It has been suggested that the magnitude of tensile forces is unlikely to lead to tensile cracking during cooling (Bourne-Webb et al., 2009); however, the increase in compressive axial forces can be significant enough to overstress concrete piles structurally, especially under fixed-end conditions. Amatya et al. (2012) state the thermally induced axial stress in the pile can be between 50% and 100% of the theoretically fully restrained values.

A generalized framework for understanding pile response to thermal loading for different ground and end restraint conditions has been provided by Bourne-Webb et al. (2009), Amatya et al. (2012) and Bourne-Webb et al. (2013). For an idealized soil column with uniform strength and a linear elastic pile with a constant cross-sectional area, and considering the typical case of a load imposed at the pile head, Figure 2-1 shows the mechanical response for a pile without end restraint (i.e., floating pile), which can be

described as diminishing axial load (P) and strain (ε) with depth, and constant mobilized unit side friction (q_s) along the pile length.

Figure 2-2 shows the idealized response of a pile to a cooling load only, with no end restraint. Combining Figure 2-1 and Figure 2-2 via superposition results in Figure 2-3, which shows the thermo-mechanical pile response in the case of combined mechanical load and cooling, without end restraint. It can be seen that depending on the intensity of the induced temperature change and the degree of soil restraint, there is potential for tensile axial forces to develop during cooling. It can also be seen that pile contraction due to cooling results in increased mobilized unit side friction above the null point, and reduced mobilized unit side friction below the null point.

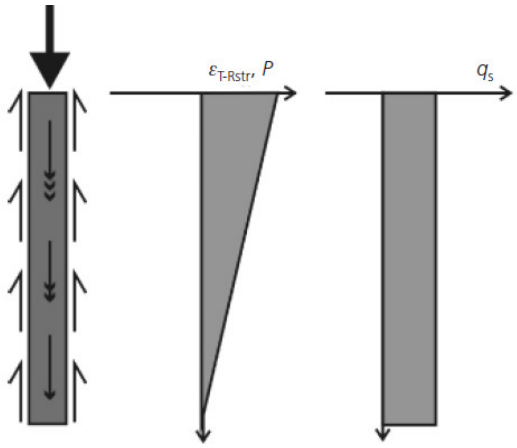

Figure 2-1 – Pile response to mechanical load only, no end restraint (from Bourne-Webb et al. 2013)

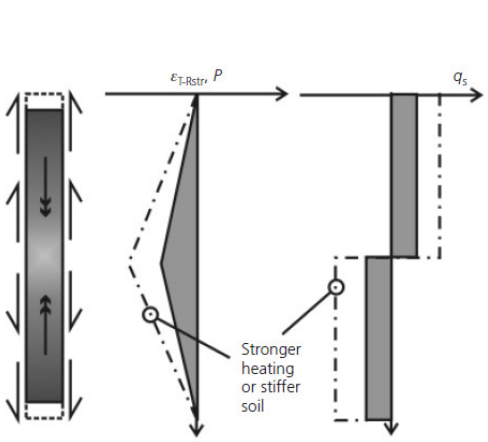

Figure 2-2 – Pile response to cooling, no end restraint

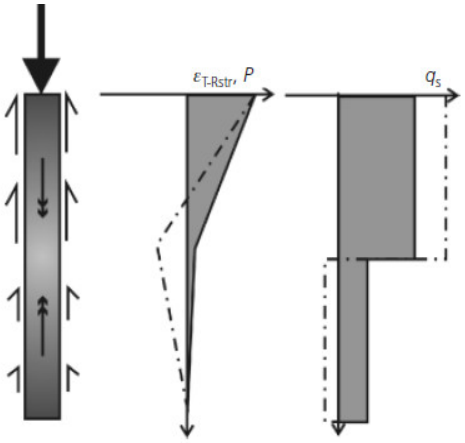

Figure 2-3 – Pile response to combined loading and cooling, no end restraint

(from Bourne-Webb, Amatya, and Soga 2013)

Figure 2-4 shows the response of a pile to a heating load only, with no end restraint. Combining Figure 2-1 and Figure 2-4 via superposition results in Figure 2-5, which shows the thermo-mechanical pile response in the case of combined mechanical load and heating, without end restraint. It can be seen that depending on the intensity of the induced temperature change and the degree of soil restraint, there is potential for additional compressive axial forces to develop during heating. It can also be seen that pile expansion due to heating results in decreased mobilized unit side friction above the null point, and increased mobilized unit side friction below the null point.

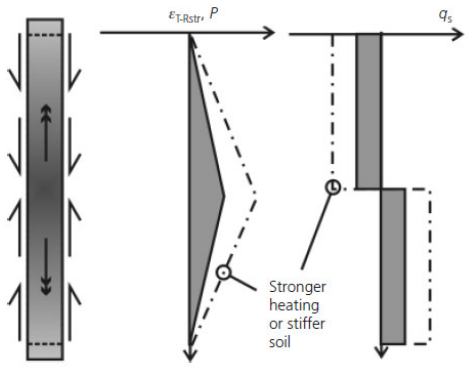

Figure 2-4 – Pile response to heating, no end restraint

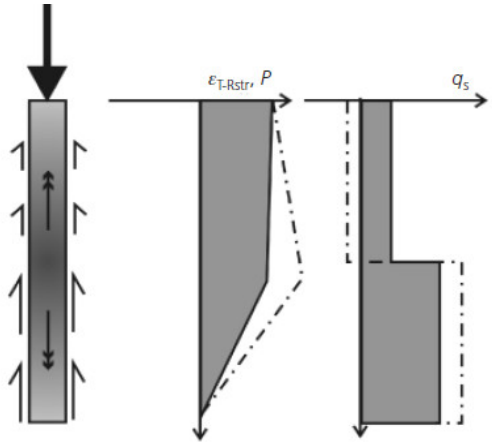

Figure 2-5 – Pile response to combined load and heating, no end restraint

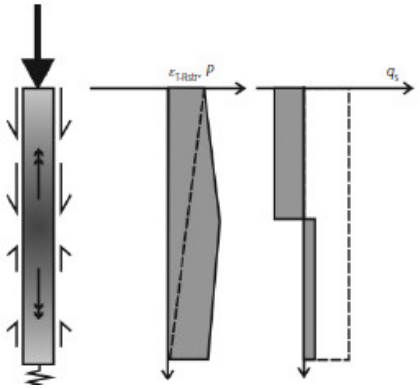

Figure 2-6 – Pile response to combined load and heating, with base restraint

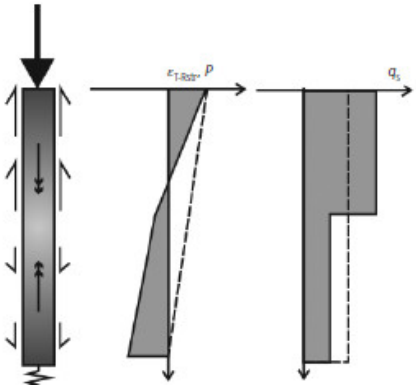

Figure 2-7 – Pile response to combined load and cooling, with base restraint

(from Bourne-Webb, Amatya, and Soga 2013)

In the presence of a base restraint (for example, a rock socket), the thermo-mechanical pile response under heating and cooling are shown on Figure 2-6 and Figure 2-7, respectively. It can be seen that in the case of heating, the pile is unable to move downward during expansion due to the base restraint. Therefore, an increase in pile toe

forces and a reduction in mobilized unit side friction occur. In the case of cooling, the contraction of the pile can result in tensile forces, especially at the pile toe.

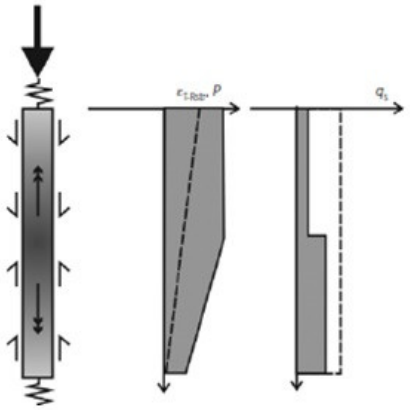

Figure 2-8 – Pile response to combined load and heating, with restraint on both ends

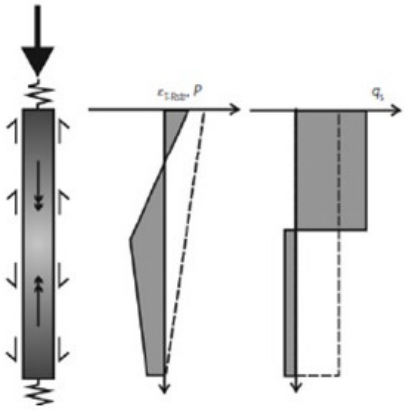

Figure 2-9 – Pile response to combined load and cooling, with restraint on both ends

Lastly, if the pile is restrained on both ends (i.e., due to rock socket at the base and the pile cap at the head) the thermo-mechanical pile response under heating and cooling are shown on Figure 2-8 and Figure 2-9, respectively. In the case of heating, the introduction of a restraint at the pile head results in additional compressive forces occurring there. In the case of cooling, the contraction of the pile can result in tensile forces, especially at the null point.

It has also been shown that even though the thermal effects propagate more in the soil than mechanical loads, the induced strains in the surrounding soils are relatively small and do not cause large changes in pore pressures and hence the effective stresses (Laloui et al., 2006); however, the thermal loading imposed by energy piles can result in changes

in pore pressures around the pile for low permeability soils, changing effective stresses and hence the contact pressure and mobilized side friction (Dupray et al., 2014). Further, prolonged periods of pile heating (without any cooling periods to balance) can induce long-term creep settlement in high plasticity, normally consolidated fine-grained soils (Akrouch et al., 2014). On the other hand, extensive periods of pile cooling can lead to ground freezing around the pile, which has significant implications on pile mechanical and thermal behavior; however, design of energy piles dictates that the ground temperatures be kept above freezing to prevent such issues (Brandl, 2006).

With regards to the impact of thermal cycles on the shaft resistance, studies show that while temperature changes in the pile leads to increases or decreases in the shaft resistance due to changes in contact pressure, depending on whether or not the pile is heated or cooled (heating results in volumetric expansion and increased radial pressure, and vice versa) and on the soil type, the mobilized friction is typically below the ultimate available friction. As such, significant changes in ultimate shaft resistance and/or significant permanent displacements are unlikely to occur as a result of thermal cycles in the typical operational temperature range of energy piles (Brandl, 2006, Laloui et al., 2006, Bourne-Webb et al., 2009, Loveridge and Powrie, 2013, Stewart and McCartney, 2013). However, significant changes in side friction behavior may occur if larger than typical temperature gradients are imposed. McCartney and Rosenberg (2011), using centrifuge testing, found a 40 percent increase in side shear above that of baseline foundations tested at ambient temperature when heated from 15 degrees Celsius to 60 degrees Celsius.

While the thermal loading imposed by energy piles can affect behavior of the pile and soil around the pile, studies have also shown that from a design perspective, the

resulting forces and displacements imposed under typical operating conditions (with an induced temperature differential on the order of ±10 to 20 degrees Celsius relative to the baseline ground temperature) are able to be withstood by the typical factors of safety used for conventional pile design parameters. Increasing the factors of safety does not provide better serviceability but can increase costs significantly (Brandl, 2006, Suryatriyastuti et al., 2012, Loveridge and Powrie, 2013, Mimouni and Laloui, 2014). In this regard, it has been suggested that the thermo-hydro-mechanical pile behavior has reached a state of mature understanding and several robust constitutive models are available for engineers; therefore, some of the focus should be shifted to other areas including optimizing heat transfer characteristics of energy foundations (Laloui et al., 2014, Olgun and McCartney, 2014, Loveridge et al., 2015, Sanchez et al., 2016).

2.1.2 Thermal Behaviour

More recently, researchers have also focused on the factors affecting the thermal performance of energy pile foundations. There are numerous factors that impact the thermal performance of an energy pile system, including:

- Thermal properties of the geomaterials, thermal properties surrounding an energy pile
- Thermal properties of the grout/concrete used in the pile
- Pile properties such as length, diameter and concrete cover depth
- Circulation pipe properties (including number and length of pipes, the configuration of pipes such as U-shape vs. W-shape vs. helical shape, and pipe spacing)
- Flow rate/velocity of the circulation fluid

- Initial and boundary conditions (including initial ground temperature, groundwater flow, solar recharge/other heat sources, etc.).

Through the use of numerical simulations, thermal conductivity of the geomaterials surrounding an energy pile has been identified as a key factor in influencing heat transfer (Abdelaziz et al., 2011, Congedo et al., 2012). All else being equal, as thermal conductivity increases, the thermal diffusivity also increases, allowing more rapid heat exchange between the pile and the surrounding geomaterials.

Thermal conductivity of the concrete/grout material which determines the thermal resistance of the system is another factor influencing heat transfer around an energy pile. In general, it has been shown that increasing thermal conductivity of the concrete/grout material results in lower thermal resistance and improved heat transfer (Allan, 1997, Abdelaziz et al., 2011, Desmedt et al., 2012, Lee et al., 2012, Cecinato and Loveridge, 2015). The addition of sand to a cement based grout results in higher thermal conductivity, with neat cement or bentonite cement grout mixtures resulting in lower thermal conductivity (Allan, 1997, Lee et al., 2012, Alrtimi et al., 2013). The use of additives such as slag or fly ash (which act as insulators), or increasing water content (which increases porosity of the mixture) also reduce the thermal conductivity (Allan, 1997, Bentz et al., 2011). On the other hand, the addition of a small amount of a highly conductive material such as graphite has been shown to increase the thermal conductivity of the grout material significantly (Lee et al., 2012, Erol and Francois, 2013, Wadso, 2015). It should also be noted that the impact of increased concrete/grout thermal conductivity decreases when the pile is surrounded by low thermal conductivity geomaterial (such as dry soil), due to poor heat transfer characteristics of such materials (Erol and Francois, 2013).

Properties such as diameter, length and number/shape of circulation pipes have also been shown to be important factors. In particular, greater length of pile and circulation pipes have been shown to increase heat transfer because of the increased pipe surface area available for convective heat transfer, provided that detrimental pipe-to-pipe interactions do not occur (Bozis et al., 2011, Jalaluddin and Miyara, 2012, Lee et al., 2012, Loveridge and Powrie, 2014, Batini et al., 2015, Cecinato and Loveridge, 2015, Kaltreider et al., 2015). All else being equal, a larger pile diameter results in improved heat transfer provided that the thermal conductivity of the concrete/grout is greater than that of the surrounding geomaterials (Loveridge and Powrie, 2014, Cecinato and Loveridge, 2015). It is also important to note that it may take larger diameter energy piles a significantly longer time to reach steady-state compared to smaller piles, which has implications with regards to design, as methods that assume steady-state thermal resistance can result in less efficient designs because the heat storage capacity of the larger pile element is neglected (Loveridge and Powrie, 2014).

In a traditional energy pile system, the number and/or configuration of circulation pipes is geometrically constrained by the space available between the edge of the pile and the reinforcing cage in the middle (i.e., the concrete cover depth). In this regard, a smaller amount of cover results in the pipes being closer to the surrounding geomaterials (i.e., reduced thermal resistance) and allows pipes to be spaced further apart, reducing detrimental pipe-to-pipe interactions and resulting in increased heat transfer (Caulk and Ghazanfari, 2015, Cecinato and Loveridge, 2015). The shape of the circulation pipes is also an important factor. Studies generally indicate that a W-shaped pipe has higher thermal performance than a U-shaped pipe (Gao et al., 2008, Batini et al., 2015, Caulk and

Ghazanfari, 2015). Some researchers have also investigated the use of spiral/helical pipes instead of the more conventional U-shaped pipes, with the helical configuration yielding higher thermal performance than U-shaped pipes (Cui et al., 2011, Congedo et al., 2012, Zarrella et al., 2013) due to increased pipe surface area available for convective heat transfer.

Fluid flow rate/velocity is another important factor influencing heat transfer, with higher velocities increasing efficiency of heat transfer due to increased heat transfer coefficient associated with turbulent flow, up to the point of turbulent flow beyond which the benefits diminish (Brandl, 2006, Gao et al., 2008, Congedo et al., 2012, Batini et al., 2015, Kaltreider et al., 2015). However, achieving turbulence requires the use of costlier high-performance pumps (Brandl, 2006).

2.1.3 Sustainability Considerations

In Switzerland, Dock Midfield at the Zurich Airport was built on 440 foundation piles, 300 of which were installed as energy piles. Long-term monitoring of the system performance indicated that approximately 85 percent of the heating demand and 50 percent of the cooling demand were able to be met with the energy pile foundations alone. It was also determined that the annual energy costs were reduced by about 54 percent. An economic analysis showed that the simple payback period (i.e., payback period where the interest of the invested capital is not taken into account) was 8 years (Pahud and Hubbuch, 2007, De Moel et al., 2010).

In Belgium, a hospital constructed using a combination of ground source heat pumps (GSHPs) and energy piles for cooling realized that 78 percent of the total cooling energy

demand of the hospital could be met by these systems, resulting in electricity savings on cooling of about 56 percent, reduction of about 10 percent in overall annual energy costs, and a reduction in $C0_2$ emissions by about 7 percent. The simple payback period for this example was about 11 years (Desmedt and Hoes, 2006).

In Germany, the International Solar Center in Berlin was constructed on 196 energy piles to meet 15 percent of the heating and 100 percent of the cooling demands (Himmler and Fisch, 2005, De Moel et al., 2010).

These examples indicate that based on the recent design approaches, shallow thermo-active foundations such as energy piles alone are typically not capable of completely meeting the heating or cooling demands of a large building. Additionally, the upfront cost of these systems associated with drilling and installation is a major barrier to more widespread adoption (Sanchez et al., 2016). In this regard, increasing the thermal performance of these systems can help them to fully meet the heating and cooling demands of larger structures, and using fewer but higher performing elements can reduce the upfront capital and construction costs.

It should also be noted that in the context of thermo-active foundations, sustainability and renewability are co-dependent. For example, if the heat injection and extraction rates are unbalanced, then the extracted energy cannot be replenished and through this unsustainable use, the geothermal source is no longer renewable (Hahnlein et al., 2013). In areas where heating and cooling demands are particularly unbalanced, this energy balance requirement raises the possibility of using fewer but higher performing elements operated in a preferential pattern to maximize heat transfer and allow sufficient time for recovery.

2.2 Heat Transfer in Thermo-Active Foundations

In general, there are three main modes of heat transfer: conduction, convection, and radiation. Conduction can be described as "the transport of energy in a medium due to a temperature gradient, and the physical mechanism is one of random atomic or molecular activity" (Bergman et al., 2011). Convection can be described as "energy transfer between a surface and a fluid moving over a surface" (Bergman et al., 2011), and consists of two mechanisms: energy transfer by the bulk fluid motion (advection), and energy transfer the random motion of fluid molecules (diffusion). Lastly, radiation is the energy emitted by matter at non-zero temperature, and the mechanism is the change in electron configurations of the constituent atoms or molecules. The energy is transported by electromagnetic waves, or alternatively by photons, and no medium is required for energy transfer to take place (Bergman et al., 2011).

In a thermo-active foundation consisting of a circulation tube embedded inside the foundation surrounded by geomaterials, radiative heat transport can be considered negligible for the ground temperatures typically associated with these foundations (~2 to 40 degrees Celsius), although radiation can contribute significantly to heat transfer at high temperatures (~500 degrees Celsius and above), especially for dry, large coarse-grained particles (Rees et al., 2000, Nasirian et al., 2015). Significant heat transfer can also occur due to freeze-thaw; however, the design of thermo-active foundations stipulates that ground freezing and thawing be avoided (Brandl, 2006).

Thus, heat transfer in thermo-active foundations primarily takes place via the following modes (Figure 2-10): convective heat transfer due to fluid flow in the circulation

pipes, conductive heat transfer across the circulation pipe walls, conductive heat transfer through the foundation material (such as concrete), then a combination of conductive and convective heat transfer in the geomaterials surrounding the pile element.

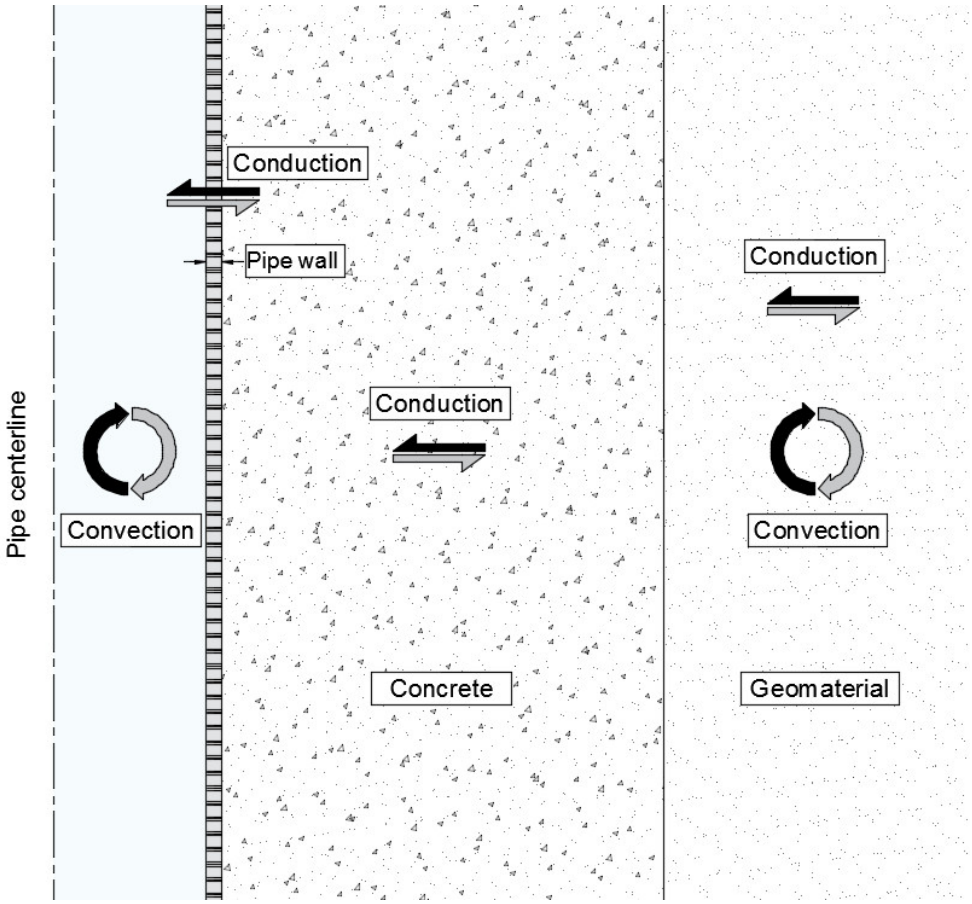

Figure 2-10 – Primary heat transfer modes in a thermo-active foundation with fluid circulation pipe embedded in concrete and surrounded by geomaterial (not to scale)

2.2.1 Heat Transfer for Pipe Flow

For fluid flowing through a pipe, in addition to conduction and mass transport, heat transfer also occurs due to friction heat dissipated due to viscous shear, conductive heat transfer through the pipe walls, as well as due to pressure work. For an incompressible

Newtonian fluid, the resulting equation for heat transfer can be expressed as follows (Lurie, 2008, Bergman et al., 2011):

$$\frac{\partial T}{\partial t} = \frac{\boldsymbol{k}\,\nabla^2 \mathrm{T}}{\rho\, C_v} - \vec{\boldsymbol{u}} \cdot \nabla T + \frac{f_D \cdot |\vec{\boldsymbol{u}}|^3}{C_v\, 2d_h} + \frac{Q_{wall}}{\rho\, A\, C_v} + \frac{q_v^T}{\rho\, C_v} + \frac{Q_p}{\rho\, A\, C_v} \qquad (1)$$

Where:

f_D = Darcy friction factor (dimensionless)

d_h = mean hydraulic diameter of pipe (m)

$Q_{wall} = h\, Z\, (T_{ext} - T)$ = heat transfer through the pipe wall (W/m)

h = heat transfer coefficient (W/m^2-K)

Z = pipe wall perimeter (m)

T_{ext} = external temperature outside the pipe (K)

A = pipe cross-sectional area (m^2)

Q_p = pressure work (W/m)

In Equation (1), the first term on the right is the diffusion term and the second is the advection term. The third term on the right corresponds to friction heat dissipated due to viscous shear (where the Darcy friction factor is a function of the Reynolds number, or the flow regime – laminar or turbulent), as well as the surface roughness and hydraulic diameter of the pipe. In the fourth term, the heat transfer coefficient (h) is a function of the

Nusselt number (which is constant dependent on cross section for laminar flow, and varies according to the Reynolds number and the Prandtl number for turbulent flow), the thermal conductivity of the pipe material, and the hydraulic diameter of the pipe.

It can be seen from Equation (1) that thermal properties of the fluid and fluid velocity, as well as the physical properties of the circulation pipes have important implications on heat transfer from the circulation pipes to the surrounding concrete (or other material in which the pipes may be embedded).

2.2.2 Heat Transfer in Geomaterials

From the energy balance for a given volume, the heat stored is the sum of the heat flux and heat generated from a volumetric heat source. This can be expressed in differential form as follows:

$$-\nabla \cdot \boldsymbol{q}^T + q_v^T = \frac{\partial \xi_T}{\partial t} \tag{2}$$

Where $\boldsymbol{q}^T$ is the heat flux vector (W/m^2), q_v^T is the volumetric heat source intensity (W/m^3), and ξ_T is the heat stored per unit volume (J/m^3).

In general, temperature changes may be caused by changes in both energy storage and volumetric strain. The thermal constitutive law relating these parameters can be expressed as follows:

$$\frac{\partial T}{\partial t} = M_T \left(\frac{\partial \xi_T}{\partial t} - \beta_v \frac{\partial \epsilon}{\partial t} \right) \tag{3}$$

Where M_T and β_v are material constants, and ϵ is strain. Assuming strain changes have negligible impact on temperature (i.e., β_v=0), this equation can be rewritten as follows:

$$\frac{\partial T}{\partial t} = M_T \left(\frac{\partial \xi_T}{\partial t}\right) \tag{4}$$

Or

$$\frac{\partial \xi_T}{\partial t} = \rho C_v \frac{\partial T}{\partial t} \tag{5}$$

Where ρ is the mass density (kg/m^3), C_v is the specific heat at constant volume (J/kg-K), and the constant M_T can be determined as $M_T = 1\ /(\rho C_v)$.

Substituting into the energy balance equation, the following expression is obtained:

$$-\nabla \cdot \boldsymbol{q}^T + q_v^T = \rho C_v \frac{\partial T}{\partial t} \tag{6}$$

From Fourier's Law for heat conduction and considering heat transfer due to mass transport, the total heat flux equation for a known velocity field ($\boldsymbol{u}$) can be expressed as follows:

$$\boldsymbol{q}^T = -\boldsymbol{k}\,\nabla T + \rho C_v\, \boldsymbol{u}\, T \tag{7}$$

Where T is the temperature (in K), $\boldsymbol{u}$ is the tangential velocity field (m/s), and $\boldsymbol{k}$ is the bulk thermal conductivity (W/m-K). The energy balance equation can then be expressed as follows:

$$-\nabla \cdot (-\boldsymbol{k}\,\nabla T + \rho C_v\,\boldsymbol{u}\,T) + q_v^T = \rho C_v \frac{\partial T}{\partial t} \tag{8}$$

Or

$$\boldsymbol{k}\,\nabla^2\mathrm{T} - \rho C_v\,\boldsymbol{u}\,\nabla T + q_v^T = \rho C_v \frac{\partial T}{\partial t} \tag{9}$$

In granular materials, for particles less than 6 mm (i.e., gravel sized), heat transfer via convection (namely, the advection component of convection) is negligible in comparison to conduction. Therefore, in the absence of an internal heat generating source, the primary heat transfer mechanism between an energy pile and the surrounding geomaterials is due to conduction (Brandl, 2006, Cortes et al., 2009, Arson et al., 2013, Nasirian et al., 2015), and Equation (9) can be simplified as follows:

$$\frac{\partial T}{\partial t} = \alpha\nabla^2\mathrm{T} \tag{10}$$

Where α is the thermal diffusivity; $\alpha = \boldsymbol{k}/(\rho C_v)$

From Equation (10), it can be seen from that the thermal properties of the material surrounding the circulation tubes (typically grout or concrete), as well as the thermal properties of the geomaterial surrounding the pile, play an important role in conduction heat transfer. A high value of thermal diffusivity, which is the ratio of a material's ability

to conduct heat to its ability to store it, implies a capacity for rapid and considerable changes in temperature. In this regard, one of the most important material properties influencing heat conduction is thermal conductivity. Specific heat capacity plays an important role in heat conduction as well.

2.3 Thermal Conductivity of Geomaterials

2.3.1 Soil

The effect of the various factors influencing thermal conductivity of soils can be summarized in general terms as shown in Table 2-1.

Table 2-1 – Summary of factors affecting soil thermal conductivity

Factor	**Generalized Effect**
Saturation	k increases rapidly up to critical moisture content; relatively little increase thereafter.
Density / gradation	k increases with increased density (decreased porosity); a small amount of fines can improve k by acting as binder and improved density
Mineralogy	k increases with increasing k_{solid}
Effective stress	k increases with increasing effective stress
Pore fluid composition	k increases as k_{fluid} increases
Particle size / shape	k increases with increasing particle size, and with increasing angularity
Temperature	k increases with increasing temperature, though the increase is very small for the range of temperatures associated with thermo-active foundations
Microstructure	k increases with enhanced effective contact area due to flattening of surface roughness, cementation, and creep/diagenesis.

From a macroscale perspective, the three primary factors that influence bulk thermal conductivity can be described as density (which is a function of packing, soil structure, soil type, and gradation), degree of saturation, and soil composition (Salomone and Kovacs, 1984). Soil mineralogical composition plays an important role in soil thermal conductivity as well. There are also other factors (such as pore fluid composition, effective stress, etc.) that influence thermal conductivity to a lesser degree. These factors are discussed in further detail below.

2.3.1.1 Packing, Porosity and Structure

For dry, coarse-grained soils, which have a granular contacting skeleton, thermal conduction is governed by the quality of interparticle contacts and number of contacts per unit volume (i.e., coordination number). As packing density/coordination number increases and porosity decreases, thermal conductivity of the dry soil increases in a linear fashion. From a macroscale perspective, porosity is the most important parameter influencing thermal conductivity in dry soils (Salomone et al., 1984, Yun and Santamarina, 2008, Cortes et al., 2009, Nasirian et al., 2015).

Thermal conductivity for fine-grained soils, which do not have a granular contacting skeleton, is governed by the structure of the particles (dispersed, blocky or flocculated). Structures with fewer air gaps (i.e., blocky or dispersed) tend to have higher thermal conductivity compared to structures with more air gaps (i.e., flocculated). Increased density (i.e., removal of air voids) will lead to higher thermal conductivity, although in general thermal conductivity of fine grained soils is lower than that of coarse-grained ones (Farouki, 1981a, Salomone et al., 1984, Cote and Konrad, 2005).

For intermediate soils (i.e., mixture of coarse and fine grained particles), the thermal conductivity depends on the volumetric proportion of the particles. Adding a small of amount of fine-grained particles to a coarse-grained mixture to create a well-graded mixture can increase thermal conductivity by increasing dry density and number of contacts (Farouki, 1981a, Wallen et al., 2016).

The amount of heat conduction is a balance between the conductivity of the individual grains and the size of the contact between them. It has been shown that conduction between particles is directly proportional to particle size and inversely proportional to the inter-contact distance (Batchelor and O'Brien, 1977). This means that the presence of larger particles leads to higher thermal conductivity (Yun and Santamarina, 2008, Cortes et al., 2009). Thermal contact resistance decreases (hence thermal conductivity increases) with increasing quality and number of contacts, which in turn increases with soil compaction (i.e., reduced porosity); therefore, angular/sub-angular particles (such as crushed rocks) which lend themselves to better compaction have higher thermal conductivity than natural, rounded/sub-rounded particles (Kersten, 1949, Farouki, 1981a, Tarnawski et al., 2002, Cote and Konrad, 2009).

2.3.1.2 Degree of Saturation

Saturation has a notable impact on thermal conductivity. As water is added to dry soil, a thin adsorbed water film develops around the points of contact between the particles, increasing the effective contact area and acting as a relatively high conductivity thermal bridge between the particles. In addition, the low conductivity air voids are displaced by higher conductivity water. These changes result in increasing thermal conductivity, especially at the initial stages of saturation. As more water is added and the soil approaches

a wet condition, the effective contact area no longer increases with increasing water content, and the thermal conductivity stays relatively constant. The water content beyond which thermal conductivity remains relatively constant depends on the particle shape, density and gradation (Farouki, 1981a, Salomone and Kovacs, 1984, Salomone and Marlowe, 1989). This "critical" water content for most soils coincides with the optimum moisture content from a compaction (i.e. Proctor) test, except for low density clays where the critical moisture content coincides with the plastic limit where there is usually no intermediate free water (Farouki, 1981a, Salomone et al., 1984). At the optimum moisture content, a more orderly (i.e., closely packed for coarse-grained soils and more dispersed for fine-grained soils) structure is achieved, resulting in maximum dry density, reduced contact resistance, and higher thermal conductivity (Beziat et al., 1988).

The effect of moisture content on the thermal conductivity of soils also depends on whether the soil is in the wetting or the drying phase (Farouki, 1981a). Research in this area is relatively limited; however, all else being equal, soil thermal conductivity appears to be higher during the drying phase then it is during the wetting phase, especially for finer grained soils (Philip, 1964, Farouki, 1981a, Bristow, 1998, Rubio et al., 2011). A similar hysteretic effect can be observed in the water retention curve for soils due to suction.

2.3.1.3 Mineralogical Composition

The thermal conductivity for solid particles is typically on the order of 2 to 3 W/m-K, while the thermal conductivity for water and air are approximately 0.6 and 0.025 W/m-K, respectively (Cote and Konrad, 2005, Yun and Santamarina, 2008). In particular, quartz particles have very high thermal conductivity. Quartz is an anisotropic material whose

thermal conductivity depends on crystallographic orientation. Depending on the orientation, the thermal conductivity of quartz can range between 6.5 and 11.3 W/m-K (Tarnawski et al., 2012). Typically, the bulk thermal conductivity of randomly oriented quartz crystals is used, taken as a weighted geometric mean with a value of about 7.7-7.8 W/m-K. This indicates that the mineralogy of the solid particles can have a significant impact on bulk thermal conductivity, especially those containing a significant amount of quartz (Cote and Konrad, 2005, Cortes et al., 2009, Tarnawski et al., 2009). On the other hand, soils with high organic content have lower thermal conductivity (Salomone and Kovacs, 1984, Abu-Hamdeh and Reeder, 2000).

2.3.1.4 Effective Stress, Pore Fluid Composition, Temperature and Microstructure

Some of the other factors that influence thermal conductivity of soils include effective stress, pore fluid composition, temperature, and microstructure effects.

An increase in effective stress leads to increased thermal conductivity due to increased packing density, coordination number and contact quality, and increased contact area. The increase in contact area between coarse grained particles follows classical Hertz theory of contact (Farouki, 1981a, Cortes et al., 2009). The bulk thermal conductivity increases with increasing thermal conductivity of the pore fluid, with the increase being in almost direct proportion when the conductivity of the saturating fluid is small compared to that of the solid grains (Woodside and Messmer, 1961).

Temperature can have a significant effect on thermal conductivity, especially below the freezing point in water-saturated soils, given that ice has a thermal conductivity about four times greater than water (Farouki, 1981b). However, as previously mentioned, the

design of thermo-active foundations stipulates that ground freezing and thawing be avoided (Brandl, 2006); therefore, the effects of freezing on thermal conductivity are not discussed. For a temperature range of about 4 to 21 degrees Celsius, which is in the typical range of ground temperatures associated with energy foundations, Kersten (1949) reported an approximately 4 percent increase in thermal conductivity with increasing temperature. Other researchers have also found that for temperatures of up to about 30 degrees Celsius, there is relatively little increase in thermal conductivity with temperature, likely because heat transfer in the low temperature range is dominated by conduction through the moist soils with limited heat transfer due to vapor migration (Nikolaev et al., 2013). In typical engineering applications related to shallow energy foundations, the slight variation in thermal conductivity with respect to temperature may be neglected (Salomone and Marlowe, 1989).

At the microstructure level, thermal conductivity increases with enhanced effective contact area due to flattening of surface roughness, cementation, and creep/diagenesis (Yun and Santamarina, 2008). The cementation effect is particularly important when the material is dry, and less important when the material is saturated with water (Farouki, 1981a). For example, it has been shown that cementation caused by microbially induced calcite precipitation (MICP) can increase the thermal conductivity of sands up to 250 percent under dry conditions and about 25 to 50 percent in the saturation range between 0.2 and 0.8 (Venuloe et al., 2016). The enhancement is attributed primarily to the formation of calcite crystals, which act as thermal bridges by increasing the contact area between particles. Martinez et al. (2018) reported similar trends in improvement of thermal conductivity based on tests performed on MICP treated sands at varying degrees of saturation; up to 330 percent

improvement was observed for dry sands, and approximately 15 to 25 percent in saturation range between 0.3 and 1.0.

2.3.2 Rock

The primary focus of this study is soil, given that shallow thermo-active foundations are often constructed in soils. However, a brief overview of thermal conduction in rock is provided for completeness.

Thermal conduction in rocks takes place through the contacts and across the fracture plane between intact blocks, as well as along the air and/or liquid filled voids. Increasing the number of fractures/discontinuities (e.g. partially weathered rock) increases the thermal resistance and results in lower thermal conductivity (Roshankhah, 2015).

Intact rocks, in particular sedimentary rocks, can be treated as cemented soils. Similar to soils, thermal conductivity of rock depends on the number and quality of the contacts (which in turn is a function of the degree of cementation, effective stress and degree of saturation), as well as temperature, the mineralogical composition of the solids, and the properties of the pore-fluid (Robertson, 1988, Salomone and Marlowe, 1989, Eppelbaum et al. 2014, Roshankhah, 2015).

The thermal conductivity of porous and soft rocks is more sensitive to effective stress than hard, crystalline rocks. An increase in effective stress closes the micro-fractures, but only up to a characteristic stress level beyond which the thermal conductivity does not increase with increasing stress (Walsh and Decker, 1966, Roshankhah, 2015).

2.4 Specific Heat Capacity of Geomaterials

The specific heat capacity is another important parameter influencing heat transfer in geomaterials. Specific heat capacity refers to the capability of a material to store heat. It can also be thought of as the amount of energy required to raise the unit temperature of a mass of a substance by one degree (Celsius or Kelvin). Specific heat capacity can be measured under constant pressure or constant volume. For an incompressible material, the specific heat capacity at constant pressure is equal to the specific heat capacity at constant volume (Eppelbaum, 2014).

For a geomaterial consisting of solid minerals, pore fluid and air, the specific heat capacity can be calculated by summing the specific heat of each component in proportion to the volumetric percentage as follows (Salomone and Marlowe, 1989):

$$c = X_s\, c_s + X_w\, c_w + X_a\, c_a \tag{11}$$

Where c is the composite specific heat capacity (J/kg-K), X_i is the volumetric percentage of individual components, and c_i is the specific heat capacity of individual components (J/kg-K). The heat capacity of geomaterials (C_H) can also be expressed in terms of the mass of the individual components, as follows (Abu-Hamdeh, 2003):

$$C_H = m_s\, c_s + m_w\, c_w + m_a\, c_a \tag{12}$$

Where C_H is the heat capacity (J/K) and m_i is the mass of individual components (kg). Assuming the mass of air to be negligible, the heat capacity of a two-phase geomaterial can then be expressed as follows:

$$C_H = m_s c_s + m_w c_w \quad (13)$$

Or

$$(m_s + m_w)c = m_s c_s + m_w c_w \quad (14)$$

Dividing by the total volume of the soil sample, the relationship can be expressed in terms of bulk density as follows:

$$\rho c = \rho_d c_s + \rho_d w c_w \quad (15)$$

Where w is the gravimetric moisture content, ρ is the wet bulk density, and ρ_d is the dry bulk density. Since the volumetric heat capacity (C_V) of a geomaterial is the product of its bulk density and specific heat capacity ($C_V = \rho c$), the volumetric heat capacity of a moist geomaterial can be expressed as follows:

$$C_V = \rho_d c_s + \rho_d w c_w \quad (16)$$

Where C_V has the units if J / m^3-K.

In terms of specific heat capacity, the above relationship can be expressed as follows:

$$c = \frac{\rho_d (c_s + w c_w)}{\rho} \quad (17)$$

Or

$$c = \frac{(c_s + wc_w)}{(1 + w)} \tag{18}$$

From the relationship above, it can be seen that the specific heat capacity of a two-phase geomaterial is a function of the specific heat capacity of the solids, water content, and the specific heat capacity of the pore fluid.

CHAPTER 3. INDEX PROPERTIES AND MINERALOGICAL COMPOSITION OF PIEDMONT RESIDUAL SOILS

The Piedmont physiographic region is located within the Appalachian Highlands Geologic Province in the eastern United States, extending from central Alabama in the south to New Jersey in the north. Several major U.S. cities are located within the region, including Atlanta, GA; Charlotte, NC; Washington, DC; Baltimore, MD; and the Philadelphia, PA metropolitan area. The exposed surface extent is approximately 1,200 kilometers long and up to 200 kilometers wide, and is bordered by the Atlantic Coastal Plain region to the east and mostly bounded by the Blue Ridge Mountains to the west. The region is characterized by a "monotonous topography of low rounded ridges and ravines largely underlain by saprolite on crystalline rocks" (Hack, 1982). The bedrock typically includes pre-dominances of schist, gneiss, and granite (Mayne et al., 2000). The saprolite or residual soils were weathered in place due to chemical and mechanical processes, and the subsurface profile is typically characterized by a gradual transition from soil to decomposed rock (often referred to as Partially Weathered Rock) to unweathered rock with depth (Sowers and Richardson, 1983, Klein and Trimble, 2008).

In this chapter, the results from a laboratory testing program are presented where six (6) different samples of Piedmont residual soils collected from several locations around the state of Georgia (see Figure 1-5) were analyzed using index tests (grain size and Atterberg Limits), as well as X-ray diffraction (XRD) and X-ray fluorescence (XRF) tests. The soils tested represent the general range of conditions that may be encountered in the Piedmont physiographic region. The XRD test data were used to identify the crystalline mineral phases,

and XRF tests were used to determine the percentage of silica oxides in the samples. Two predictive methods were then used for estimating quartz content of the samples based on grain size data, and the results were compared to the apparent quartz content obtained via inverse modeling from saturated thermal conductivity measurements made on the samples. Quartz minerals are particularly important because their thermal conductivity is much higher (on the order of 8 W/m-K) than that of other soil minerals (typically on the order of 2-3 W/m-K) and water (about 0.6 W/m-K). In practical terms, this means that a soil that is rich in quartz would have a higher thermal conductivity, all else being equal.

It should be noted that a preliminary attempt was made to quantify the crystalline mineral phases by polynomial profile fitting of the XRD scans. Please refer to Wirth and Atalay (In Press) for further details.

3.1 Methodology

From the several locations sampled in the state of Georgia (see Figure 1-5), six samples were selected for further analysis based on grain size distribution and Atterberg Limits test results. Grain size distribution was determined using a combination of sieve analyses and hydrometer tests. Specific gravity of the soil samples was analyzed using a Quantachrome UltraPyc 1200e helium pycnometer at Boral Resources in Taylorsville, Georgia. The soils that range from high plasticity silts (JCS and SMS) to low plasticity clays (ATLP) and silty sands (TYRN) and clayey sands (JCC and RUBY), represent the general conditions encountered in the Piedmont physiographic region. The relevant physical properties of the samples tested are summarized in Table 3-1. The results from the grain size distribution tests are shown on Figure 3-1.

Table 3-1 – Summary of index test results for Piedmont soils

Sample ID	Sand (%)	Silt (%)	Clay (%)	G_S	LL	PI	USCS
JCS	5	62	33	2.59	61	24	MH
SMS	14	18	68	2.72	56	26	MH
ATLP	43	33	24	2.59	37	18	CL
JCC	54	26	20	2.65	53	25	SC
RUBY	62	14	24	2.65	33	15	SC
TYRN	73	22	5	2.64	NP	NP	SM

NP = Non-plastic

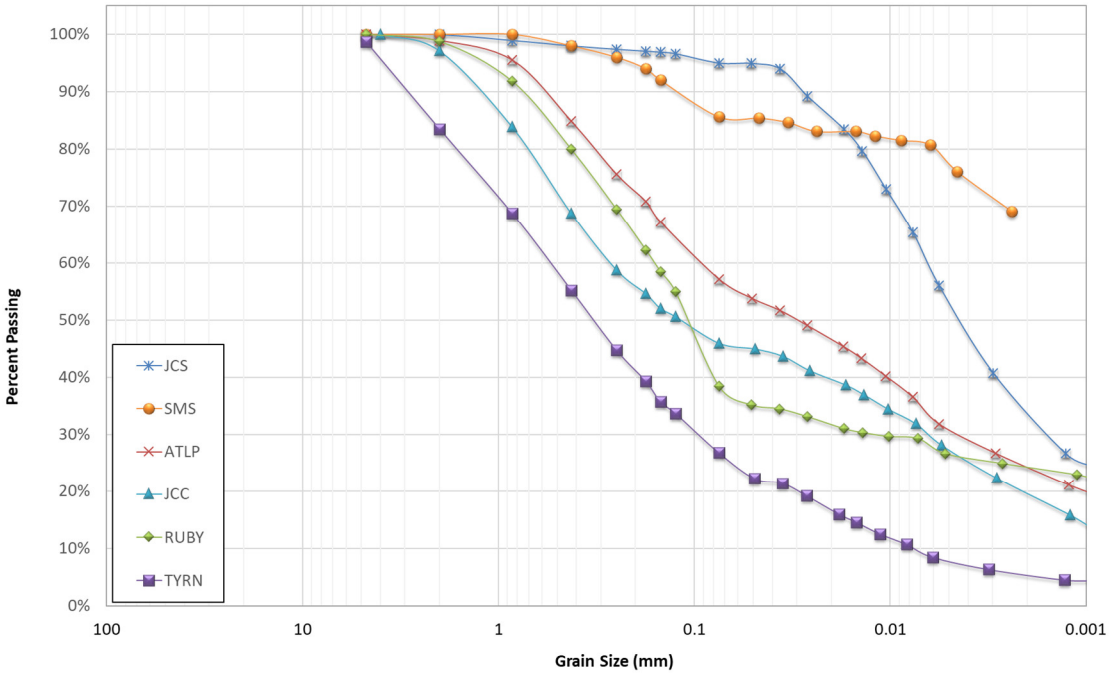

Figure 3-1 – Grain size distribution results for Piedmont soils

Prior to XRD and XRF testing, the samples were ground into a relatively uniform powder using a planetary ball mill grinder. XRF spectrometry was performed on ignited samples (Bruker S8 Tiger) after they were fused into glass beads with a lithium metaborate flux (VFD 3000) (see Figure 3-2). Powder XRD analysis was performed at Georgia Institute of Technology's IEN/IMat Materials Characterization Facility, using a Panalytical Empyrean with a Cu-K-alpha radiation source, for a 2θ range of 5 to 35° with a step size of 0.013° and 79 seconds per step.

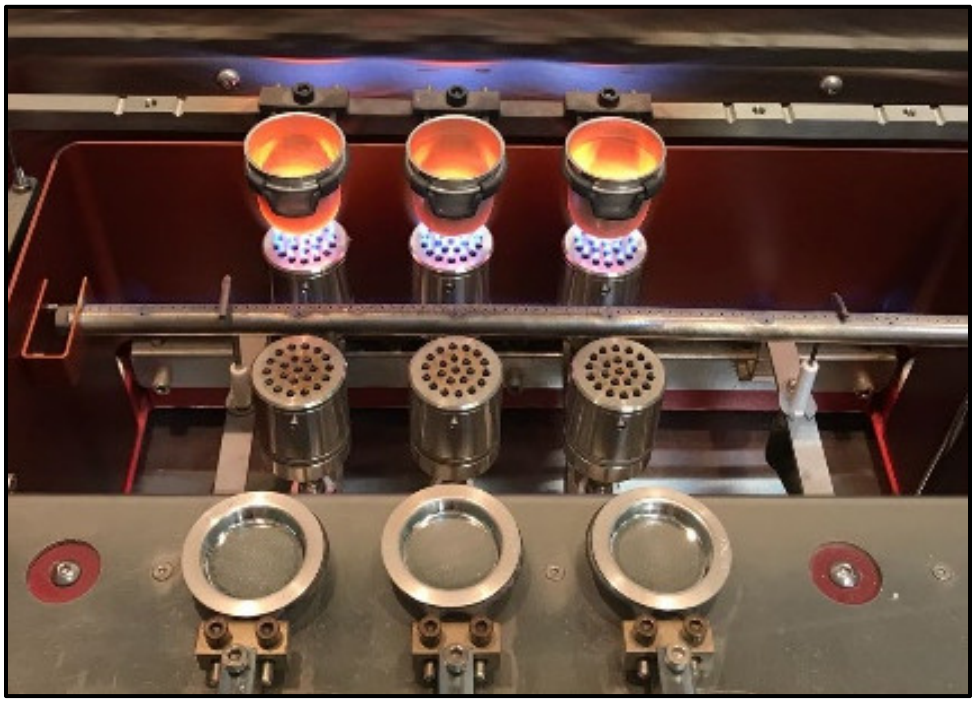

Figure 3-2 – Fusion of flux and samples for XRF

The quartz content q is typically used to estimate the thermal conductivity of the solid fraction, k_s (W/m-K), which is subsequently used in calculating the saturated thermal conductivity. In the absence of specific knowledge regarding the soil mineralogical composition, the following relationship is typically used to estimate k_s:

$$\mathrm{k_s} = (\mathrm{k_q})^{\mathrm{q}}\,(\mathrm{k_o})^{1-\mathrm{q}} \tag{19}$$

Where k_q (W/m-K) is the thermal conductivity of quartz (typically taken as 7.7) and k_o (W/m-K) is the lumped thermal conductivity of the non-quartz fraction. Johansen (1975) proposed a value of k_o = 2.0 W/m-K, except soils with a low quartz fraction ($q \leq 0.2$) in which case a value of k_o = 3.0 W/m-K was proposed.

Prior studies have made simplifying assumptions such as taking quartz content (q) to be equal to that of the sand (coarse) fraction (Peters-Lidard et al., 1998, Lu et al., 2007):

$$q = m_{co} \tag{20}$$

Where m_{co} is the coarse fraction. Others have attempted to correlate the sand and/or the sand plus silt fraction to the quartz content (Tarnawski et al., 2009, Tarnawski et al., 2012). According to Tarnawski et al. (2009), the quartz fraction can be estimated from grain size distribution results as follows:

$$q = 0.339 + 0.417 \cdot m_{co} \tag{21}$$

The form of this relationship implies that some of the fine-grained particles are expected to contain silica (quartz) as well.

On the other hand, it is possible to determine the "apparent" quartz content (q_a) of a sample via inverse modeling based on the saturated thermal conductivity (Tarnawski et al., 2011), by rearranging Equation (19):

$$q_a = \frac{ln(k_s/k_o)}{ln(k_q/k_o)} \tag{22}$$

Where k_s can be obtained from the experimentally measured saturated thermal conductivity ($k_{sat-exp}$) and porosity (n) as follows:

$$k_s = \left(\frac{k_{sat-exp}}{k_w{}^n}\right)^{1/(1-n)} \tag{23}$$

k_w is the thermal conductivity of water at standard conditions (taken as 0.6 W/m-K), and k_q and k_o as previously defined.

For this study, Equation (20) and (21) were used to estimate the quartz content of the Piedmont residual soils; then the results compared to the back-calculated apparent quartz content using Equation (22) and the saturated thermal conductivity measurements (details of which are presented in Chapter 4). The apparent quartz content results presented in the next section were taken as the average of the two different readings (corresponding to saturated thermal conductivity measurements taken at two different porosity values). The predicted and back-calculated quartz content were then compared, using XRD results as a qualitative way to explain the observed behavior. In addition, the XRF results were used to evaluate the relationship between silica oxides and the apparent quartz content.

3.2 Results & Discussion

3.2.1 X-Ray Diffraction

The mineral phases identified in the XRD scans are shown in Figure 3-3 through Figure 3-8. Primary crystalline phases in the Piedmont samples included quartz (Q), muscovite (M), gibbsite (G), kaolinite (K), montmorillonite (Mn) and feldspar (F). These findings appear to be relatively consistent with the phases identified by Pavich et al. (1989) from scans performed on Piedmont samples obtained from the state of Virginia, which identified vermiculite, muscovite, kaolinite/halloysite, quartz and feldspar as the primary mineral phases on XRD scans performed on the clay fraction. The identified phases are also generally consistent with those identified by Calvert et al. (1980) from scans performed on Piedmont samples obtained from North Carolina.

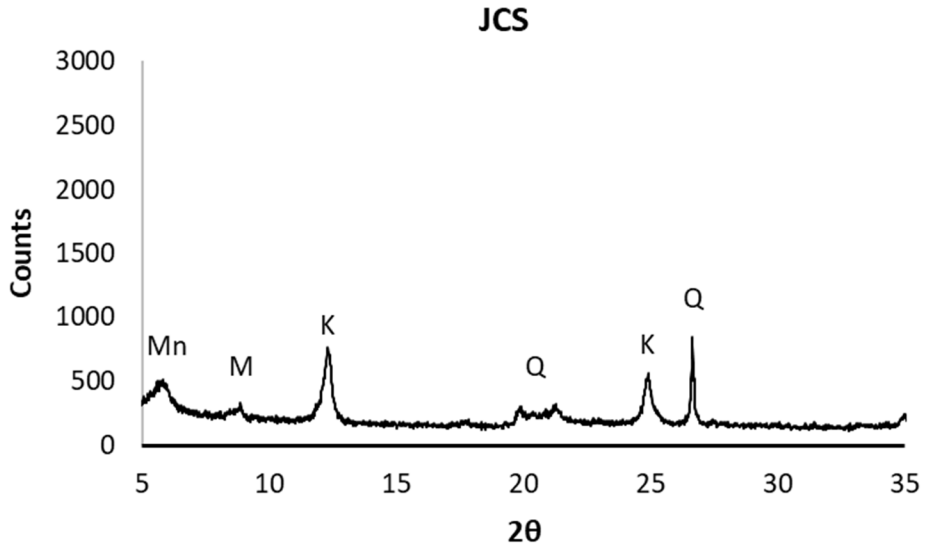

Figure 3-3 – XRD scan data for sample JCS

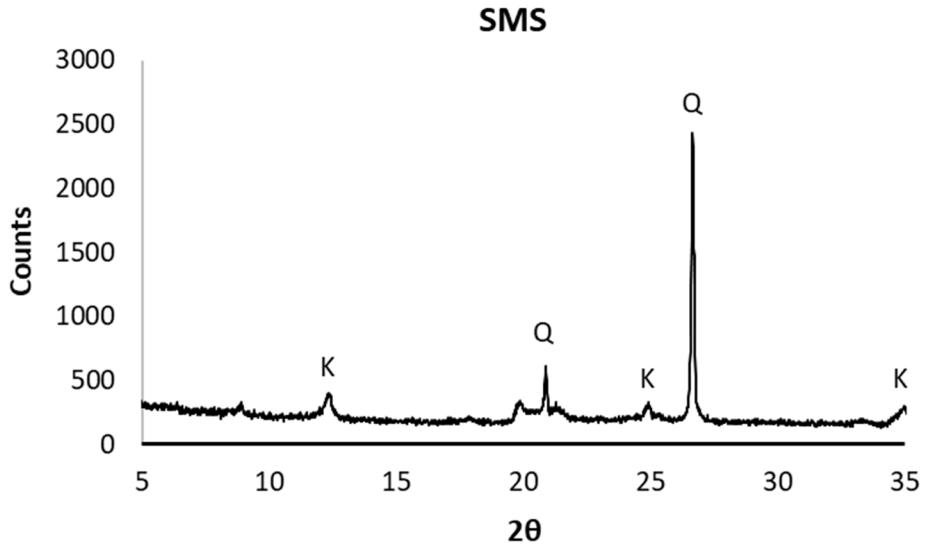

Figure 3-4 – XRD scan data for sample SMS

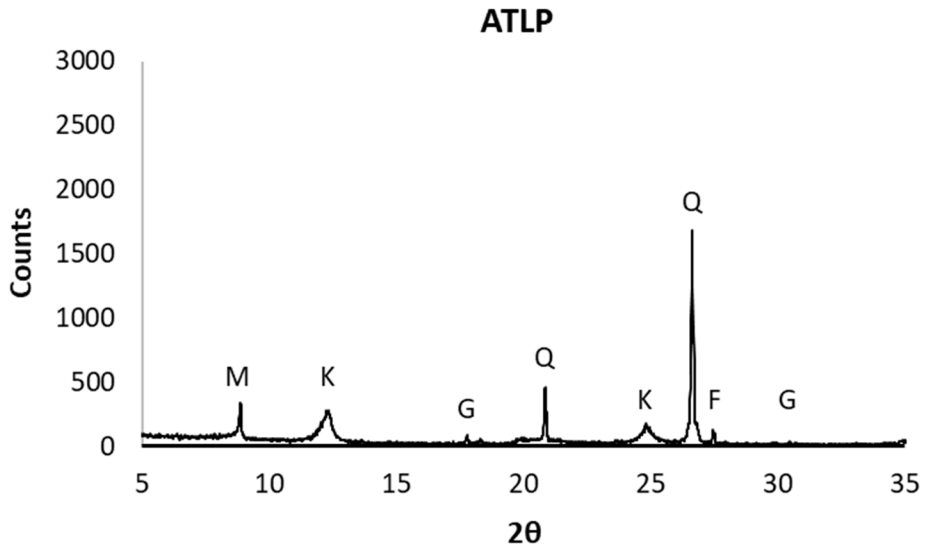

Figure 3-5 – XRD scan data for sample ATLP

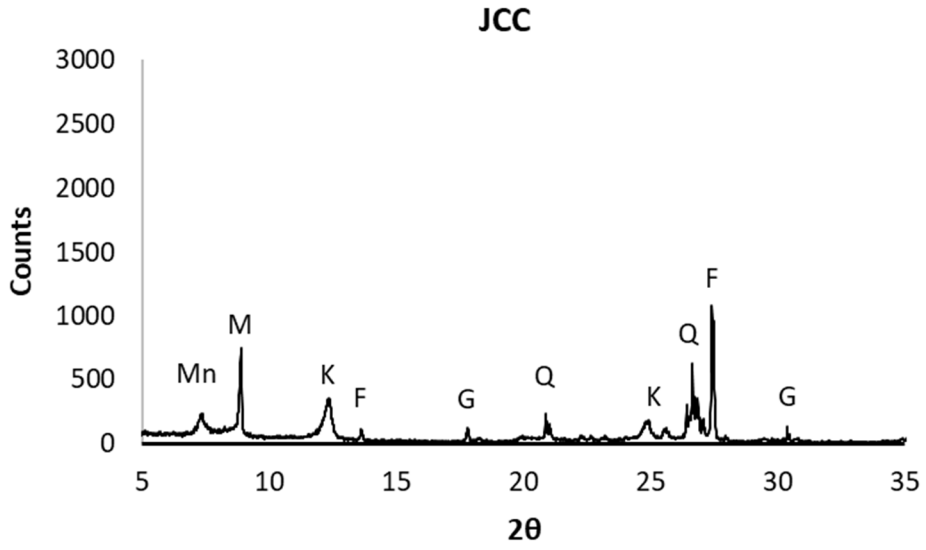

Figure 3-6 – XRD scan data for sample JCC

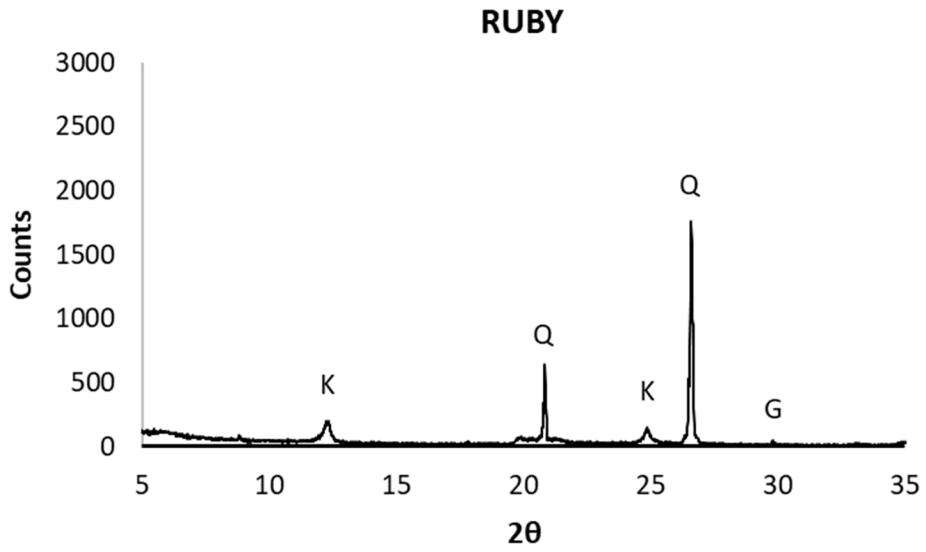

Figure 3-7 – XRD scan data for sample RUBY

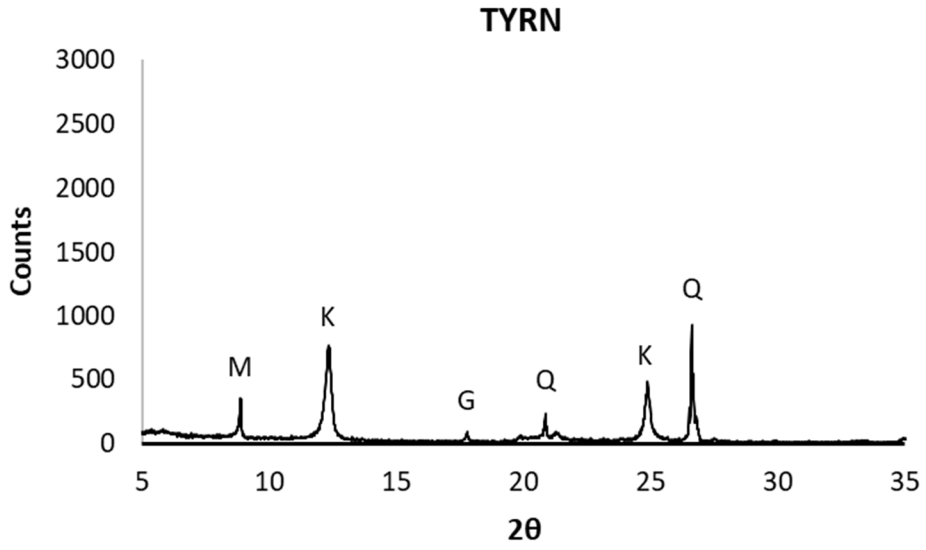

Figure 3-8 – XRD scan data for sample TYRN

3.2.2 X-Ray Fluorescence

XRF data (Table 3-2) indicates that Piedmont soil consists primarily of inorganic silica, aluminum and iron oxides. Minor oxide phases include alkali and alkali-earth metals (Ca, Mg, K, and Na) and titanium oxides; trace amounts of sulfur, phosphorous, strontium and barium oxides were also seen. The percentage of silica and aluminum oxides indicated by the XRF results appear to be in good agreement with the percentages reported by Calvert et al. (1980) from tests performed on Piedmont samples obtained from North Carolina, where percentage of silica oxides were in the range of about 58 to 80 percent, aluminum oxides were in the range of about 11 to 24 percent, and the iron oxides were in the range of about 1 to 9 percent.

Table 3-2 – Summary of XRF results for Piedmont soils

Sample ID	SiO_2 (%)	Al_2O_3 (%)	Fe_2O_3 (%)	MgO (%)	K_2O (%)
JCS	54	31	10	1.5	1.4
SMS	61	22	9.3	1.5	2.8
ATLP	72	20	5.2	0.5	1.8
JCC	69	21	6.8	0.2	1.3
RUBY	81	12	4.0	0.1	0.2
TYRN	61	26	3.9	0.8	6.5

3.2.3 Quartz Content

The quartz contents predicted using Equation (20) and (21), as well as the back-calculated quartz content using Equation (22) as described in Section 3.1, are summarized in Table 3-3 and Figure 3-9. It can be seen that compared to the quartz content predicted using Equation (21) and back-calculated quartz content using Equation (22), the simplistic assumption that quartz content is equal to that of the coarse fraction yields much lower values for the fine-grained soils (JCS and SMS). For the intermediate soils (ATLP, JCC and RUBY), the quartz content indicated by the three different methods are in better agreement, though the predictive relationships appear to have slightly underpredicted quartz content relative to back-calculated values. Lastly, it can be seen both Equation (20) and (21) appear to over-predict quartz content of the predominantly coarse-grained sample (TYRN) in comparison to the back-calculated quartz content. An inspection of the XRD

results for TYRN (Figure 3-8) appears to indicate that the quartz content of this sample is relatively low in comparison to the other predominantly coarse-grained samples.

Table 3-3 – Summary of quartz content predictions for Piedmont soils

Sample ID	Coarse Fraction	q_1	q_2	q_3
JCS	0.05	0.05	0.36	0.39
SMS	0.14	0.14	0.40	0.37
ATLP	0.43	0.43	0.52	0.61
JCC	0.54	0.54	0.56	0.72
RUBY	0.62	0.62	0.60	0.76
TYRN	0.73	0.73	0.64	0.46

q_1 = predicted quartz content using Equation (20)
q_2 = predicted quartz content using Equation (21)
q_3 = predicted quartz content using Equation (22)

Figure 3-10 shows the relationship between the apparent quartz content predicted using Equation (22) and the silica oxides ($Si0_2$) as indicated by the XRF results. It can be seen that $Si0_2$ appears to be a relatively robust indicator of quartz content. This is as expected, given that quartz is entirely comprised of silica (but not vice versa).

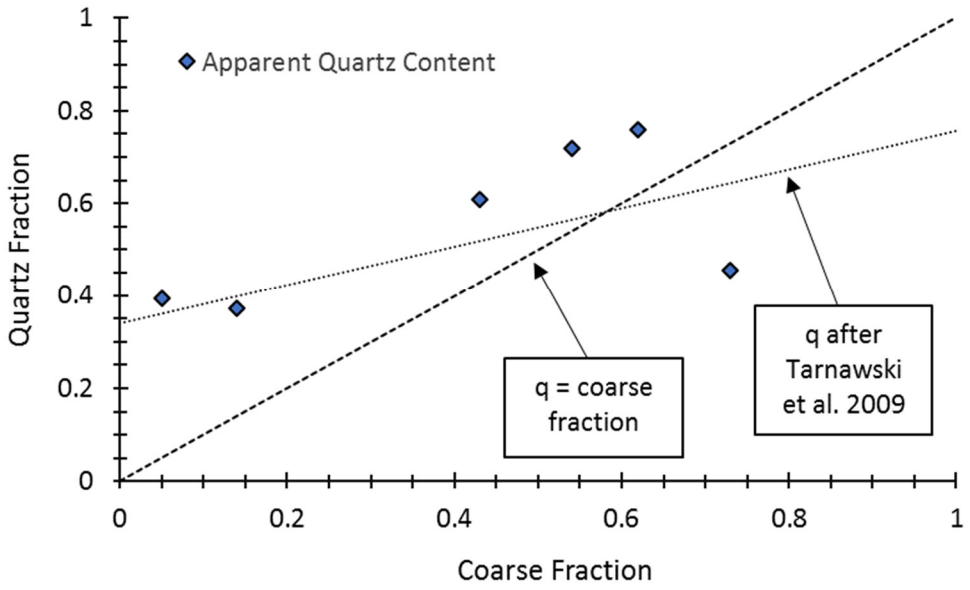

Figure 3-9 – Relationship between coarse fraction and quartz fraction for Piedmont soils

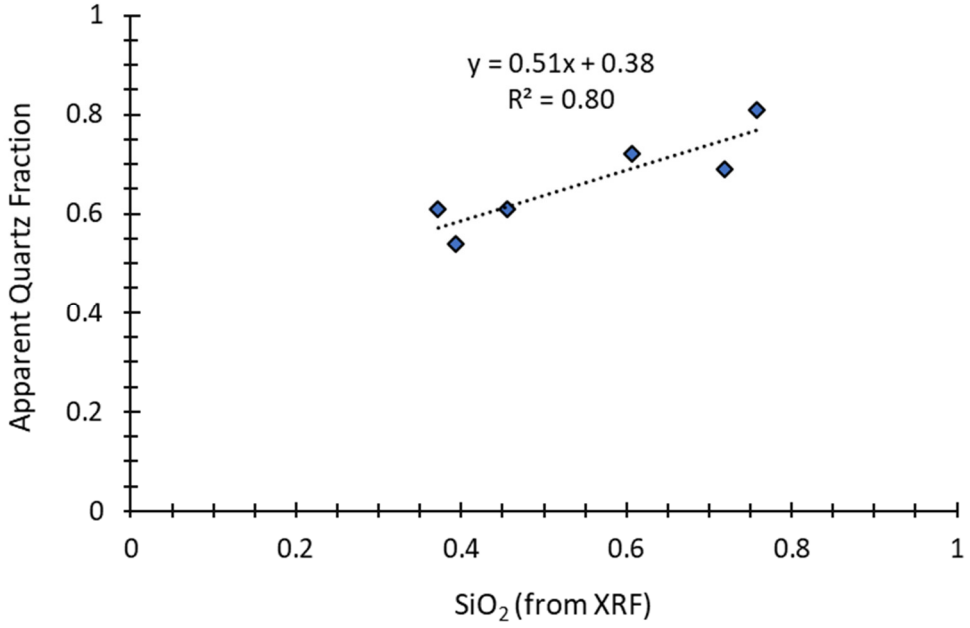

Figure 3-10 – Relationship between apparent quartz content and SiO_2 content from XRF tests for Piedmont soils

As a practical example, the impact of inaccurately predicting thermal conductivity can be quantified by calculating the saturated thermal conductivity resulting from each prediction, based on the following relationship:

$$k_{sat} = {k_s}^{(1-n)} {k_w}^{(n)} \quad (24)$$

For this example, porosity (n) is assumed to be 0.5. Two samples are considered:

(i) Sample ATLP, where the predicted quartz fraction using Equation (20) was 0.43, while the back-calculated quartz fraction using Equation (22) was 0.61. This indicates that the predicted quartz content was approximately 29 percent lower than the back-calculated value. Using Equation (19), based on q = 0.43, k_s can be calculated as 3.89 W/m-K, and k_{sat} can be calculated as 1.53 W/m-K. On the other hand, based on q = 0.61, k_s can be calculated as 4.77 W/m-K, and k_{sat} can be calculated as 1.69 W/m-K. This example shows that a 29 percent difference in quartz content results in an approximately 10 percent difference in predicted thermal conductivity.

(ii) Sample TYRN, where the predicted quartz fraction using Equation (20) was 0.73, while the back-calculated quartz fraction using Equation (22) was 0.46. This indicates that the predicted quartz content was approximately 60 percent greater than the back-calculated value. Using Equation (19), based on q = 0.73, k_s can be calculated as 5.64 W/m-K, and k_{sat} can be calculated as 1.84 W/m-K. On the other hand, based on q = 0.46, k_s can be calculated as 3.99 W/m-K, and k_{sat} can be calculated as 1.55 W/m-K. This example shows that a 60 percent difference in quartz content results in an approximately 20 percent difference in predicted thermal conductivity.

3.3 Conclusions

XRF and XRD tests were performed on six different samples of Piedmont residual soils collected from several locations around the state of Georgia. Sieve analyses and hydrometer tests were performed for determination of the grain size distribution of the samples, and Atterberg Limits tests were performed for evaluation of their plasticity characteristics.

The results show that simply assuming quartz content to be equal to that of the coarse fraction may lead to unreliable estimates of quartz content. The relationship proposed by Tarnawski et al. (2009) appears to provide a better estimate of quartz content relative to the back-calculated values, although in one case (sample TYRN) the prediction was significantly different. An evaluation of the XRD and XRF results for TYRN show that this sample had relatively low quartz content and silica oxide content, despite the fact that the soil classified as primarily coarse-grained based on grain size distribution and Atterberg Limits test results and hence was expected to have relatively high quartz content. This highlights the importance of having a good understanding of the mineralogical composition of samples when possible.

In this regard, accurate prediction of quartz content, which in turn allows for a more accurate prediction of soil thermal conductivity, can have important practical implications for problems related to energy geotechnics such as design of shallow thermo-active foundations. The thermal conductivity of soils surrounding a thermo-active foundation has a direct impact on the thermo-hydro-mechanical behavior of the foundation system, as well as on the total length of the fluid circulation loop that exchanges heat energy with the

ground. For example, an overestimation of thermal conductivity would lead to a fluid circulation loop length shorter than required, which in turn may result in inadequate system performance. Alternatively, an underestimation of thermal conductivity would lead to a fluid circulation loop length longer than required, which would have an economic impact in the form of elevated construction costs.

CHAPTER 4. THERMAL PROPERTIES OF PIEDMONT RESIDUAL SOILS FROM LABORATORY TESTS

Estimation of thermal conductivity of different soils under varying density and saturation conditions has been the topic of several previous studies (Kersten, 1949, Johansen, 1975, Campbell et al., 1994, Cote and Konrad, 2005, Lu et al., 2007, Lu et al., 2014). In establishing empirical relationships, the parameters typically utilized are the density/porosity, soil texture (sand, clay, etc.), and degree of saturation.

In this chapter, results are presented from a laboratory testing program, in which the thermal properties of the six bulk samples of Piedmont residual soils discussed in the previous chapter were measured at room temperature under varying density and saturation conditions. A predictive relationship has been developed which allows estimation of the thermal conductivity during both wetting and drying of Piedmont residual soils for a given density and composition, and for moisture conditions ranging from dry to full saturation. A predictive relationship has also been developed to estimate heat capacity as a function of the moisture content. The estimated thermal properties can in turn be used in numerical or analytical models for predicting the preliminary performance of shallow thermo-active foundations.

4.1 Methodology

4.1.1 Test Apparatus and Sample Preparation

A custom acrylic chamber (see Figure 4-1) was designed for remolding and subsequent saturation of the samples. The chamber has an inner diameter of 62.8 mm, and

a height of 38.1 mm. These dimensions were chosen to allow for relatively uniform saturation of the samples during wetting and to maximize the sensed volume within the thermal probe range, while minimizing the boundary effects of the thermal load imposed by the heat-pulse probe.

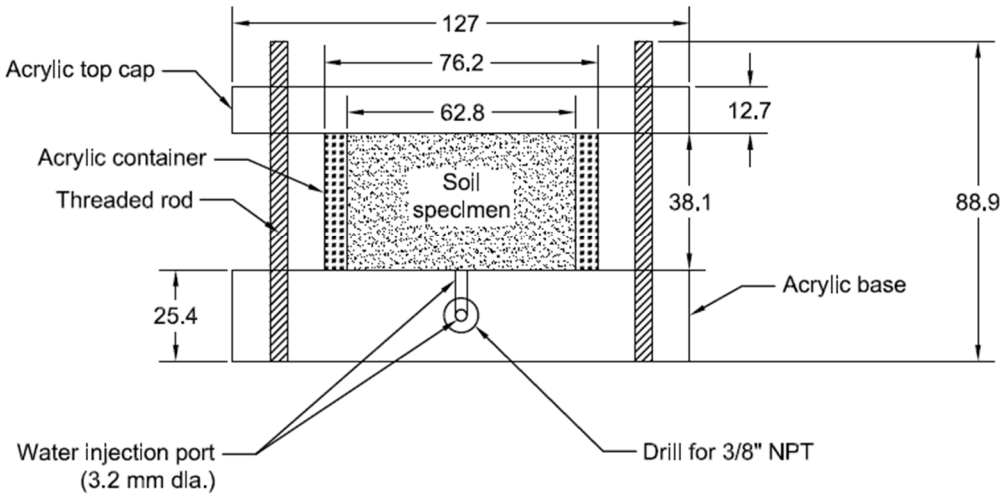

Figure 4-1 – Acrylic chamber (side view) for measurement of thermal properties (all measurements in millimeters, unless otherwise noted)

The samples were first oven dried and tested in their oven-dry state under varying density conditions to determine the relationship between porosity and thermal conductivity under dry conditions. For each bulk soil sample, specimens were then remolded in the acrylic chambers using soil stored under ambient room conditions to a desired dry density by dry tamping in uniform layers. Four specimens were prepared to approximately the same dry density (with standard deviation less than 1%).

One of the four specimens was tested immediately to determine the thermal conductivity under ambient room and hygroscopic moisture conditions. Subsequently, the remaining specimens were wetted with de-ionized water through an injection port at the bottom of the chamber. The specimens were given a minimum of 24 hours to allow the water column to diffuse more uniformly into the specimen. For example, Figure 4-2(a) shows the conditions immediately following water injection into the Atlanta Residuum sample. Figure 4-2(b) shows the same sample after a 6-hour period. The distribution of the water column throughout the sample through capillary action is evident from the before and after pictures. The actual moisture content was determined after measurement of thermal properties, and the corresponding degree of saturation calculated based on the known moisture content, void ratio, and the specific gravity of each sample.

Each bulk sample was tested under two different dry density conditions and five different degrees of saturation during wetting (see Figure 4-4). For the denser condition of each material, samples were reconstructed and measurements were also taken to determine the thermal properties of the samples during drying. Drying was achieved by exposing the top of the container to ambient room conditions to facilitate evaporation of water from the sample. The soil and water masses and the water loss during drying were measured using a calibrated benchtop scale.

(a)

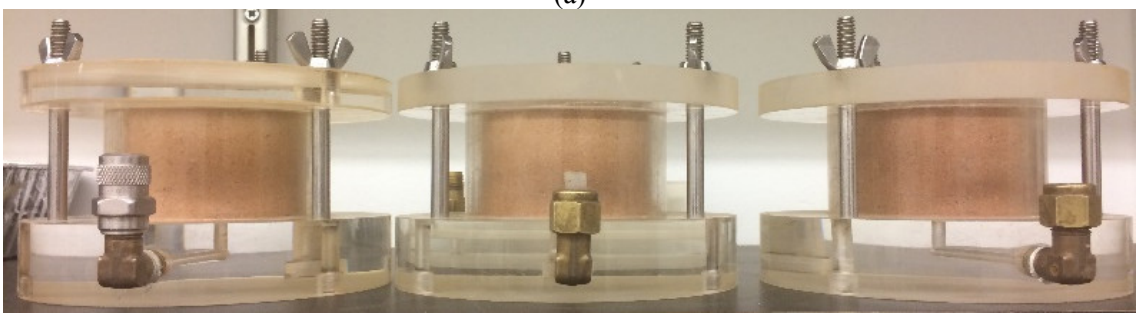

(b)

Figure 4-2 – (a) Sample conditions immediately after water injection (at three different saturation levels); (b) Sample conditions after a 6-hour period, showing the diffusion of the water column.

4.1.2 Thermal Properties Measurement

The 3 cm long, 1.3 mm diameter SH-1 dual-needle heat-pulse probe manufactured by Decagon Devices was used in order to measure thermal conductivity as well as volumetric heat capacity of the samples under varying density and saturation conditions. The SH-1 sensor allows for simultaneous measurement of thermal conductivity and volumetric heat capacity (related to the specific heat through the bulk density, which is known a priori). Sensor calibration followed the manufacturer recommended procedure using a calibration block of known thermal conductivity and heat capacity, and was performed on a regular basis. Data logging and analysis of the thermal properties was performed using a KD2 Pro Thermal Properties Analyzer, also manufactured by Decagon Devices.

4.1.3 Development of Predictive Relationship

4.1.3.1 Thermal Conductivity

Thermal conductivity of soils can be expressed using the normalized thermal conductivity concept initially proposed by Johansen (1975):

$$k = \left(k_{sat} - k_{dry}\right) K_e + k_{dry} \tag{25}$$

Where k is thermal conductivity, k_{sat} is the saturated thermal conductivity, k_{dry} is the dry thermal conductivity, and K_e is the Kersten number, which allows for estimation of thermal conductivity between the dry and fully saturated states.

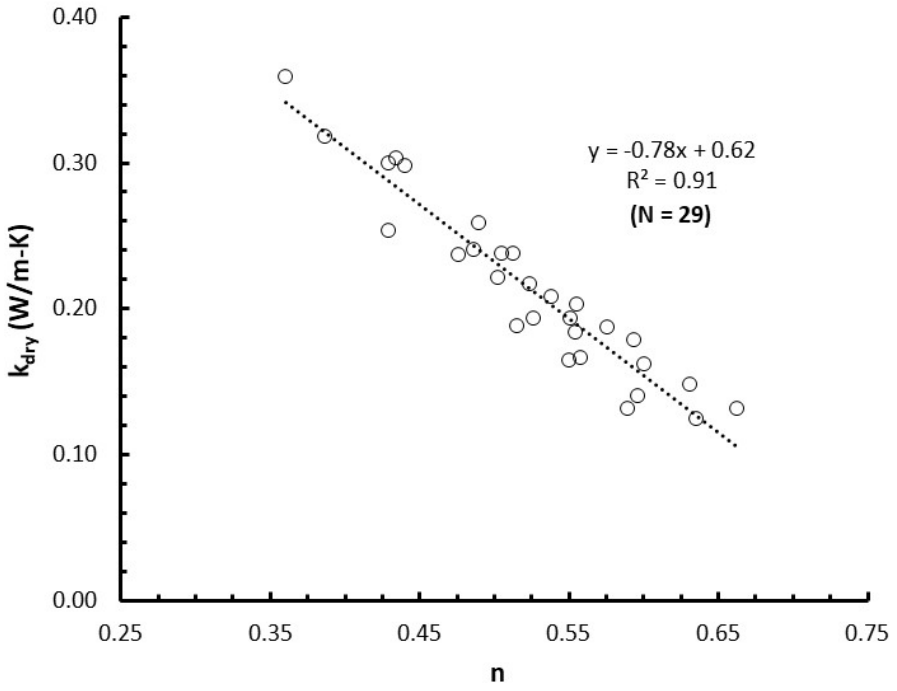

Figure 4-3 – Relationship between porosity and dry thermal conductivity for Piedmont residual soils

Porosity is the most important macroscale parameter governing the thermal conductivity of dry soils (Yun and Santamarina, 2008). For this study, an empirical relationship was developed based on measurements taken on oven-dry samples of Piedmont residual soils under varying porosity conditions (see Figure 4-3). The resulting relationship between porosity (n) and k_{dry} can be expressed as follows:

$$k_{dry} = -0.78\, n + 0.62 \tag{26}$$

Saturated thermal conductivity can be expressed as a geometric mean based on the thermal conductivity of water (k_w) and effective thermal conductivity of the solids (k_s) as follows:

$$k_{sat} = {k_s}^{1-n} \times {k_w}^{n} \tag{27}$$

The effective thermal conductivity of the solids can be calculated based on the quartz fraction (q) of the soil mass as follows:

$$k_s = {k_q}^{q} \times {k_o}^{1-q} \tag{28}$$

Where k_q is the thermal conductivity of quartz minerals, and k_o is the lumped thermal conductivity of all other non-quartz soil minerals. If specific knowledge exists about the mineralogical make-up of the soil mass, then the weighted geometric mean method can be used to calculate k_s.

For this study, k_{sat} was determined experimentally. The samples were saturated as high as practically possible given the experimental setup limitations, typically resulting in a degree of saturation of slightly less than one. These results were then extrapolated linearly to full saturation using Equation (25).

Once k_{sat} was determined, the best-fit prediction curve was obtained by minimizing the root-mean square error (RMSE) between measured and predicted values of K_e. Various researchers have proposed different forms of K_e for estimation of thermal conductivity between the dry and fully saturated states. In this study, the form proposed by Lu et al. (2007) was used:

$$K_e = \exp\left[\alpha \left(1 - S^{(\alpha-\beta)}\right)\right] \tag{29}$$

In Equation (29), α is a soil texture dependent coefficient, S is the degree of saturation, and β is a curve-fitting coefficient controlling the shape of the thermal conductivity-saturation curve. Thermal conductivity measurements from the six samples for degrees of saturation between dry (S = 0) and fully saturated (S = 1.0) were used to calibrate the model by determining the α and β coefficients which minimize the RMSE between the measured and predicted values of K_e.

During drying, the samples not only undergo a change in moisture content, but also in porosity as the samples tend to shrink radially and vertically. This was quantified by taking measurements of the sample height and diameter at various stages during drying. To account for this change in porosity during drying and its corresponding effect on saturated thermal conductivity for the predictive relationship, the "apparent" quartz content

(q_a) of the sample was determined based on the initial saturated thermal conductivity measurement by rearranging Equation (28) as follows:

$$q_a = \frac{ln(k_s/k_o)}{ln(k_q/k_o)} \tag{30}$$

Where k_s can be obtained from the experimentally measured saturated thermal conductivity ($k_{sat-exp}$) and porosity as follows:

$$k_s = \left(\frac{k_{sat-exp}}{k_w{}^n}\right)^{1/(1-n)} \tag{31}$$

k_w is the thermal conductivity of water at standard conditions (taken as 0.6 W/m-K), and k_q and k_o were taken as 7.7 W/m-K and 2.0 W/m-K, respectively. With q_a determined, the corresponding saturated thermal conductivity for a given porosity can then be calculated based on Equations (27) and (28), and K_e back-calculated using Equation (25).

4.1.3.2 Specific Heat Capacity

As previously discussed in Chapter 0, assuming the mass of air to be negligible, the specific heat capacity (c) of a two-phase geomaterial (i.e. solids and water) can be expressed as follows:

$$c = \frac{(c_s + wc_w)}{(1+w)} \tag{32}$$

Where c_s is the specific heat of the solids, w is the gravimetric water content, and c_w is the specific heat of water (typically taken as 4,200 J/kg-K). The value of c was measured

using the dual-needle heat pulse probe under various moisture conditions. More specifically, the volumetric heat capacity (in units of J/m^3-K) was measured with the probe and converted to specific heat (in units of J/kg-K) by dividing the volumetric heat capacity by the corresponding bulk density (in units of kg/m^3). The value of c_s was then determined by minimizing the RMSE between the measured and predicted values using Equation (32).

4.2 Results & Discussion

4.2.1 Thermal Conductivity

The measured thermal conductivity as a function of the degree of saturation during wetting for the six soils tested are shown on Figure 4-4 (a)-(f). Each sample was tested under two different dry density conditions to observe the effect of dry density on thermal conductivity. It can be seen from these figures that generally, decreasing void ratio (or porosity) results in higher thermal conductivity. It can also be seen that increasing degree of saturation results in higher thermal conductivity, and that the effect of increased saturation is significantly greater than the effect of decreased void ratio especially in the early stages of saturation. Lastly, it can be seen that the fine-grained soils that classified as high-plasticity silts have a lower maximum thermal conductivity as compared to the other soils tested. These trends are in line with the anticipated behavior based on published literature as previously discussed in Chapter 2.3.1.

The measured thermal conductivity as a function of the degree of saturation during drying for the six soils tested are shown on Figure 4-5 (a)-(f). It can be seen that the curves follow a distinctly different path during drying, and that thermal conductivity is general higher during drying than wetting, especially in the moderate to lower ranges of saturation

(S ~ 0.1 to 0.6). It can also be seen that the difference in thermal conductivity during wetting versus drying is less pronounced in the sample containing the least amount of fines (TYRN).

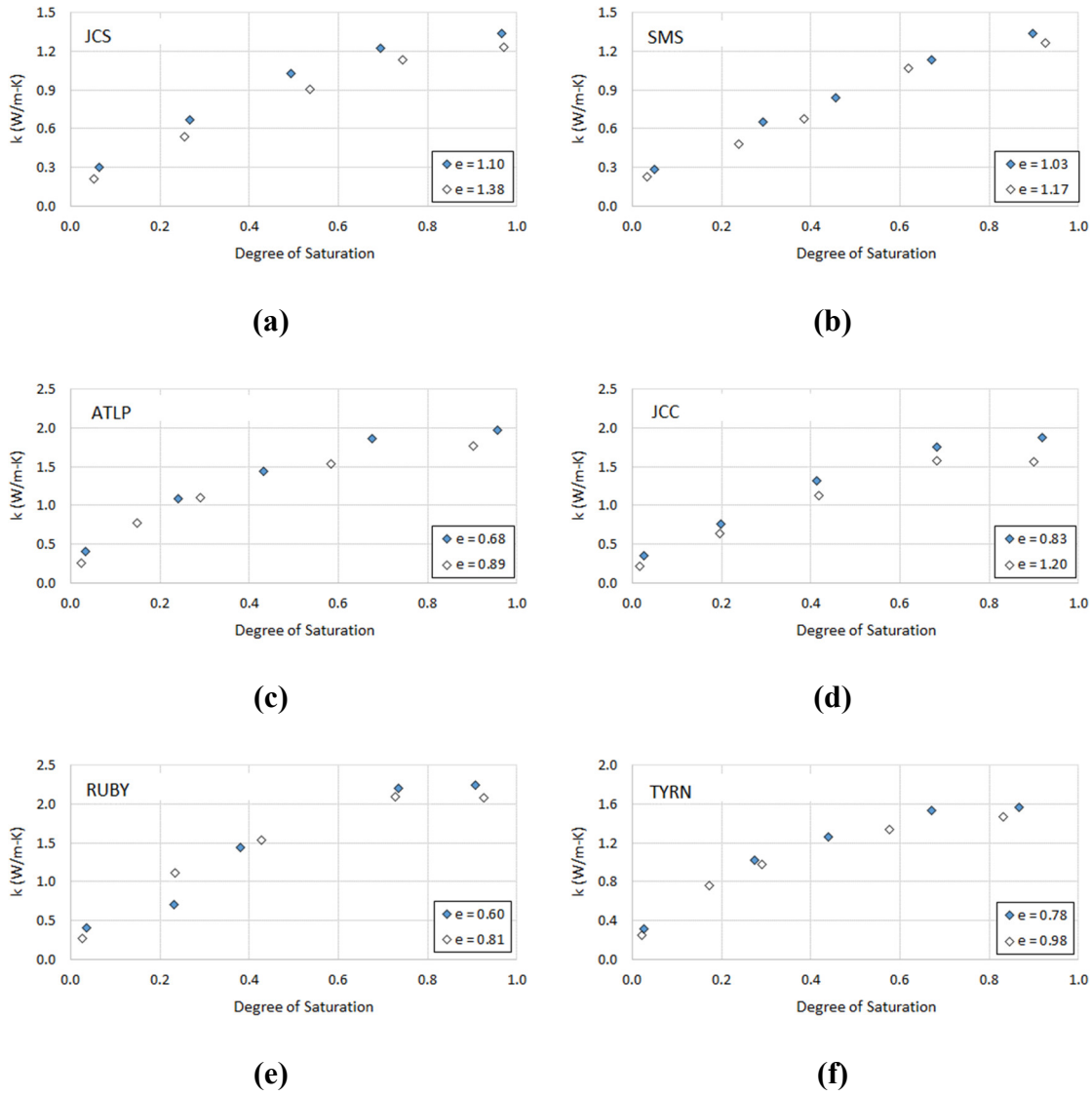

Figure 4-4 – Thermal conductivity vs. degree of saturation for the six Piedmont soil samples tested (two void ratios/densities and five different degrees of saturation

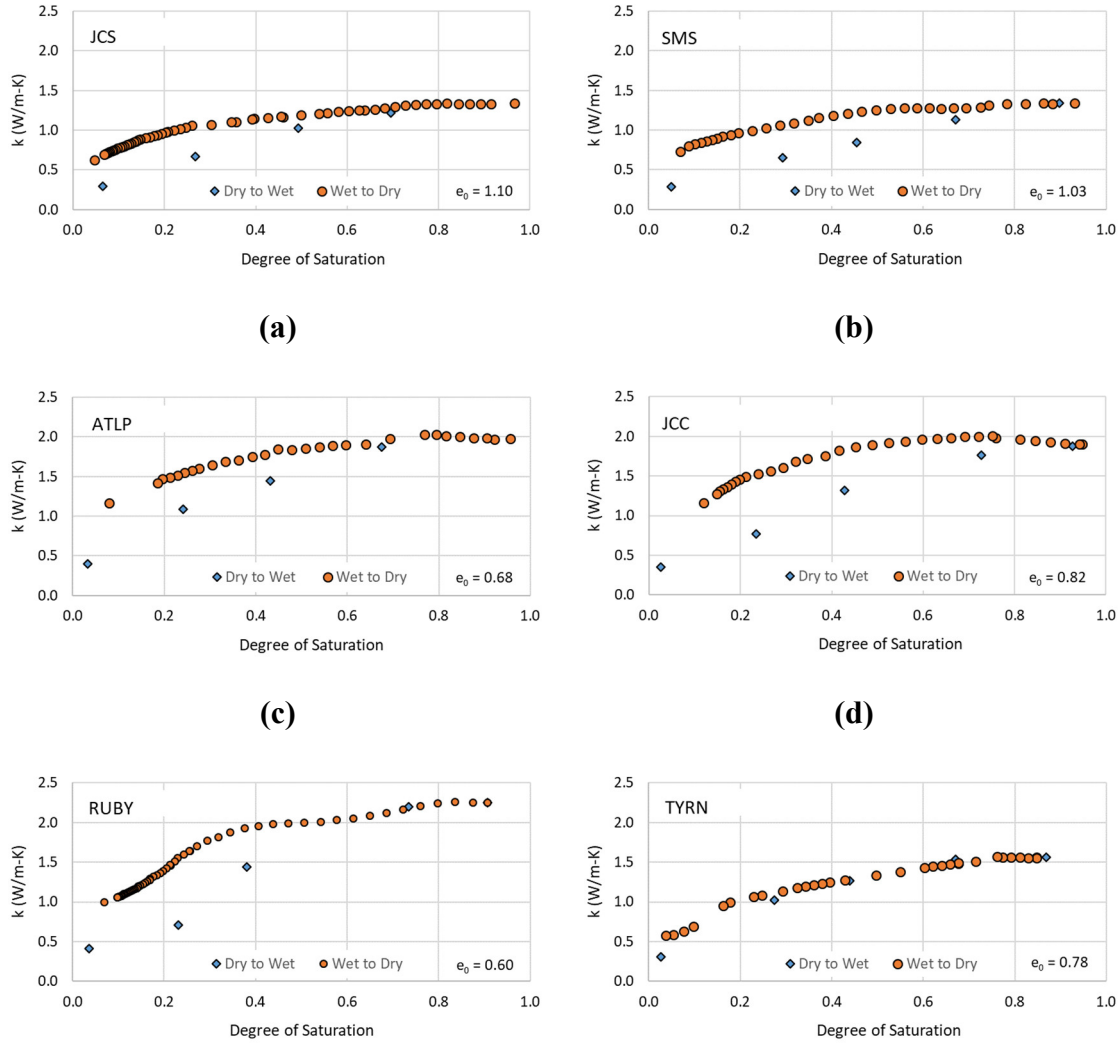

Figure 4-5 – Thermal conductivity vs. degree of saturation for the six Piedmont soil samples tested (two void ratios/densities and five different degrees of saturation

Figure 4-6 and Figure 4-7 show the model calibration results during wetting for the coarse and fine-grained soils, respectively. A total of 40 measurements were made in coarse-grained and 20 measurements in fine-grained samples. It should be noted that for this study, fine-grained was defined as soils with high plasticity (i.e., samples JCS and

SMS). This is because it is not uncommon for some residual soils such as sample ATLP, which classifies as fine-grained based on the USCS classification system (low-plasticity clay), to present "transitional" behavior (Mayne et al., 2000). RMSE minimization resulted in an α coefficient of 0.28 and a β coefficient of 1.26 for coarse-grained soils, and an α coefficient of 0.89 and a β coefficient of 1.48 for fine-grained soils.

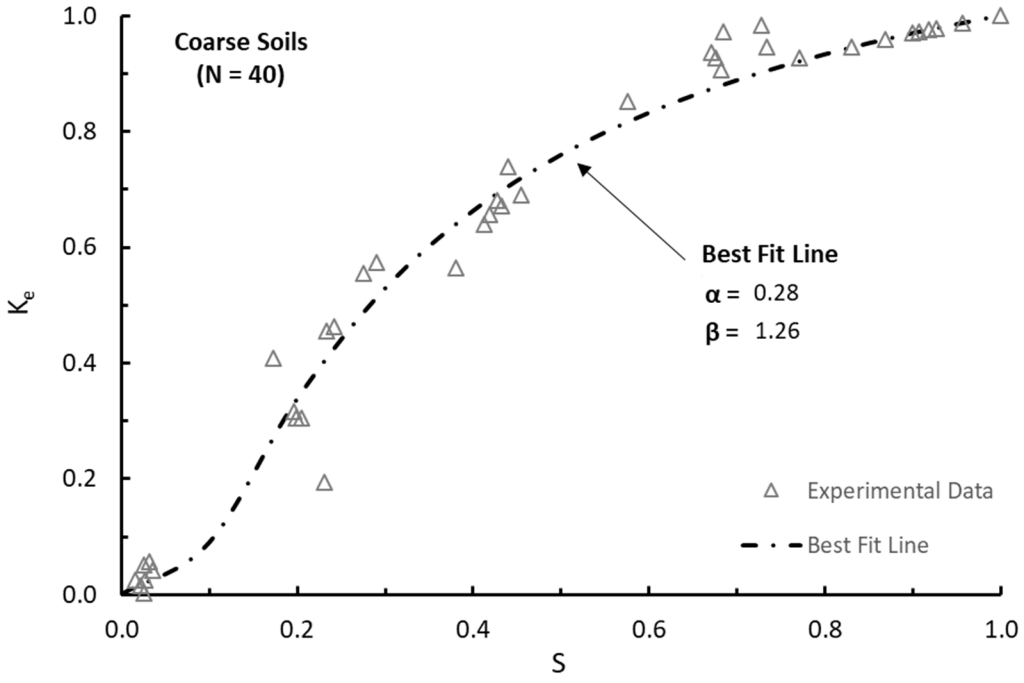

Figure 4-6 – Model calibration results for coarse Piedmont soils – wetting

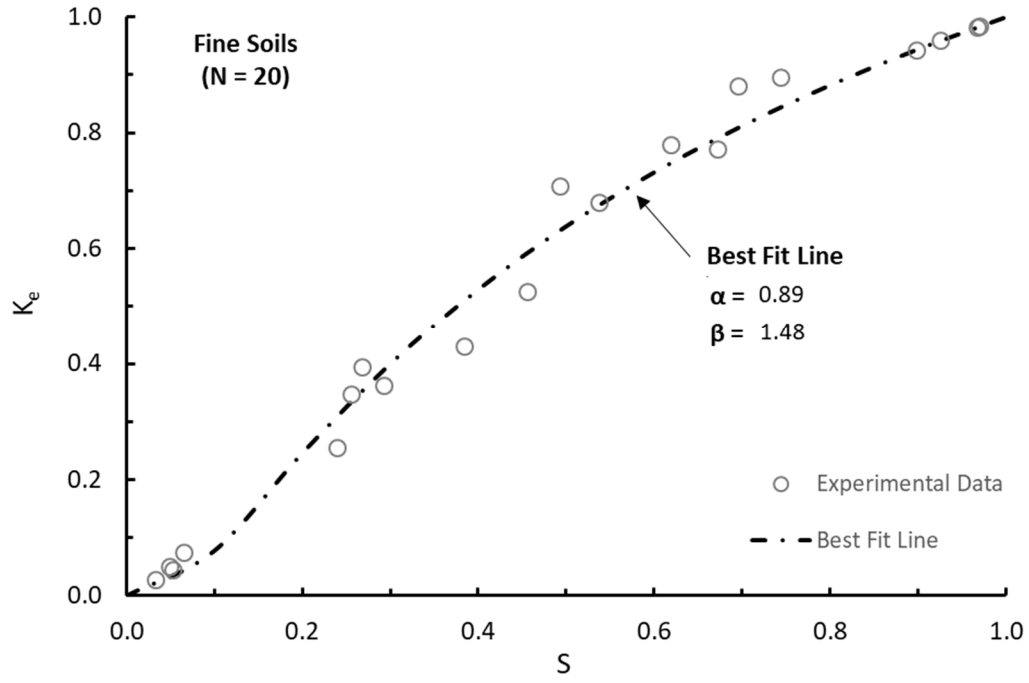

Figure 4-7 – Model calibration results for fine Piedmont soils – wetting

Figure 4-8 shows the relationship between predicted and measured values of thermal conductivity during the wetting phase for the six Piedmont soils tested using the aforementioned coefficients. It can be seen that overall, there is very good agreement between the predicted and measured values. Approximately 78 percent of the predicted values are within 10 percent of those measured, and 90 percent are within 20 percent of those measured. The largest differences were typically observed in the very low saturation range (i.e. soils with low thermal conductivity), most likely due to challenges with achieving a uniform moisture distribution in the soil column at low moisture contents and, also because a small difference constitutes a higher percentage difference for low values

of thermal conductivity. The relationship shows a very slight negative bias, meaning that on average the predicted values are slightly lower than the measured ones.

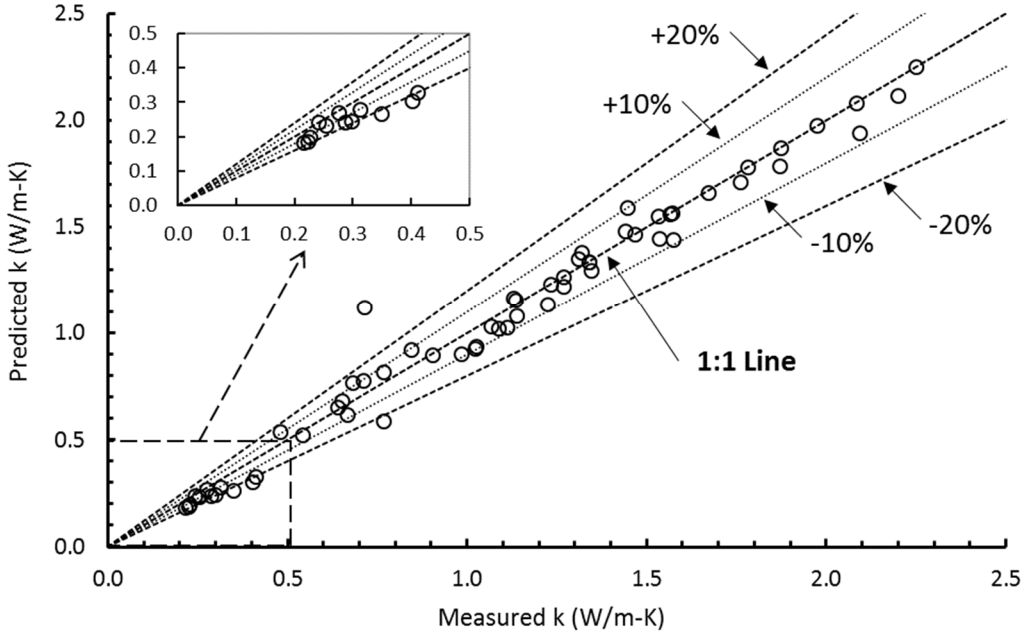

Figure 4-8 – Relationship between predicted and measured thermal conductivity for Piedmont soils during wetting

Figure 4-9 and Figure 4-10 show the model calibration results for the coarse and fine-grained soils during drying, respectively. A total of 151 measurements were made in coarse-grained and 93 measurements in fine-grained samples. RMSE minimization resulted in an α coefficient of 0.20 and a β coefficient of 0.99 for coarse-grained soils, and an α coefficient of 0.42 and a β coefficient of 0.86 for fine-grained soils. These values differ from those obtained during the wetting phase, indicating that the shape of the wetting and drying thermal conductivity curves are different.

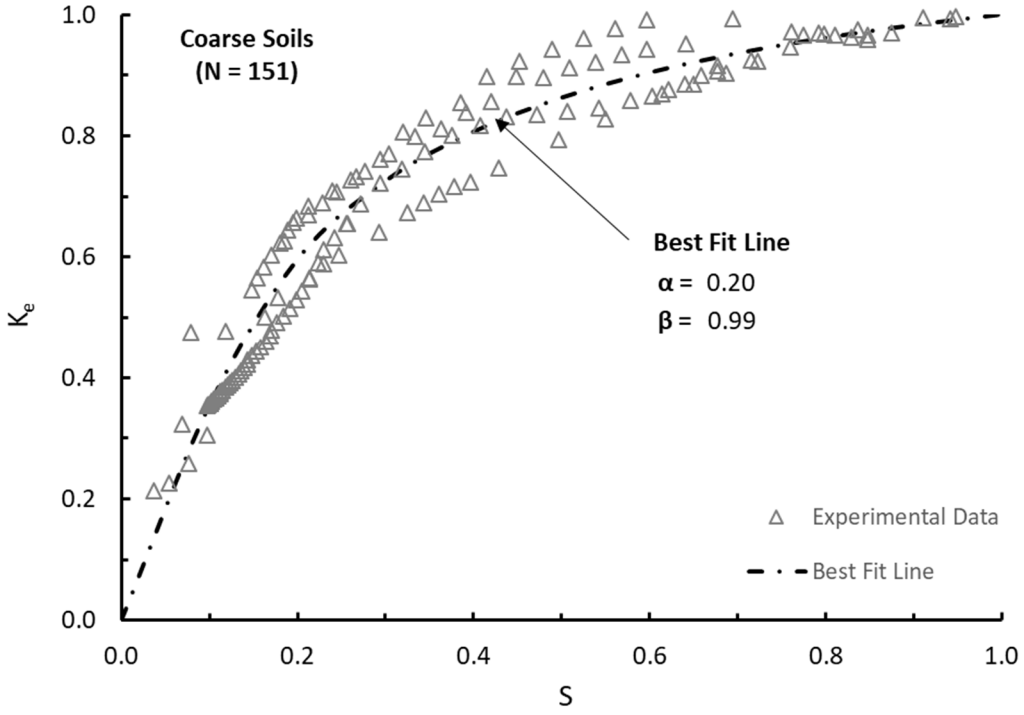

Figure 4-9 – Model calibration results for coarse Piedmont soils – drying

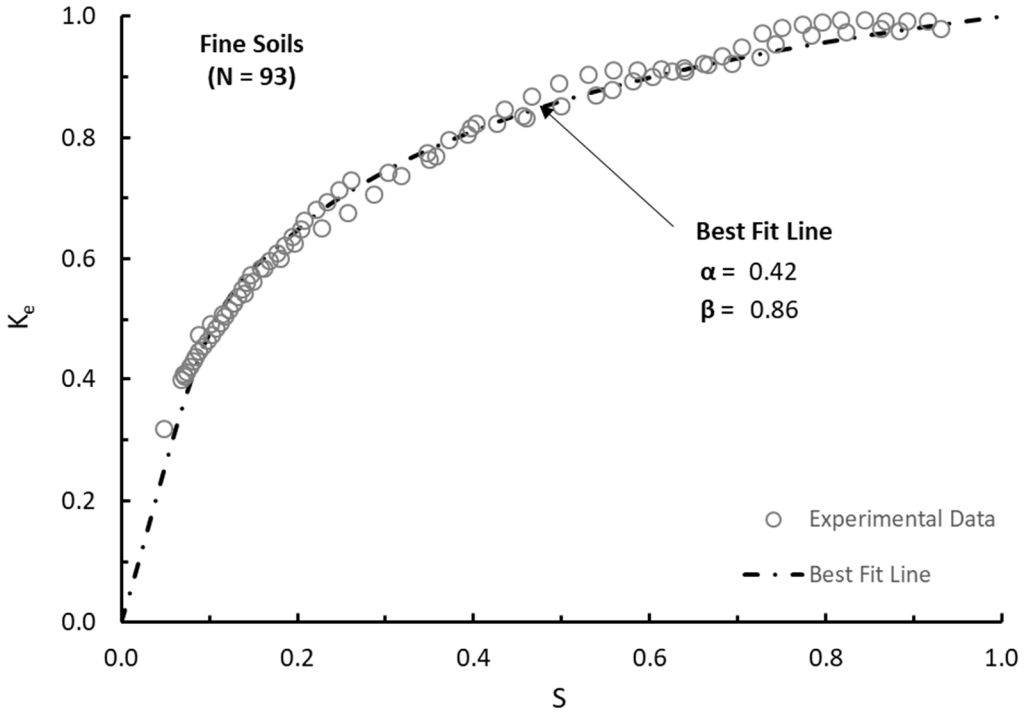

Figure 4-10 – Model calibration results for fine Piedmont soils – drying

Figure 4-11 shows the relationship between predicted and measured values of thermal conductivity during the drying phase for the six Piedmont soils tested using an α coefficient of 0.20 and a β coefficient of 0.99 for coarse-grained soils, and an α coefficient of 0.42 and a β coefficient of 0.86 for fine-grained soils. It can be seen that overall there is very good agreement between the predicted and measured values, as approximately 98 percent of the predicted values are within 10 percent of the measured values.

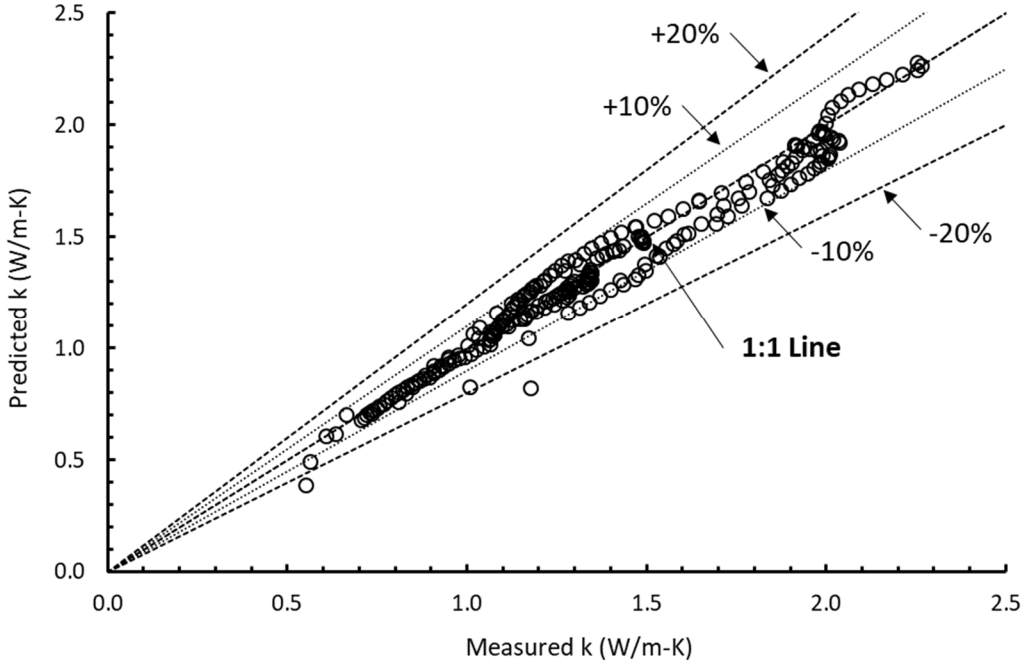

Figure 4-11 – Relationship between predicted and measured thermal conductivity for Piedmont soils during drying

To illustrate the difference in behavior during wetting and drying, Figure 4-12 and Figure 4-13 show a comparison between the K_e values during wetting and drying using the coefficients for coarse-grained and fine-grained soils, respectively. It can be seen that K_e (and hence, the thermal conductivity) is higher during drying than wetting, especially in

the low to moderate saturation range (S ~ 0.1 to 0.6). It can also be seen that the difference between the wetting and drying curves is much more pronounced for the fine-grained soils in comparison to the coarse-grained soils. The difference between the values during wetting and drying were noted to be much smaller for the coarsest sample tested (see Figure 4-5(f) for sample TYRN). This may be related to suction effects, localized moisture retention near the sensors during the drying phase, or a combination of these factors.

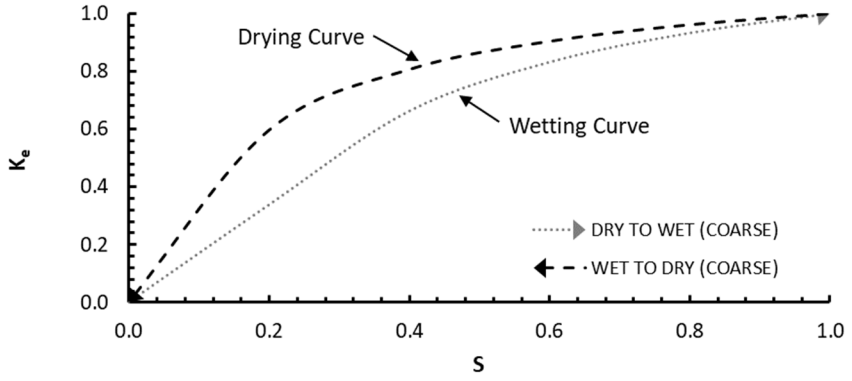

Figure 4-12 – Kersten number (K_e) of coarse Piedmont soils during wetting and drying

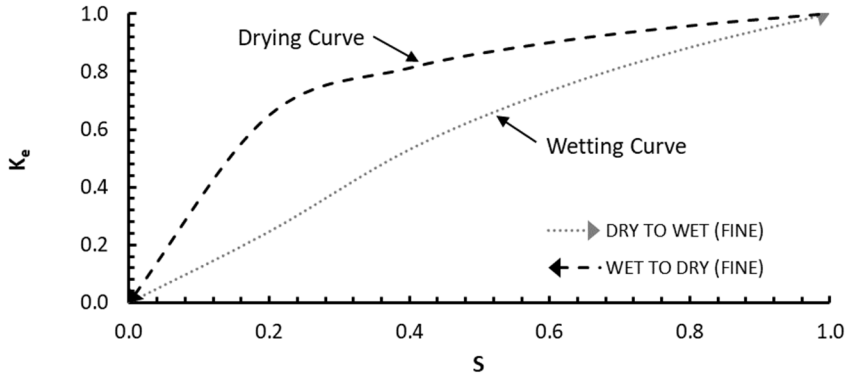

Figure 4-13– Kersten number (K_e) of fine Piedmont soils during wetting and drying

The prediction of thermal conductivity requires knowledge of the saturated thermal conductivity, which can be determined experimentally or calculated using the weighted geometric mean method if there is sufficient knowledge of the mineralogical composition of the materials. Otherwise, a predictive method such as Equation (21) can be used to estimate quartz content, and then the saturated thermal conductivity. Figure 4-14 shows a comparison between the values of saturated thermal conductivity measured experimentally and estimated based on Equation (21). It can be seen that there is good overall agreement between the experimentally measured and the empirically estimated values; all but two measurements are within 10 percent of the XRD-indicated values. The two outliers are associated with samples RUBY and TYRN, which as previously discussed in Chapter 3.2, were the two samples where the empirical estimates of quartz content different most significantly from the back-calculated quartz content.

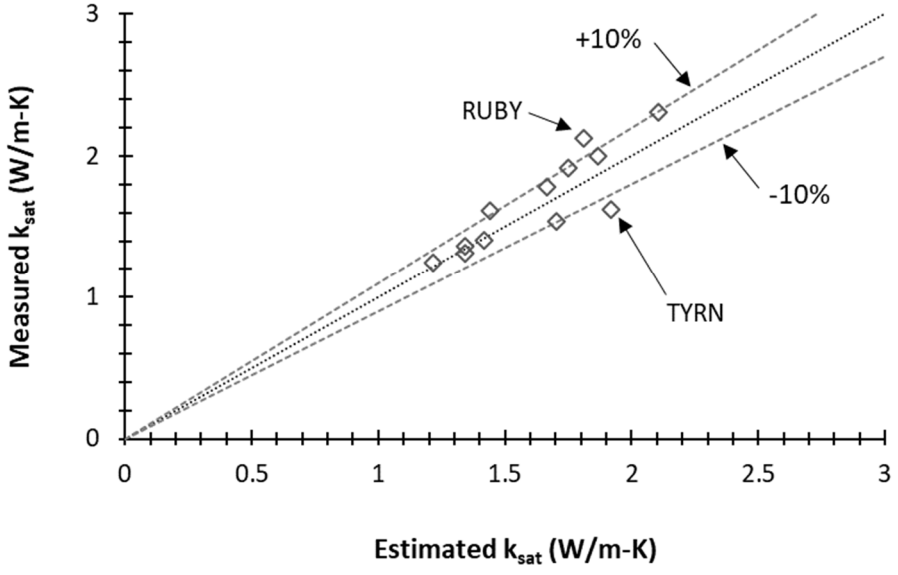

Figure 4-14 – Relationship between saturated thermal conductivity calculated from XRD results and measured from laboratory tests

4.2.2 Specific Heat Capacity

Figure 4-15 and Figure 4-16 show the relationship between the values of specific heat predicted using Equation (32) and measured with the dual-needle heat pulse probe during wetting and drying, respectively. RMSE minimization resulted in a c_s value of 838 J/kg-K during wetting, and 881 J/kg-K during drying. Figure 4-15 and Figure 4-16 show that overall, there is good agreement between the predicted and measured values. In the wetting phase, approximately 90 percent of the predicted values are within 10 percent of those measured, and 98 percent are within 20 percent of those measured. In the drying phase, approximately 68 percent of the predicted values are within 10 percent of those measured, and 100 percent are within 20 percent.

It can also be seen from Figure 4-15 and Figure 4-16 that during the wetting phase, the scatter around the 1:1 line is relatively greater but more uniform in comparison to the drying phase. Additionally, for the drying phase, there appear to be six subsets of data, which correspond to the six soils tested. This becomes more apparent when the results are color coded by their sample ID, as shown in Figure 4-17. The finer grained soils (JCS and SMS) generally plot to the right of the 1:1 line, indicating the measured value is greater than predicted. As previously discussed, this may be related to suction effects, localized moisture retention near the sensors during the drying phase, or a combination of these factors.

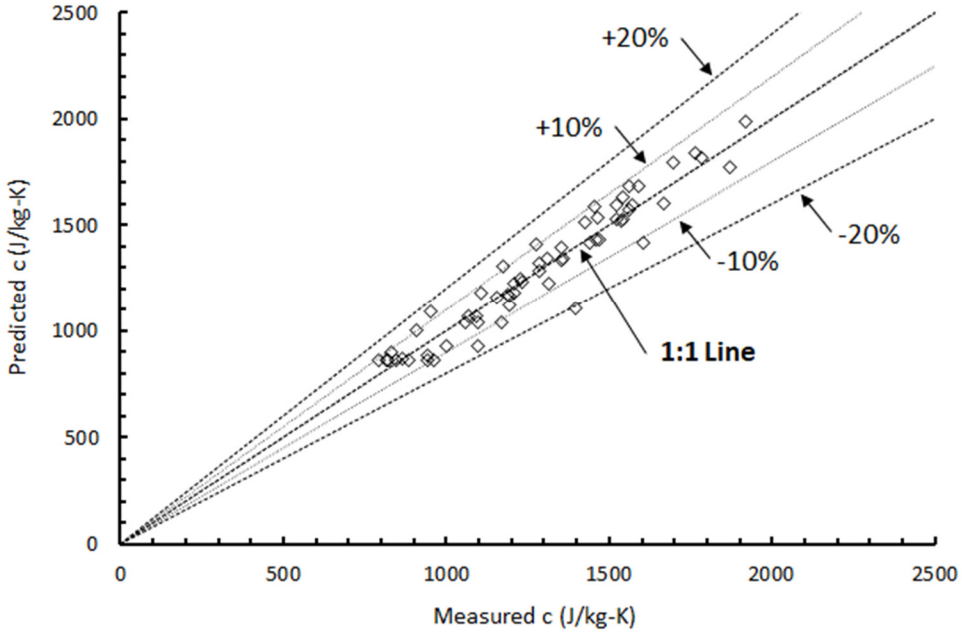

Figure 4-15 – Relationship between predicted and measured specific heat for Piedmont soils during wetting

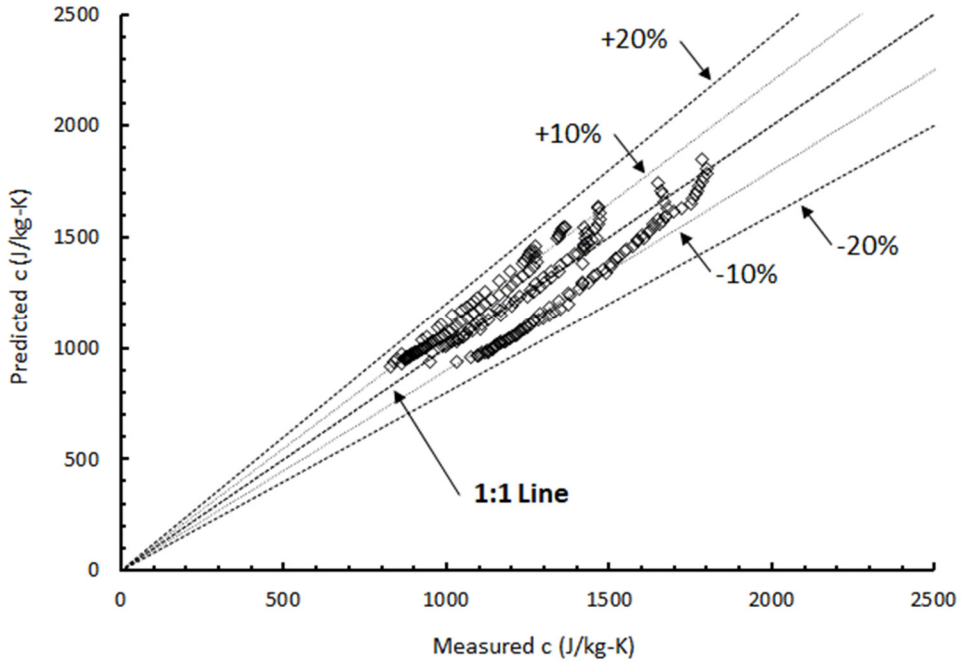

Figure 4-16 – Relationship between predicted and measured specific heat for Piedmont soils during drying

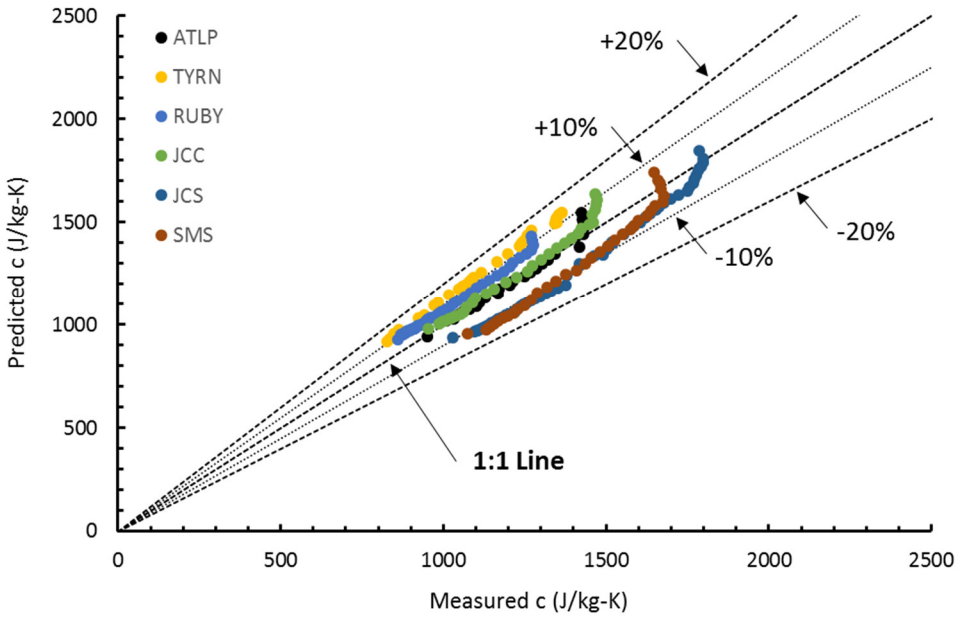

Figure 4-17 – Relationship between predicted and measured specific heat for Piedmont soils during drying (color coded by sample ID)

Specific heat is linear function of the moisture content as indicated by Equation (32). Figure 4-18 shows the relationship between specific heat and moisture content (w), using only the wetting results. The value of c_s was taken as 860 J/kg-K, which is the average of the results from the wetting and the drying phases. Figure 4-18 shows that it is possible to make relatively robust estimates of specific heat assuming that the moisture content is known. Moisture content determination is very simple and typically a standard procedure for geotechnical explorations.

Figure 4-19 shows the relationship between specific heat and moisture content, using only the drying results. It can be seen that the goodness-of-fit is not as robust in comparison to the data from the wetting phase. It can also be seen that the relationship is not quite linear

and could be described as more curvilinear. As previously discussed, this may be due to suction effects and/or localized moisture retention near the sensors during the drying phase.

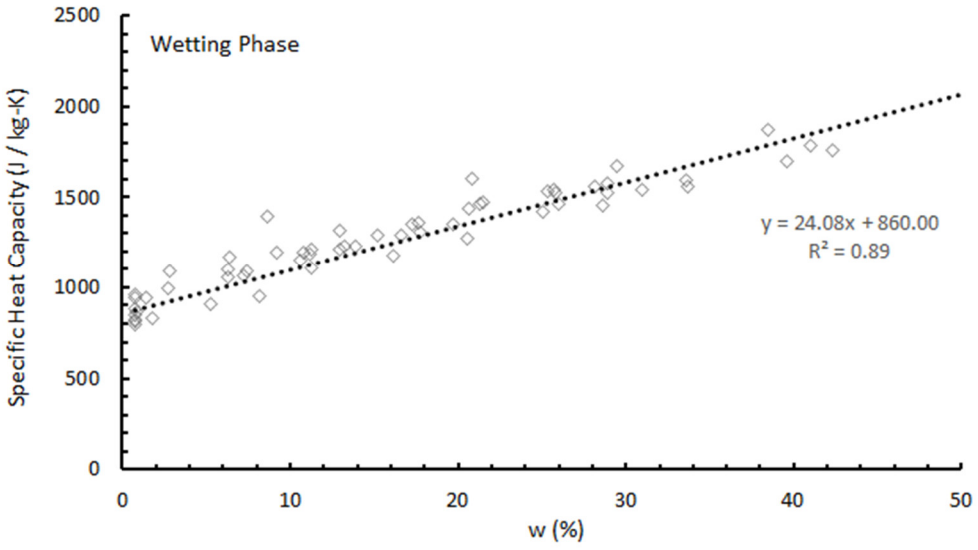

Figure 4-18 – Relationship between moisture content and specific heat for Piedmont soils – wetting phase

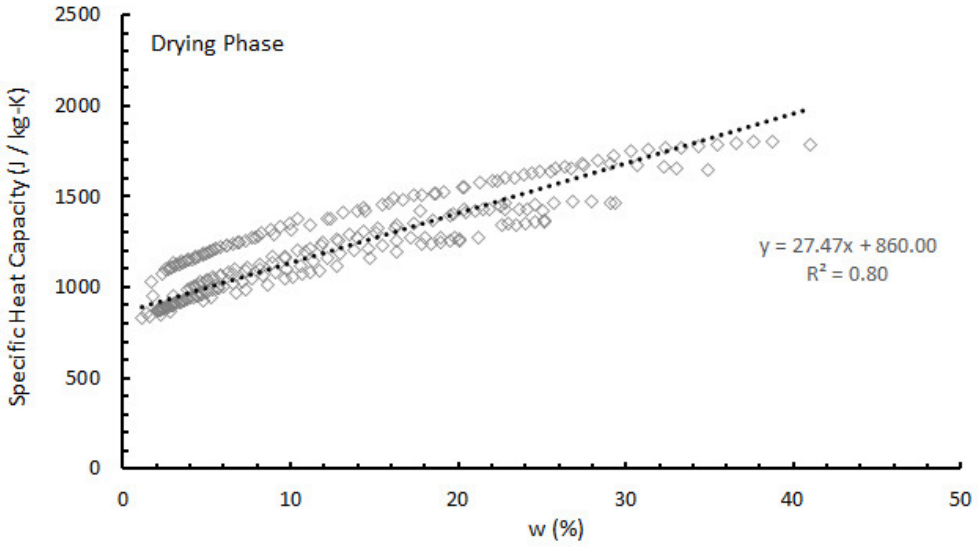

Figure 4-19 – Relationship between moisture content and specific heat for Piedmont soils – drying phase

4.3 Conclusions

The thermal properties of six Piedmont residual soils, ranging from silty sands to high plasticity silts, have been tested in the laboratory under varying density and saturation conditions. Based on the test results, a predictive relationship has been developed for estimation of thermal conductivity (during both wetting and drying) for a given porosity and composition, and for moistures ranging from dry to full saturation. In addition, a predictive relationship has been developed for estimation of specific heat capacity as a function of soil moisture content.

It has also been observed that thermal conductivity is higher during drying than wetting, especially in the low to moderate saturation range (S ~ 0.1 to 0.6). A practical example of the potential impact of soil drying and subsequent change in thermal conductivity is presented in Chapter 7.2.8.

It should be noted that repetitive wetting-drying cycles to observe the hysteresis of the thermal conductivity characteristic curve could not be applied given the test chamber limitations. The soil samples (especially the finer grained ones) would contract both radially and vertically during drying, creating a gap between the rigid chamber walls and the sample, in turn preventing uniform re-saturation of the sample. A new chamber design with flexible walls could allow for measurement of the thermal conductivity characteristic curve under repetitive wetting and drying cycles. This new chamber can also be fitted with a high capacity tensiometer for measurement of suction during testing.

It should also be noted that the predictive relationship presented herein is based on a relatively small sample size, especially for fine-grained soils. Further testing would help to refine the predictive relationship for Piedmont soils.

CHAPTER 5. ESTIMATING THERMAL CONDUCTIVITY FROM CONE PENETRATION TESTS

Cone Penetration Test (CPT) soundings are commonly used in geotechnical engineering for estimation of strength, compressibility, permeability and many other soil parameters (Lunne et al., 1997, Mayne, 2007, Robertson, 2009, Mayne, 2014). CPT soundings are also commonly used for soil classification purposes (Robertson, 1990, Schneider et al., 2008, Robertson, 2016), as well as for estimation of soil density (Mayne et al., 2010, Robertson and Cabal, 2010) and fines content (Robertson and Wride, 1998, Boulanger and Idriss, 2014). Moisture content and soil composition (e.g., determination of coarse and fine fractions) of soils can be evaluated by supplementing the CPT soundings with more conventional soil test borings and sampling, as is commonly done in practice. Determination of both the moisture content and fines content in the laboratory are very straightforward, and do not require a very large sample size for testing. In fact, these tests can be performed on soil samples retrieved from a typical split-spoon sampler that is used for Standard Penetration Testing. Moisture content can also be estimated by incorporating resistivity measurements into the CPT soundings (Kalinsky and Kelly, 1993, Singh et al., 1997), although this requires an understanding of the electrical properties of the pore fluid. Others have attempted to correlate electrical resistivity directly with thermal resistivity (inverse of thermal conductivity) based on laboratory measurements (Singh et al., 2001, Sreedeep et al., 2005, Erzin et al., 2010). There have also been more recent efforts on direct in-situ measurement of thermal conductivity using thermal CPT probes (Akrouch et al., 2016, Vardon et al., 2018).

In this chapter, results are presented from an in-situ testing and laboratory testing program. In-situ tests were performed at the NGES in Opelika, Alabama (see Figure 1-5), located within the Piedmont physiographic region in the eastern U.S. The site has been studied extensively, including geotechnical subsurface characterization using various in-situ and laboratory tests (Mayne et al., 2000, Finke et al., 2001, Mayne and Brown, 2003, McGillivray, 2007). However, to date, the characterization efforts have primarily focused on the mechanical properties. To the best of the author's knowledge, no testing has been performed to date to characterize the thermal properties of the residual soils at this site.

The testing consisted of seismic resistivity piezocone penetration test (SRCPTu) soundings with adjacent soil test borings. The SRCPTu soundings were used to evaluate subsurface stratigraphy, characterize soil behavior, and estimate relevant engineering soil properties. Shelby tube samples obtained from the adjacent soil test borings were subjected to various laboratory tests for determination of moisture content, unit weight, grain size distribution, and Atterberg Limits, as well as measurement of thermal properties. It is shown that CPT soundings coupled with soil test borings can not only provide rapid characterization of the mechanical properties, but also help to establish a first-order approximation of the thermal conductivity of Piedmont residual soils.

5.1 Methodology

Field testing at the NGES in Opelika, Alabama included the performance of two seismic resistivity piezocone penetration test soundings (SRCPTu-1 and SRCPTu-2), and two soil test borings (B-1 and B-2) adjacent to the sounding locations to obtain Shelby tube samples from several depths. The test locations are shown in Figure 5-1.

Figure 5-1 – Opelika NGES and SRCPTu sounding and Shelby tube sample locations

The SRCPTu test locations were approximately 25 m apart, and the ground elevation of the test locations was similar. The borings were located about 1.5 m from the associated SRCPTu sounding. The soundings were performed using a 15-cm^2 electronic piezocone with a tip net area ratio of 0.80 and with the pore pressure sensor at the shoulder (u_2) position. Seismic shear wave velocity measurements were made in approximately 1-meter intervals throughout the soundings. Undisturbed sampling was performed using 7.5 cm outside diameter, 75 cm long Shelby tubes.

The Shelby tube samples were sealed and transported to the Georgia Tech Sustainable Geosystems laboratory. The extraction and testing sequence is shown in Figure 5-2 (a)-(c). Once the Shelby tubes were in the laboratory, the soil samples were extruded incrementally using a hydraulic extraction device. Prior to extraction of each increment, a 10-cm long, 2.4 mm diameter thermal needle probe (TR-1, manufactured by Decagon Devices) was inserted while the sample was still confined in the Shelby tube in order to measure thermal conductivity. Sensor calibration followed the manufacturer recommended procedure using a calibration block of known thermal conductivity and was performed on a regular basis. Data logging and analysis of thermal conductivity was performed using a handheld KD2 Pro Thermal Properties Analyzer (also manufactured by Decagon Devices).

After measurement of thermal conductivity inside the tube, each sample was extruded, trimmed, the sample dimensions measured, and the sample placed in the oven for determination of unit weight/void ratio and moisture content. These steps were repeated until the samples were fully extracted from the Shelby tubes. Out of the 38 total samples extracted and measured for thermal conductivity, seventeen (17) representative samples were selected for sieve analysis, nine (9) for hydrometer analysis, and ten (10) for Atterberg

Limits tests (see Table 5-1 and Table 5-2). Some of the samples were not subjected to further testing because they appeared to be non-natural fill soils (the upper approximate 2 m at the location of B-1, and upper approximate 1 m at the location of B-2).

(a)
Prior to extruding the sample, insert (a) thermal needle (TR-1) probe to measure thermal conductivity while sample is still confined in the Shelby tube.

(b)
Extrude sample from the tube in ~15 to 30-cm increments

(c)
Trim and measure sample for unit weight and moisture content determination

Figure 5-2 – Sample testing and extraction sequence for determination of thermal and index properties of the Shelby Tube samples

Table 5-1 – Summary of unit weight, moisture content and thermal conductivity at the Opelika NGES

Test ID	Depth (m)	Sample	Total Unit Weight (kg/m^3)	Moisture Content (%)	Dry Unit Weight (kg/m^3)	Void Ratio	Degree of Saturation (%)	Thermal Cond. (W/m-K)
B-1	2.4 - 3	A	1,647	43.8	1,146	1.31	88.3	0.995
		B	1,541	36.7	1,127	1.35	72.1	1.070
		C	1,614	40.8	1,147	1.31	82.4	1.111
	4.6 - 5.2	A	1,832	22.9	1,491	0.78	78.1	1.713
		B	1,851	25.2	1,479	0.79	84.3	1.718
	6.7 - 7.3	A	1,900	17.9	1,612	0.64	73.5	1.675
		B	1,948	17.6	1,657	0.60	77.7	1.271
		C	1,894	17.0	1,620	0.64	70.7	1.388
	8.8 - 9.4	A	1,868	27.2	1,468	0.81	89.7	1.645
		B	1,868	22.7	1,523	0.74	81.1	2.385
		C	1,886	20.6	1,564	0.69	78.7	2.311
	11 - 11.6	A	1,943	23.1	1,579	0.68	90.2	2.174
		B	1,884	21.8	1,547	0.71	80.9	2.189
		C	1,881	21.0	1,555	0.70	78.8	2.231
	12.5 - 13.1	A	1,954	26.6	1,543	0.72	98.3	2.086
		B	1,893	30.0	1,456	0.82	96.9	1.550
		C	1,886	27.9	1,475	0.80	92.7	1.875
		D	1,884	21.6	1,550	0.71	80.6	1.534
	13.7 - 14.5	A	1,942	23.9	1,567	0.69	91.7	2.062
		B	1,935	23.4	1,568	0.69	89.9	2.085
		C	1,927	21.5	1,587	0.67	84.9	2.121

Table 5 1 (cont.) – Summary of unit weight, moisture content and thermal conductivity at the Opelika NGES

Test ID	Depth (m)	Sample	Total Unit Weight (kg/m^3)	Moisture Content (%)	Dry Unit Weight (kg/m^3)	Void Ratio	Degree of Saturation (%)	Thermal Cond. (W/m-K)
B-2	1.1 - 1.8	A	1,965	27.1	1,546	0.71	100.0	2.142
	2.7 - 3.5	A	1,769	41.9	1,246	1.13	98.7	1.339
		B	1,758	41.8	1,240	1.14	97.4	1.328
		C	1,809	36.2	1,328	0.99	96.4	1.420
	3.5 - 4.3	A	1,898	24.8	1,522	0.74	88.5	2.179
		B	1,929	21.5	1,588	0.67	85.1	2.065
	5.2 - 5.9	A	1,833	24.0	1,478	0.79	80.4	2.001
	6.7 - 7.5	A	1,915	21.8	1,573	0.69	84.3	1.881
		B	1,893	18.7	1,594	0.66	74.9	1.842
	8.2 - 9	A	1,948	23.7	1,574	0.68	92.0	1.953
		B	1,912	18.6	1,612	0.64	76.5	1.750
	9.8 - 10.5	A	1,914	26.6	1,512	0.75	93.7	1.836
		B	1,928	23.6	1,560	0.70	89.6	1.852
	11.3 - 12	A	1,906	21.3	1,571	0.69	82.3	2.068
	12.8 - 13.6	A	1,926	22.7	1,569	0.69	87.5	2.005
		B	1,899	22.5	1,551	0.71	84.0	1.947
	17.4 - 18.1	A	1,956	29.3	1,513	0.75	100.0	1.551
		B	1,927	23.5	1,561	0.70	89.1	1.864

Table 5-2 – Summary of index tests at the Opelika NGES

Test ID	Depth (m)	Sample	Liquid Limit (%)	Plastic Limit (%)	Plasticity Index (%)	Fines Content (%)	Clay Fraction (%)	USCS Class.
B-1	2.4 - 3	A B C	59.7	41.3	18.4	62	14	ML
	4.6 - 5.2	A B				30		
	6.7 - 7.3	A B C	43.5	30.9	12.6	30	5	SM
	8.8 - 9.4	A B C				23		
	11 - 11.6	A B C				19		
	12.5 - 13.1	A B C D	41.4	29.5	11.9	30	4	SM
	13.7 - 14.5	A B C	40.8	29.6	11.2	21	4	SM

Table 5 2 (cont.) – Summary of index tests at the Opelika NGES

Test ID	Depth (m)	Sample	Liquid Limit (%)	Plastic Limit (%)	Plasticity Index (%)	Fines Content (%)	Clay Fraction (%)	USCS Class.
B-2	1.1 - 1.8	A	47.6	28.0	19.6	58	23	ML
	2.7 - 3.5	A B C	70.4	41.6	28.8	93	33	MH
	3.5 - 4.3	A B	46.5	34.4	12.1	38		SM
	5.2 - 5.9	A				34		
	6.7 - 7.5	A B	43.1	32.6	10.5	34	3	SM
	8.2 - 9	A B				29		
	9.8 - 10.5	A B	39.4	32.5	6.9	44	5	SM
	11.3 - 12	A				24		
	12.8 - 13.6	A B	40.0	35.6	4.4	25	2	SM
	17.4 - 18.1	A B				31		

As previously mentioned, researchers have attempted to correlate electrical resistivity with thermal resistivity (inverse of thermal conductivity). Both thermal resistivity and electrical resistivity are a function of soil texture, density and degree of saturation (Sreedeep et al., 2005, Erzin et al., 2010). Bulk soil electrical resistivity is also strongly influenced by the electrical properties of the pore fluid, mainly the salinity (Rhoades et al., 1976, Kalinsky and Kelly, 1993). Based on laboratory measurements on two different soil types (silty sand and black cotton soil), Singh et al. (2001) proposed the following generalized relationship between soil electrical resistivity and thermal resistivity:

$$\log(R_E) = C_R \log(R_T) \tag{33}$$

Where R_E is electrical resistivity (in ohm-cm), C_R is a constant which is a function of the soil type, and R_T is thermal resistivity (in °C-cm/W). Sreedeep et al. (2005) subsequently expanded upon the generalized relationship proposed by Singh et al. (2001) by including additional soil samples in the analysis, and incorporating the effect of the degree of saturation on the constant C_R. In this chapter, the electrical resistivity measured directly in the SCRPTu soundings is evaluated against the thermal resistivity measured in the laboratory. The back-calculated values of C_R are then compared against published values.

Additionally, as shown previously in Chapter 3 and 4, thermal conductivity of soils can be estimated based on their texture, density/porosity and degree of saturation. In this regard, data from SRCPTu soundings can be used to provide an indication of soil density and texture. Numerous empirical relationships have been proposed for estimation of total

soil unit weight from cone penetration test results (Lunne et al., 1997, Mayne, 2007, Mayne et al., 2010, Robertson and Cabal, 2010). Of the various relationships available, the one reported in Figure 31 of Mayne (2007) was noted to result in the best fit between the measured and predicted unit weights using a root mean square error minimization approach:

$$\gamma_{sat} = 2.6 \log(f_s) + 15\ G_s - 26.5 \tag{34}$$

Where γ_{sat} is the saturated unit weight (in kN/m^3), f_s is the sleeve friction (in kPa) and G_s is the specific gravity of the soil solids (assumed as 2.65). It should be noted that while this relationship was developed for saturated soils, it was observed to provide the best fit even in the unsaturated zone of the Opelika NGES. Hence, this relationship was used for estimation of total unit weight (γ_t) from the SCRPTu soundings for this study.

Using the estimated total unit weight and the measured moisture content (MC) from laboratory tests, the corresponding dry density (ρ_d), porosity (n), and degree of saturation (S) can be calculated as follows:

$$\rho_d = \frac{\gamma_t}{(1 + MC)} \tag{35}$$

$$n = 1 - {}^{\rho_d}/_{\rho_s} \tag{36}$$

$$S = \frac{w\ G_s\ (1 - n)}{n} \tag{37}$$

The density of the solids (ρ_s) was taken as 2.65 gm/cm^3. The thermal conductivity of the soil solids was calculated using Equation (19), with the quartz content estimated using Equation (21) based on the measured fines content in the laboratory. The soil-texture dependent coefficients presented in Chapter 4 were then used to estimate the thermal conductivity of the samples, using Equations (25) through (29).

5.2 Results & Discussion

5.2.1 USCS Classification & Index Properties

Figure 5-3 shows a summary of the grain size distribution tests performed on representative samples obtained from the Shelby tubes. Table 5-2 shows a summary of the measured fines content, clay fraction and Atterberg Limits test results, as well as the corresponding USCS soil classification.

The fines content of the samples tested varied between 19 and 93 percent. In general, the fines fraction consists primarily of silt-sized particles. Clay fraction, defined as a particle size smaller than 2 microns, was between approximately 2 and 33 percent based on hydrometer tests performed on selected samples. The soils generally classify as silty sands (SM), with zones of finer grained of low to high plasticity soils (ML or MH) in the upper approximate 3 to 4 meters. In the samples that classify as SM, the average liquid limit was approximately 42 percent, and the average plasticity index was approximately 10 percent. For the entire sample group, the average liquid limit was about 47 percent, and the average plasticity index was about 14 percent.

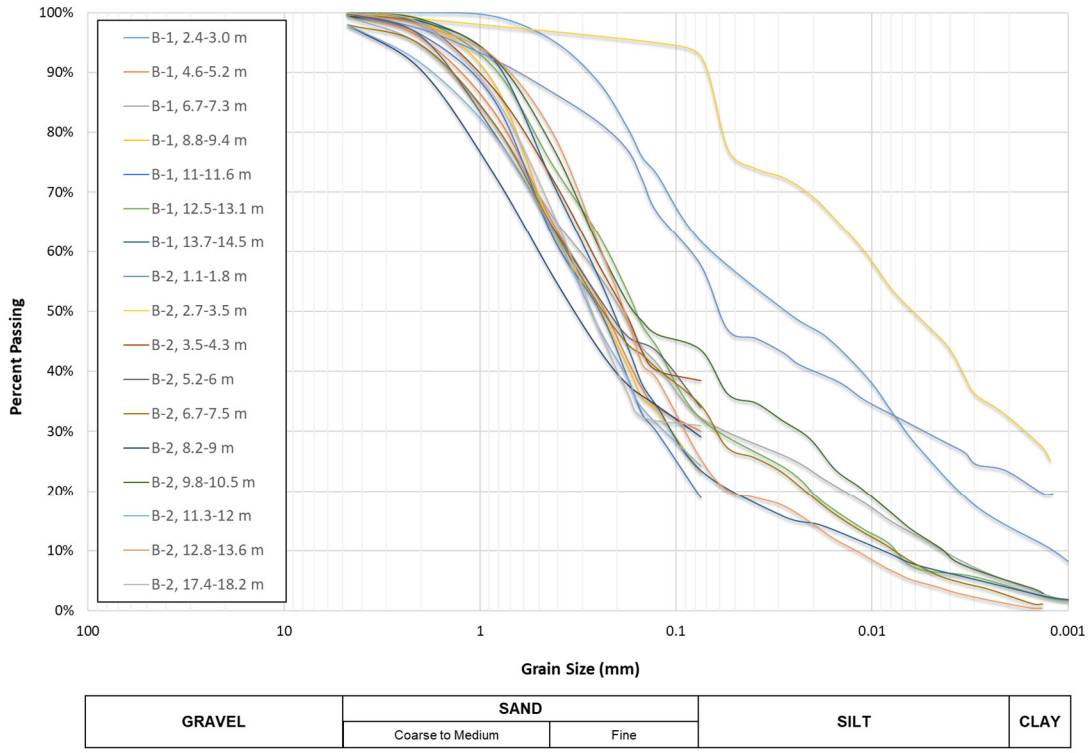

Figure 5-3 – Summary of grain size distribution tests at the Opelika NGES

5.2.2 SRCPTu Soundings – General

The SRCPTu sounding results are summarized in graphical format in Figure 5-4. The tip stresses have been corrected as per recommended practice, although the correction from q_c to q_t is not significant in these residual soils because of the magnitude of the pore water pressures (Mayne et al., 2000, Finke et al., 2001).

The cone tip stresses measure about 1 to 5 MPa in the upper 10 meters. Corresponding sleeve frictions are between approximately 100 to 200 kPa. From 10 to approximately 18 meters, the cone tip stresses measure about 4 to 10 MPa, while the corresponding sleeve frictions are between approximately 100 to 300 kPa. The relatively

higher tip resistances and sleeve frictions below 18 meters indicate the soundings were most likely terminated in the transitional zone from completely weathered saprolite to the underlying partially weathered rock.

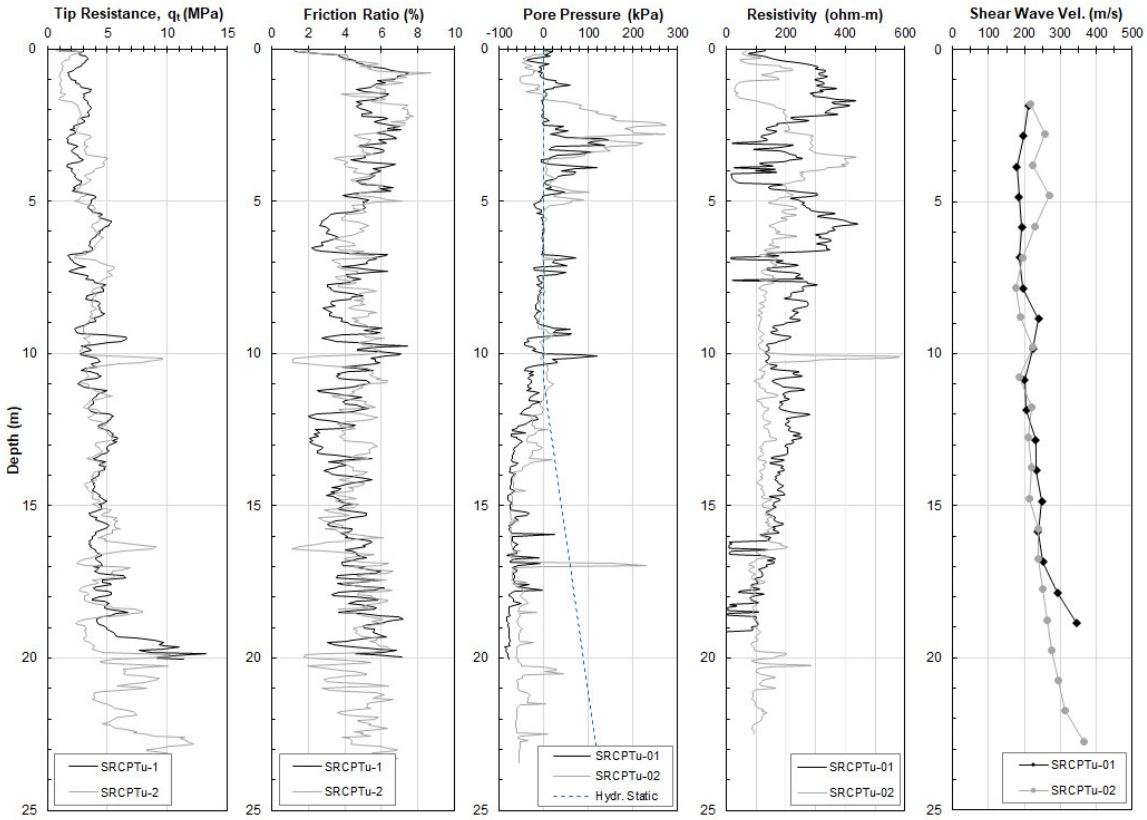

Figure 5-4 – Summary of SRCPTu soundings

The porewater pressure behavior is somewhat more complex. In the unsaturated zone above the groundwater table, negative, positive and near zero pore pressures were observed. This has been attributed to the transient capillary conditions as a result of physical and environmental factors (i.e., varying degree of saturation due to infiltration and prior rainfall activities, etc.) at the time of testing (Mayne et al., 2000). Of particular note

are the zones of relatively high positive pore pressure between 1.5 and 3 meters in sounding SRCPTu-1, and between 2.5 and 5 meters in sounding SRCPTu-2. Below the groundwater table, readings were typically negative and near cavitation (u_2 = -90 kPa). Negative porewater pressures during CPT soundings are typically observed in stiff fissured geomaterials. In Piedmont residuum, this behavior has been attributed to the shoulder location of the u_2 porewater pressure sensor and the resulting shear-induced pore pressures, as well as the remnant discontinuities such as fissures, fractures and jointing of the parent rock (Sowers and Richardson, 1983, Mayne et al., 2000).

It is also worth noting that the test results suggest the water table depth at the time of testing was approximately 10 to 11 meters. Previous CPT soundings performed at the site have typically indicated a much shallower water table depth, on the order of 2 to 3 meters below the ground surface (Mayne et al., 2000, Finke et al., 2001).

Seismic shear wave velocities measure between about 180 and 275 meters per second in the upper approximate 10 meters. Below this depth, the measured velocities were generally noted to increase with depth, reaching as high as about 345 meters per second at a depth of around 19 meters in sounding SRCPTu-1, and about 365 meters per second at a depth of around 23 meters in sounding SRCPTu-2.

Electrical resistivity measurements showed more variance between the two test locations. SRCPTu-1 encountered a zone of relatively higher resistivity in the upper 2.5 meters, and seams of lower resistivity from 2.5 to about 5 meters. Below 5 meters, the resistivity is generally decreasing with depth. Lower resistivity soils were also encountered between about 16 and 17 meters, and between about 18 and 19 meters. SRCPTu-2

encountered a zone of lower resistivity between about 1 and 2 meters, and a zone of higher resistivity from about 2.5 to 4 meters. From a depth of 4 to 10 meters, the resistivity is generally decreasing with depth. A thin seam of high resistivity soils was encountered just below 10 feet, and the resistivity was generally between 100 and 200 ohm-m from 10 to 17 meters. Below 17 meters, the resistivity was generally constant at around 100 ohm-m.

Figure 5-5 presents a range of typical resistivity values for geomaterials. Resistivity measurements from the site indicate values ranging between those associated with clays and sands, but the typical values of 100 to 200 ohm-m are associated with clayey sands to sands.

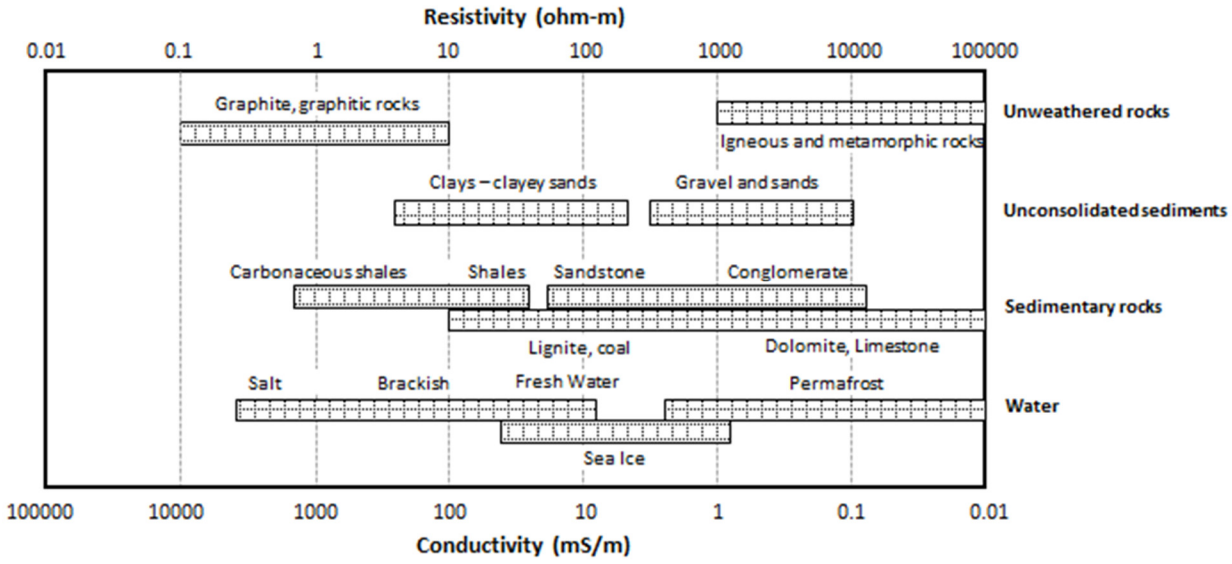

Figure 5-5 – Electrical resistivity/conductivity of various geological materials (modified after Palacky, 1987). Clay and sand differ in conductivity by up to three orders of magnitude.

5.2.3 SRCPTu Soundings – Soil Behavior

Soil behavior type from a cone penetration test sounding can be assessed in several different ways. One common method is to use the non-normalized soil behavior type (SBT) chart (Robertson et al., 1986), by plotting the cone resistance (q_c) against the friction ratio (R_f). This method has subsequently been updated to include the dimensionless cone resistance (q_c/p_a, where p_a is the atmospheric pressure) and reduce the number of soil behavior types from 12 to 9 (Robertson, 2010). The SBT indicated by the updated non-normalized classification scheme is shown in Figure 5-6. It can be seen that the Piedmont soils at this site typically classify as ranging between silty clays to clays (Zone 3) and silty sands to sandy silts (Zone 5) when using this method. Some near surface soils also classify as very stiff fine grained (Zone 9).

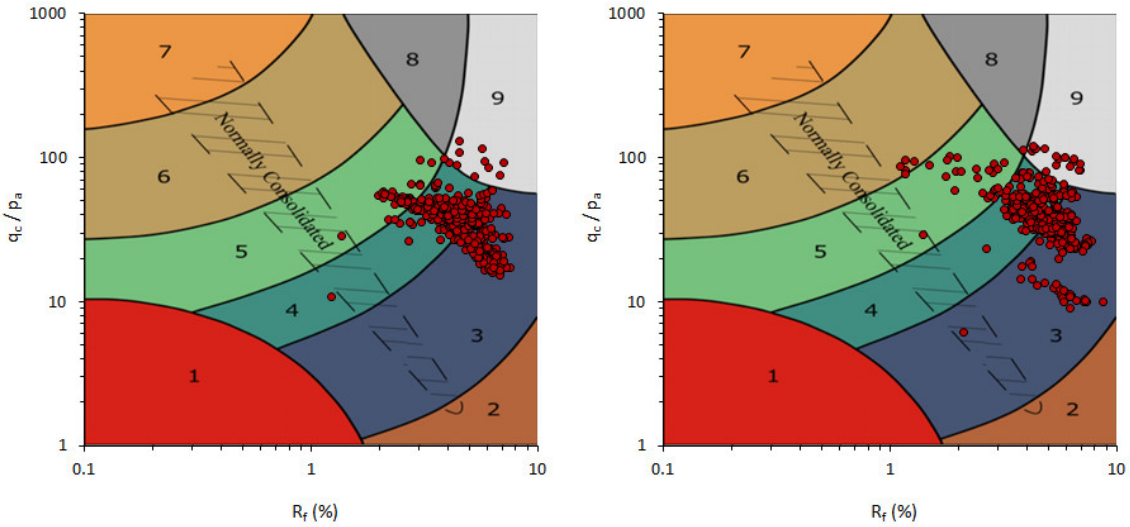

(a) (b)

Figure 5-6 – Non-normalized SBT Charts for (a) SRCPTu-1, and (b) SRCPTu-2

Alternatively, normalized parameters can be used for cone resistance and friction ratio (Robertson, 1990). These parameters are the normalized cone resistance (Q_{tn}) and normalized friction ratio (F_r). The SBT indicated by this classification scheme is shown on Figure 5-7. It can be seen that the site soils typically classify as ranging between clays to silty clays (Zone 3) and clayey silts to silty clays (Zone 4) when using this method.

An interpretation based on the pore pressure parameter (B_q) and the normalized cone resistance can also be used. The SBT indicated by this classification scheme is shown in Figure 5-8. Using this method, the site soils classify as between clayey silts to silty clays (Zone 4) and clean sands to silty sands (Zone 6), with a majority of the soils classifying as sand mixtures–silty sands to sandy silts (Zone 5).

More recently, Schneider et al. (2008) have proposed a classification method based on normalized cone resistance (Q) and normalized excess pore pressure (Δu_2). The SBT indicated by this classification scheme is shown in Figure 5-9. It can be seen that the site soils typically classify as between Essentially Drained Sands (Zone 2) and Transitional Soils (Zone 3) (i.e., behavior somewhere between that of either sand-like or clay-like soil, such as low plasticity silts), with some of the shallower soils classifying as silts and low rigidity index (I_r) clays, particularly at the location of SRCPTu-2.

Lastly, Robertson (2016) has proposed modified SBT charts to account for soil microstructure as well as soil behavior type. Figure 5-10 shows that the site soils typically classify as transitional-dilative (TD) or clay-like-dilative (CD), with some soils in SRCPTu-2 showing sand-like-dilative (SD) and clay-like-contractive (CC) behavior.

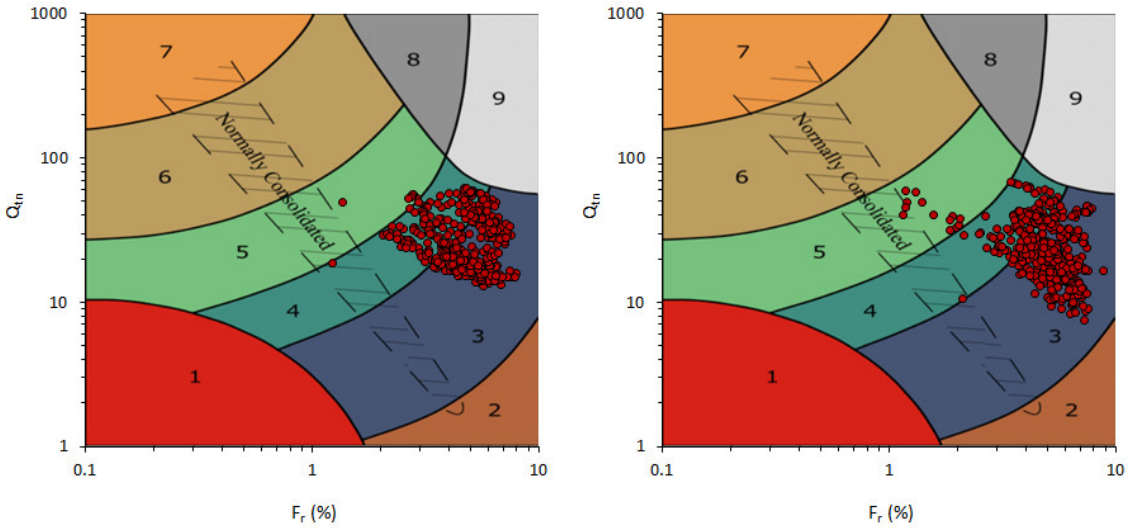

(a) (b)

Figure 5-7 – Normalized SBT Charts for (a) SRCPTu-1, and (b) SRCPTu-2

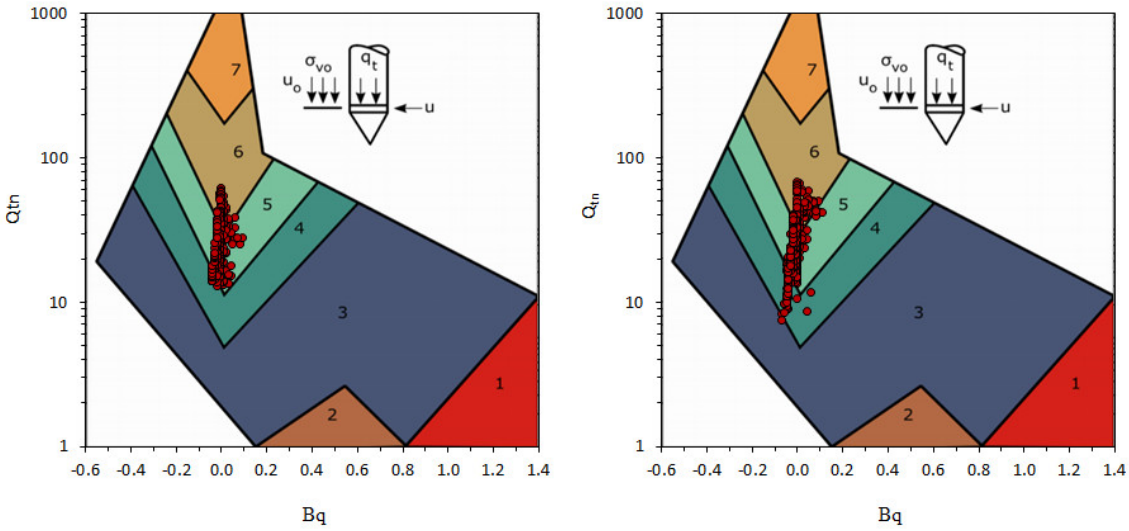

(a) (b)

Figure 5-8 – Normalized Bq SBT Charts for (a) SRCPTu-1, and (b) SRCPTu-2

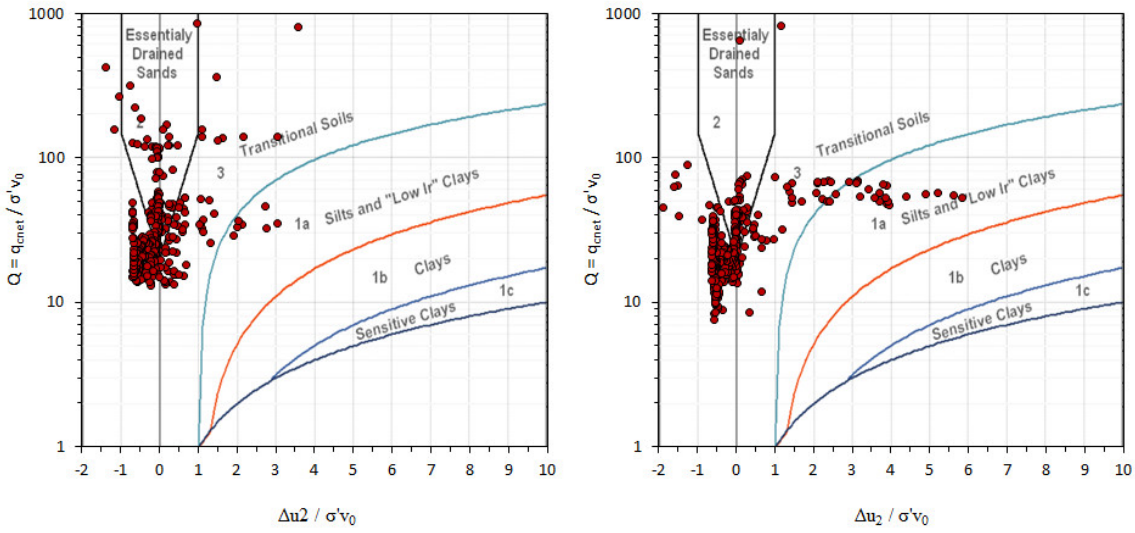

(a) (b)

Figure 5-9 – Schneider et al. (2008) SBT Charts for (a) SRCPTu-1, and (b) SRCPTu-2

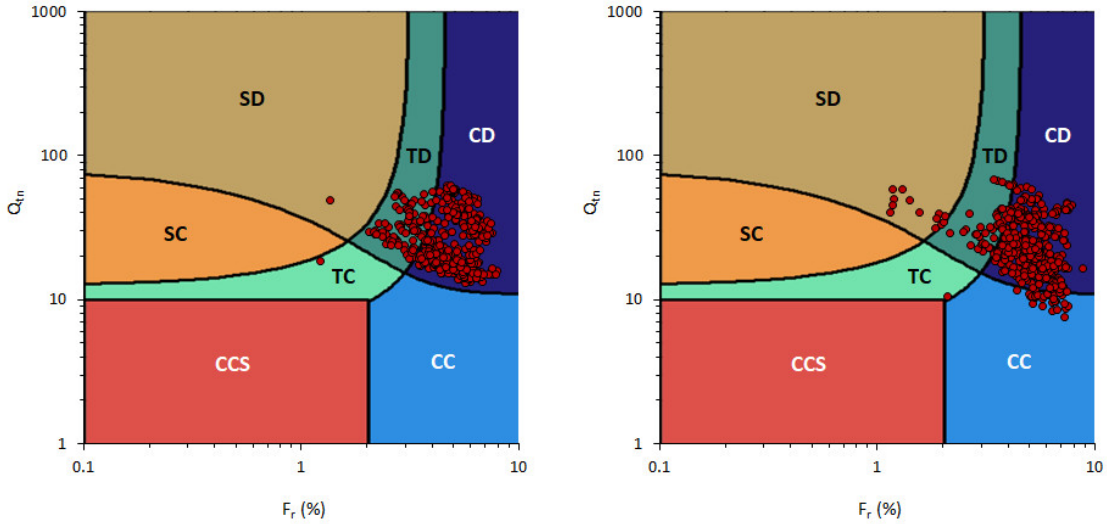

(a) (b)

Figure 5-10 – Modified SBTn Charts for (a) SRCPTu-1, and (b) SRCPTu-2

While pore pressure based methods are often not used for onshore projects due to issues with saturation of the pore pressure element (Robertson and Cabal, 2015), at this site the pore-pressure based classification methods, in particular the method proposed by Schneider et al. (2008), appear to provide the best soil behavior type interpretation. Using the cone resistance and friction ratio based charts would lead to a more fine-grained interpretation of the site soils than indicated by the laboratory test results, which can have important implications on interpretation of engineering as well as thermal properties of soils.

5.2.4 Thermal Conductivity

The measured thermal conductivities of the extracted tube samples were summarized in Table 5-1. The thermal conductivity ranged between approximately 1.0 W/m-K and 2.4 W/m-K. The lower values were associated with the shallow finer grained silts, while the higher values were observed in the coarser grained silty sands.

5.2.4.1 Electrical Resistivity and Thermal Conductivity

A comparison was performed between the thermal resistivity (inverse of thermal conductivity) of the tube samples as measured in the laboratory and the electrical resistivity readings from the SRCPTu soundings, using Equation (33). For the comparison, the average electrical resistivity was calculated using the SRCPTu data and the average thermal conductivity was calculated using the laboratory data between the depth intervals shown in Table 5-1. These values were then used in order to back-calculate the value of the constant C_R. The results are summarized in Table 5-3.

Table 5-3 – Relationship between electrical resistivity and thermal conductivity

Test ID	Depth (m)	Avg. k (W/m-°C)	Avg. R_t (^{0}C-cm/W)	Avg. R_e (ohm-cm)	log(R_t)	log(R_e)	C_R
B-1	2.4 - 3	1.06	94.5	14,607	1.98	4.16	2.11
	4.6 - 5.2	1.72	58.3	24,958	1.77	4.40	2.49
	6.7 - 7.3	1.44	69.2	14,903	1.84	4.17	2.27
	8.8 - 9.4	2.11	47.3	18,725	1.67	4.27	2.55
	11 - 11.6	2.20	45.5	20,539	1.66	4.31	2.60
	12.5 - 13.1	1.76	56.8	22,393	1.75	4.35	2.48
	13.7 - 14.5	2.09	47.9	17,890	1.68	4.25	2.53
B-2	1.1 - 1.8	2.14	46.7	5,405	1.67	3.73	2.24
	2.7 - 3.5	1.36	73.4	28,911	1.87	4.46	2.39
	3.5 - 4.3	2.12	47.1	33,757	1.67	4.53	2.71
	5.2 - 5.9	2.00	50.0	19,025	1.70	4.28	2.52
	6.7 - 7.5	1.86	53.7	14,274	1.73	4.15	2.40
	8.2 - 9	1.85	54.0	11,785	1.73	4.07	2.35
	9.8 - 10.5	1.84	54.2	22,029	1.73	4.34	2.50
	11.3 - 12	2.07	48.4	13,271	1.68	4.12	2.45
	12.8 - 13.6	1.98	50.6	12,295	1.70	4.09	2.40
	17.4 - 18.1	1.71	58.6	9,407	1.77	3.97	2.25
						Avg =	**2.43**

It can be seen that C_R at this site ranged between 2.11 and 2.71, with an average value of 2.43. This is considerably higher than the range of C_R reported by Sreedeep et al. (2005), who noted values of C_R to be between approximately 1.3 and 1.9 for degrees of saturation ranging between 70 and 100 percent and for coarse content ranging between about 10 and 90 percent (see Figure 5-11). The difference may be due to a difference in the chemical composition of the pore fluids between the samples reported in that study and the samples at the Opelika NGES.

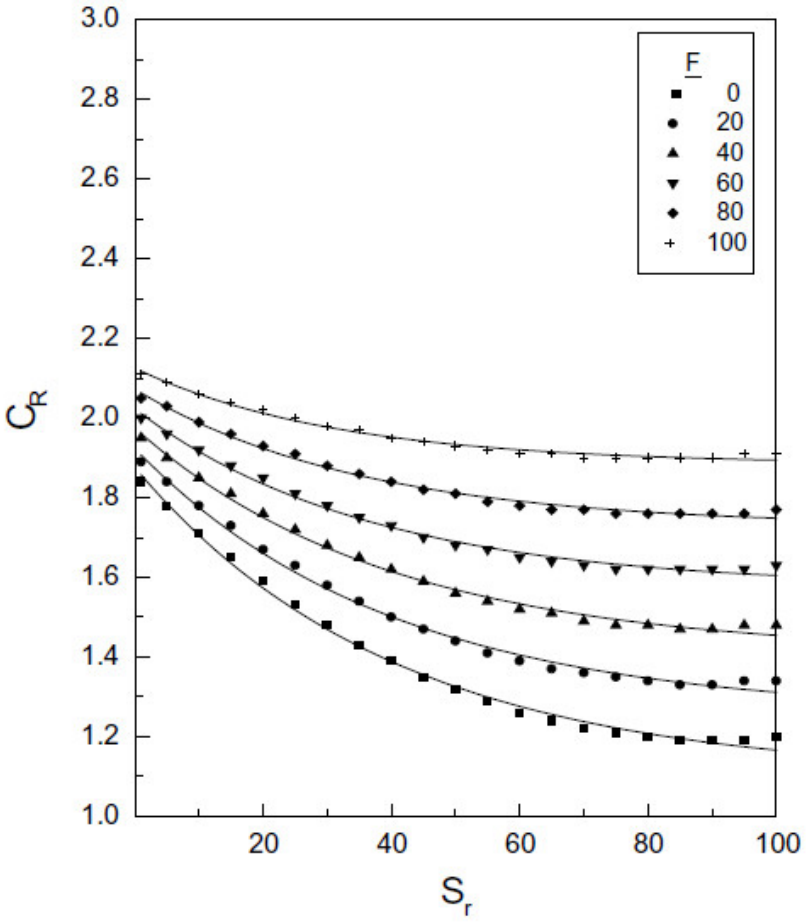

Figure 5-11 – Variation of C_R with degree of saturation (S_r) and coarse content (F), from Sreedeep et al. (2005)

Figure 5-12 shows a comparison between predicted thermal conductivities using the average C_R value of 2.43 and the laboratory measured thermal conductivities. The results show that there is considerable scatter and suggests that using electrical resistivity for prediction of thermal conductivity may not produce robust outcomes.

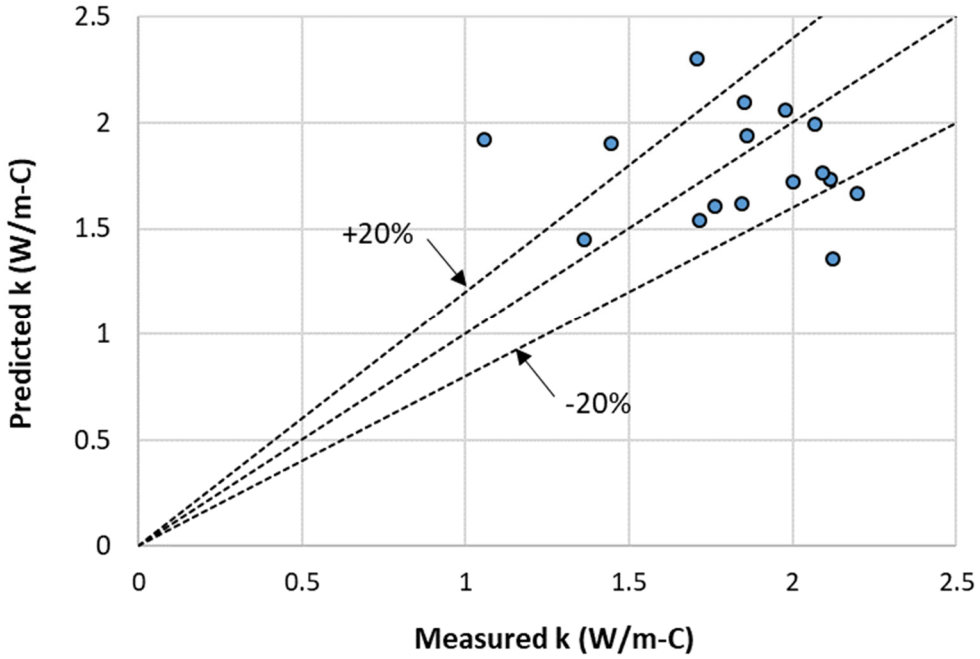

Figure 5-12 – Comparison of predicted and measured thermal conductivity based on electrical resistivity

5.2.4.2 Thermal Conductivity from CPT

Figure 5-13 shows a comparison between soil unit weights predicted using Equation (34) and those as determined from laboratory measurements as shown in Table 5-1. It can be seen that overall the predictive equation does a reasonable job of estimating soil unit weight, with approximately 82 percent of the predicted values within 10 percent of the measured ones.

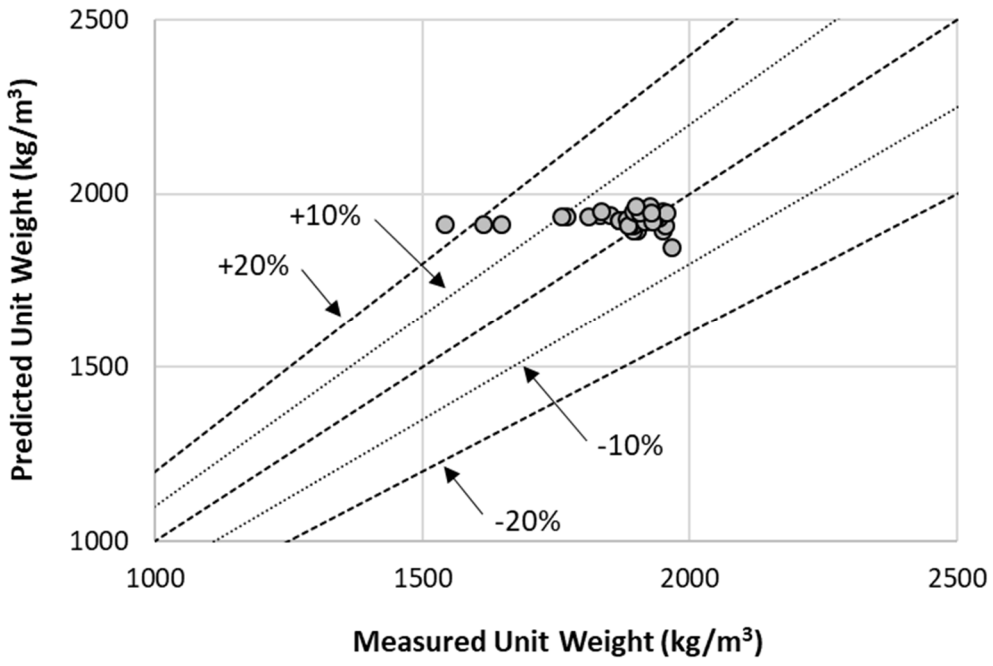

Figure 5-13 – Comparison between predicted and measured soil unit weights

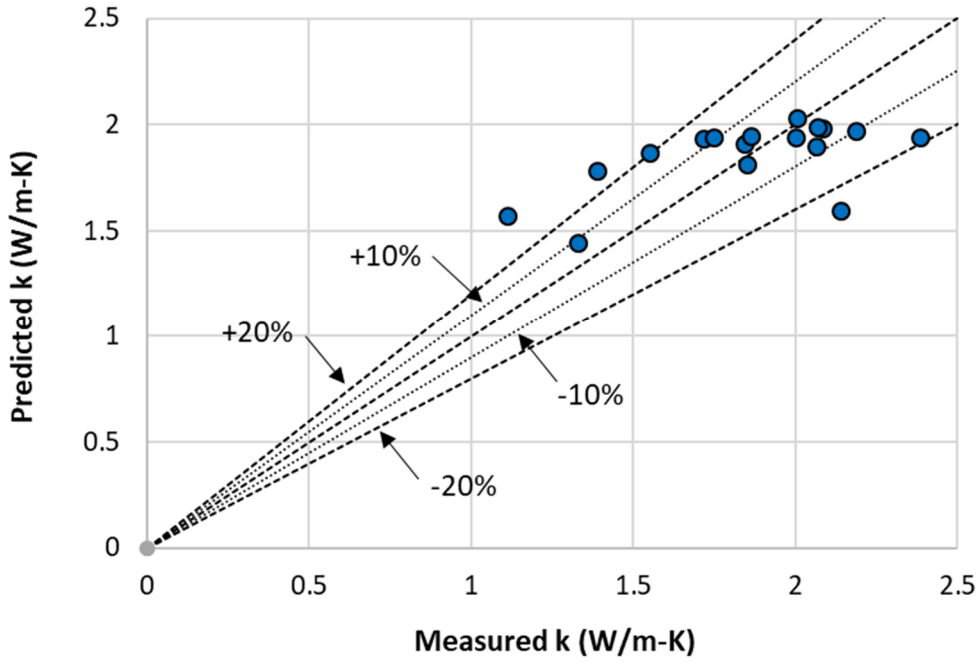

Figure 5-14 – Comparison between predicted and measured thermal conductivities

Figure 5-14 shows a comparison between the predicted and measured thermal conductivity for the Opelika NGES samples. It can be seen that overall the CPT-based prediction does a reasonable job of estimating thermal conductivity, with about 59 percent of the predicted values within 10 percent of the measured ones and 82 percent of the predicted values within 20 percent of the measured ones. The three data points outside ±20 percent are the two shallow silt samples (B-1, 2.4-3 m, Sample C and B-2, 1.1-1.8 m, Sample A) and one silty sand sample (B-1, 6.7-7.3 m, Sample C). In the case of the shallow silts, the discrepancy in the prediction is most likely due to an overestimation of the quartz content by Equation (21), which in turn results in an over-prediction of thermal conductivity. For the silty sand sample, a review of the results from another sample inside the Shelby tube (B-1, 6.7-7.3 m, Sample A) shows a thermal conductivity of 1.68 W/m-K for the same void ratio and similar degree of saturation, which is much closer to the predicted value of 1.78 W/m-K.

5.3 Conclusions

Results from an in-situ testing and laboratory testing program at the Opelika NGES have been presented. The data were used to evaluate the thermal properties of the site soils, and to assess whether thermal conductivity can be reliably estimated from in-situ test data. The results show the challenges associated with estimating thermal conductivity directly from the electrical resistivity measurements. Both thermal and electrical conductivity are dependent upon similar factors (such as density, texture and degree of saturation). However, while it may be possible to correlate the two parameters in a laboratory environment when using a consistent pore fluid with identical chemical composition, it is challenging to establish a reliable correlation between them for the field where there is

likely to be differences in the chemical composition of the pore fluid (particularly the salt concentration).

On the other hand, the results indicate that it may be possible to obtain a first-order estimate of thermal conductivity from CPT results when combining the estimated unit weight with simple laboratory measurements of moisture content and fines content. In practice, CPT soundings are often accompanied by adjacent soil test borings at select representative locations for "ground-truthing" (i.e., for comparison of soil behavior type estimated from CPT with examination and/or testing of actual soil samples from soil test borings). This allows for collection of split-spoon samples, which can be used for determination of moisture content and fines content using routine and relatively quick laboratory experiments. The texture-dependent relationship for Piedmont residual soils as described in Chapter 4 was utilized to show that a reasonably accurate first-order estimate of thermal conductivity can be made. A more accurate prediction would require a better understanding of the mineralogical composition of the soils (namely, the quartz content). Alternatively, the use of emerging technologies such as thermal CPT probes may allow for direct in-situ measurement of thermal conductivity.

CHAPTER 6. A COMPARISON BETWEEN THERMAL CONDUCTIVITY OF UNDISTURBED LAB AND REMOLDED TUBE SAMPLES

As discussed previously in Chapter 2.3.1.4, soil microstructure can have an impact on thermal conductivity. The presence of microstructure in soils can be detected based on small-strain wave velocity measurements. In particular, based on work by Schneider and Moss (2011), Robertson (2016) has proposed a methodology based on seismic cone penetration test results for identifying soils with microstructure, using the net cone resistance, q_n, normalized cone resistance, Q_{tn}, and modified normalized small-strain rigidity index, $K^*(G)$, which is a function of the small-strain stiffness, G_0, that in turn is a function of the measured shear wave velocity, V_s:

$$K^*(G) = (G_0/q_n)(Q_{tn})^{0.75} \tag{38}$$

$$G_0 = \rho\,(V_s)^2 \tag{39}$$

Using this methodology, the line defined $K^*(G) = 330$ delineates the soils with significant microstructure from those with little to no microstructure (Robertson, 2016).

Additionally, it has been shown that microstructure disturbance due to sample remolding can manifest as reduced small-strain stiffness, when comparing field measurements to remolded laboratory measurements (Rinaldi and Santamarina, 2008, Dai and Santamarina, 2014). The disturbance effects are particularly evident for predominantly sandy soils in contrast to clayey soils. With regard to thermal conductivity, Low et al.

(2015) showed that laboratory thermal conductivity measurements on undisturbed samples of London clay differed significantly from those calculated from the results of an in-situ thermal response test (TRT). The differences were attributed to effective stress, sample disturbance (including potential drying during and after the sampling process), and differences in the sensed volume between the laboratory and field measurements.

In this chapter, the results from a field and laboratory testing program are presented. The results from the seismic cone penetration tests as described in Chapter 5 were used to assess the presence of microstructure at the Opelika NGES. The undisturbed Shelby tube samples obtained from the site were used for determination of thermal conductivity, using both measurements from the intact tube samples as described in Chapter 5, as well as measurements taken on remolded samples as described below. A comparison was then performed between the results from the intact tube samples and the results from the remolded samples.

6.1 Methodology

Thirteen (13) representative samples of Piedmont residual soils were selected from Borings B-1 and B-2 for remolding in an acrylic chamber. The relevant index properties of the test samples are summarized in Table 6-1. Based on the test results, the soils can typically be described as silty sands (SM), with a surficial layer of sandy silts of low to high plasticity (ML and MH) at location B-2.

Table 6-1 – Summary of index test results on select Opelika NGES samples

Sample ID	Location / Depth (m)	FC (%)	LL (%)	PI (%)	USCS
1	B-1 / 4.6-5.2	30	NM	NM	SM
2	B-1 / 6.7- 7.3	30	44	13	SM
3	B-1 / 8.8- 9.4	23	NM	NM	SM
4	B-1 / 12.5-13.1	30	41	12	SM
5	B-1 / 13.7-14.5	21	41	11	SM
6	B-2 / 1.1-1.8	58	48	20	ML
7	B-2 / 2.7-3.5	93	70	29	MH
8	B-2 / 5.2- 6.0	34	NM	NM	SM
9	B-2 / 6.7-7.5	34	43	11	SM
10	B-2 / 8.2-9.0	29	NM	NM	SM
11	B-2 / 9.7-10.5	44	39	7	SM
12	B-2 / 11.3-12.0	24	40	4	SM
13	B-2 / 17.4-18.2	31	NM	NM	SM

FC = fines content (passing #200 sieve)

NM = not measured

The acrylic chamber had an inner diameter of 63.5 mm and a height of 41.5 mm. The specimens were remolded to match the field density (as determined from laboratory unit weight/density tests) as closely as possible via dry tamping in uniform layers. De-aired water was then injected through a port located at the bottom of the sample until the target degree of saturation was achieved (to also match the field saturation as closely as possible).

The samples were allowed to rest for a minimum of 24 hours, and the thermal conductivity of the samples was measured using a 3 cm long, 1.3 mm diameter dual-needle

heat-pulse probe (SH-1, manufactured by Decagon Devices). Sensor calibration followed the manufacturer recommended procedures using a calibration block of known thermal conductivity and was performed on a regular basis. Data logging and analysis of the thermal properties was performed using a KD2 Pro Thermal Properties Analyzer, also manufactured by Decagon Devices.

6.2 Results & Discussion

Figure 6-1 shows the soil microstructure charts based on Robertson (2016). It can be seen that most of the points plot within the range between K*(G) = 215 and K*(G) = 330 (with a few outliers), though most of the points are closer to the K*(G) = 330 line and some even above. This indicates that there may be microstructure effects present at this site.

The results of the thermal conductivity measurements on the Shelby tube samples and the remolded samples are summarized in Table 6-2, and also shown graphically in Figure 6-2. In Table 6-2, the suffixes "-t" and "-r" refer to "tube" and "remolded", respectively. It can be seen from Table 6-2 and Figure 6-2 that in general, the thermal conductivity as measured in the undisturbed tube samples is higher than that of the remolded samples. There was only one instance where the thermal conductivity of the tube sample was lower than that of the remolded sample. With the exception of the outliers, the ratio of the thermal conductivity of the tube samples to that of the remolded samples ranged between 1.05 and 1.26, with an average of 1.14 and a standard deviation of 0.07. For the two sandy silt samples, the average ratio was about 1.1, while for the silty sand samples the ratio was approximately 1.15.

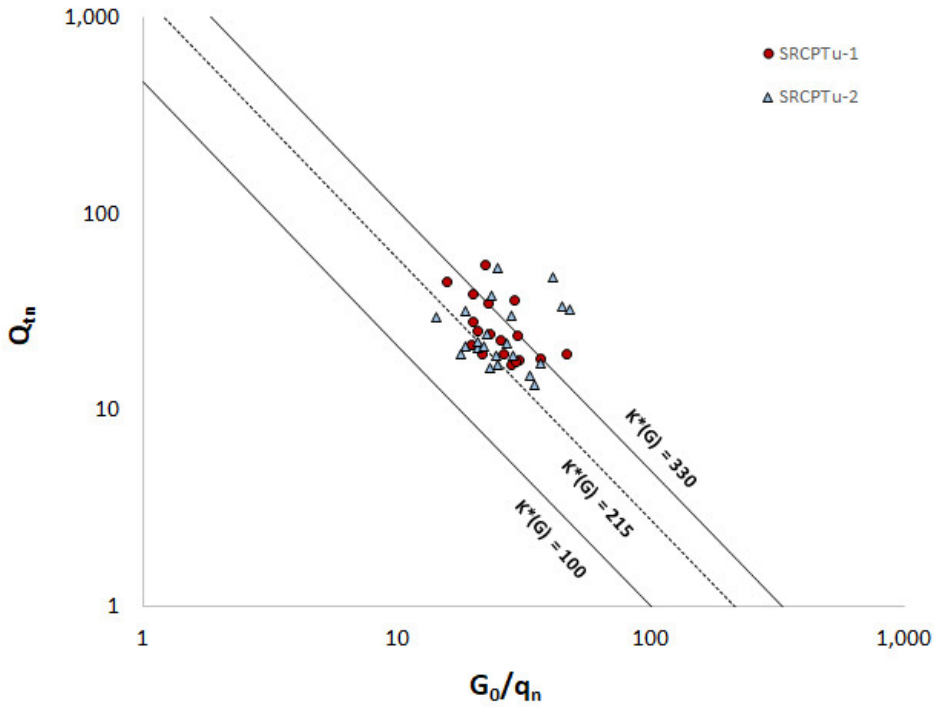

Figure 6-1 – Soil microstructure charts for sounding SRCPTu-1 and SRCPTu-2

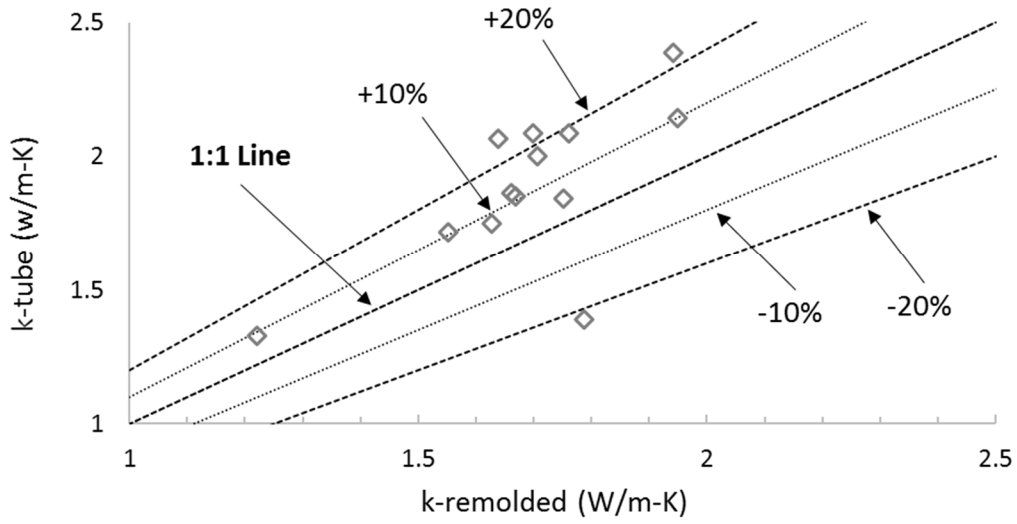

Figure 6-2 – Comparison of thermal conductivity for remolded and Shelby tube samples

Table 6-2 – Summary of measured thermal conductivity on select Opelika NGES samples

Sample ID	Location / Depth (m)	e	S	k-t	k-r	k-t / k-r
1	B-1 / 4.6-5.2	0.81	0.83	1.718	1.553	1.11
2	B-1 / 6.7- 7.3	0.65	0.70	1.388	1.788	0.78
3	B-1 / 8.8- 9.4	0.75	0.80	2.385	1.943	1.23
4	B-1 / 12.5-13.1	0.73	0.97	2.086	1.761	1.18
5	B-1 / 13.7-14.5	0.71	0.89	2.085	1.699	1.23
6	B-2 / 1.1-1.8	0.73	0.99	2.142	1.950	1.10
7	B-2 / 2.7-3.5	1.17	0.96	1.328	1.220	1.09
8	B-2 / 5.2- 6.0	0.81	0.79	2.001	1.707	1.17
9	B-2 / 6.7-7.5	0.68	0.74	1.842	1.752	1.05
10	B-2 / 8.2-9.0	0.66	0.76	1.750	1.628	1.08
11	B-2 / 9.7-10.5	0.71	0.89	1.852	1.670	1.11
12	B-2 / 11.3-12.0	0.70	0.82	2.068	1.639	1.26
13	B-2 / 17.4-18.2	0.71	0.89	1.864	1.661	1.12

e = void ratio; S = degree of saturation; k = thermal conductivity (W/m-K)

A likely explanation for the difference between the tube samples and the remolded samples is the loss of structure upon remolding. As indicated by the SRCPTu results and Figure 6-1, the soils at this site appear to have some microstructure, most likely due to diagenesis. The loss of this microstructure upon remolding may have resulted in lower measured thermal conductivity values. The findings are also consistent with previous findings (Rinaldi and Santamarina, 2008, Dai and Santamarina, 2014), in that the sandy soils were more susceptible to remolding effects than fine-grained soils, though the sample size for fine grained soils in this study was very small. The other factors listed in Table 2-1

are not believed to have been a factor, given that both the tube and remolded samples were tested with no confining stress, water was the pore fluid in both tests, and there would have been no change in mineralogy. The high durometer rubber tamper used to remold the samples is also not believed to have altered particle size or shape, given that hand pressure alone is not sufficient to result in particle crushing.

Another possible explanation for the difference is the sensed volume associated with the two sensors used for measurement of thermal conductivity. Even though the sensors were calibrated regularly during testing and no issues were observed, the SH-1 sensor used to test the remolded samples has a smaller sensed volume in comparison to the TR-1 sensor. As previously discussed, Low et al. (2015) showed that the back-calculated thermal conductivity from a full-scale thermal response test (TRT) is significantly greater than the thermal conductivity measured in the laboratory. This was attributed to differences in sensed volume, especially due to the heterogeneity which is likely to exist in the field (or in a larger tube sample) but may not exist in a small laboratory specimen, as well as sample disturbance effects (even "undisturbed" samples experience some disturbance during sampling, transport and storage), potential drying during and after the sampling process, and effective stress which increases the quality of particle-to-particle contacts in the field. In regard to potential drying during and after sampling, while a lower degree of saturation implies a lower thermal conductivity, drying also results in increased suction. Suction forces in turn act to improve the quality of the particle-to-particle contacts, and may thereby counteract the reduction in thermal conductivity due to loss of moisture.

6.3 Conclusions

The thermal conductivity of undisturbed Shelby tube samples and laboratory samples remolded to the same density/void ratio and degree of saturation were measured using needle probe sensors. The results indicate that in general, the thermal conductivity of the remolded samples is noticeably lower than those of the undisturbed samples. A review of the normalized cone resistance and normalized rigidity index based on the seismic cone penetration test results indicate that the soils at this particular site typically plot near the boundary of the young, relatively non-structured soils and soils showing microstructure effects due to cementation, bonding or aging effects. These results suggest there may be microstructure effects influencing the soil thermal behavior at the NGES.

In addition, based on results from literature, it appears that the thermal conductivity of undisturbed samples would be expected to be smaller than those from a full-scale in-situ experiment such as a thermal response test (TRT). In this regard, the present study highlights some of the challenges associated with determination of thermal conductivity from field and laboratory tests. In the laboratory, while samples can be prepared under relatively controlled conditions, variances can still occur due to sample size and preparation, sensor size and accuracy, and other factors. In the field, while a test such as a TRT provides a larger sensed volume (and hence better captures the natural vertical and lateral variation of soil properties), it is also subject to higher costs relative to laboratory testing, as well as differences in the models used to interpret the TRT results.

These challenges also have practical implications for design of thermo-active foundations, as the fluid circulation loop length is directly influenced by the thermal conductivity of the geomaterials surrounding the foundation. In this regard, the findings presented herein suggest that using values obtained from remolded samples may be conservative, resulting in longer loop lengths and additional cost. On the other hand, some level of conservatism may be beneficial because the design of the thermal aspect of thermo-active foundations are typically not subject to a relatively high factor of safety, as is commonly used for design of the mechanical aspects of the foundations.

CHAPTER 7. ENGINEERED TRANSITION ZONE: PROOF-OF-CONCEPT VIA NUMERICAL MODELING

In this chapter, the results from a multi-physics COMSOL® numerical model are presented, using a novel concept termed the "engineered transition zone" between the structural pile element and the surrounding geomaterials. Thermal properties representative of Piedmont residual soils are used in the numerical models to incorporate the findings from the previous chapters. It is shown that an engineered transition zone can significantly improve the thermal performance of a shallow energy pile foundation, especially when used in conjunction with a fluid circulation loop configuration such as helical loops which maximize the pipe surface area available for heat transfer. It is also demonstrated that the use of an engineered transition zone can reduce the magnitude of temperature changes in the pile, which can have implications on thermal stresses within the pile element. Lastly, long-term performance of an enhanced shallow thermo-active foundation using an ETZ with a helical loop is evaluated.

7.1 Methodology

7.1.1 Engineered Transition Zone Concept

The proposed engineered transition zone (ETZ) concept is shown in Figure 7-1 and Figure 7-2. Under current practices, there can be a sharp contrast between the thermal properties of the pile (typically concrete) and there is limited ability to change the interface properties between the pile and the surrounding geomaterials. The proposed ETZ presents an opportunity to create a zone between the pile and the surrounding geomaterials with

controlled properties to enhance heat transfer. The transition zone can be manufactured in-situ, using engineered materials that aim to reduce thermal resistance and improve thermal properties (mainly, the thermal diffusivity) for more efficient heat transfer in and out of the surrounding geomaterials. With this approach, the circulation tubes no longer have to be inserted into the limited space between the reinforcement cage and the outside edge of the pile and can instead be placed in the transition zone. The removal of this geometrical constraint can in turn allow for different fluid circulation pipe shapes/configurations to be used to optimize heat transfer. The introduction of an ETZ can also act to isolate the structural component of the pile from the heat transfer component. The length of each pile component (structural and thermal) can be optimized independently from one another as shown on Figure 7-1(b).

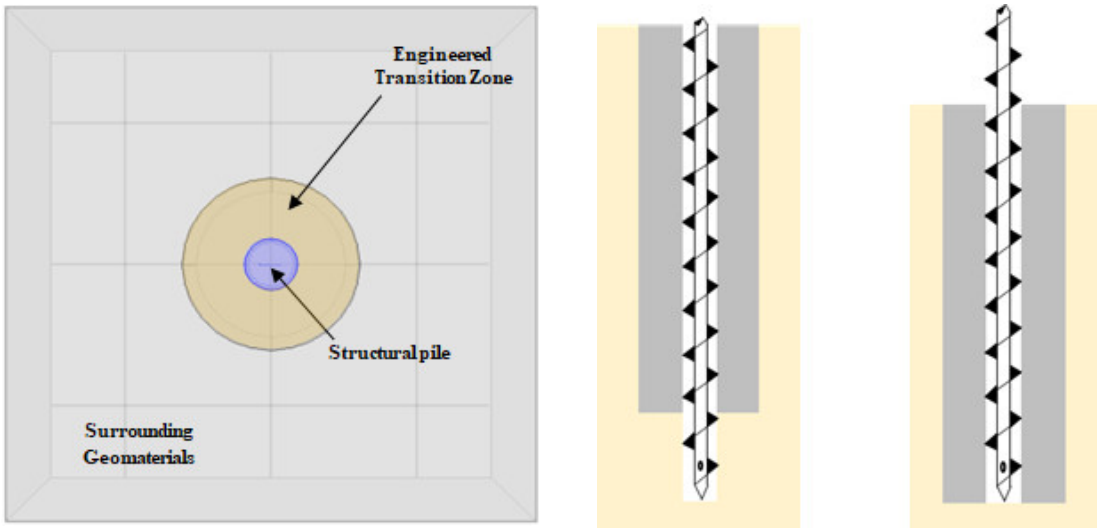

(a) (b)

Figure 7-1 – (a) Engineered foundation system concept for enhanced heat transfer (plan view) (b) Pile tip extending below transition zone (left) or the same depth as the transition zone (right)

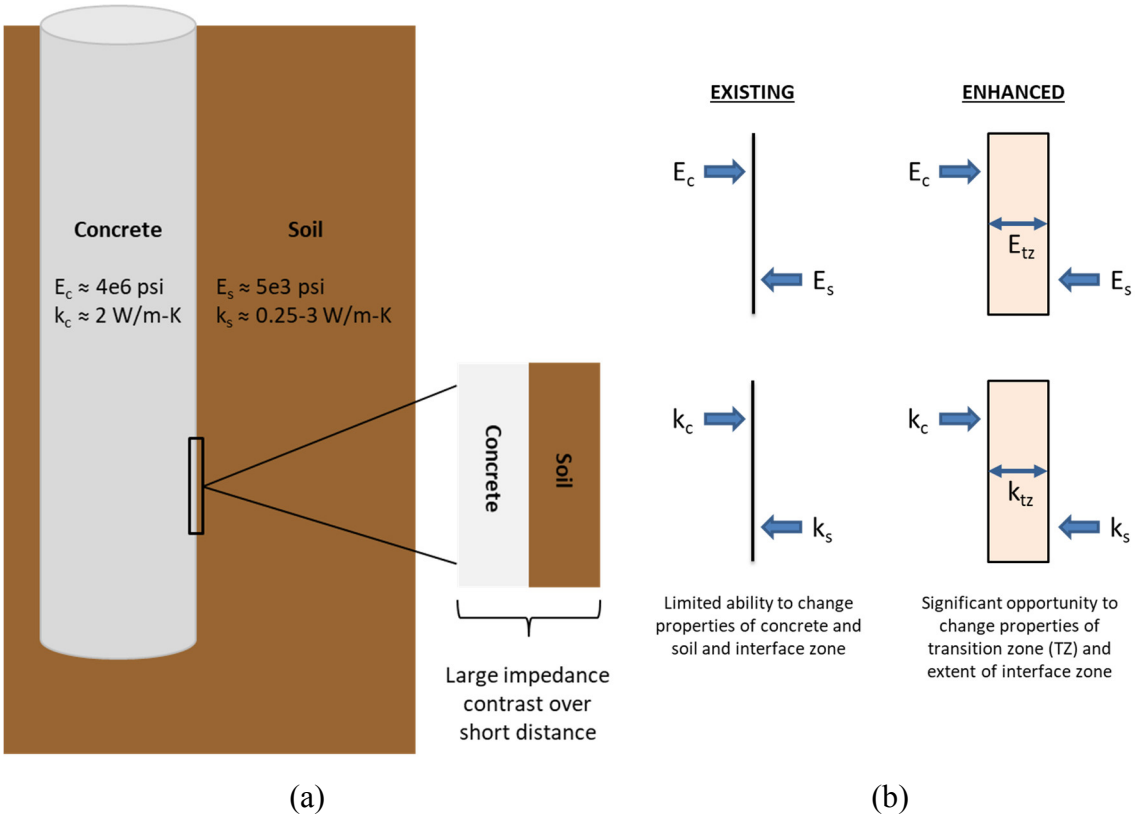

Figure 7-2 – (a) Typical configuration for a concrete pile in direct contact with soil, resulting in high impedance contrast at the interface; (b) ETZ concept to create transition zone between pile and soil for optimized heat transfer

7.1.2 Numerical Model Validation

A coupled 3D finite-element numerical model was constructed using COMSOL Multiphysics®. The model couples the non-isothermal pipe flow module to simulate convective heat transfer which takes place due to fluid circulation in the pipes as well as conduction through the pipe walls as described in Chapter 2.2.1, with the heat transfer in solids module to simulate conduction heat transfer through the pile and the surrounding geomaterials as described in Chapter 2.2.2.

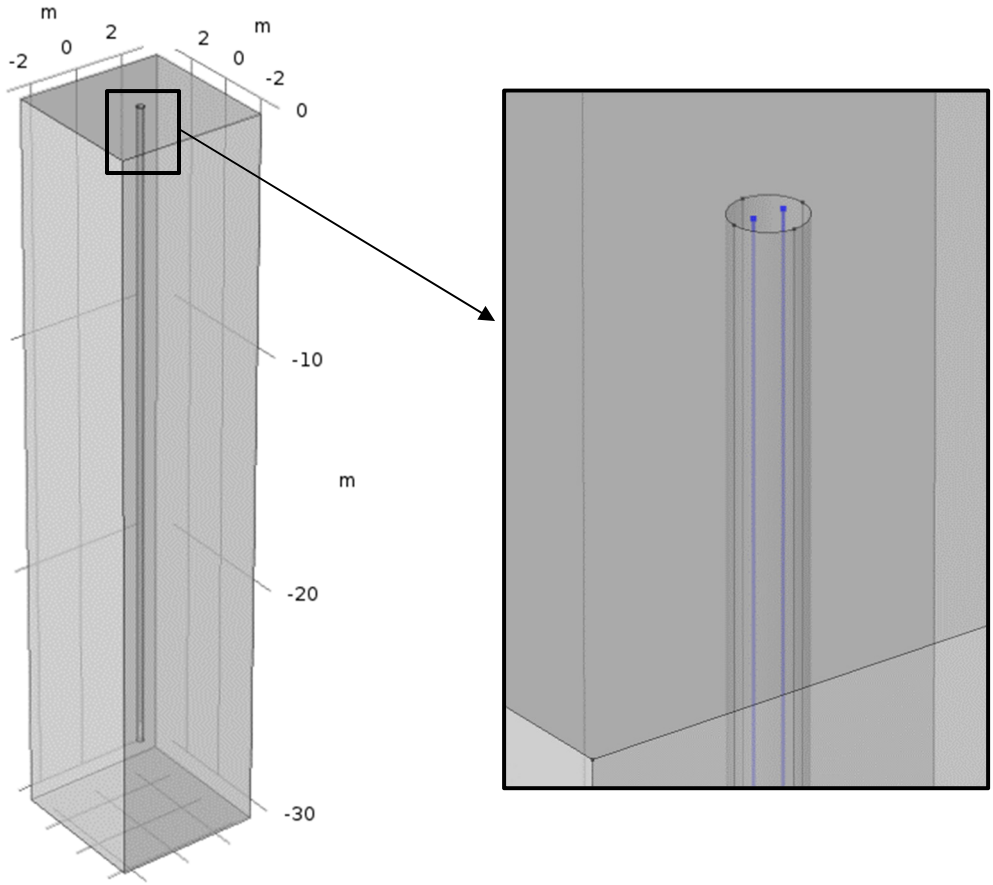

(a) (b)

Figure 7-3 – (a) Model pile geometry (b) Close-up of the pile top showing the single U-loop configuration for model validation using published results from Cecinato and Loveridge, 2015

The COMSOL model was validated using the results of a published thermal response test (Cecinato and Loveridge, 2015). The pile used in the thermal response test was 0.3 meter in diameter, and 26.8 meters in length. The pile was fitted with a single high-density polyethylene (HDPE) U-tube in the middle, with an inner diameter of 26.2 mm and a wall thickness of 2.9 mm (see Figure 7-3). During the test, fluid (water) was circulated

through the pipes embedded in the energy pile at a constant power to either inject or extract heat from the surrounding geomaterials for a total period of around 19,200 minutes (320 hours), and the inlet and the outlet temperatures were monitored and recorded (see Figure 7-4).

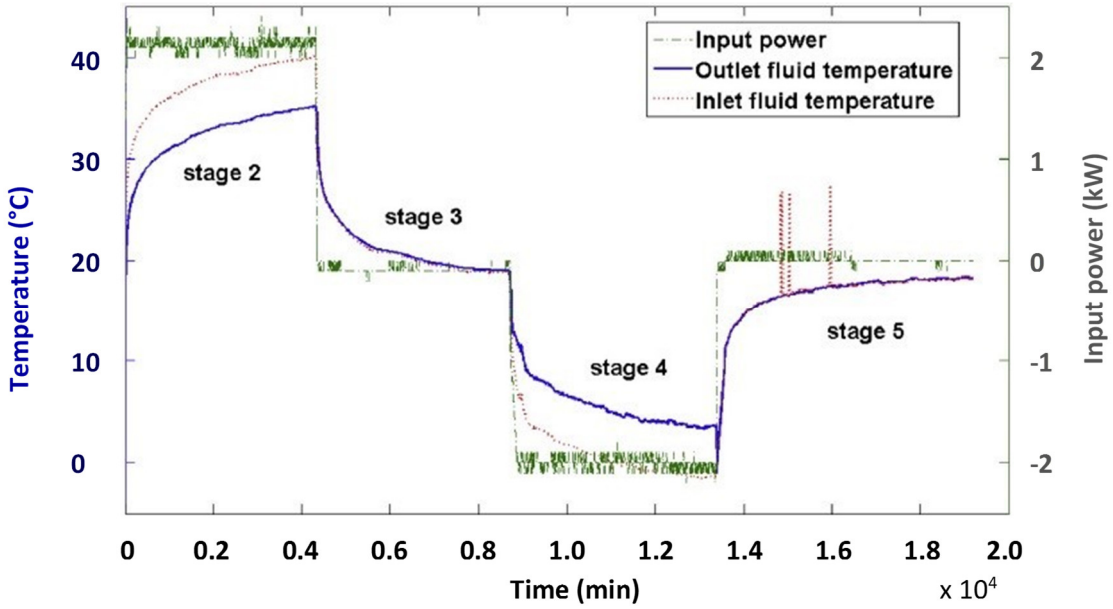

Figure 7-4 – Thermal response test results (from Cecinato and Loveridge, 2015)

The material thermal properties given are shown in Table 7-1. The soil and concrete were assumed to be homogeneous and isotropic.

The initial ground temperature prior to the start of the test was given as 17.4 degrees Celsius. As a boundary condition for ground temperature, the far-field temperature was taken to be equal to the reported initial ground temperature. The lateral model extent was chosen as 20 times the pile diameter to avoid boundary effects.

Table 7-1 – Thermal properties for numerical model validation (from Cecinato and Loveridge, 2015)

Material description	Property and assigned value
Circulating fluid (water)	Density = 1,000 kg/m^3
	Specific heat capacity = 4,200 J/kg-K
	Thermal conductivity = 0.6 W/m-K
	Dynamic viscosity = 1.0e-3 Pa-s
	Mass flow rate = 0.108 kg/s
Concrete	Density = 2,210 kg/m^3
	Specific heat capacity = 1,050 J/kg-K
	Thermal conductivity = 2.8 W/m-K
HDPE pipe	Thermal conductivity = 0.385 W/m-K
Soil	Density = 1,900 kg/m^3
	Specific heat capacity = 1,820 J/kg-K
	Thermal conductivity = 2.3 W/m-K

The initial fluid temperature (T_in) was taken as equal to the initial ground temperature, 17.4 degrees Celsius. As a boundary condition for fluid flow, the inlet fluid temperatures as shown on Figure 7-4 were digitized, and those temperatures were imposed at the inlet of the U-tube. The simulated outlet temperatures as predicted by the numerical model were then compared against the reported measured outlet temperatures (T_out).

The effect of the mesh size was evaluated as mesh density can affect the accuracy of the numerical results. Four different meshes of free tetrahedral elements were considered: “Normal” mesh consisting of a total of 8,863 elements, “Fine” mesh consisting of 18,984 elements, “Finer” mesh consisting of 117,706 elements, and lastly, a hybrid mesh

where the smaller pile element was meshed using fine density (to better capture the interaction between the pile element and fluid circulation pipes) and the surrounding geomaterials were meshed using normal density resulting in 15,768 elements. The simulated outlet temperatures as predicted by the numerical model using the four different meshes are shown on Figure 7-5. It can be seen that increasing the number of elements beyond the "Normal" mesh has a very small impact on model outcome. For simulations moving forward, the hybrid mesh was used as it provides a good compromise between accuracy and computational time. The final model pile geometry and mesh are shown in Figure 7-6.

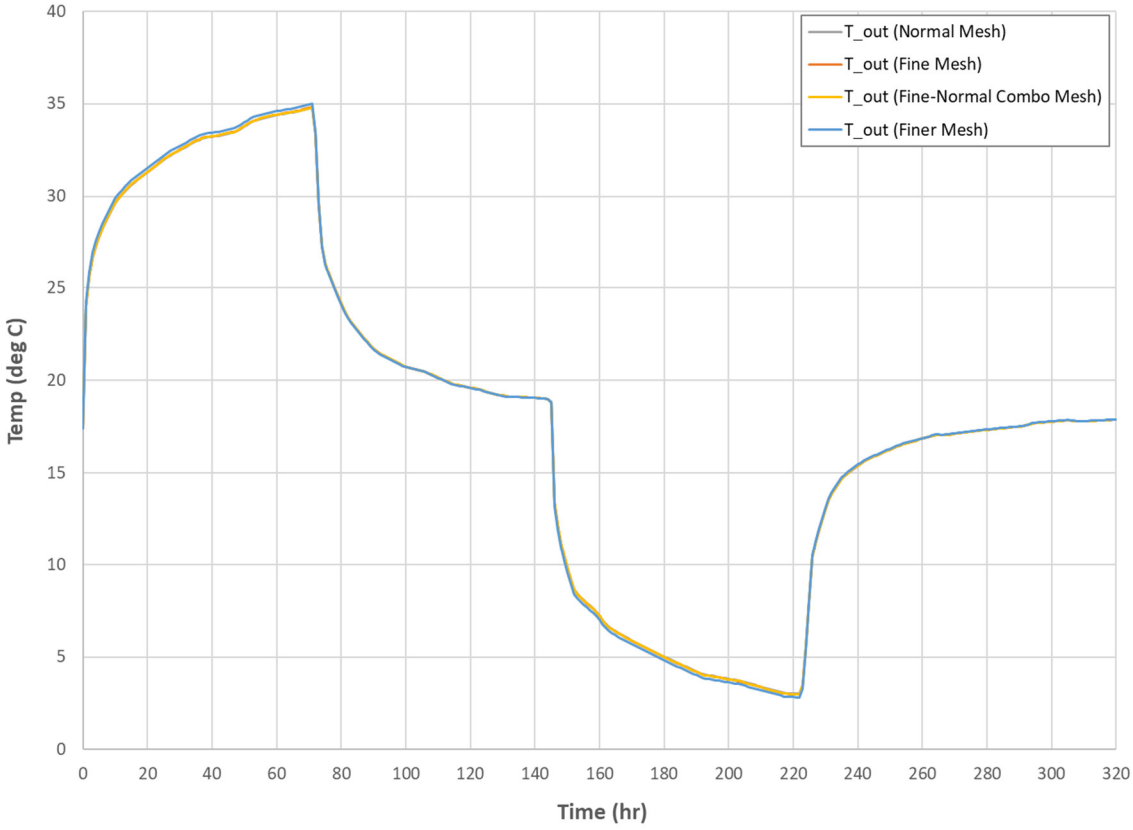

Figure 7-5 – Mesh size comparison

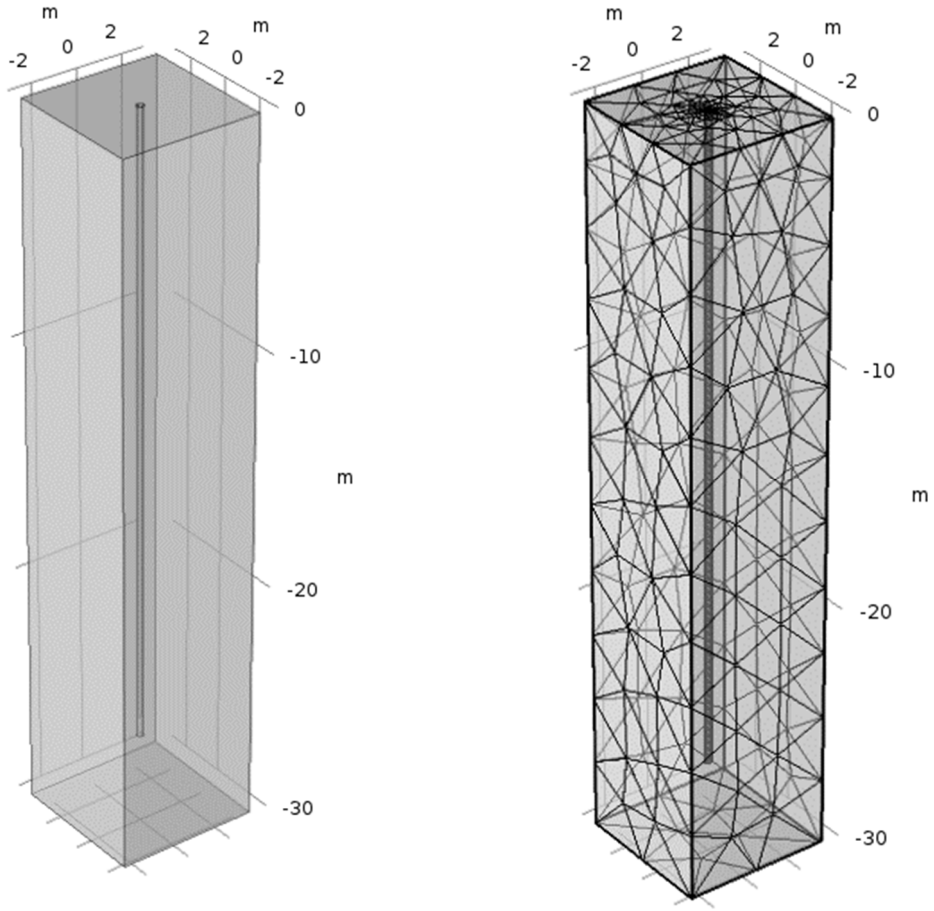

(a) (b)

Figure 7-6 – (a) Model pile geometry (b) Meshed model for validation using TRT data from Cecinato and Loveridge, 2015

As shown on Figure 7-7, the COMSOL model shows very good agreement with the published results, with the simulated outlet temperatures (indicated by the gray diamonds) essentially identical to the measured outlet temperatures from the thermal response test (indicated by the red dots).

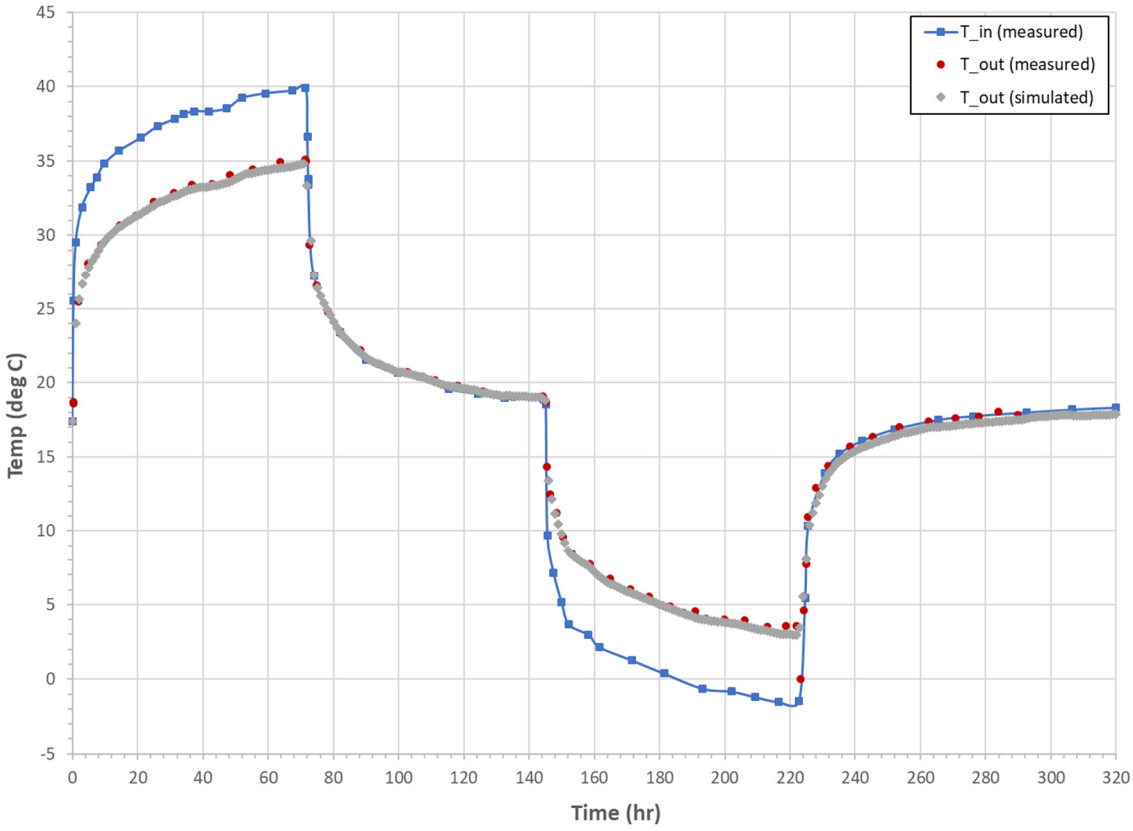

Figure 7-7 – COMSOL model validation results using TRT data from Cecinato and Loveridge, 2015

In addition, a validation study was performed using the results from a full-scale field test performed at École des Ponts – ParisTech (Nguyen, 2017). The pile used in the field test was 0.42 meter in diameter, and 12 meters in length. The pile was fitted with a HDPE W-tube in the middle, with an inner diameter of 20.4 mm and a wall thickness of 2.3 mm (see Figure 7-8). During the test, a mixture of water (80%) and glycol (20%) was circulated through the pipe embedded in the energy pile for a total period of approximately 22.5 days, and the inlet and the outlet temperatures were monitored and recorded (see Figure 7-9).

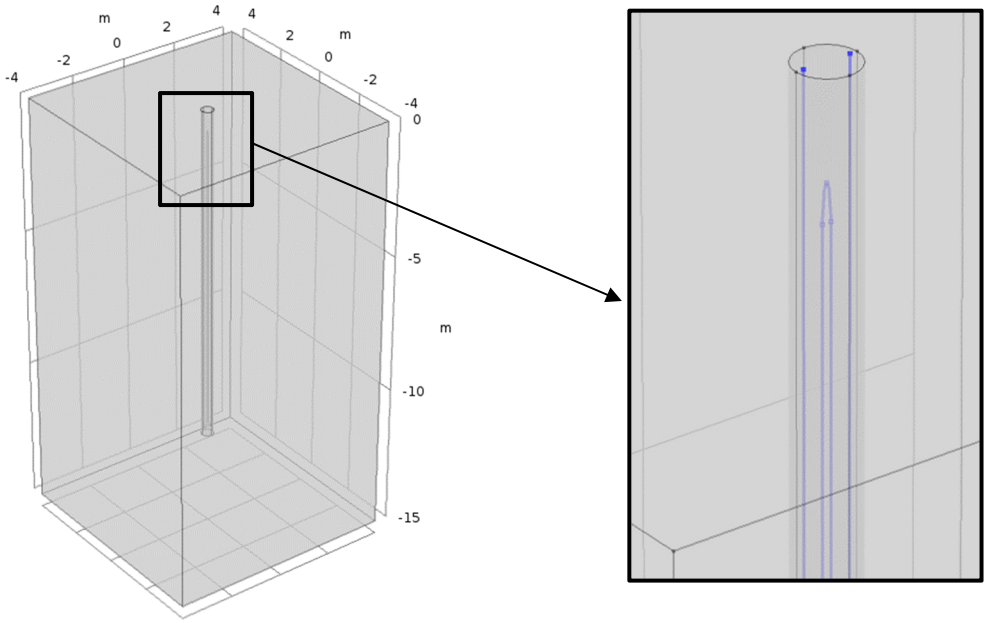

(a) (b)

Figure 7-8 – (a) Model pile geometry (b) Close-up of the pile top showing the W-loop configuration for model validation using results from Nguyen, 2017

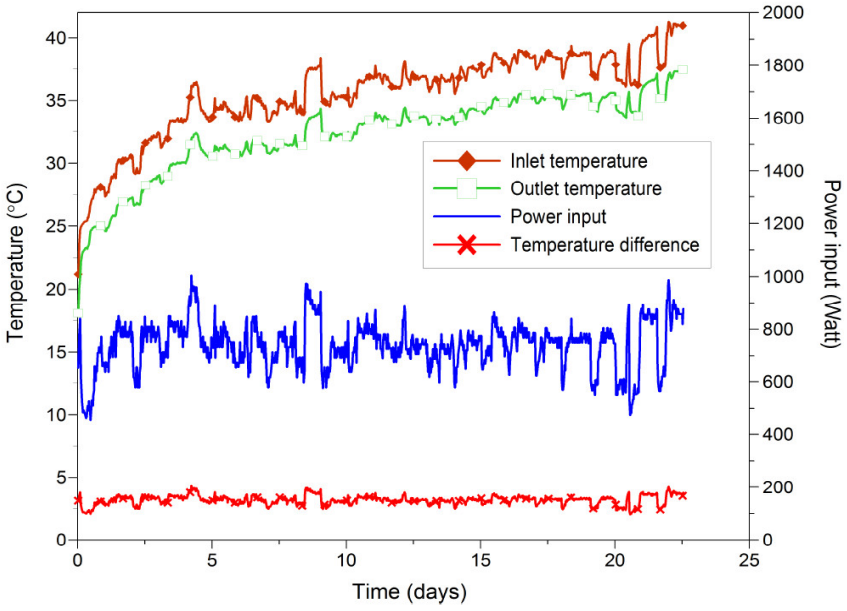

Figure 7-9 – Thermal response test results from Nguyen, 2017

The material thermal properties used for the second validation study are shown in Table 7-2. For the circulating fluid, the properties represent an 80-20 mixture of water and glycol, respectively. For concrete, the values were obtained directly from Table 4.1 of Nguyen, 2017. For soil, thermal conductivities ranging from 1.1 and 1.2 W/m-K were reported in Table 3.1 of Nguyen, 2017, with specific heat capacity reported as between 1,000 and 1,150 J/kg-K and unit weight reported as between 18 and 20 kN/m^3. For validation, a soil thermal conductivity of 1.15 W/m-K, a specific heat capacity of 1,100 J/kg-K, and a density of 1,900 kg/m^3 were used. The soil and concrete were assumed to be homogeneous and isotropic.

Table 7-2 – Thermal properties for numerical model validation (from Nguyen, 2017)

Material description	Property and assigned value
Circulating fluid (water/glycol mixture)	Density = 1,020 kg/m^3 Specific heat capacity = 3,840 J/kg-K Thermal conductivity = 0.53 W/m-K Dynamic viscosity = 4.0e-3 Pa-s Mass flow rate = 0.0584 kg/s
Concrete	Density = 2,500 kg/m^3 Specific heat capacity = 1,100 J/kg-K Thermal conductivity = 1.5 W/m-K
HDPE pipe	Thermal conductivity = 0.385 W/m-K
Soil	Density = 1,900 kg/m^3 Specific heat capacity = 1,100 J/kg-K Thermal conductivity = 1.15 W/m-K

For simulation purposes, a regression analysis was performed using a power function to approximate the inlet temperatures as a function of time as shown in Figure 7-10. The measured temperature shows some variation, but it can be seen that it can be reasonably approximated using a power function. In addition, as shown in Figure 7-10, the average power was reported as 740 Watts (W), and the average temperature differential between the inlet and outlet temperatures was approximately 3.3 degrees Celsius. Based on this, the average mass flow rate ($\dot{m}$) during the test was calculated as 0.0584 kg/second.

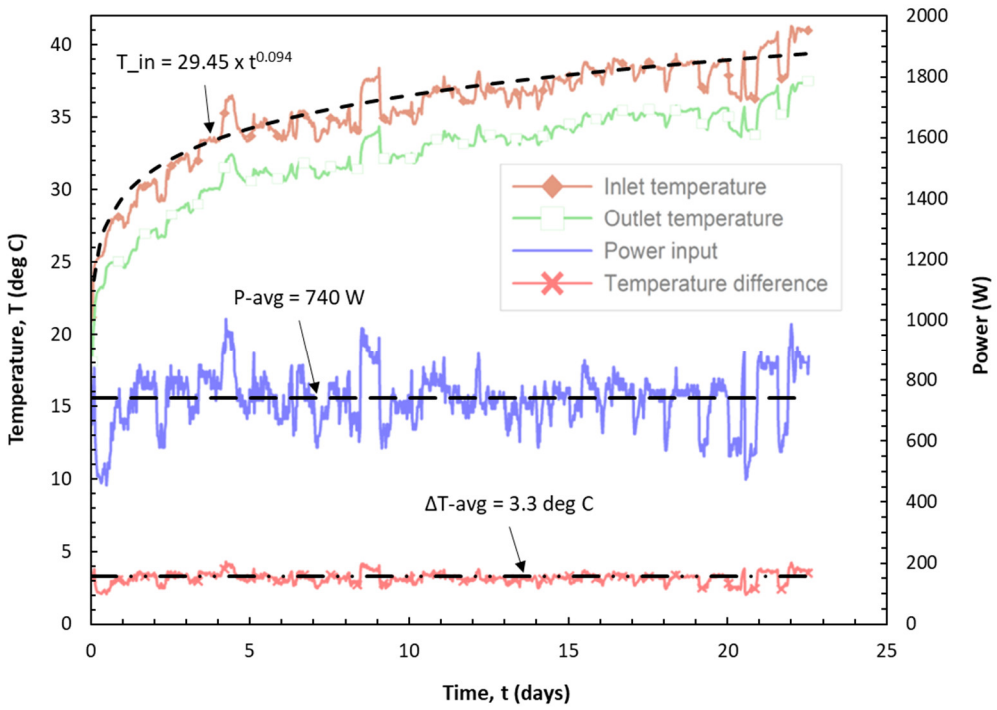

Figure 7-10 – Regression analysis for approximation of inlet temperatures as a function of time

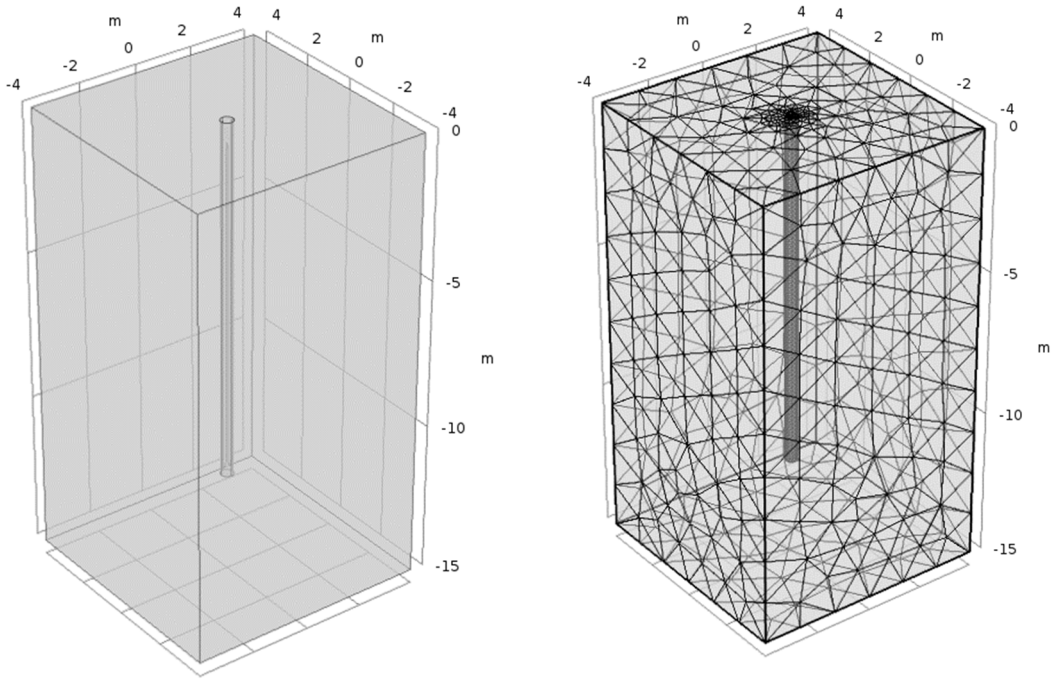

(a) (b)

Figure 7-11 – (a) Model pile geometry (b) Meshed model for validation using published results from Nguyen, 2017

The initial ground temperature prior to the start of the test was given as 12.5 degrees Celsius. As a boundary condition for ground temperature, the far-field temperature was taken to be equal to the reported initial ground temperature. The lateral model extent was chosen as approximately 20 times the pile diameter to avoid boundary effects (see Figure 7-11). The initial fluid temperature was taken as 19.8 degrees, which is the average of the inlet and outlet temperatures reported at the start of the test. As a boundary condition for fluid flow, the fluid inlet temperature was imposed as a power function (as shown in Figure 7-10) at the inlet of the U-tube. The simulated outlet temperature as predicted by the model were then compared against the reported measured outlet temperature.

As shown on Figure 7-12, the COMSOL model shows very good agreement with the trend shown by the reported outlet temperatures. The average power (P-avg) indicated by the COMSOL simulation was 699 W (compared to 740 W), and the temperature differential between the inlet and outlet temperatures (ΔT-avg) was 3.1 degrees (compared to 3.3 degrees). Both P-avg and ΔT-avg are within six percent of the values reported by Nguyen, 2017.

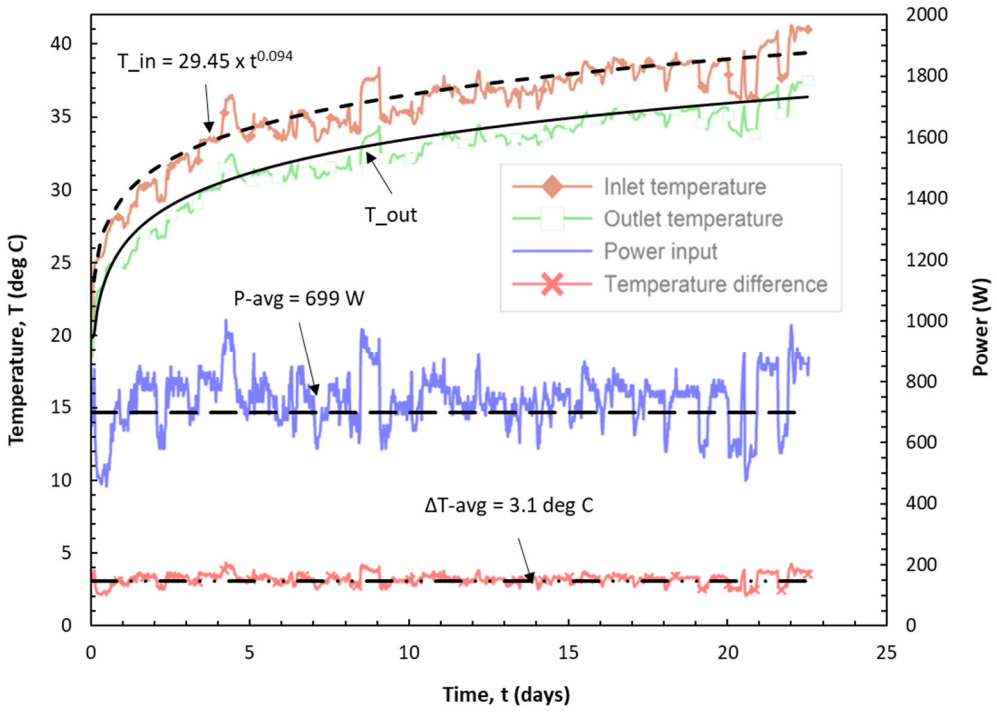

Figure 7-12 – COMSOL model validation results using data from Nguyen, 2017

7.1.3 Parametric Study

Following model validation, a parametric study was performed using COMSOL to evaluate the impact of introducing an ETZ into a conventional energy pile system with a diameter of 0.3 m (which is a typical pile size for buildings), and a length of 15 m. For the parametric study, the modeling was performed using a steady-state approach (with a tolerance of 10^{-3}) to facilitate comparison between the different scenarios. Four different scenarios were considered:

- Scenario #1: Four (4) single U-shaped fluid circulation loops connected in series and located inside the pile near its outside edge (as is current practice); this is considered to be the "baseline" case.
- Scenario #2: Same as above, but with the introduction of the ETZ surrounding the pile element. The ETZ was introduced with various aspect ratios (i.e., diameter of the ETZ relative to pile diameter). Aspect ratios of 2, 4, 6 and 10 were considered, with an aspect ratio of 10 (i.e., 3 m ETZ diameter) representing the approximate upper bound of conventional drilling equipment currently available.
- Scenario #3: Helical fluid circulation loop located in the middle of the ETZ, using an AR of 6. The presence of the ETZ removes the geometric constraint associated with pipe placement; therefore, the helical pipe was placed directly in the ETZ (instead of in the pile). Four different helical configurations were considered: 1) helical loop length equal to the length of the 4 U-loops in the baseline case (115.5 m), 2) loosely spaced helical loop with a length of 135.8 m, 3) moderately spaced with a loop length of 194.5 m, and 4) tightly spaced with a loop length of 253.4 m.

Note that the scenario considering a tightly spaced helical loop is referred to hereinafter as "Scenario #3-4", and so on.

- Scenario #4: A hypothetical scenario in which the helical fluid circulation loop is assumed to be installed outside the pile without an ETZ or otherwise modifying the thermal properties of the ground. This scenario was considered to evaluate how much of the improvement in thermal performance is due to the ETZ, as compared to the additional surface area associated with a helical loop configuration. Two helical loop configurations were evaluated for this scenario: 1) a loop length of 115.5 m, and 2) a loop length of 253.4 m.

For soil thermal properties, three values of mass density, thermal conductivity and heat capacity were considered, based on data presented in Chapter 4. The soils were assumed to be homogeneous and isotropic. The thermal properties used in the parametric study are summarized in Table 7-3.

A constant mass flow rate ($\dot{m}$) of 0.189 kg/s (3 gallons per minute) was assumed, which is a typical flow rate for shallow thermo-active systems. The circulation fluid was assumed to be water, with a density of 1,000 kg/m^3, thermal conductivity of 0.6 W/m-K, and a specific heat capacity of 4,200 J/kg-K. The fluid circulation loops were assumed to be nominal "1-inch" HDPE tubing, with an inner diameter of 27.4 mm and a wall thickness of 3 mm. The thermal conductivity of the HDPE tubing was taken as 0.4 W/m-K.

Table 7-3 – Soil thermal properties for parametric study

Description	Property and assigned value
Soil A	Density = 1,600 kg/m^3 Specific heat capacity = 1,000 J/kg-K Thermal conductivity = 0.6 W/m-K Thermal diffusivity = 3.8 x 10^{-7} m^2/s
Soil B	Density = 1,750 kg/m^3 Specific heat capacity = 1,250 J/kg-K Thermal conductivity = 1.2 W/m-K Thermal diffusivity = 5.5 x 10^{-7} m^2/s
Soil C	Density = 1,900 kg/m^3 Specific heat capacity = 1,500 J/kg-K Thermal conductivity = 2.0 W/m-K Thermal diffusivity = 7.0 x 10^{-7} m^2/s

For thermal properties of the concrete pile, typical values for medium density concrete as suggested by ISO/FDIS 10456:2007(E) were used. Concrete thermal conductivity was taken as 1.65 W/m-K, with a density of 2,200 kg/m^3 and a heat capacity of 1,000 J/kg-K. For the ETZ, typical values associated with thermal grout were used. Grout thermal conductivity was taken as 2.4 W/m-K, with a density of 1,250 kg/m^3 and heat capacity of 1,000 J/kg-K.

The initial ground and fluid temperatures, as well as the far-field ground temperatures, were assumed to be 17 degrees Celsius, which is typical of the mean ground temperature in the Atlanta area. A constant fluid inlet temperature of 35 degrees Celsius

was imposed as a boundary condition for fluid flow. The effect of introducing a transition zone was analyzed by calculating the power extracted from the system. The power extracted was determined from the temperature of the water entering and exiting the system:

$$P = \dot{m} \times c_f \times |T_{out} - T_{in}| \tag{40}$$

Where P is power (in Watts), $\dot{m}$ is the mass flow rate of circulation fluid (in kg/s), c_f is the specific heat capacity of circulation fluid (in J/kg-K), and T_{out} and T_{in} are the measured outlet and inlet water temperatures (in K), respectively.

Table 7-4 – Model extent for steady-state analyses

Model Extent	T_out (deg C) Soil A	T_out (deg C) Soil C
5 m x 5 m	33.52	32.10
10 m x 10 m	33.80	32.65
20 m x 20 m	33.90	32.87
25 m x 25 m	33.92	32.90
30 m x 30 m	33.92	32.91

A hybrid mesh consisting of finer density free tetrahedral elements for the pile and the ETZ, and normal density elements for the surrounding geomaterials were used for the steady-state simulations. In order to determine the appropriate numerical model extent to avoid boundary interference, a progressive refinement approach was used to determine the

model size for which a further increase in size results in a negligible change in outlet temperature for a constant inlet temperature of 35 degrees Celsius. The results are summarized in Table 7-4. Based on these findings, a conservative model extent of 30 m by 30 m was used for the subsequent numerical models.

7.2 Results & Discussion

7.2.1 Scenario #1 – Baseline Case

The results of the "baseline" simulations (i.e., no ETZ) using the different soils as described in Table 7-3 are shown in Figure 7-13:

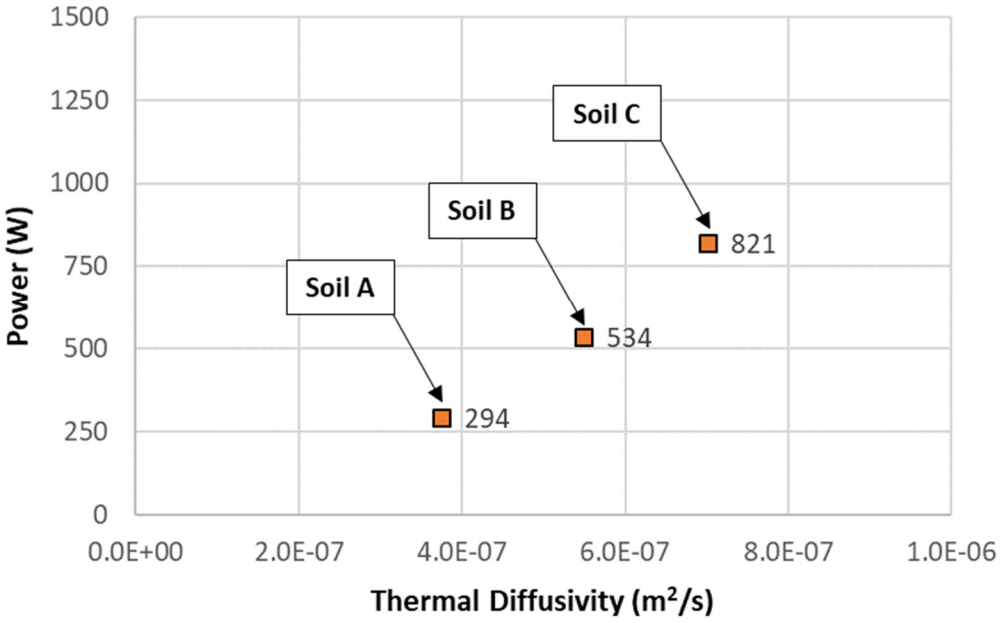

Figure 7-13 – COMSOL simulation results for baseline case, Soils A – C

As anticipated, the soil with the higher thermal diffusivity (i.e., Soil C) yields significantly higher thermal performance in comparison to the soils with lower thermal

diffusivity. In this case, the power extracted from the pile surrounded by Soil C (823 W) was approximately 2.8 times that of Soil A (294 W), and approximately 1.5 times that of Soil B (534 W).

7.2.2 Scenario #2 – Baseline Case with ETZ

Next, simulations were performed using the same configuration except the addition of the ETZ to the system. The results for Soil A, B and C are shown in Figure 7-14, which shows the improvement ratio, IR, defined as the ratio of the post-ETZ thermal performance (i.e., power) to the pre-ETZ performance, for the three different soils.

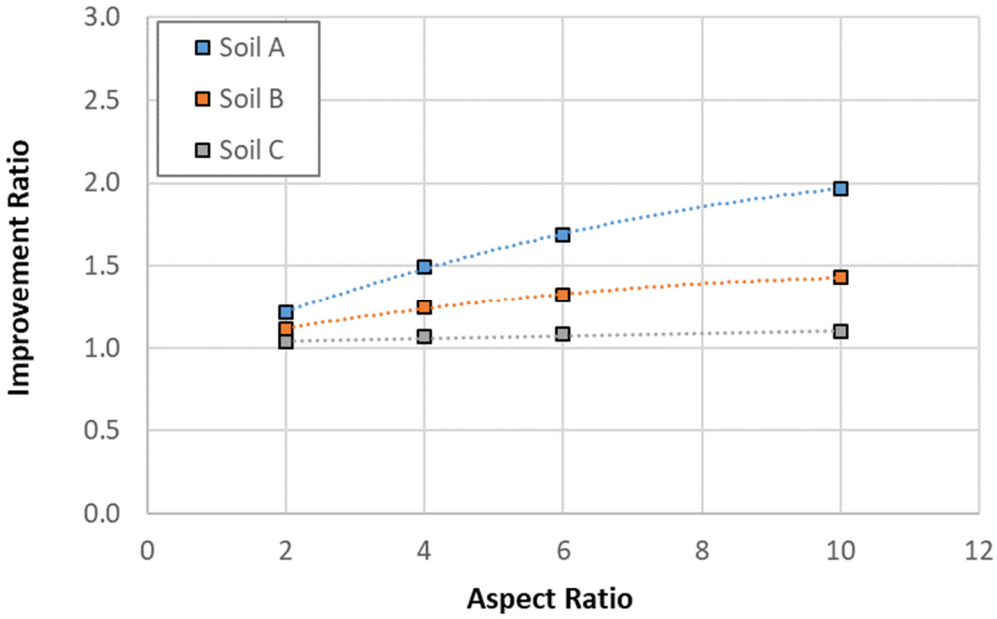

Figure 7-14 – Improvement ratios after introduction of ETZ for Soils A – C

It can be seen that for soil with low thermal diffusivity relative to the ETZ (e.g., Soil A), the introduction of an ETZ increases power extracted from the system, and that the

increase is related to the aspect ratio, AR. For soil with moderate thermal diffusivity (e.g., Soil B), the ETZ also results in increased power, albeit at a smaller rate. On the other hand, for soil with high thermal diffusivity (e.g., Soil C), the introduction of an ETZ has very little impact on thermal performance. This is because the thermal conductivity of the ETZ material, which has the highest impact on thermal performance, is only slightly greater than the thermal conductivity of Soil C.

7.2.3 Scenario #3 – Helical Loop with ETZ

One of the main advantages of introducing an ETZ is the ability to use novel fluid circulation loop configurations that maximize the pipe surface area available for heat transfer. In this regard, four different helical loop configurations were considered for the parametric study: 1) helical loop length equal to the length of the 4 U-loops in the baseline case (115.5 m), 2) loosely spaced helical loop with a length of 135.8 m, 3) moderately spaced helical loop with a loop length of 194.5 m, and 4) tightly spaced helical loop with a loop length of 253.4 m.

For simulation purposes, a constant ETZ aspect ratio of six (6) was used. The helical loop was placed halfway between the outside pile edge and the outside edge of the ETZ (see Figure 7-15).

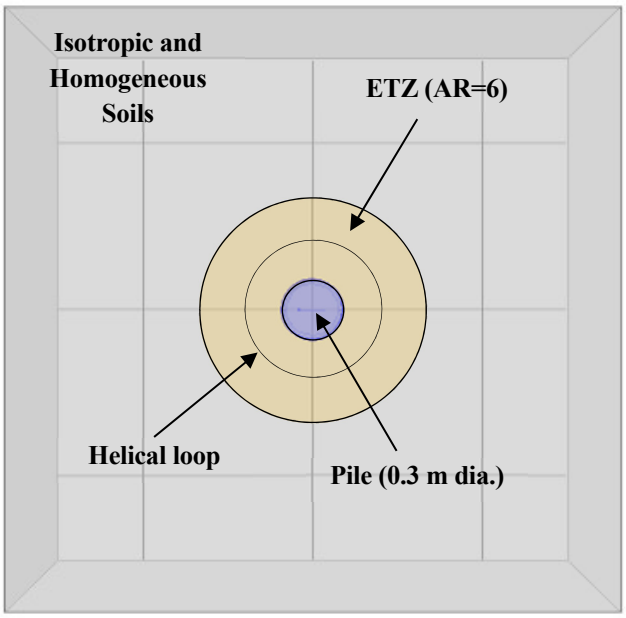

Figure 7-15 – Pile configuration with ETZ and helical loop

It can be seen from Figure 7-16 and Figure 7-17 that a helical loop configuration increases thermal performance significantly relative to the baseline case (Scenario #1), as well as relative to the baseline case with an ETZ (Scenario #2). When compared with Scenario #1, the combination of the ETZ and helical loop increases thermal performance by a factor of approximately 2.4 to 2.9 for Soil A, and by a factor of approximately 1.7 to 2.0 in the case of Soil C. When compared with Scenario #2, the addition of the helical loop increases thermal performance by a factor of approximately 1.6 to 1.9 for Soil C, and by a factor of approximately 1.4 to 1.7 in the case of Soil A.

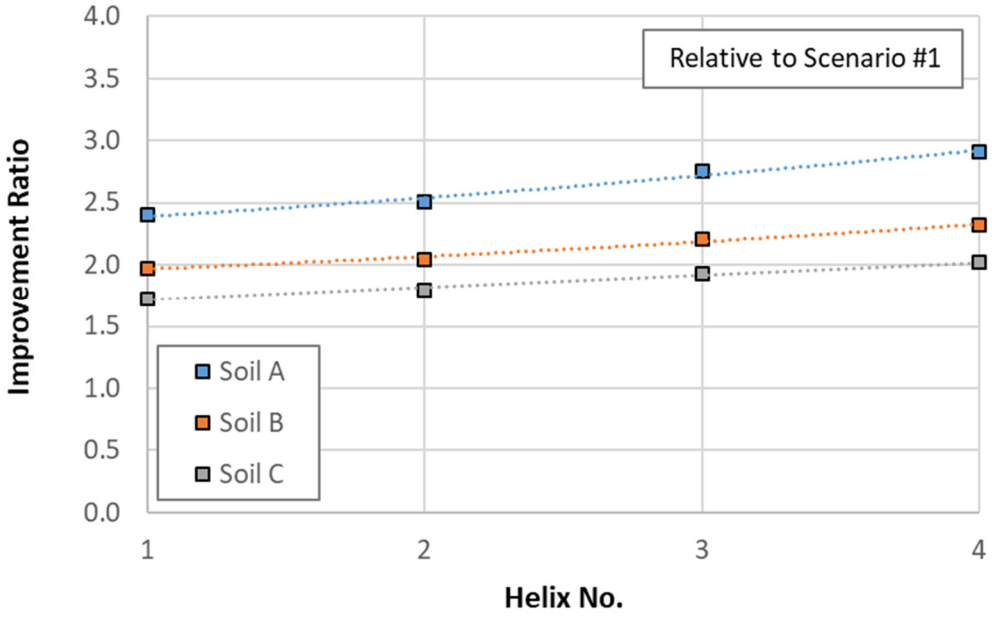

Figure 7-16 – Improvement ratios for Scenario #3 relative to Scenario #1 for Soils A - C

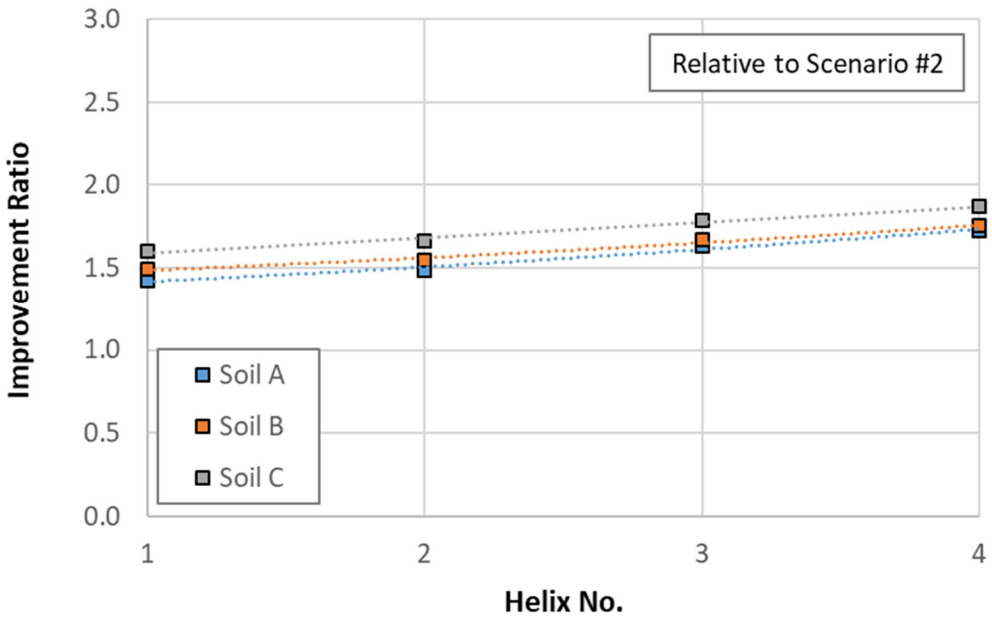

Figure 7-17 – Improvement ratios for Scenario #3 relative to Scenario #2 for Soils A - C

These results suggest that the use of helical loops with an ETZ are particularly beneficial in soils with lower thermal diffusivity. These results also suggest that for a helical loop configuration, greater improvement in thermal performance can be expected in soils with higher thermal diffusivity, which better compliment the additional pipe surface area available for heat transfer.

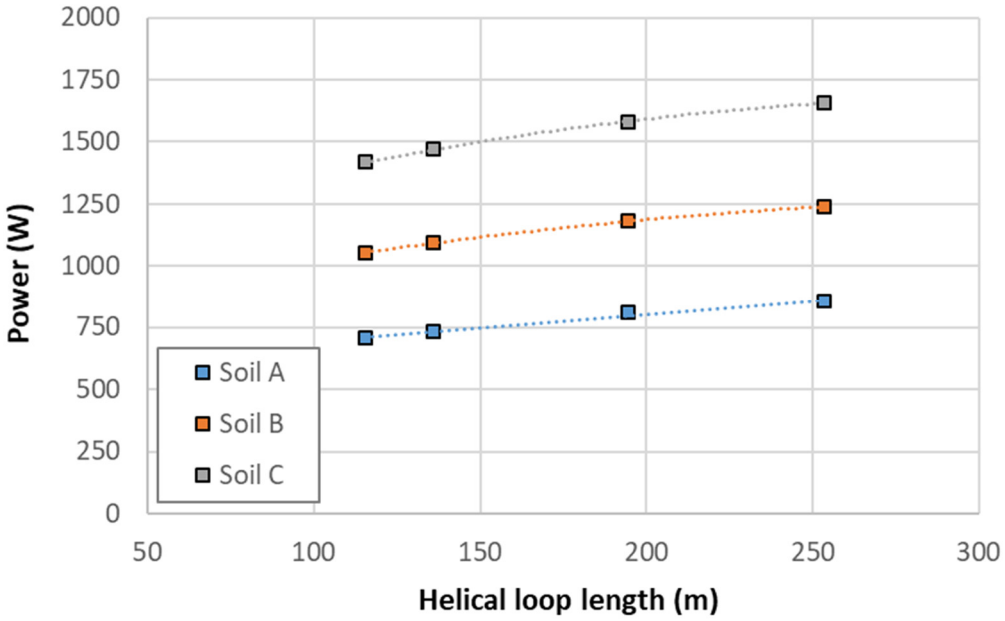

Figure 7-18 – Power extracted for Scenario #3 for various helical loop lengths

Figure 7-18 shows the power extracted from the system under Scenario #3 for various loop lengths considered. It can be seen that, in general, the power extracted from the system increases with increasing loop length because of greater pipe surface area available for conduction. However, the increase in thermal performance appears to diminish with increasing loop length, most likely due to detrimental pipe-to-pipe interactions as the pitch of the helical system (i.e., the distance between subsequent helixes) gets smaller.

7.2.4 Scenario #4 – Helical Loop without ETZ

Figure 7-19 shows the improvement ratios relative to Scenario #1 resulting from considering two different helical loop configurations (No. 1 with a length of 115.5 m, and No. 4 with a loop length of 253.4 m). It can be seen that relative to the baseline case, the improvement with the introduction of a helical loop alone ranges from about 1.5 to 1.8 for Soil A, and 1.6 to 1.9 for Soil C. Another important observation that can be made from these results is that helical loop No.1, while having the same length as the 4 U-loops in Scenario #1, is significantly more efficient in transferring heat. This can be attributed to the fact that having the loops inside the pile element results in higher pile temperatures (as discussed further in Chapter 7.2.6); therefore, reducing the thermal performance of the system due to the smaller thermal gradient.

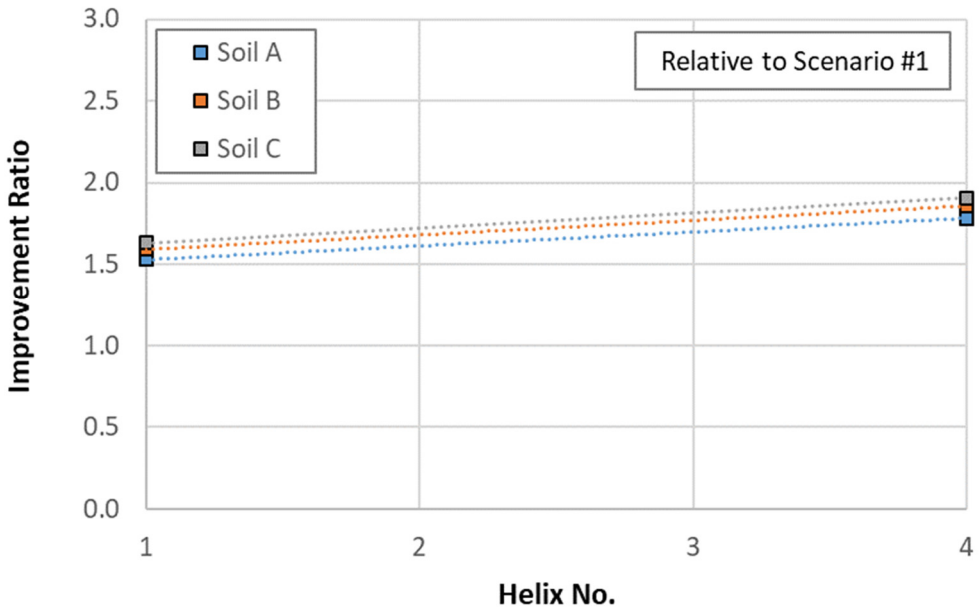

Figure 7-19 – Improvement ratios for Scenario #4 relative to Scenario #1 for two helical loop configurations

Figure 7-20 shows the improvement ratios relative to Scenario #3. As indicated by improvement ratios that are less than 1.0, the system with the helical loop alone (without an ETZ) does not perform as well as the system with both the helical loop and an ETZ. This is especially evident for soils with lower thermal diffusivity (e.g., Soil A) relative to the ETZ. The impact of the ETZ is diminished for soils with similar thermal diffusivity (e.g., Soil C) relative to the ETZ.

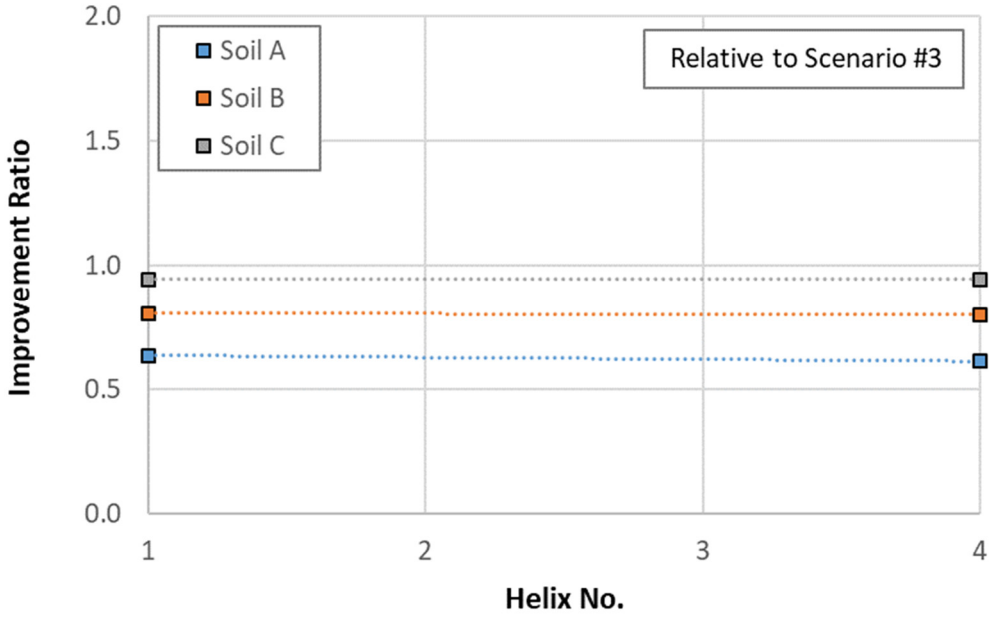

Figure 7-20 – Improvement ratios for Scenario #4 relative to Scenario #3 for two helical loop lengths

7.2.5 Summary of Parametric Study

Figure 7-21 and Figure 7-22 show a summary of the power extraction and improvement ratios for Scenarios #1 through #4. For comparison purposes, helical loop configuration no. 4 and an ETZ aspect ratio of six (6) were used.

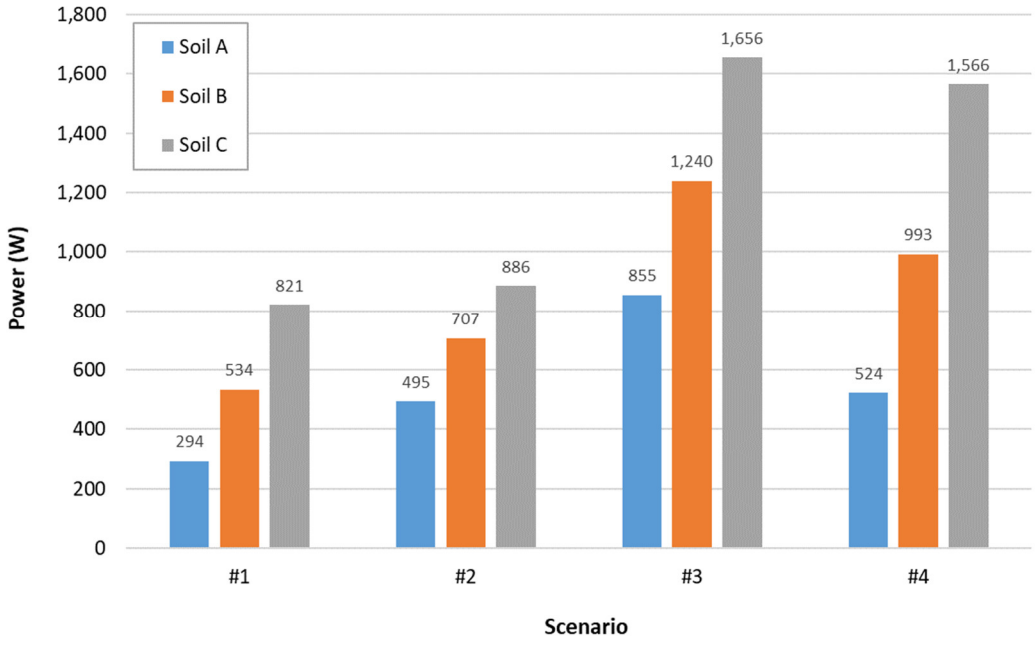

Figure 7-21 – Summary of power extraction for Scenarios #1 - #4

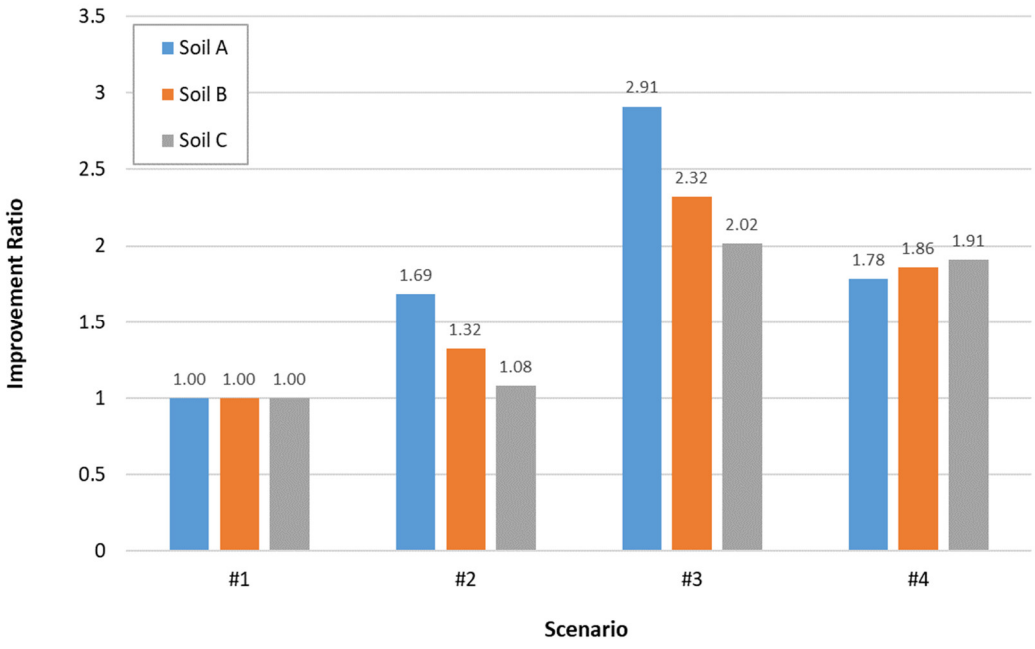

Figure 7-22 – Summary of improvement ratios for Scenarios #1 - #4

It can be seen that compared to the baseline case, the introduction of an ETZ with AR = 6 can improve thermal performance by a factor of about 1.1 to 1.7, with higher increase in thermal performance observed in soils with lower thermal diffusivity (e.g., Soil A). On the other hand, introducing an ETZ and installing a helical loop can improve thermal performance by a factor of approximately 2 to 3. It should also be noted that while not discussed herein, the trends indicated are also applicable to a system operating under heat extraction mode.

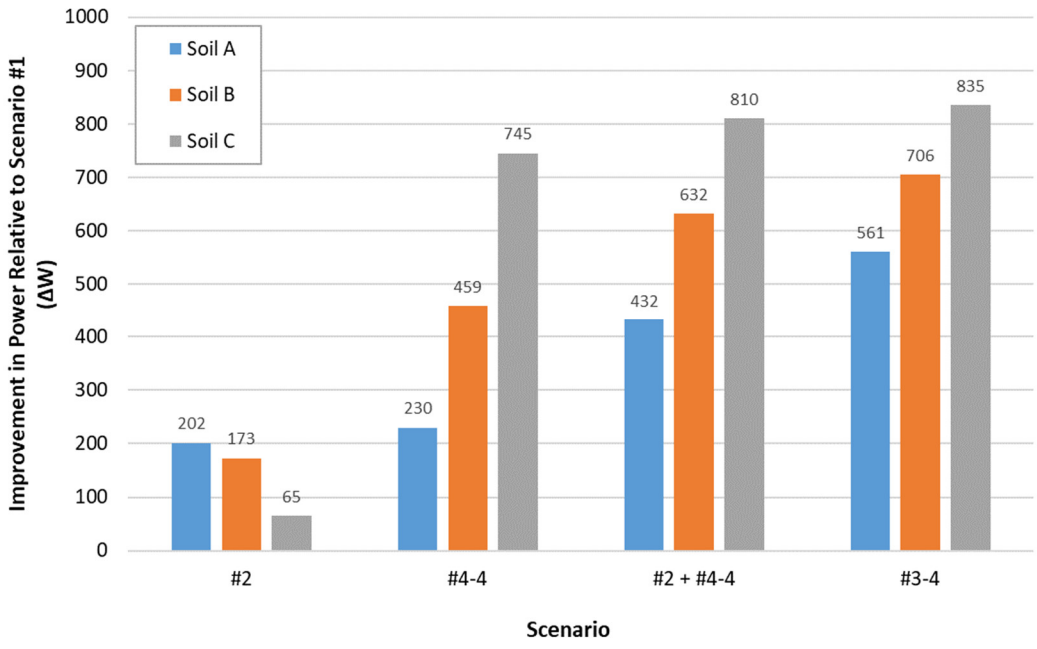

Figure 7-23 – Improvement in power for Scenario #2 (ETZ alone), Scenario #4 (helical loop alone), sum of Scenarios #2 and #4, and Scenario #3 (ETZ plus helical loop)

Lastly, these results indicate that the improvement from the combination of the active ETZ with a helical loop configuration (Scenario #3) is greater than the sum of their individual parts (Scenario #2 plus Scenario #4). This is shown in Figure 7-23. This is due to the high thermal diffusivity of the ETZ combined with the additional pipe surface area offered by the helical loop configuration. As expected, the benefits are especially evident when the system is surrounded by lower thermal diffusivity soils (e.g., Soil A) and diminish when the system is surrounded by higher diffusivity soils (e.g. Soil C).

7.2.6 Pile Temperature

Another important consideration for energy piles is the change in temperature in and around the pile, as these changes can impact the geotechnical and structural performance of the pile element. Namely, temperature changes in the pile center impact pile expansion and contraction, while changes along the pile face impact shaft friction. Figure 7-24 presents the temperatures in the center of the pile and along the pile face for the baseline case (Scenario #1) and for the system with the ETZ and tightly-spaced helical loops (Scenario #3-4) under steady-state conditions. The smooth shape of the curves as shown in this figure is due to averaging of the numerical variations in the results.

It can be seen that the temperature at the center of the pile is almost identical between the two scenarios at the pile head. It can also be seen that for Scenario #3-4, the pile center and pile face temperatures are essentially identical under steady-state conditions (as seen by the overlapping temperature distributions). The pile center temperature becomes cooler under Scenario #3-4 with increasing depth, due to the direction of fluid flow in the helical loop configuration and the circulation loops being outside of the pile, while it remains more

or less constant under Scenario #1 due to the U-loop configuration and the circulation loops being located inside the pile. The maximum temperature difference between Scenario #1 and #3-4 at the center of pile is approximately 0.6 degree near the pile tip.

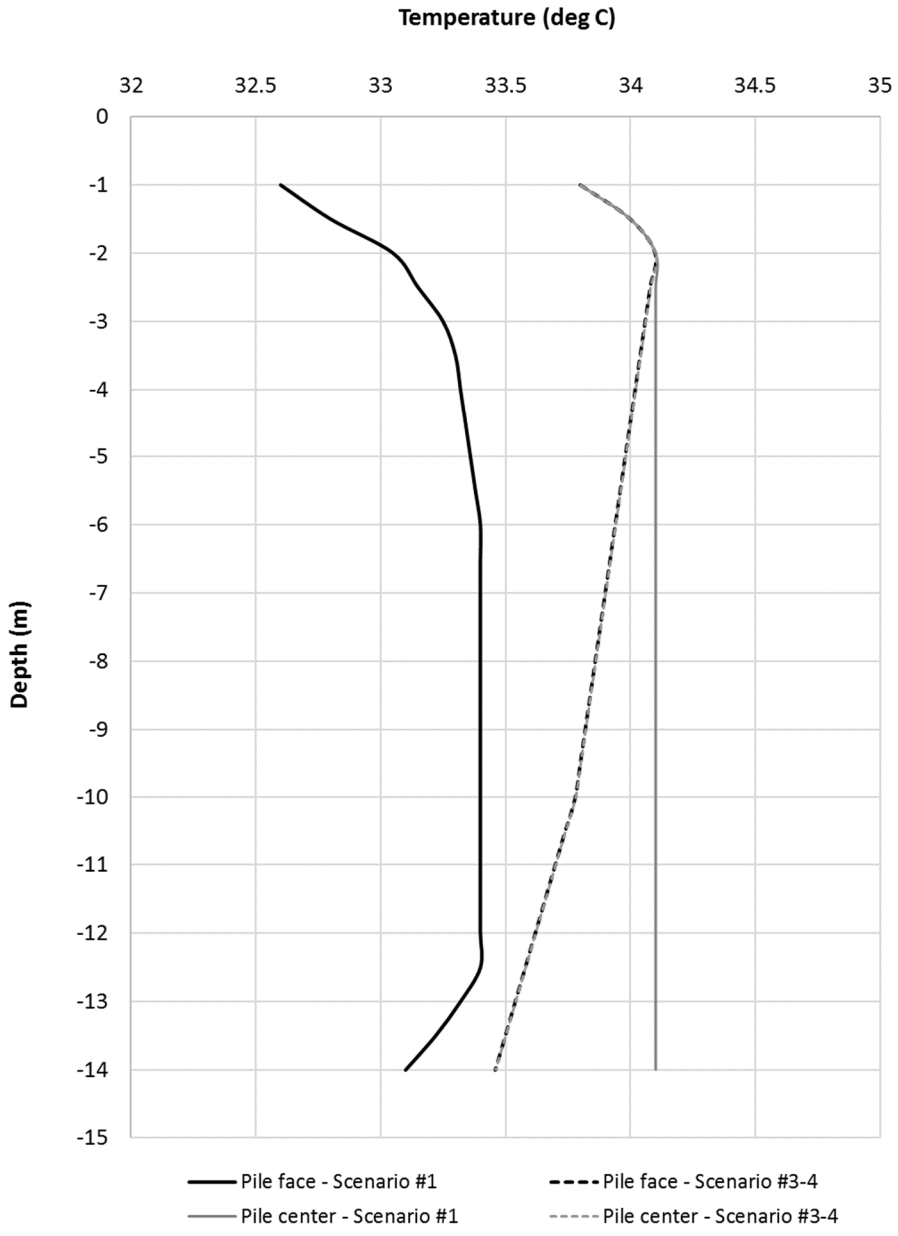

Figure 7-24 – Temperature along the pile face and pile center for baseline case (Scenario #1) and ETZ with tightly-spaced helical loops (Scenario #3-4)

On the other hand, slightly higher temperatures are observed at the pile face for Scenario #3-4 due to the higher rate of heat injection associated with this configuration. However, the temperature increase along the pile face relative to Scenario #1 is relatively small, with a maximum of about 1.2 degrees. This temperature increase along the pile face would not be expected to adversely impact the geotechnical performance, especially given that it can be accounted for in the original design using one or more of the robust constitutive models (one that relates changes in soil temperature to changes in shaft friction) which are already available to engineers.

7.2.7 Transient Operation

In the previous sections, results from steady-state models were shown to demonstrate the potential for increased thermal performance when using an ETZ. Reaching steady state in relatively large diameter thermo-active elements can take a long period of time, especially depending on how precisely steady-state is defined. In this regard, transient simulations were also performed to demonstrate the time-dependent system performance. This was done by simulating heat injection with a constant mass flow rate of 0.189 kg/s (3 gallons per minute) and an inlet temperature of 35 degrees Celsius continuously for a 3-month period (for example, one season of cooling). The initial and boundary conditions were otherwise identical to the steady-state model. Soil C was used in the simulations.

Results from Scenario #1 (baseline case, 4 U-loops, no ETZ) and Scenario #3-4 (ETZ and tightly spaced helical loop configuration) are shown in Figure 7-25. It can be seen that the average power for Scenario #1 was 1,062 W, and the power diminished slightly to 937 W at the end of the 3-month injection period. In comparison, the steady state power

for the same system was 821 W. Similarly, it can be seen that the average power for Scenario #3-4 was 2,373 W, and the power diminished to 1,978 W at the end of the 3-month injection period. In contrast, the steady state power for the same system was 1,656 W. These results indicate that it can take a long time for the system to reach steady state, and slightly higher power extraction can be expected for the system operating under transient conditions (in this example, higher by a factor of about 1.15 to 1.2 when comparing steady state results to the 3-month injection results).

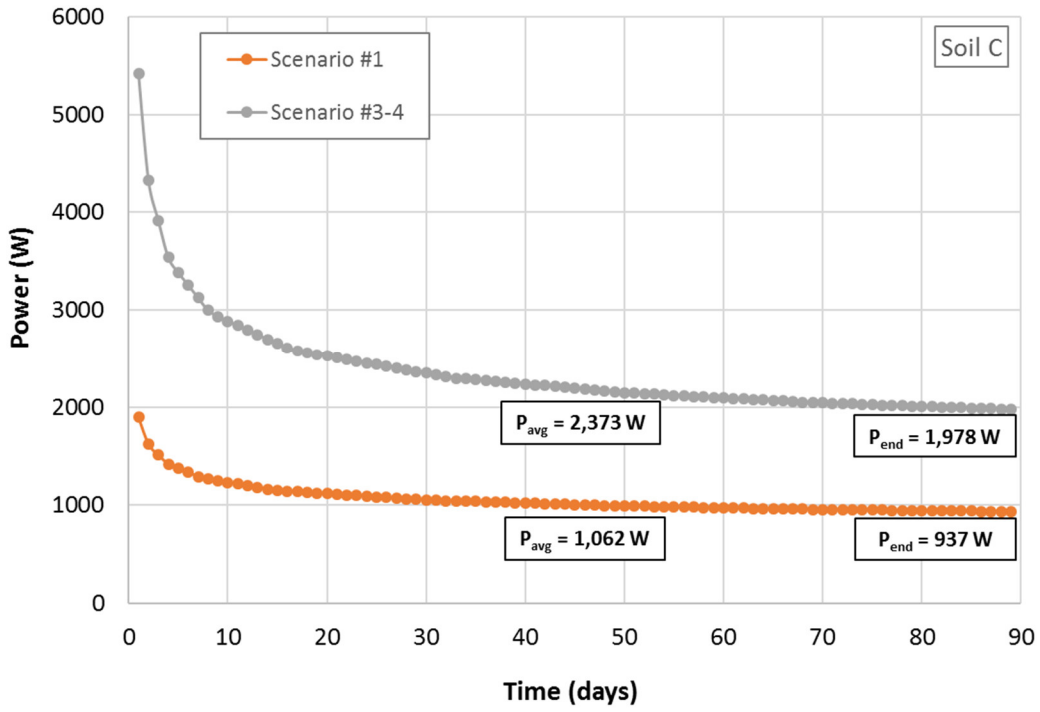

Figure 7-25 – Transient simulation results for Scenario #1 and Scenario #3-4

Additionally, the steady-state and aforementioned transient simulations assume a constant operation mode, in which flow is continuous and heat is injected into the ground constantly. However, under normal circumstances, the heat injection (or extraction) are performed in an intermittent fashion, with the system operational when needed (e.g., during business hours for a commercial building) and vice versa. To simulate intermittent operation, transient simulations were also performed in COMSOL. This was done by simulating heat injection with a mass flow rate of 0.189 kg/s (3 gallons per minute) and an inlet temperature of 35 degrees Celsius for a 12-hour period, followed by a 12-hour recovery phase. This cycle was repeated over the course of a 3-month period. The initial and boundary conditions were otherwise identical to the steady-state model. Once again, Soil C was used in the simulations.

The outlet temperature response of Scenario #1 (baseline case, 4 U-loops, no ETZ) and Scenario #3-4 (ETZ and tightly spaced helical loop configuration) operating in an intermittent mode are shown in Figure 7-26 and Figure 7-27. For comparison, the transient outlet temperature response from a system operating in continuous mode is also shown. It can be seen that when allowed to recover in between period of heat injection, the outlet temperatures are significantly lower in the long term, indicating higher thermal performance. This can also be quantified by plotting the power extracted from the system for the 90-day period, as shown in Figure 7-28 and Figure 7-29. It can be seen that in the case of intermittent operation, the average power and the power at the end of the 90-day period are approximately 1.6 times that of the power extracted from a system operating in a continuous mode.

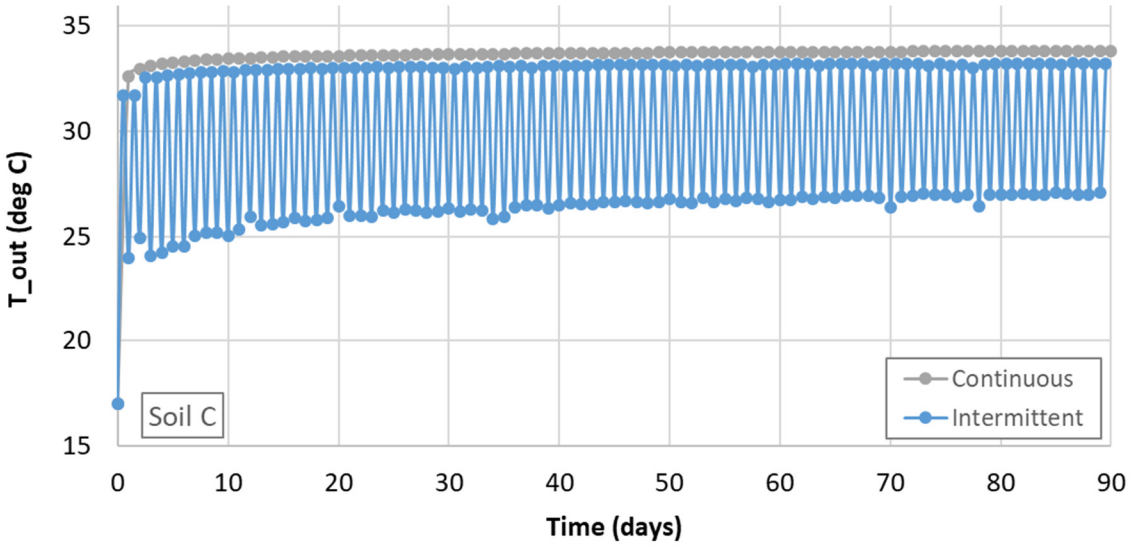

Figure 7-26 – Outlet temperature response of energy pile (Scenario #1) operating under continuous and intermittent modes

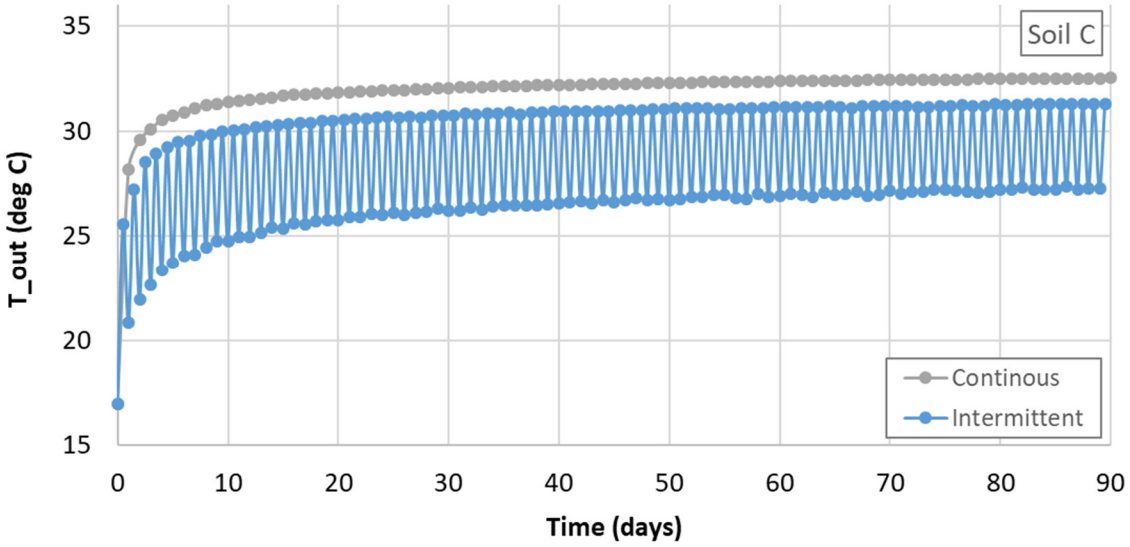

Figure 7-27 – Outlet temperature response of energy pile (Scenario #3-4) operating under continuous and intermittent modes

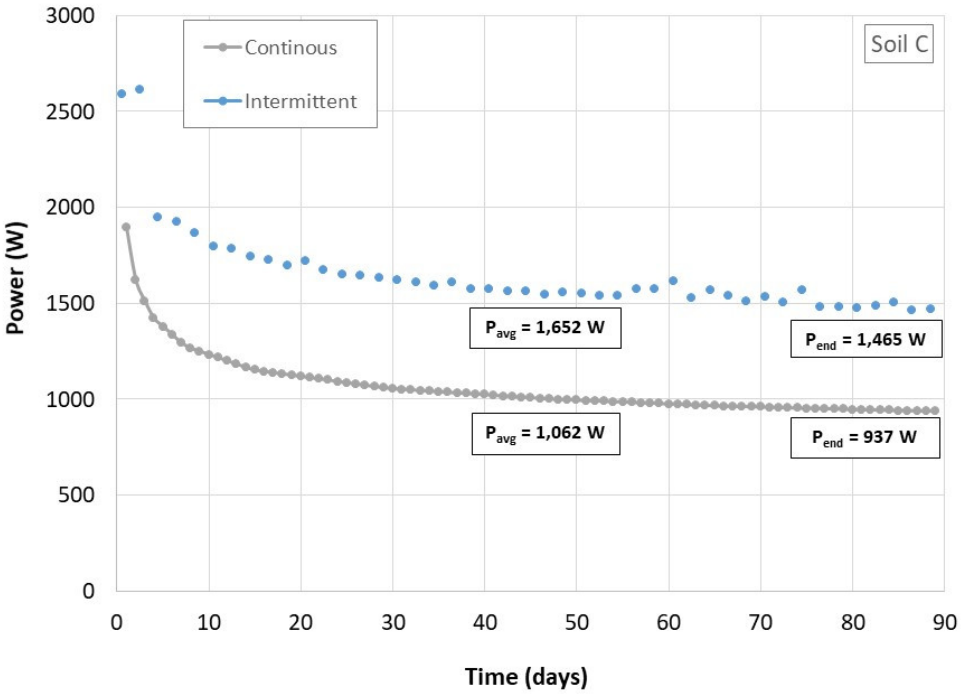

Figure 7-28 – Power extracted from energy pile under continuous and intermittent modes (Scenario #1)

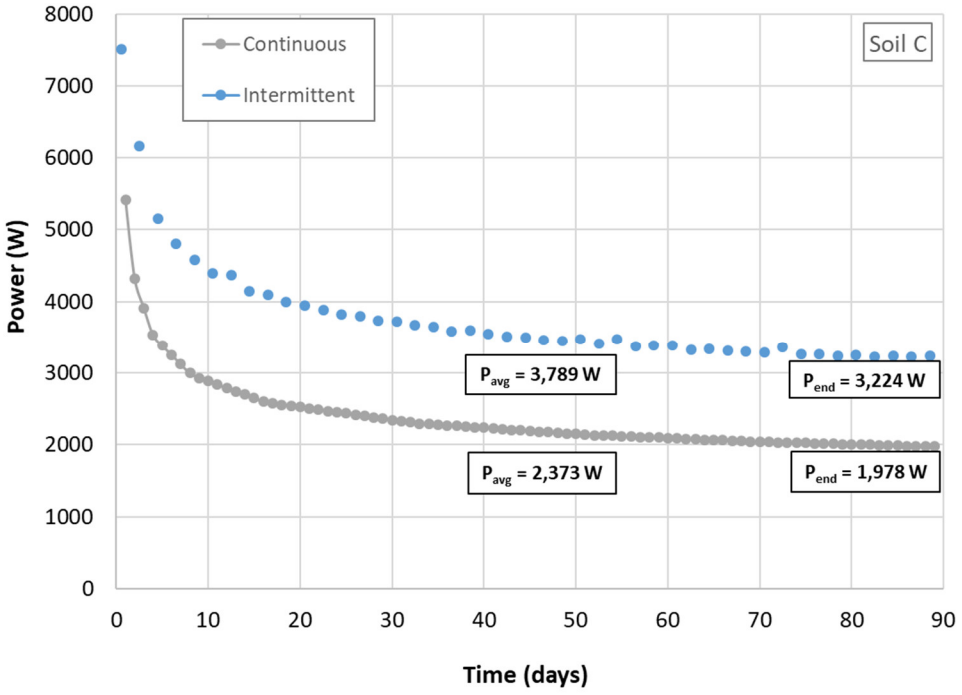

Figure 7-29 – Power extracted from energy pile under continuous and intermittent modes (Scenario #3-4)

With regard to transient and intermittent operation, the use of high thermal performance systems, such as those using an ETZ combined with a helical fluid loop configuration, can allow for the sequential operation of the thermo-active foundation elements. This would allow longer recovery periods in between thermal cycles to maximize system performance as indicated by the intermittent simulation results, while also taking advantage of the fact that the systems perform at their peak during the initial stages of heat extraction (or injection) as seen from the transient simulation results. In other words, it may be possible to meet thermal demands by operating each thermo-active element for shorter periods with longer recovery periods in between thermal cycles. This can also help to achieve a better balance between heat injection and extraction, to better manage the depletion of the ground heat source / sink (which can occur if a high thermal performance system is allowed to operate for a long period, thereby reducing the thermal gradient and system performance).

7.2.8 Drying Effects

It was shown in Chapter 4 that not only is thermal conductivity a function of density and saturation, but also that Piedmont soils exhibit a different behavior during the drying phase in comparison to the wetting phase. While it may be possible to control the thermal properties of the ETZ material such that enhanced heat transfer does not result in changes to thermal conductivity, the soils surrounding the enhanced thermo-active foundation may undergo drying due to combined heat and moisture transport. In this regard, a hypothetical scenario was considered to evaluate the effects of soils drying around the thermo-active foundation. A primarily coarse-grained Piedmont soil with an initial saturated thermal conductivity of 2.0 W/m-K and a dry thermal conductivity of 0.3 W/m-K was considered.

Using Equations (25) and (29), and the coefficients shown in Figure 4-9, the relationship shown in Figure 7-30 between saturation and thermal conductivity can be obtained during the drying phase in this hypothetical scenario.

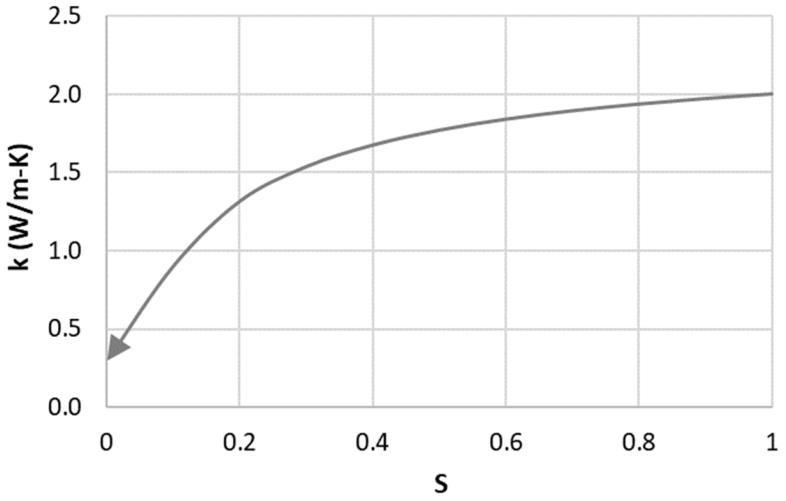

Figure 7-30 – Thermal conductivity for hypothetical drying scenario

It was further shown in Chapter 4 that specific heat capacity is a function of the moisture content. For an assumed porosity of 0.40 and specific gravity of 2.65, the degree of saturation, corresponding water content, thermal conductivity, and the specific heat capacity of the soil calculated using the regression results shown in Figure 4-19 for this hypothetical scenario is summarized in Table 7-5:

Table 7-5 – Thermal properties for hypothetical drying scenario

Degree of Saturation (%)	Water Content (%)	Specific Heat Capacity (J/kg-K)	Thermal Conductivity (W/m-K)
0	0	860	0.30
20	5	998	1.32
40	10	1136	1.67
60	15	1275	1.84
80	20	1413	1.94
100	25	1551	2.00

For comparison, it is assumed that the soil density remains constant at 1,900 kg/m^3. Scenario #3-4 (tightly spaced helical loop with an active ETZ) was considered. Using COMSOL and the steady-state modeling approach, the effects of soil drying on the thermal performance of the system are shown in Figure 7-31. As expected, it can be seen that the power extracted from the system is reduced as the thermal diffusivity of the soil is reduced. However, it can also be seen that the reduction in power is only on the order of 10 percent going from fully saturated down to a degree of saturation of 0.4. This is not only because the thermal conductivity remains relatively high during the drying phase, but also because there is a decrease in specific heat capacity, which means that the overall reduction in thermal diffusivity during drying is relatively small. The hysteresis effect of repeated wetting and drying cycles was not investigated in this study but would be of interest for future work.

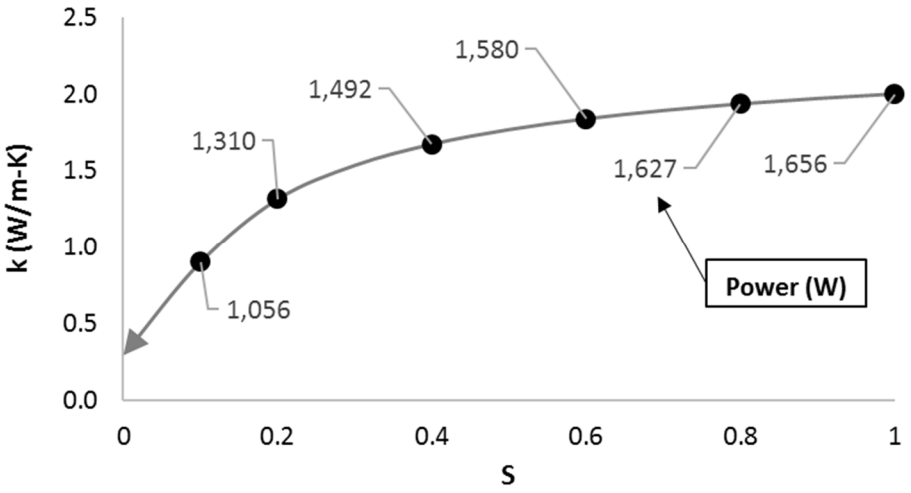

Figure 7-31 – Power extraction for hypothetical drying scenario

7.3 Conclusions

While the hydro-mechanical behavior of energy piles subjected to thermal loads have been investigated extensively using laboratory, field and numerical studies, relatively little attention has been given to enhancing their heat transfer capacity. This study demonstrates that there is potential for considerably increasing the thermal performance of an energy pile with the use of an engineered transition zone.

As a simple demonstration of the potential impact of using a foundation system engineered to optimize heat transfer, we can consider a typical office building minimally complying with the ASHRAE Standard 90.1-1989. Such an office might have a HVAC demand of 75,000 Btu/sq.ft/yr. For a 50,000 square feet building, this would be about 428,000 Btu/hr or about 36 tons of air conditioning, which is equivalent to a power of about 125 kW. In the case of Scenario #1 (no transition zone and four U-loops), considering

moderately favorable soil conditions (Soil B), this would require the use of approximately 234 pile elements in order to meet the thermal demand when considering steady state conditions. On the other hand, in the case of Scenario #3-4 (active ETZ and a tightly spaced helical loop) and same soil conditions, this demand can be met with the use of approximately 100 pile elements.

An ETZ provides a means to introduce a thermally optimized zone between the pile and the surrounding geomaterials to reduce thermal resistance. It also allows decoupling of the structural portion of the pile from the thermal portion, such that the length of each component can be selected to meet the specific structural and thermal needs. Additionally, and perhaps more importantly, it allows for various circulation pipe configurations to be used (for example, helical loops) to further enhance heat transfer due to increased pipe surface area available for heat transfer. It has also been shown that the thermal performance is higher under intermittent operation conditions, by allowing the pile to recharge in between periods of heat injection.

Further, placing the fluid circulation loops outside the pile element can reduce temperature changes inside the pile, thereby decreasing the magnitude of induced thermal stresses. There is some increase in temperature at the soil-pile interface with the enhanced configuration consisting of an ETZ with a helical loop relative to a more conventional configuration; however, this temperature increase along the pile face would not be expected to adversely impact the geotechnical performance, especially given that it can be accounted for in the original design using one or more of the robust constitutive models (one that relates changes in soil temperature to changes in shaft friction) which are already available to engineers.

Ultimately, improvements in thermal performance resulting from using an ETZ with a helical loop configuration can make energy piles a more feasible renewable and sustainable energy alternative for heating and cooling of buildings, particularly in areas where poor subsurface thermal properties might otherwise preclude the use of energy piles. Another potential benefit is that enhanced thermal performance could allow for the use of shorter thermo-active foundation elements, in comparison to deep geothermal boreholes, which is especially important for urban areas where the value of underground space (for transit and other utility / infrastructure purposes) is becoming increasingly important.

CHAPTER 8. LABORATORY SCALE CHAMBER TESTING

Results from a proof-of-concept study using COMSOL numerical modeling to demonstrate the benefits of an ETZ were shown in the previous chapter. In this chapter, the results from a laboratory scale physical model using the ETZ concept are presented to evaluate its effect on thermal performance of the physical model. The study was performed in collaboration with École des Ponts – ParisTech, utilizing a chamber which had previously been used to investigate thermo-mechanical aspects of a laboratory scale model.

8.1 Methodology

8.1.1 Experimental Setup

A physical, laboratory scale model was developed to investigate the effect of using an ETZ on the thermal performance of an energy pile system. Nguyen et al. (2017) previously used a large chamber to measure thermo-mechanical response of a model energy pile from applied thermal cycles. The chamber was reconfigured to focus solely on heat transfer characteristics.

Figure 8-1 presents an overall schematic of the experimental design. Outside of the chamber is the fluid circulation system consisting of a constant temperature bath, peristaltic pump, flow meter, and two small containers to measure the inlet and outlet temperatures. The circulation fluid (water) was pumped in a continuous loop through insulated tubing. The chamber was also insulated using a radiant barrier.

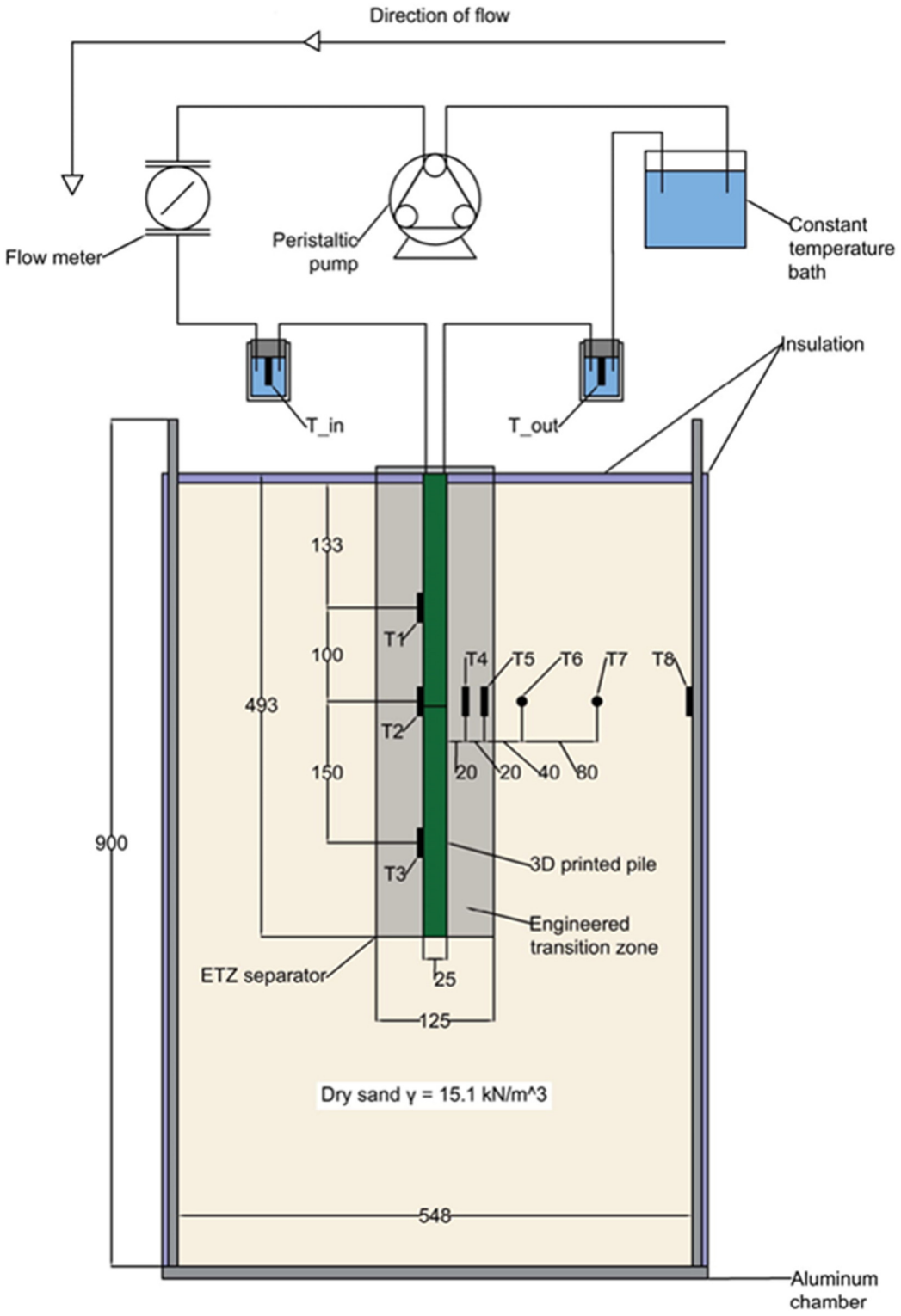

Figure 8-1 – Experimental setup for physical laboratory scale model (all dimensions in mm)

Inside of the chamber were the following components:

- The model pile, which was 3D printed from ABS plastic with a diameter of 25 mm and length of 493 mm for an aspect ratio just under 20. A single U-loop was printed into the pile and then tightly threaded with plastic tubing (2.4 mm inside diameter, 0.4 mm wall thickness) coated in a thermal grease (to minimize contact resistance between the tubing and the pile) in order to create a fluid circulation loop (see Figure 8-2). The distance from the outside edge of the pile to the outside edge of the fluid circulation tubing was 1.5 mm.
- The ETZ separator, which is a 125 mm diameter, thin-walled, watertight aluminum chamber inside which the soil could be saturated to create an "active" ETZ with higher thermal conductivity relative to the surrounding dry soil. In two of the test trials, a helical fluid circulation loop was placed inside the ETZ, halfway between the pile and separator wall. The helical loop was also 3D printed, with an overall diameter of 80 mm, inside pipe diameter of 2.4 mm, and a nominal wall thickness of 2 mm (see Figure 8-2). The total loop length was approximately 5.3 m.

Test soil was Fontainebleau sand, a commonly used benchmark soil in France. Relevant physical properties (as obtained from Nguyen, 2017) are summarized in Table 8-1.

Table 8-1 – Relevant physical properties of Fontainebleau sand

Description	Value
Density of solids, ρ_s	2.67 Mg/m^3
Mean particle diameter, D_{50}	0.23 mm
Max. void ratio, e_{max}	0.94
Min. void ratio, e_{min}	0.54

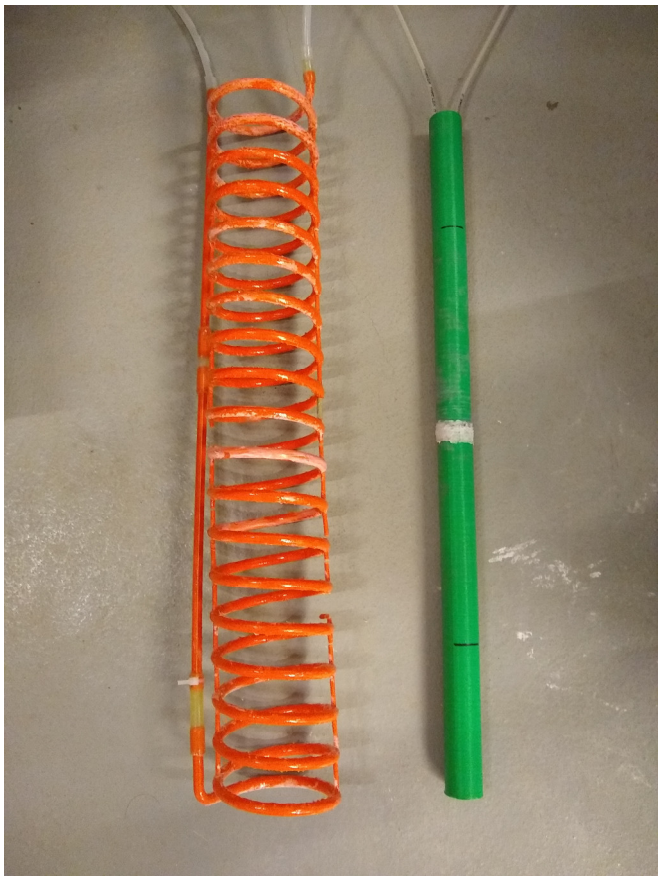

Figure 8-2 – Model pile (right) and 3D fluid circulation loop (left) used during laboratory scale model tests

Dry tamping method was used to fill the chamber in uniform layers to a unit weight of γ_d = 15.1 kN/m^3, corresponding to a relative density of D_R = 50%. Temperature sensors were placed along the pile and throughout the chamber at various depths and distances from the pile as shown in Figure 8-1. After placing the bottom sand layers, the ETZ separator was placed inside the chamber. Then, dry sand was placed on the outside of the ETZ separator. With the ETZ separator in place, the model pile was placed in the center, and sand was then placed to the same relative density as the outside. As previously mentioned, in two of the test trials, a helical loop was also placed inside the ETZ, halfway between the pile and separator wall. In order to saturate the sand inside the ETZ separator after performing the dry baseline tests, a plastic tubing was attached to the inside wall of the ETZ separator, and a simple gravity-fed system was used to add water to inside the ETZ from the bottom up.

Table 8-2 – Density and thermal properties for experimental program

Parameter	Dry Sand	Saturated Sand	Pile / Helical Loop	Fluid
Bulk Density (kg/m^3)	1,540	1,956	1,000	1,000
Thermal Conductivity (W/m-K)	0.26	2.90	0.13	0.60

The density and thermal properties of the experimental materials are shown in Table 8-2. The thermal conductivity of the dry and saturated sand were measured in the chamber, using a KD2 Pro Thermal Properties Analyzer and a TR-1 thermal needle. The density and

thermal conductivity of the pile/helical loop material was measured from a 3D printed calibration block, using a KD2 Pro Thermal Properties Analyzer and a SH-1 dual thermal needle.

8.1.2 Testing Program

Originally, a testing program consisting of six different trials was planned as summarized in Table 8-3. The goal was to perform all trials in four phases: 1) 24 hours of heat injection, 2) 24 hours recovery, 3) 24 hours of heat extraction, and 4) 24 hours recovery. However, while performing Trials 2 and 4, which were meant to investigate the effect of a higher flow rate, some issues were noted with the peristaltic pump used for testing, as well as rapid changes in the ambient temperature during Trial 4. As a result, these tests have been excluded from further analyses.

Table 8-3 – Summary of lab scale model testing program

Trial	Nominal Flow rate (mL/min)	ETZ Condition	Pile Configuration
1	25	Dry sand	Single U-Loop
2	50	Dry sand	Single U-Loop
3	25	Saturated sand (active)	Single U-Loop
4	50	Saturated sand (active)	Single U-Loop
5	25	Dry sand	Helical Loop in ETZ
6	25	Saturated sand (active)	Helical Loop in ETZ

Additionally, due to time limitations, Trial 5 was only able to be run for a total 48 hours, without a recovery period between the heat injection and heat extraction phases. Further, Trial 6 was only able to be performed for approximately 43 hours, also without a recovery period between the heat injection and heat extraction phases. Nonetheless, Trials 1, 3, 5 and 6 all produced good quality data in the initial 24-hour heat injection phase, and these results are presented and analyzed in this chapter. The heat injection phase of the test is analogous to a thermal response test, which is standard practice for evaluating the in-situ thermal response of energy pile systems. The inlet temperature (as imposed in the constant temperature bath) during the heat injection phase was 15 degrees Celsius above the initial soil temperature.

8.2 Results & Discussion

The temperature response of Trial 1, 3, 5 and 6 are shown on Figure 8-3 through Figure 8-6. For the single U-loop configuration (Trial 1 and 3), it can be seen that the inlet and outlet temperatures rise rapidly and reach steady-state within the first few hours of injection. For the helical loop configuration (Trial 5 and 6), the inlet temperatures rise rapidly and reach steady-state within the first few hours of injection, while the outlet temperatures take longer to reach steady-state. The response in the soil can be characterized by a steady increase in temperatures throughout the duration of testing, with the increase in soil temperature typically decreasing with distance from the pile and depth from the ground surface. Sensor T8, which was placed against the inner wall of the chamber, showed a very small response, indicating that the chamber was well insulated against changes in ambient temperature.

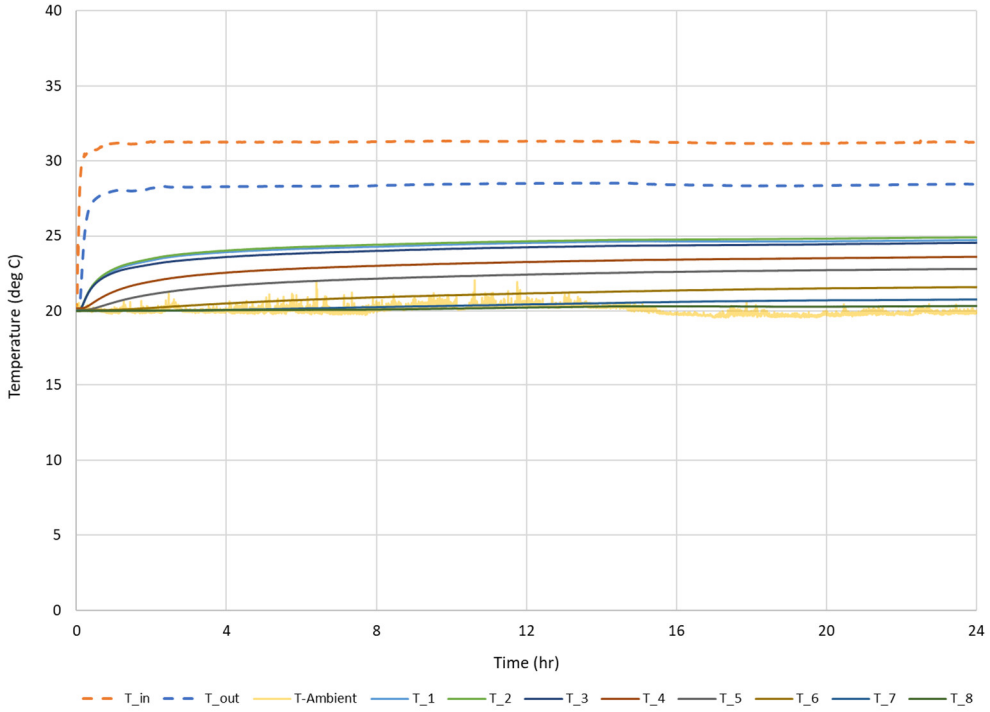

Figure 8-3 – Temperature response for Trial 1

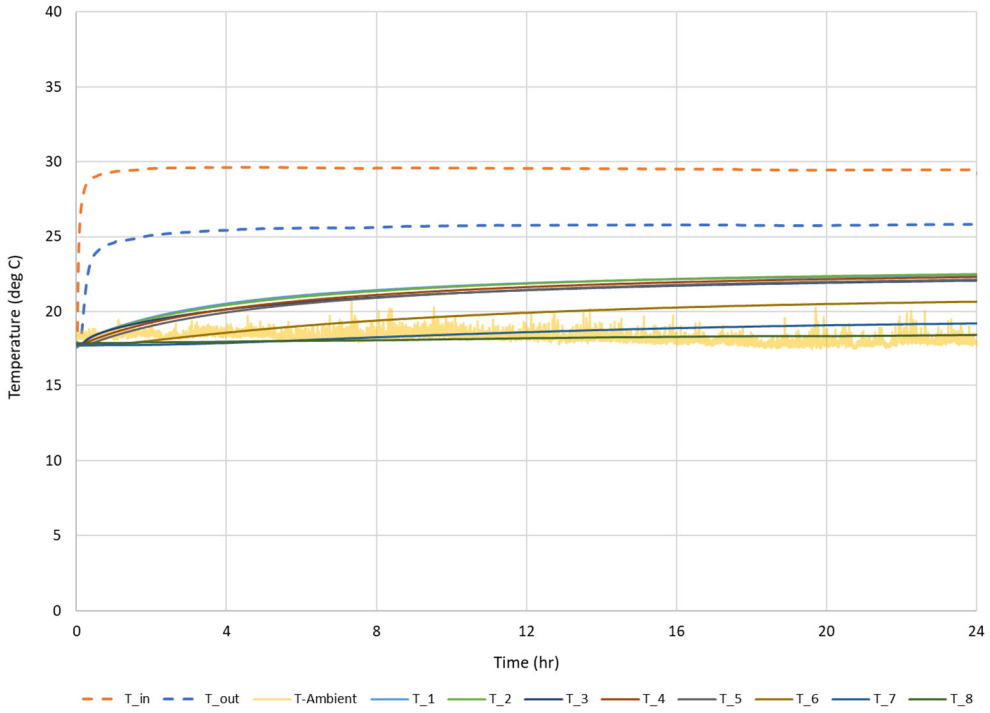

Figure 8-4 – Temperature response for Trial 3

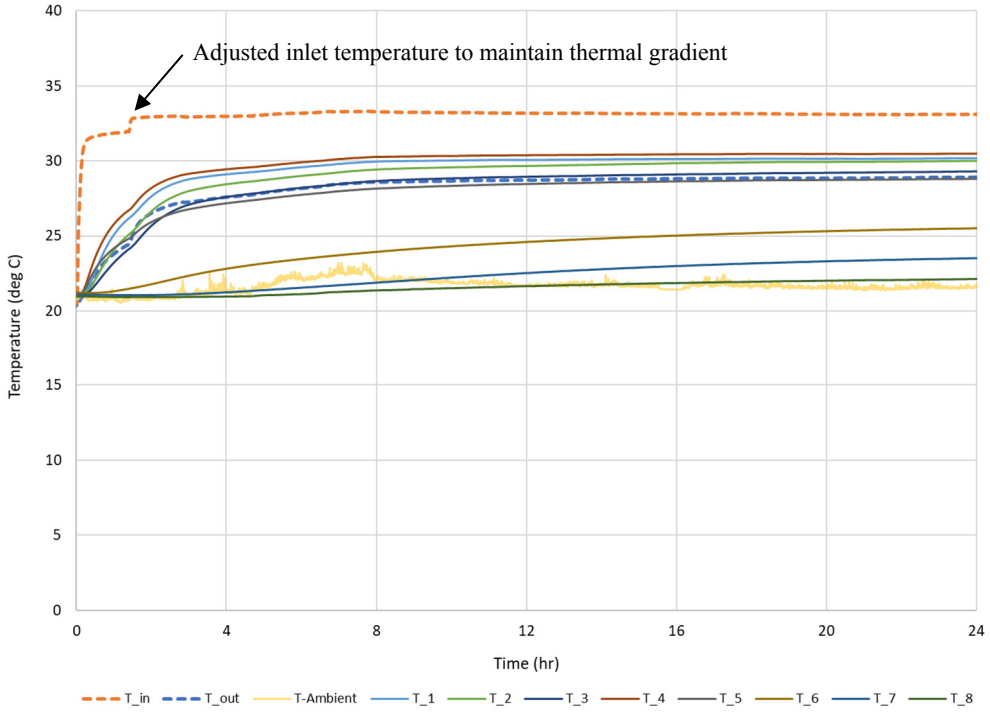

Figure 8-5 – Temperature response for Trial 5

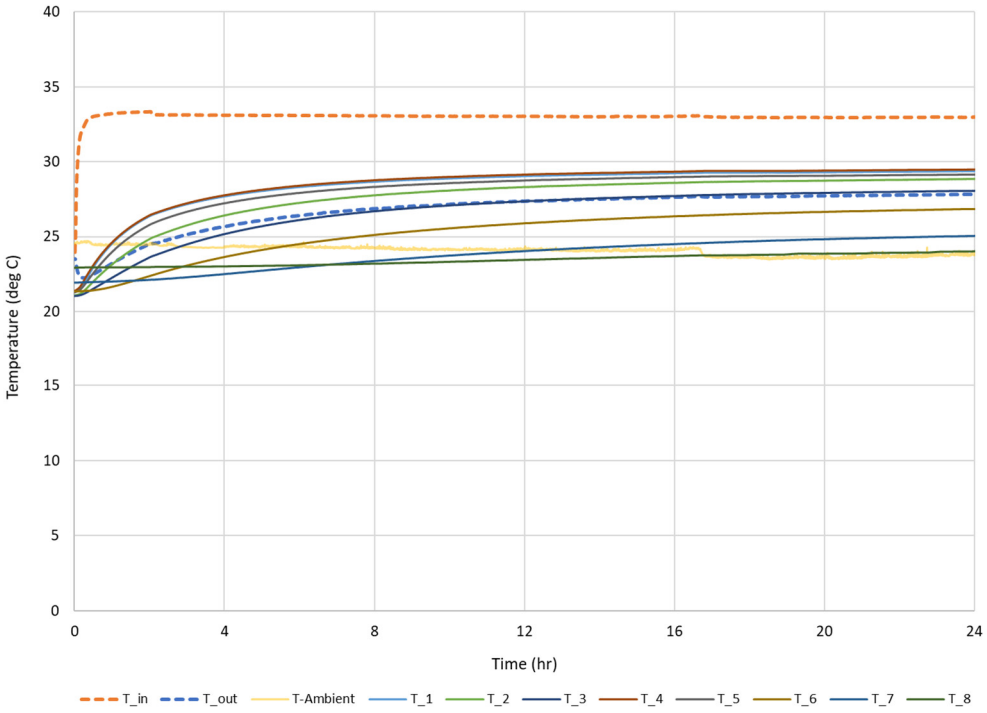

Figure 8-6 – Temperature response for Trial 6

Figure 8-7 shows the recorded flow rates during the heat injection phase of the selected trials. While a nominal flow rate of 25 mL/min was chosen, the peristaltic pump operated with some variability as shown. The average flow rates for each trial are also tabulated in this figure. Figure 8-8 and Figure 8-9 show the difference between inlet and outlet temperature and the corresponding power extraction of the system, respectively. The power output was calculated using Equation (40) as given in Chapter 7. Figure 8-9 shows both the raw calculated power (variable due to the flow rate; shown using transparent lines) and a smoothed curve using the average flow rate for the entire run. The figures show that in all trials, the temperature difference and power output is high at the start of testing, and then quickly converge towards a steady-state value.

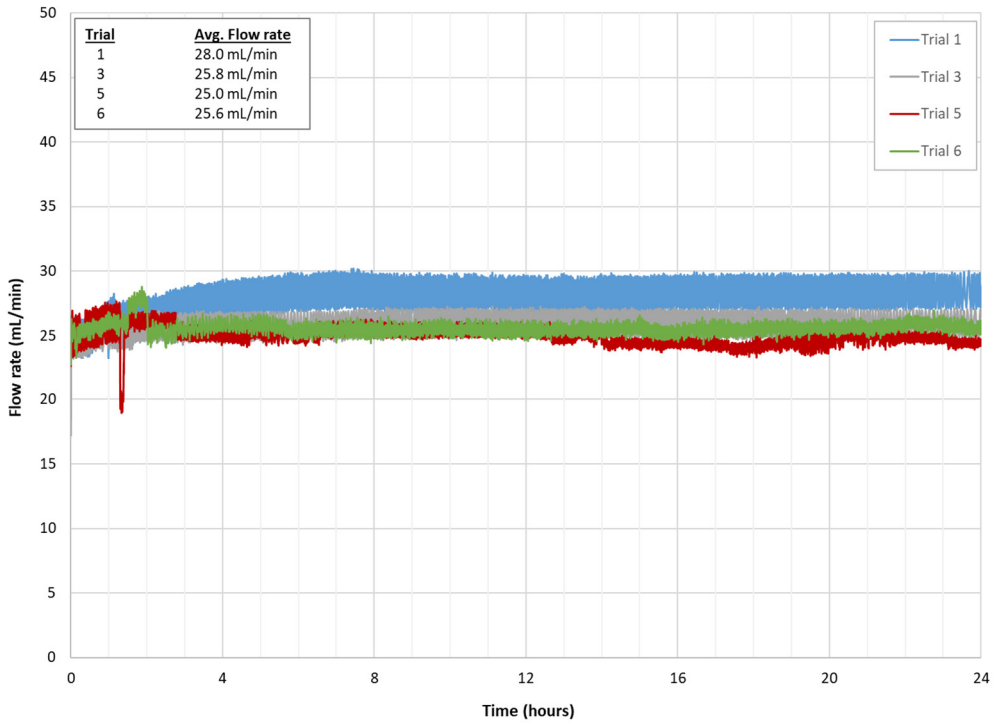

Figure 8-7 – Recorded flow rates during heat injection

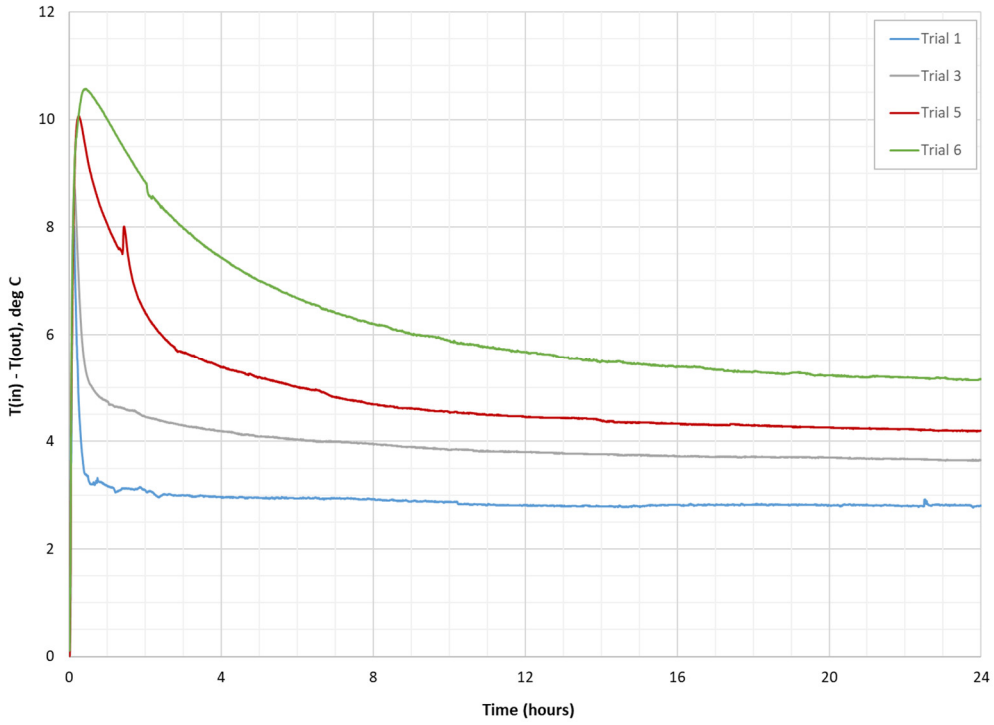

Figure 8-8 – Inlet and outlet temperature difference during heat injection

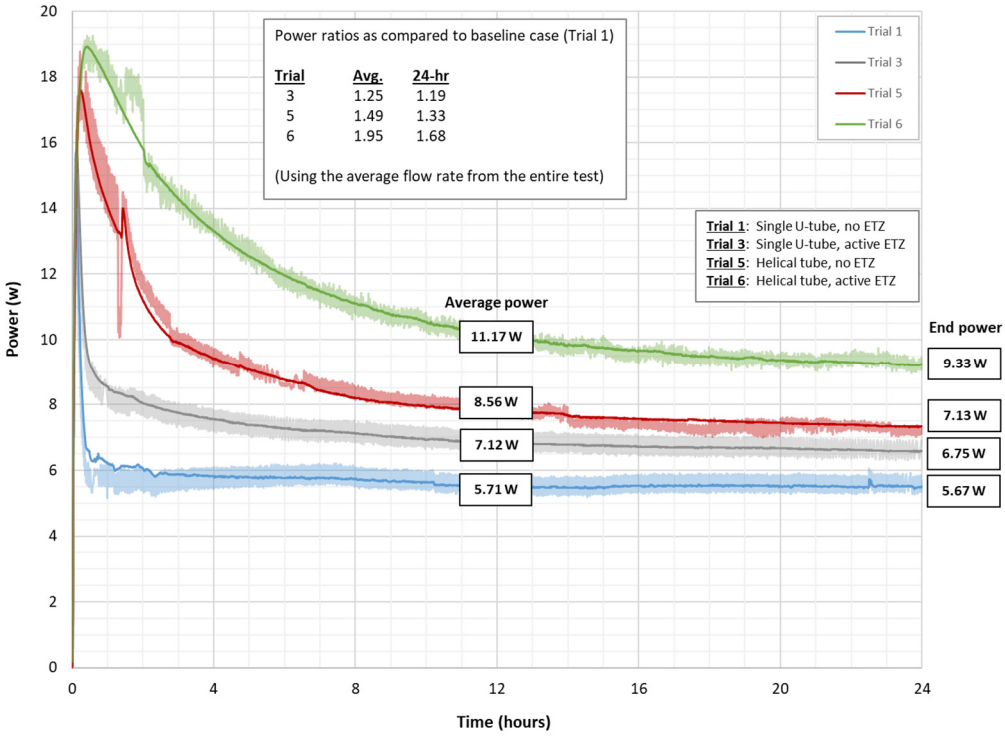

Figure 8-9 – Power extraction during heat injection

Table 8-4 – Summary of power extraction from lab scale model

Trial Nos.	Description	Power Ratio	
		Average	End of cycle
1	Single U-loop, no ETZ (baseline)	1.00	1.00
1 vs. 3	Single U-loop, active ETZ	1.25	1.19
1 vs. 5	Helical loop, no ETZ	1.49	1.33
1 vs. 6	Helical loop, active ETZ	1.95	1.68

Table 8-4 summarizes the power extraction results for all trials, looking at both the average power (i.e., average of power during the 24-hour test period) and that at the end of the heat injection cycle. The power ratio is defined as the calculated average or end power of a trial divided by that of Trial 1, the baseline case.

Table 8-4 shows that the presence of an active ETZ only results in an improvement of 25 percent on average, and 19 percent at the end of the cycle. Table 8-4 also shows that using a helical loop configuration increased the thermal performance of the system by 49 percent on average, and 33 percent at the end of the cycle. This increase in performance can be attributed to increased fluid circulation pipe surface area available for heat transfer, as well as removal of the circulation loop to outside of the pile element. Lastly, Table 8-4 shows that combining an active ETZ with a helical loop configuration results in an improvement of 95 percent on average, and 68 percent at the end of the cycle. It can also

be seen that the improvement from the combination of the active ETZ with a helical loop configuration is greater than the sum of their parts, as was indicated by the numerical modeling results as well.

The pile surface temperature response, as indicated by sensors T1, T2 and T3, are shown in Figure 8-10. It can be seen that compared to the baseline case (Trial 1), the system with an active ETZ and a helical loop configuration (Trial 6) results in an approximately 5-degree Celsius temperature increase at the pile surface. This increase in pile surface temperature is in general agreement with the numerical modeling results, which also indicated an increase in pile surface temperatures, although the magnitude of the increase was smaller. This is likely because of the poor thermal properties of the dry sand soils outside the ETZ, resulting in more heat transfer inside the ETZ and towards the pile element.

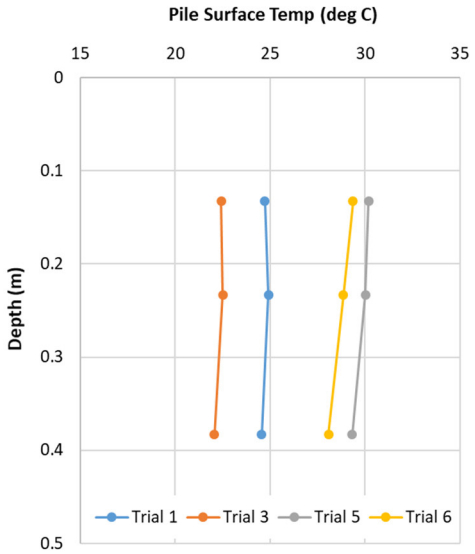

Figure 8-10 – Scale model pile surface temperature response

8.3 Conclusions

The purpose of this study was to evaluate, using a laboratory scale physical model, whether the implementation of an ETZ can improve the thermal performance of an energy pile system. The experimental work also serves as further proof-of-concept in addition to the numerical work presented in Chapter 7.

The test results show that the use of an ETZ alone improves thermal performance slightly. The test results also show that increasing pipe length by using a helical loop, and therefore increasing pipe area available for heat transfer, can also increase thermal performance. Additionally, the test results show that decoupling the structural and thermal components of an energy pile system (e.g., by creating an ETZ and placing a helical fluid circulation loop in the ETZ) can further improve performance. In this case, the use of a helical fluid loop in an active ETZ was shown to nearly double the average power extracted from the model system. Lastly, the test results show an increase in pile surface temperatures as was previously indicated by the numerical modeling results.

The experimental setup was subject to some limitations. There were variations in ambient temperature of the room in which the tests were performed. While the impact on soil temperatures in the chamber were minimal due to insulation applied on the outside of the chamber, using a temperature-controlled environment would have provided a more representative scenario as the ground temperatures are not subject to such variations below a depth of about 3 to 5 meters. Additionally, the system for measuring the inlet and outlet temperatures was affected by thermal inertia; temperature readings were taken from the fluid (water) mass inside of small containers and not directly from the fluid lines. For

quantification of power extracted from the system, this is not a serious issue because the power is a function of the difference between the inlet and outlet temperatures, both of which were subject to the same limitation. However, for numerical validation purposes, actual measurements of inlet and outlet temperatures directly from the lines would be required.

CHAPTER 9. PUBLIC POLICY CONSIDERATIONS

Despite being a relatively mature technology (see Figure 9-1; note that this figure is from 2007 and more advancements have taken place since then) and the apparent benefits including reductions in energy consumption, peak demand, and $C0_2$ emissions, ground-source heat pumps (GSHPs) currently account for only about two percent of the U.S. heating and cooling market (Battocletti and Glassley, 2013). Studies on GSHPs often cite lack of information (for both the consumers and installers), high first cost premium over the incumbent technology, and lack of incentives (subsidies, financing alternatives, split incentives, etc.) as barriers to more wide-spread adoption of the technology (Hughes and Pratsch, 2002, Hughes, 2008, Seyboth et al., 2008, Goetzler et al., 2009, Connor et al., 2013).

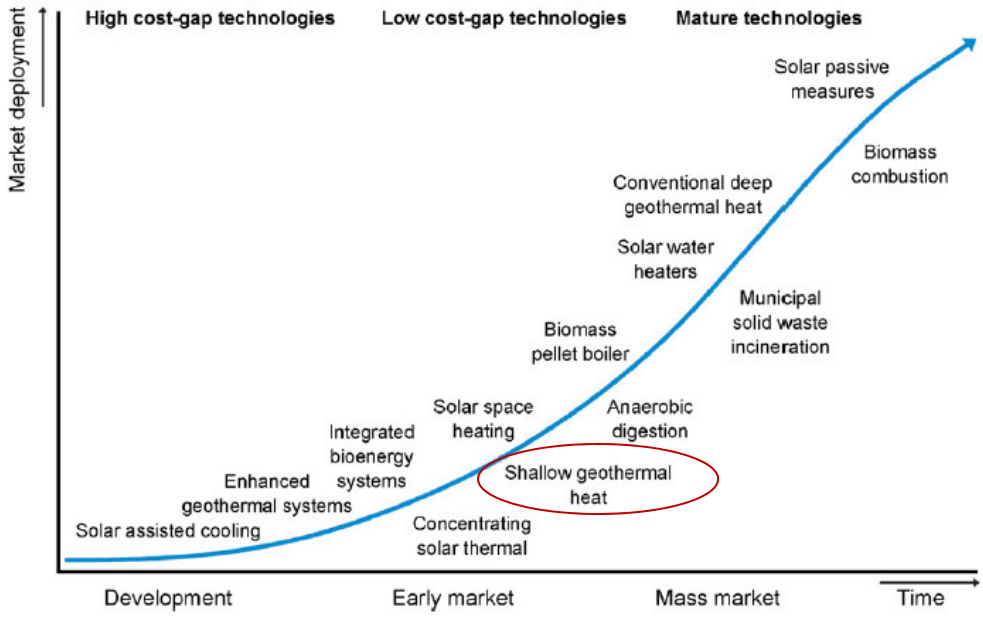

Figure 9-1 – Current state of deployment of renewable heating and cooling (REHC) technologies; from IEA (2007)

One question that arises is that whether or not this is a case of the "energy paradox" or "energy efficiency gap"; that is, the low adoption of an energy-efficient technology despite the apparent benefits (Jaffe and Stavins, 1994, Alcott, 2015). In other words, is the GSHP's low market share an expression of well-informed preferences, or are consumers unaware of or inattentive to how much money they could save? Further, are there other market failures at play such as investment inefficiencies? While there is a large body of literature assessing investment inefficiencies related to energy efficiency, Alcott and Greenstone (2012) suggest that the actual empirical magnitude of such investment inefficiencies are substantially smaller than indicated by engineering analyses (such as those typically performed by governmental organizations or consultants). Alcott and Greenstone (2012) also suggest that imperfect information is "perhaps the most important form of investment inefficiency that could cause an energy efficiency gap", and that inattention (i.e., the idea that the effort of making an informed choice is greater than the benefit of a correct choice) can result in consumers failing to optimize their choice when purchasing energy-efficient durable goods.

In this regard, one question that arises is whether or not policy density (number of policies getting passed) can lower information barriers by signaling/informing the markets and creating awareness (Sexton and Sexton, 2014, Noonan et al., 2015), as well as legitimizing a technology, in turn resulting in higher adoption rates for energy-efficient technologies. The concept of policy density has been used previously to evaluate policy output (Knill et al., 2010, Knill et al., 2012, Schraffrin et al., 2015), with the basic idea being that the greater the number of targeted policies, the greater the desired policy output.

In this chapter, the goal is to assess if there is any relationship between policy density (i.e., the number of GSHP-related policies) and the adoption of GSHPs. It is hypothesized that there should be a positive relationship between the number of policies and the adoption rates. In this regard, rated capacity of GSHP shipments is used as a proxy for adoption rates; that is, an increase in capacity of GSHP shipments is indicative of increased demand and therefore market adoption. This hypothesis is tested in two ways: 1) through the application of punctuated equilibrium theory and the Bass Diffusion Model, and 2) through the use of longitudinal data analysis.

9.1 Methodology

9.1.1 Punctuated Equilibrium & Bass Diffusion Model

Punctuated equilibrium theory in social sciences is derived from the hypothesis in evolutionary biology, which suggests that evolution is marked by sudden shocks followed by periods of little or no change. In public policy, it refers to the fact that most policies are relatively stable over a long period, and that external shocks are a necessary (but not sufficient) condition to result in major policy change (Dunn, 2012).

Diffusion is the primary process governing heat transfer in and around a thermo-active foundation. The general concept of diffusion has also been applied to social sciences such as marketing, sociology and public policy to model diffusion of innovations, ideas and policies. It has been observed that in particular, "policy diffusion, with its S-shaped curve, is remarkably like a punctuated equilibrium model in which the system shifts rapidly from one stable point to another" (Baumgartner and Jones, 2009, Boushey, 2012).

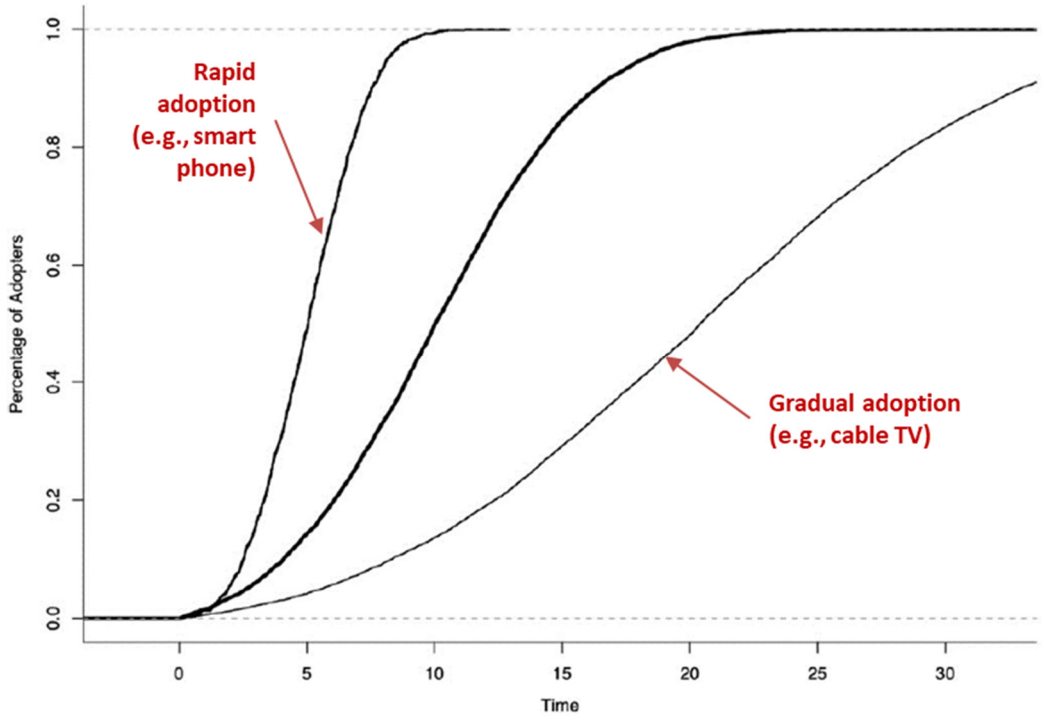

Figure 9-2 – S-shaped curves of diffusion (modified after Boushey, 2012)

A case study was performed looking at the application of the punctuated equilibrium theory and policy diffusion to gain insight into GSHP related policies in the U.S. between 2000 and 2015, as well as GSHP adoption rates between 2002 and 2009. The policy data were obtained from the Database of State Incentives for Renewables & Efficiency (DSIRE). This database was queried for all state and federal level policies (for both regulatory policies and financial incentives) between 2000 and 2015, which yielded a total of 589 GHP related policies (including residential, commercial and public sectors). Data for rated capacity (in HVAC tons) of GSHP shipments were obtained from the "Geothermal Heat Pump Manufacturing Activities" reports published annually by the U.S. Energy Information Administration (EIA). The rated capacity of GSHP shipments is

directly related to the number of units shipped; i.e., higher the units shipped, the greater the capacity. In other words, rated capacity of GSHP shipments is a proxy for GSHP adoption. The data is based on a survey of the 27 known domestic manufacturers of GSHPs.

It is hypothesized that federal policies acted as an external shock to the status quo at the time, and this signal resulted in GHP related policies to be enacted at the state level. The Bass Diffusion Model (BDM) was used (Bass, 1969) in order to test this hypothesis. The BDM, also referred to as "mixed influence diffusion model", has been used in the past to study both external and internal factors contributing to diffusion of technological innovations as well as policy diffusion (Mahajan and Peterson, 1985, Rossman, 2009, Boushey, 2012). The model can be expressed in its differential form as follows:

$$\frac{dN(t)}{dt} = (a + b \cdot N(t))\,[N^* - N(t)] \tag{41}$$

Where N represent the number of policies, a represents the coefficient of external influence (e.g., external shock or innovation), b represents the coefficient of internal influence (e.g., imitation or word-of-mouth), and N^* represents the total number of units adopting the innovation. A high value of a indicates that external factors are driving diffusion, while a high value of b indicates that internal factors are driving diffusion.

It is worth noting that the form of the mixed influence model as shown in Equation (41) differs from the form of the diffusion equation that is more familiar to engineers, for example as shown in Equation (10). This is because the mixed-influence model is a particular application of the generalized diffusion equation for modeling of innovation

diffusion. However, it can also be used for modeling other processes such as policy diffusion (e.g., Boushey, 2012).

9.1.2 Longitudinal Data Analysis

The BDM analysis is based on data at the national level. Longitudinal data analysis was performed to investigate the data at a regional level. Longitudinal data consist of multi-dimensional data involving measurements over time and contain observations of multiple phenomena obtained over multiple time periods for the same variables. In this case, the data were first assembled at the state level, then aggregated into regional level data, representing the four main U.S. Census Regions.

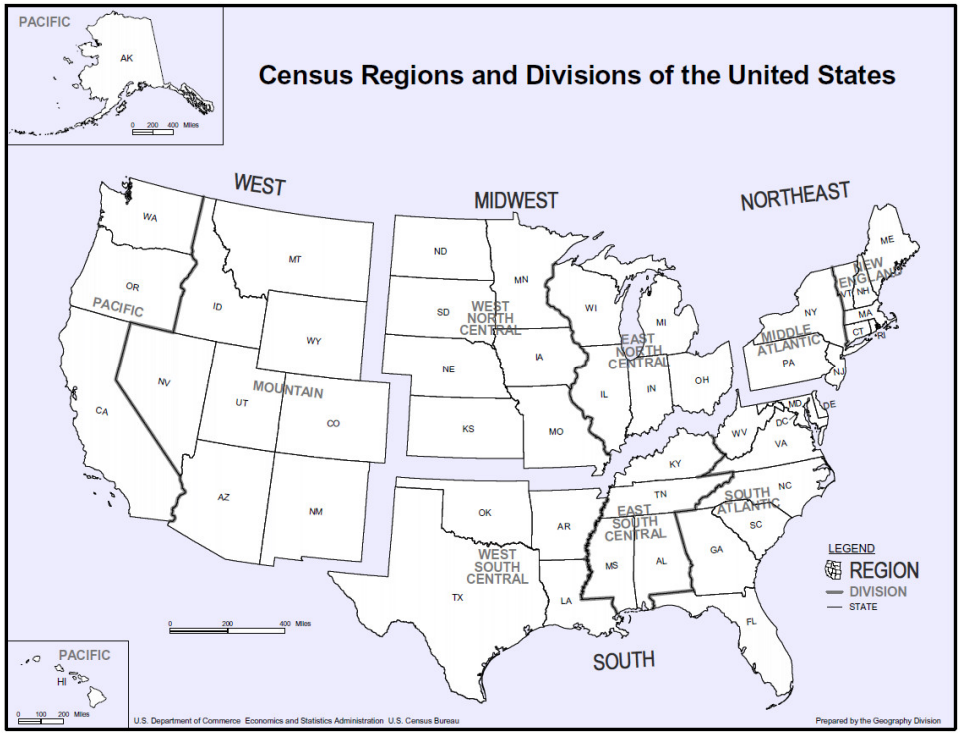

Figure 9-3 – U.S. Census Regions

Policy density and GSHP shipment data were obtained from the sources previously described. Other information considered for the longitudinal data analysis included historical data on new privately owned housing units completed in the four U.S. Census Regions, obtained from the U.S. Census Bureau. Population data was also obtained from the U.S. Census Bureau. Real Gross State Product (GSP) data (chained to 2009 dollars) was obtained from the Bureau of Economic Analysis (BEA). Historical data on average annual residential electricity (₵/kWh), natural gas ($/thousand ft^3) and heating oil prices ($/gallon) were obtained from the EIA.

In addition, historical data on heating degree days (HDD) and cooling degree days (CDD) were also obtained from the EIA (using base 65 degrees Fahrenheit). Residential and commercial energy consumption data were obtained from the Residential Energy Consumption (RECS) and Commercial Building Energy Consumption Survey (CBECS), published by the EIA. The median new home value, household income data and disposable personal income (personal income less personal taxes) data (in 2009 dollars) were obtained from the BEA.

9.2 Results & Discussion

9.2.1 Bass Diffusion Model

A distribution of the GHP related policies by year is shown on Figure 9-4. A significant increase in GHP-related policies can be seen starting in 2006, with another small perturbation in 2009, then tapering off over the years. A closer examination of the dataset obtained from DSIRE revealed that in August 2005, the U.S. Congress approved the Residential Renewable Energy Tax Credit (which provided a 30% tax credit for GSHP

installations) with an effective start date of January 1, 2006. In addition, the American Recovery and Reinvestment Act of 2009, signed into law in February 2009, extended the 30% tax credit for residential GSHP installations, and provided up to a 10% grant for commercial building installations.

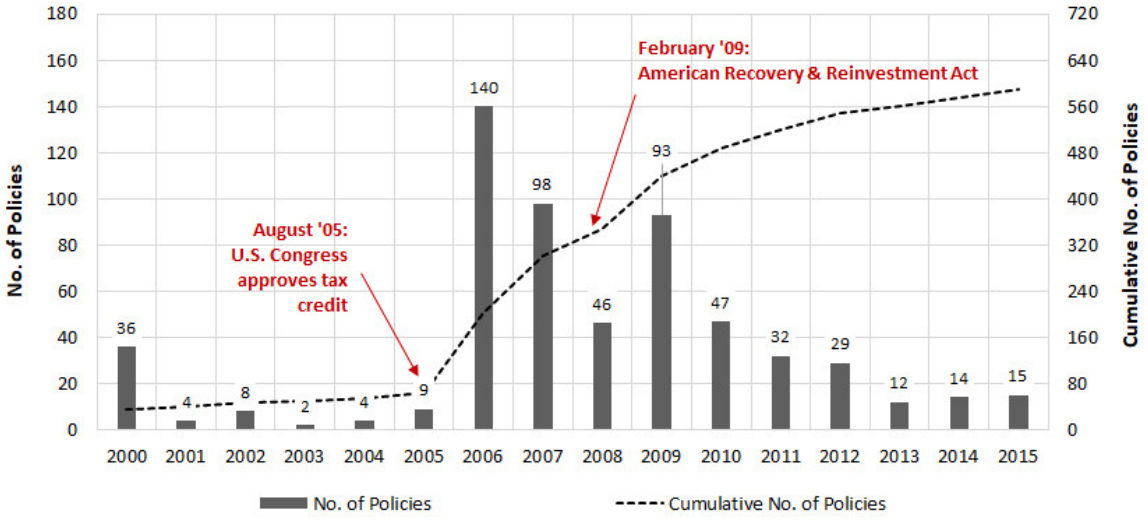

Figure 9-4 – Distribution of GSHP-related policies by year

Figure 9-5 shows the distribution of GSHP shipment capacities by year. It can be seen that prior to year 2006, the capacity was relatively flat, with an average capacity of approximately 129,000 tons. From 2006 to 2009, a significant uptake in shipment capacity can be observed, with an average capacity of approximately 292,000 tons, or about 2.3 times that of the pre-2006 levels.

Figure 9-6 shows the cumulative number of GHP related policies from 2000 to 2015, as well as the BDM results. The BDM coefficients that provided the best fit to the post-2005 data (after the federal tax credit was introduced) were $a = 0.23$ and $b = 0.01$. This

indicates that external influence (e.g., external shock) is the most likely driver of policy diffusion.

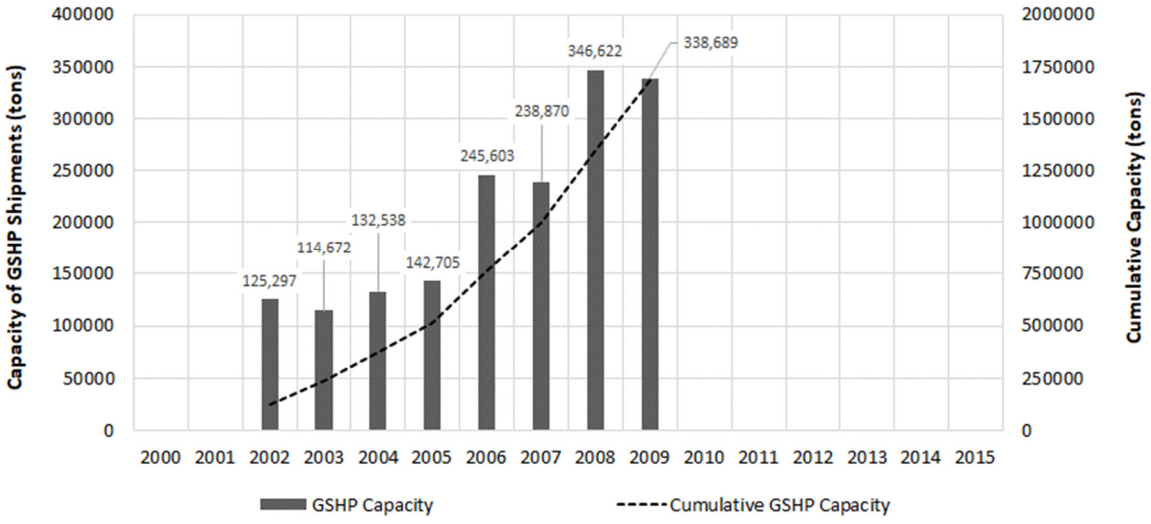

Figure 9-5 – Distribution of GSHP shipment capacities by year

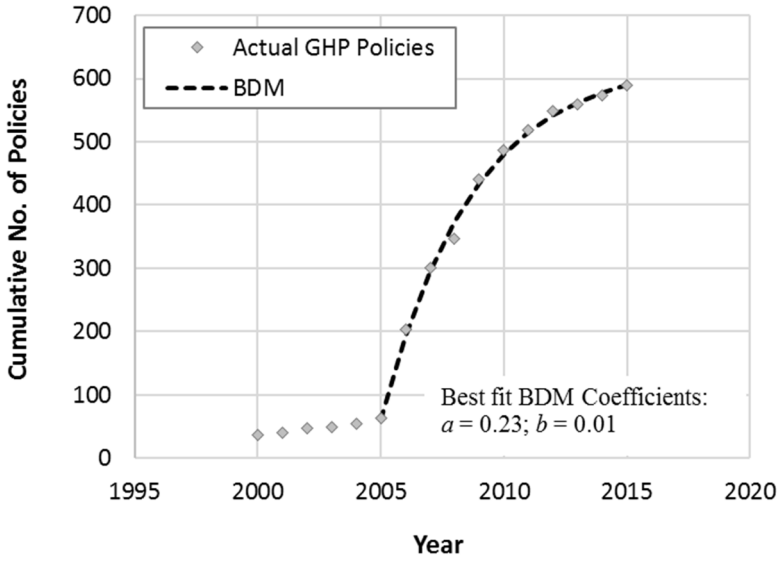

Figure 9-6 – Cumulative number of GHP-related policies (2000-2015) and Bass Diffusion Model (BDM) Results

Figure 9-7 shows the cumulative rated capacity of GHP shipments from 2002 to 2009. In this case, the BDM coefficients that provided the best fit to the actual post-2005 data were $a = 0$ and $b = 0.54$. This indicates that internal influence (e.g., imitation or word-of-mouth) is the most likely driver of adoption.

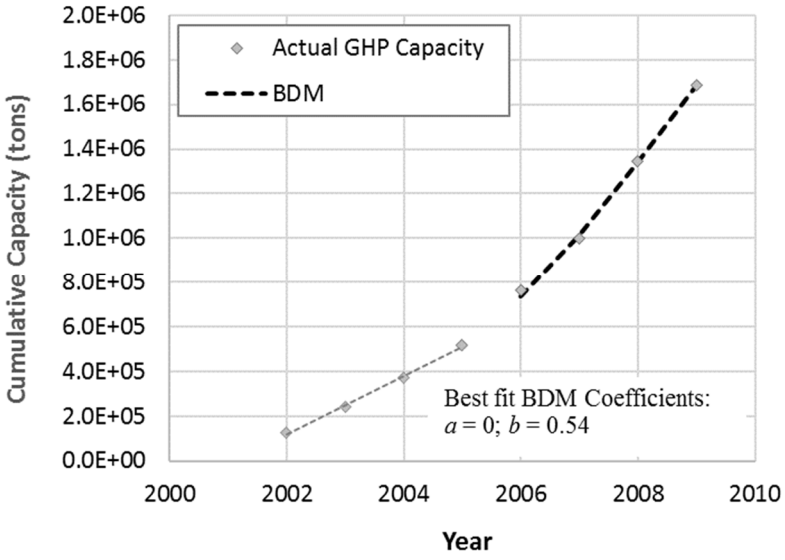

Figure 9-7 – Cumulative rated capacity (in HVAC tons) of GSHP shipments (2002-2009) and Bass Diffusion Model (BDM) Results

9.2.2 Longitudinal Data Analysis

The BDM results are based on analysis of data at the national level. The regional data for years 2003-2009 are summarized on Figure 9-8 and Figure 9-9. Note that prior to 2003, GSHP shipment data was not available at the state level.

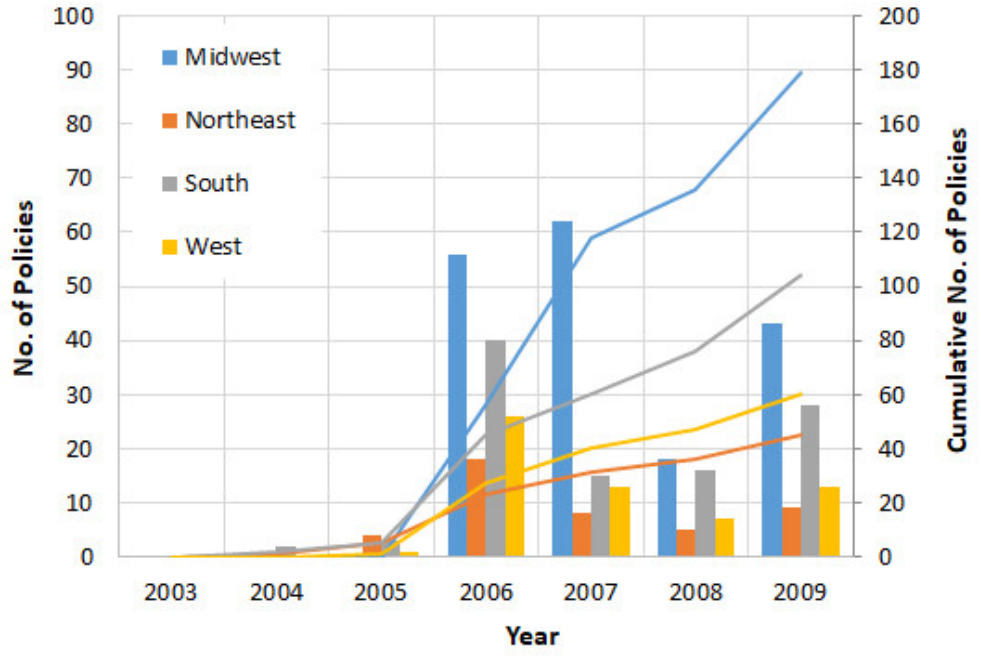

Figure 9-8 – Distribution of GSHP-related policies by year for the four U.S. Census Regions

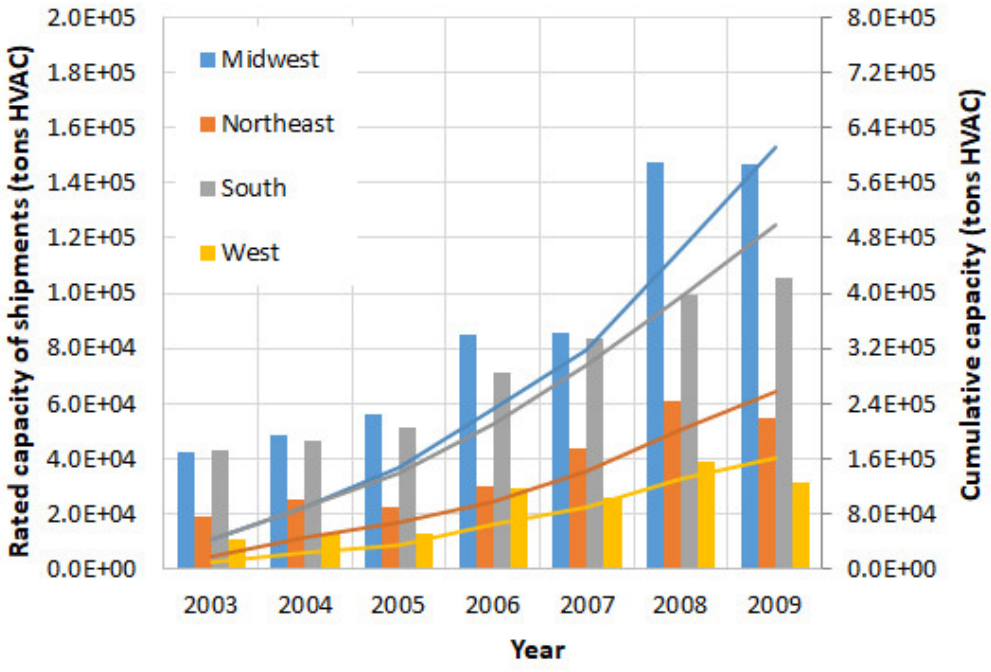

Figure 9-9 – Distribution of rated capacity of GSHP shipments by year for the four U.S. Census Regions

Figure 9-8 shows that after year 2005, there was a significant increase in the number of policies, particularly for the Midwest region and for the South region. Figure 9-9 indicates an increase in the rated capacity of the GSHP shipments as well, especially in these two regions. The Northeast and the West regions exhibited more modest growth patterns. There was a flattening of the GSHP adoption rates starting in year 2009, likely in response to the housing and economic crisis.

Figure 9-10 shows a summary of the other factors considered for the analysis. The effects of the housing and economic crisis can be observed in several of the indicators (housing units, median home value, median income, real GSP). The data indicate that the uptake in GSHP adoption may potentially be attributed to increasing energy prices (electricity, natural gas and heating oil). In particular, the uptake in capacity of GSHP shipments in the Midwest (where the heating demands are very high, and often met with gas or oil burning furnaces) and in the South (where cooling demands are very high, and typically met with electric air conditioners) may have been in response to not only the number of policies, but also due to rising energy costs.

The data also show that the population increase was concentrated in the South, which would have resulted in increased housing demand in this region. This is also indicated by the large increase in the new privately owned housing units until 2006, after which the housing crisis resulted in significantly lower numbers. There was also a large increase in both the number of policies and the capacity of GSHP shipments for the South region from 2005 to 2006. On the other hand, there was a significant uptake in GSHP adoption rates in the Midwest region but no appreciable population increase.

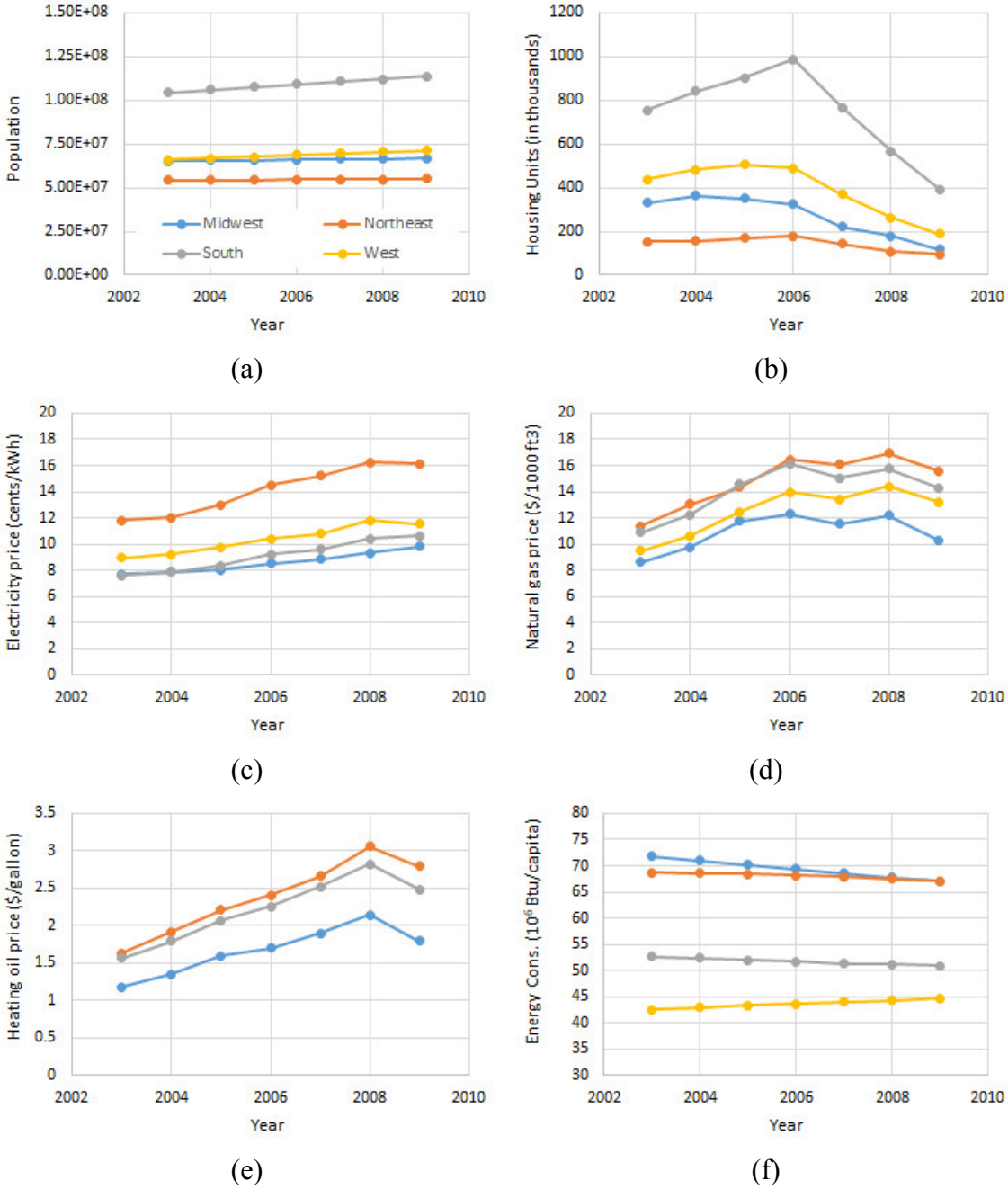

Figure 9-10 – Other factors with potential impacts on GSHP adoption for U.S. census regions

(a) Population (b) New privately owned housing units completed (c) Electricity prices (d) Natural gas prices (e) Heating oil prices (f) Energy consumption per capita

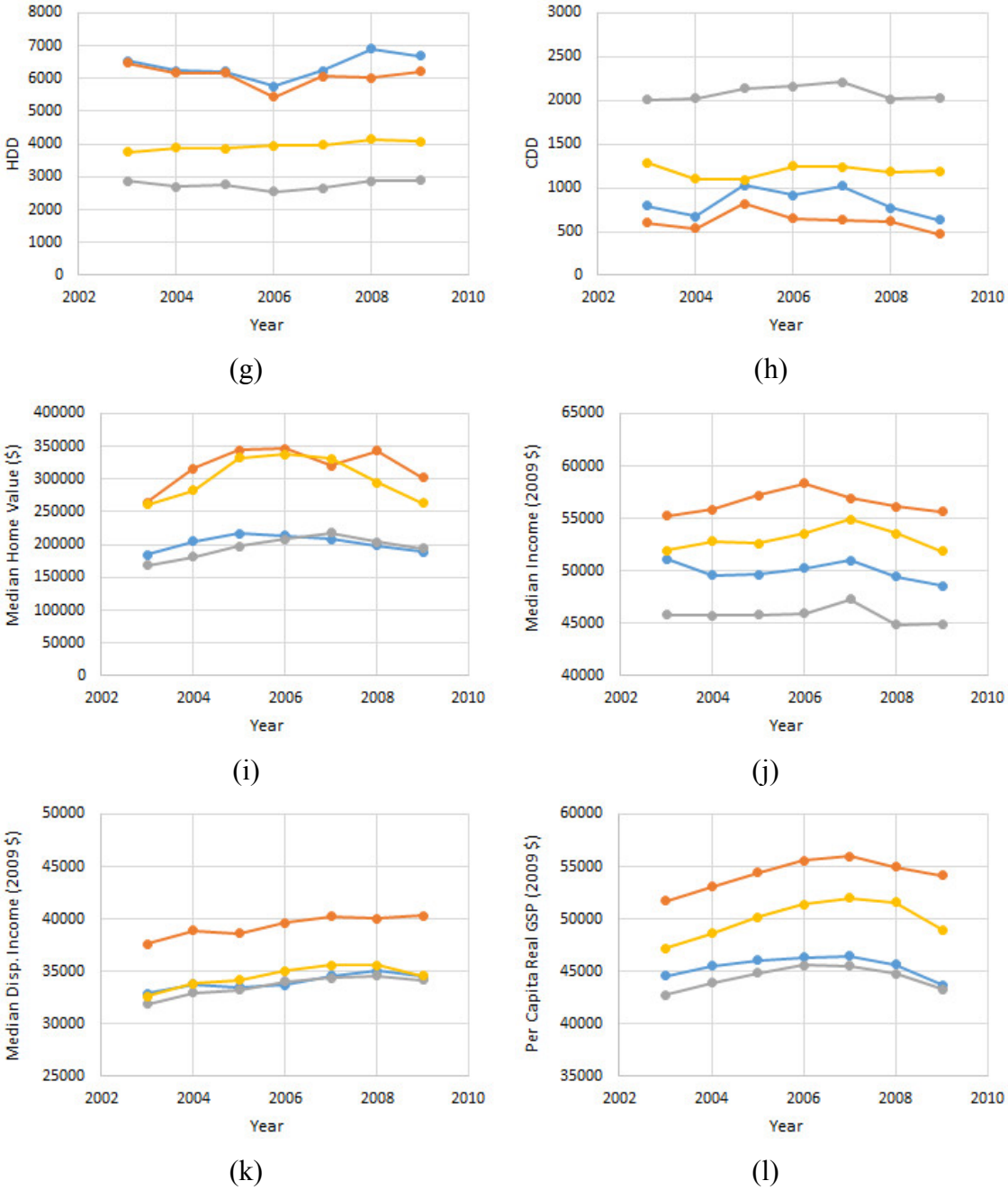

Figure 9-10 (Cont.) – Other factors with potential impacts on GSHP adoption for U.S. census regions

(g) Heating degree days (HDD) (h) Cooling degree days (CDD) (i) Median home value (j) Median income (k) Median disposable income (l) Per capita real gross state product (GSP)

These results can provide some important insights into the diffusion and market adoption of emerging technologies such as energy foundations. In this case, the results shown in Chapter 9.2.1 indicate that the introduction of a federal policy (tax credit) for GSHPs in 2005 most likely acted as an external shock, perturbing the equilibrium and driving the diffusion of policies at the state level, most likely due to policy mimicking by the states (Boushey, 2012). Policy diffusion can in turn create awareness through signaling and information, leading to more widespread market adoption. Figure 9-7 shows that there was an increase in the adoption of GSHPs after 2005 (as indicated by the steeper slope of the curve compared to pre-2005 levels), though in this case diffusion seems to be driven by internal factors and the increase in adoption rates is more gradual. Some likely causes for this observed behavior include higher initial costs relative to more conventional HVAC systems, as well as other market failures such as information asymmetry (e.g., potential buyers have incomplete information with regards to the benefits and the drawbacks of the system), and split incentives between owners and building tenants (e.g., a commercial building owner has little incentive to use more efficient energy foundations coupled with GSHPs when the renters are paying the energy bills).

The longitudinal data analysis appears to confirm that the accumulation of GSHP related policies has an impact on GSHP adoption. Additionally, it highlights some of the other factors that may have contributed to higher adoption of GSHPs, such as increasing energy prices.

State or local level policies can be devised to complement federal incentives to help overcome some of aforementioned challenges, and to further increase the rate of adoption of emerging technologies such as GSHPs and other shallow thermo-active foundations.

Examples of policy alternatives include tax credits (similar to the one approved in August 2005), loans, or grants to overcome high initial costs, or programs such as Property Assessed Clean Energy (PACE) which pays for 100 percent of a project's initial costs and the costs are repaid over a period of time with an assessment added to the property tax bill. Other policy alternatives include creating information programs to increase awareness and knowledge regarding these emerging energy efficient technologies, or to provide property tax credits to commercial building owners to overcome the split incentives problem. Residential, commercial and public sector buildings will continue to be responsible for a large percentage of total energy consumption in the U.S., and policies can be crafted to encourage more widespread use of green technologies such as thermo-active foundations for energy savings and subsequent reduction in carbon emissions.

In this regard, significantly improving the thermal performance of shallow thermo-active foundations through the use of an ETZ, as was demonstrated in Chapters 7 and 8, can also act to accelerate the rate of adoption of shallow thermo-active foundations by enabling the use of these systems in subsurface conditions that would otherwise preclude their use, and also by potentially reducing the payback period associated with these installations through the use of fewer but much higher performing elements. Additionally, the use of validated numerical models for design can address issues related to information asymmetry, and can allow for rapid prototyping of new concepts. Lastly, a lifecycle cost analysis (LCCA) can also provide further insight into the feasibility and the payback period of shallow thermo-active foundations utilizing an ETZ.

9.3 Conclusions

The Bass Diffusion Model and longitudinal data analysis techniques have been applied to evaluate the diffusion of GSHP related policies in the U.S. between 2000 and 2015, as well as GSHP adoption rates between 2002 and 2009. The results indicate that policies enacted at the federal level can act as a trigger and a signal for GSHP related policies to be enacted at the state level. Increasing the market adoption is more challenging due to market failures such as high initial costs and information asymmetry; however, policy alternatives can be devised at the state and local levels to complement federal incentives, to help overcome market failures, and to encourage more widespread adoption of emerging energy efficient technologies such as shallow thermo-active foundations.

CHAPTER 10. CONCLUSIONS AND FUTURE WORK

This study presents results from laboratory tests on Piedmont residual soils to demonstrate the importance of density, saturation, and texture on soil thermal properties, which in turn are critical to evaluating the performance of shallow thermo-active foundations in this physiographic region. In this regard, a predictive relationship was developed for estimation of thermal conductivity (during both wetting and drying) for a given porosity and composition, and for moistures ranging from dry to full saturation for Piedmont residual soils. In addition, a predictive relationship was developed for estimation of specific heat capacity as a function of soil moisture content.

Using the predictive relationship obtained from the thermal property measurements on Piedmont soils, it was also shown that results from Seismic Piezocone Penetration Test (SCPTu) soundings and simple laboratory index tests (moisture content and percent fines) can be used to obtain a first-order estimate of thermal conductivity. In addition, the results from the thermal property measurements on Piedmont soils were used to provide a range of thermal properties that were subsequently used in the parametric study performed using the aforementioned numerical model.

This study also highlights some of the challenges associated with determination of thermal conductivity from field and laboratory tests. In the laboratory, while samples can be prepared under relatively controlled conditions, variances can still occur due to sample size and preparation, sensor size and accuracy, test method used, and other factors. In the field, there are natural variations in the ground conditions, and while a test such as a thermal response test (TRT) can capture a larger sensed volume (and hence better captures the

natural vertical and lateral variation of soil properties), it is also subject to higher costs relative to laboratory testing, as well as variances resulting from the difference in the analytical models used to interpret the TRT results.

Using thermal properties representative of the Piedmont soils, results are presented from both a numerical model and a laboratory scale physical model to demonstrate the potential for improvement in thermal performance of shallow thermo-active foundations resulting from a novel concept termed the Engineered Transition Zone (ETZ). An ETZ provides a means to introduce a thermally optimized zone between the foundation and the surrounding geomaterials to reduce thermal resistance. It also allows decoupling of the structural portion of the foundation from the thermal portion, such that the length of each component can be selected individually to meet the specific structural and thermal needs. Additionally, it allows for various novel circulation pipe configurations to be used (for example, helical loops) to further enhance heat transfer due to increased pipe surface area available for heat transfer. Both the numerical and physical models show that there is a potential for significant improvement in thermal performance. Such improvements can make shallow thermo-active foundations such as energy piles a more feasible renewable and sustainable energy alternative for heating and cooling of buildings (provided that the ground energy balance can be equilibrated; that is, there is balance between heat extracted for heating and heat re-injected for cooling), particularly in areas where poor subsurface thermal properties might otherwise preclude their use.

Lastly, this study presents some of the public policy challenges related to the adoption of shallow thermo-active foundations. A case study was performed looking at the application of the punctuated equilibrium theory and policy diffusion to gain insight into

ground source heat pump (GSHP) related policies in the U.S. between 2000 and 2015, as well as GSHP adoption rates between 2002 and 2009. Using the Bass Diffusion Model (BDM) and longitudinal data analysis, it is shown that that policies enacted at the federal level can act as a trigger and a signal for GSHP related policies to be enacted at the state level. Policy diffusion can in turn create awareness through signaling and information, leading to more widespread market adoption. In this case, the increase in GSHP adoption rates is observed to be more gradual, most likely because of higher initial costs relative to more conventional HVAC systems, as well as other market failures such as information asymmetry and split incentives between owners and building tenants. The longitudinal data analysis appears to confirm that the accumulation of GSHP related policies has an impact on GSHP adoption. Additionally, it highlights some of the other factors that may have contributed to higher adoption of GSHPs, such as increasing energy prices. These findings suggest that policy alternatives can be devised at the state and local levels to complement federal incentives, to help overcome market failures, and to encourage more widespread adoption of emerging energy efficient technologies such as shallow thermo-active foundations. Significantly improving the thermal performance of shallow thermo-active foundations through the use of an ETZ can also act to accelerate the rate of adoption of shallow thermo-active foundations by enabling the use of these systems in subsurface conditions that would otherwise preclude their use, and also by potentially reducing the payback period associated with these installations through the use of fewer but much higher performing elements.

Recommendations for future work include the following:

- Performance of additional laboratory tests with Piedmont residual soils, using a chamber that is instrumented with a high capacity tensiometer in order to measure soil suction during drying. This will allow quantification of the suction effects on the thermal conductivity of soils during drying. In addition, it would be desirable to perform repeated wetting-drying cycles to evaluate the hysteresis of the thermal conductivity characteristic curve; however, this would require a chamber with flexible boundaries, especially for the fine-grained samples, as the soil samples were observed to undergo shrinking (both vertically and radially) when drying.
- Studies on combined heat and moisture transfer around a thermo-active foundation and its effects (for example, soil drying) for both a conventional system and an enhanced system configuration including an ETZ and a helical loop configuration.
- Performance of additional laboratory scale physical model tests, using controlled temperature boundaries, different thermal load conditions and direct measurement of inlet and outlet temperatures, different soil types (including Piedmont residual soils instead of sand), and different fluid circulation loop configurations.
- Performance of at least two full-scale model tests (preferably near the location of the in-situ tests performed at the Opelika NGES as part of this study, as the thermal properties of the site soils have already been characterized), one constructed conventionally without an ETZ, and another with an ETZ, in order to measure the thermal response of the systems in the field under short and long term loading conditions.

- Additional numerical modeling using results from the above-mentioned laboratory and field tests for further model calibration.
- Performance of additional in-situ tests using a thermal CPT probe at the Opelika NGES, and comparison to the results obtained from laboratory tests.
- Study of the mechanical effects of an ETZ on shallow thermo-active foundation behavior. This study focused solely on thermal performance of these systems; however, as indicated by the numerical modeling results, the presence of an ETZ can have an impact on the pile surface temperatures. Additionally, the introduction of an ETZ means that the load-bearing foundation element now interfaces directly with the ETZ material instead of the surrounding soils. This means that there may be an opportunity to improve not only the thermal performance but the mechanical performance of the system as well.
- Studies to evaluate novel additives (such as graphene, with thermal conductivity that is significantly greater than those of typical soils and concrete), as well as to identify affordable additives to natural soils to optimize ETZ material properties.
- Performance of a lifecycle cost analysis (LCCA) to provide further insight into the feasibility of shallow thermo-active foundations utilizing an ETZ.
- Further studies on the public policy drivers of energy efficient technologies such as shallow thermo-active foundations, to reduce the gap between science/engineering and public policy, and to better understand how policies can be designed to increase the adoption rates of these technologies.

REFERENCES

ABDELAZIZ, S. L., OLGUN, C. G. & MARTIN, J. R. 2011. Design and operational considerations of geothermal energy piles. GeoFrontiers 2011, Dallas, TX, American Society of Civil Engineers, GSP 211, 450-459.

ABU-HAMDEH, N. H. 2003. Thermal Properties of Soils as affected by Density and Water Content. *Biosystems Engineering*, 86(1), 97-102.

ABU-HAMDEH, N. H. & REEDER, R. C. 2000. Soil Thermal Conductivity: Effects of Density, Moisture, Salt Concentration, and Organic Matter. *Soil Science Society of America Journal*, 64, 1285-1290.

AKROUCH, G., BRIAUD, J. L., SANCHEZ, M. & YILMAZ, R. 2016. Thermal Cone Test to Determine Soil Thermal Properties. *Journal of Geotechnical and Geoenvironmental Engineering*, 142(3), 04015085, 1-12.

AKROUCH, G. A., SANCHEZ, M. & BRIAUD, J. L. 2014. Thermo-mechanical behavior of energy piles in high plasticity clays. *Acta Geotechnica*, 9(3), 399-412.

ALCOTT, H. & GREENSTONE, M. 2012. Is There an Energy Efficiency Gap? *Journal of Economic Perspectives*, 26(1), 3-28.

ALCOTT, H. T., D. 2015. Evaluating Behaviorally Motivated Policy: Experimental Evidence from the Lightbulb Market. *American Economic Review*, 105(8), 2501-2538.

ALLAN, M. L. 1997. Thermal conductivity of cementitious grouts for geothermal heat pumps. Progress Report FY 1997. Report No. BNL-65129, Office of Geothermal Technologies, U.S. Department of Energy, Washington D.C.

ALRTIMI, A. A., ROUAINIA, M. & MANNING, D. A. C. 2013. Thermal enhancement of PFA-based grout for geothermal heat exchangers. *Applied Thermal Engineering*, 54, 559-564.

AMATYA, B. L., SOGA, K., BOURNE-WEBB, P. J., AMIS, T. & LALOUI, L. 2012. Thermo-mechanical behavior of energy piles. *Géotechnique*, 62(6), 503-519.

ARSON, C. F., BERNS, E., AKROUCH, G., SANCHEZ, M. & BRIAUD, J. L. 2013. Heat Propagation around Geothermal Piles and Implications on Energy Balance. In: *Materials and Processes for Energy: Communicating Current Research and Technological Developments*, MENDEZ-VILAS, A. (ed.), 628-635.

BASS, F. M. 1969. A New Product Growth Model for Consumer Durables. *Management Science*, 15(5), 215-227.

BATCHELOR, G. K. & O'BRIEN, R. W. 1977. Thermal or electrical conduction through a granular media. *Proceedings of the Royal Society of London*, 355, 313-333.

BATINI, N., LORIA, A. F. R., CONTI, P., TESTI, D., GRASSI, W. & LALOUI, L. 2015. Energy and geotechnical behaviour of energy piles for different design solutions. *Applied Thermal Engineering*, 86, 199-213.

BATTOCLETTI, E. & GLASSLEY, W. E. 2013. Measuring the Costs and Benefits of Nationwide Goethermal Heat Pump Deployment. California Geothermal Energy Collaborative, Department of Geology, University of California at Davis, CA.

BAUMGARTNER, F. R. & JONES, B. D. 2009. *Agendas and Instability in American Politics*, University of Chicago Press, Chicago.

BENTZ, D. P., PELTZ, M. A., DURAN-HERRERA, A., VALDEZ, P. & JUAREZ, C. A. 2011. Thermal properties of high-volume fly ash mortars and concretes. *Journal of Building Physics*, 34(3), 263-275.

BERGMAN, T. L., LAVINE, A. S., INCROPERA, F. P. & DEWITT, D. P. 2011. *Fundamentals of Heat and Mass Transfer*, John Wiley & Sons, New York.

BEZIAT, A., DARDAINE, M. & GABIS, V. 1988. Effect of Compaction Pressure and Water Content on the Thermal Conductivity of Some Natural Clays. *Clays and Clay Minerals*, 36(5), 462-466.

BIDARMAGHZ, A. & NARSILIO, G. 2018. Heat exchange mechanisms in energy tunnel systems. *Geomechanics for Energy and the Environment*, 16, 83-95.

BOULANGER, R. W. & IDRISS, I. M. 2014. CPT and SPT Based Liquefaction Triggering Procedures. Report No. UCD/CGM-14/01, Center for Geotechnical Modeling, University of California at Davis, Davis, CA.

BOURNE-WEBB, P. J., AMATYA, B. & SOGA, K. 2013. A framework for understanding energy pile behaviour. *Proceedings of the Institution of Civil Engineers*, 166(GE2), 170-177.

BOURNE-WEBB, P. J., AMATYA, B., SOGA, K., AMIS, T., DAVIDSON, C. & PAYNE, P. 2009. Energy pile test at Lambeth College, London: geotechnical and thermodynamic aspects of pile response to heat cycles. *Géotechnique*, 59(3), 237-248.

BOUSHEY, G. 2012. Punctuated Equilibrium Theory and the Diffusion of Innovations. *The Policy Studies Journal*, 40(1), 127-146.

BOZIS, D., PAPAKOSTAS, K. & KYRIAKIS, N. 2011. On the evaluation of design parameters effects on the heat transfer efficiency of energy piles. *Energy and Buildings*, 43, 1020-1029.

BRANDL, H. 2006. Energy foundations and other thermo-active ground structures. *Géotechnique*, 56(2), 81-122.

BRISTOW, K. L. 1998. Measurement of thermal properties and water content of unsaturated sandy soil using dual-probe heat-pulse probes. *Agricultural and Forest Meteorology*, 89, 75-84.

CALVERT, C. S., BUOL, S. W. & WEED, S. B. 1980. Mineralogical characteristics and transformations of a vertical rock-saprolite-soil sequence in the North Carolina piedmont: I. profile morphology, chemical composition, and mineralogy. *Soil Science Society of America Journal*, 44, 1096-1103.

CAMPBELL, G. S., JUNGBAUER JR., J. D., BIDLAKE, W. R. & HUNGERFORD, R. D. 1994. Predicting the effect of temperature on soil thermal conductivity. *Soil Science*, 158(5), 307-313.

CAULK, R. A. & GHAZANFARI, E. Investigation of Construction Specification Effects on Energy Pile Efficiency. Proceedings of the International Foundations Conference and Equipment Exposition, American Society of Civil Engineers, San Antonio, TX, 1648-1657.

CECINATO, F. & LOVERIDGE, F. A. 2015. Influences on the thermal efficiency of energy piles. *Energy*, 82, 1021-1033.

CONGEDO, P. M., COLANGELO, G. & STARACE, G. 2012. CFD simulations of horizontal ground heat exchangers: A comparison among different configurations. *Applied Thermal Engineering*, 33-34, 24-32.

CONNOR, P., BURGER, V., BEURKENS, L., ERICSSON, K. & EGGER, C. 2013. Devising renewable heat policy: Overview of support options. *Energy Policy*, 59, 3-16.

CORTES, D. D., MARTIN, A. I., YUN, T. S., FRANCISCA, F. M., SANTAMARINA, J. C. & RUPPEL, C. 2009. Thermal conductivity of hydrate bearing sediments. *Journal of Geophysical Research*, 114, B11103, 1-10.

COTE, J. & KONRAD, J.-M. 2005. A generalized thermal conductivity model for soils and construction materials. *Canadian Geotechnical Journal*, 42, 443-458.

COTE, J. & KONRAD, J.-M. 2009. Assessment of structure effects on the thermal conductivity of two-phase porous geomaterials. *International Journal of Heat and Mass Transfer*, 52, 796-804.

CUI, P., LI, X., MAN, Y. & FANG, Z. 2011. Heat transfer analysis of pile geothermal heat exchangers with spiral coils. *Applied Energy*, 88, 4113-4119.

DAI, S. & SANTAMARINA, J. C. 2014. Sampling disturbance in hydrate-bearing sediment pressure cores: NGHP-01 expedition, Krishnae – Godavari Basin example. *Marine and Petroleum Geology*, 58, 178-186.

DE MOEL, M., BACH, P. M., BOUAZZA, A., SINGH, R. M. & SUN, J. O. 2010. Technological advances and applications of geothermal energy pile foundations in Australia. *Renewable and Sustainable Energy Reviews*, 14, 2683-2696.

DESMEDT, J. & HOES, H. 2006. Case study of a BTES and energy piles application for a Belgian hospital. Ecostock 2006, Galloway, NJ, 1-7.

DESMEDT, J., VAN BAEL, J., HOES, H. & ROBEYN, N. 2012. Experimental performance of borehole heat exchangers and grouting materials for ground source heat pumps. *International Journal of Energy Research*, 36, 1238-1246.

DUNN, W. N. 2012. *Public Policy Analysis*, Fifth Edition, Pearson Education Inc., Boston, MA.

DUPRAY, F., LALOUI, L. & KAZANGBA, A. 2014. Numerical analysis of seasonal heat storage in an energy pile foundation. *Computers and Geotechnics*, 55, 67-77.

EIA 2015. Annual Energy Outlook 2015 with projections to 2040. DOE/EIA-0383(2015), U.S. Energy Information Administration, Washington D.C.

EIA. 2018. Energy Consumption by Sector [Online]. U.S. Energy Information Administration. Available: http://www.eia.gov/consumption [Accessed 2018].

EPPELBAUM, L., KUTASOV, I. & PILCHIN, A. 2014. Thermal Properties of Rocks and Density of Fluids. In: *Applied Geothermics*, Chapter 2, 99-149. Lecture Notes in Earth System Sciences. Springer, Berlin, Heidelberg.

EROL, S. & FRANCOIS, B. 2013. Thermal, hydraulic and mechanical performances of enhanced grouting materials for borehole heat exchanger. In: *Coupled Phenomena in Environmental Geotechnics,* 491-499. Taylor & Francis Group, London.

ERZIN, Y., RAO, H. B., PATEL, A., GUMASTE, S. D. & SINGH, D. N. 2010. Artificial neural network models for predicting electrical resistivity of soils from their thermal resistivity. *International Journal of Thermal Sciences*, 49, 118-130.

FAROUKI, O. T. 1981a. Thermal properties of soils. *CRREL Monograph 81-1*. United States Army Corps of Engineers, Hanover, NH.

FAROUKI, O. T. 1981b. The Thermal Properties of Soils in Cold Regions. *Cold Regions Science and Technology*, 5, 67-75.

FINKE, K. A., MAYNE, P. W. & KLOPP, R. A. 2001. Piezocone Penetration Testing in Atlantic Piedmont Residuum. *Journal of Geotechnical and Geoenvironmental Engineering*, 127(1), 48-54.

GAO, J., ZHANG, X., LIU, J., LI, K. & YANG, J. 2008. Numerical and experimental assessment of thermal performance of vertical energy piles: An application. *Journal of Applied Energy*, 85, 901-910.

GOETZLER, W., ZOGG, R., LISLE, H. & BURGOS, J. 2009. Ground-Source Heat Pumps: Overview of Market Status, Barriers to Adoption, and Options for Overcoming Barriers. Final Report, Navigant Consulting, Inc.

HACK, J. T. 1982. Physiographic Divisions and Differential Uplift in the Piedmont and Blue Ridge. Geological Survey Professional Paper 1265, United States Geological Survey, Washington D.C.

HAHNLEIN, S., BAYER, P., FERGUSON, G. & BLUM, P. 2013. Sustainability and policy for the thermal use of shallow geothermal energy. *Energy Policy*, 59, 914-925.

HEMINGWAY, P. & LONG, M. 2011. Energy Foundations – Potential for Ireland. GeoFrontiers 2011, Dallas, TX, American Society of Civil Engineers, GSP 211, 460-469.

HIMMLER, R. & FISCH, M. N. 2005. International Solar Centre Berlin – A comprehensive energy design. Fifth International Conference for Enhanced Building Operations, Pittsburgh, PA, 1-7.

HUGHES, P. J. 2008. Geothermal (Ground-Source) Heat Pumps: Market Status, Barriers to Adoption, and Actions to Overcome Barriers. Report No. ORNL/TM-2008/232, U.S. Department of Energy Oak Ridge National Laboratory, Oak Ridge, TN.

HUGHES, P. J. & PRATSCH, L. 2002. Technical and Market Results of Major U.S. Geothermal Heat Pump Programs. Seventh IEA Heat Pump Conference, Beijing, China, 1, 325-342.

IEA 2007. Renewables for Heating and Cooling – Untapped Potential. Renewable Energy Technology Deployment, International Energy Agency, Paris.

JAFFE, A. B. & STAVINS, R. N. 1994. The Energy Paradox and the Diffusion of Conservation Technology. *Resource and Energy Economics*, 16(2), 91-122.

JALALUDDIN & MIYARA, A. 2012. Thermal performance investigation of several types of vertical ground heat exchangers with different operation mode. *Applied Thermal Engineering*, 33-34, 167-174.

JOHANSEN, O. 1975. *Thermal conductivity of soils*. PhD Dissertation, University of Trondheim, Trondheim, Norway.

KALINSKY, R. J. & KELLY, W. E. 1993. Estimating Water Content of Soils from Electrical Resistivity. *Geotechnical Testing Journal*, 16(3), 323-329.

KALTREIDER, C., KRARTI, M. & MCCARTNEY, J. 2015. Heat transfer analysis of thermo-active foundations. *Energy and Buildings*, 86, 492-501.

KERSTEN, M. S. 1949. Thermal Properties of Soils. Bulletin No. 28, Volume LII, No. 21, University of Minnesota Institute of Technology, Minneapolis, MN.

KLEIN, E. M. & TRIMBLE, J. L. 2008. Characterization of Piedmont Residual Soil and Saprolite in Maryland. Sixth International Conference on Case Histories in Geotechnical Engineering, Arlington, VA, American Society of Civil Engineers, Paper No. 6.07a, 1-13.

KNELLWOLF, C., PERON, H. & LALOUI, L. 2011. Geotechnical analysis of heat exchanger piles. *Journal of Geotechnical and Geoenvironmental Engineering*, 137(10), 890-902.

KNILL, C., DEBUS, M. & HEICHEL, S. 2010. Do parties matter in internationalised policy areas? The impact of political parties on environmental policy outputs in 18 OECD countries, 1970–2000. *European Journal of Political Research*, 49, 301-336.

KNILL, C., SCHULZE, K. & TOSUN, J. 2012. Regulatory policy outputs and impacts: Exploring a complex relationship. *Regulation & Governance*, 6, 427-444.

LALOUI, L., NUTH, M. & VULLIET, L. 2006. Experimental and numerical investigations of the behaviour of a heat exchanger pile. *International Journal for Numerical and Analytical Methods in Geomechanics*, 30, 763-781.

LALOUI, L., OLGUN, C. G., SUTMAN, M., MCCARTNEY, J. S., COCCIA, C. J., ABUEL-NAGA, H. M. & BOWERS, G. A. 2014. Issues involved with thermoactive geotechnical systems: characterization of thermomechanical soil behavior and soil-structure interface behavior. *DFI Journal: The Journal of the Deep Foundations Institute*, 8(2), 108-120.

LEE, C., PARK, M., NGUYEN, T.-B., SOHN, B., CHOI, J. M. & CHOI, H. 2012. Performance evaluation of closed-loop vertical ground heat exchangers by conducting in-situ thermal response tests. *Renewable Energy*, 42, 77-83.

LOVERIDGE, F., OLGUN, G. C., BRETTMANN, T. & POWRIE, W. 2015. The Thermal Behaviour of Three Different Auger Pressure Grouted Piles Used as Heat Exchangers. *Geotechnical and Geological Engineering*, 33, 273-289.

LOVERIDGE, F. & POWRIE, W. 2013. Pile heat exchangers: thermal behavior and interactions. *Proceedings of the Institution of Civil Engineers*, 166(GE2), 178-196.

LOVERIDGE, F. & POWRIE, W. 2014. 2D thermal resistance of pile heat exchangers. *Geothermics*, 50, 122-135.

LOW, J. E., LOVERIDGE, F., POWRIE, W. & NICHOLSON, D. 2015. A comparison of laboratory and in situ methods to determine soil thermal conductivity for energy foundations and other ground heat exchanger applications. *Acta Geotechnica*, 10(2), 209-218.

LU, S., REN, T., GONG, Y. & HORTON, R. 2007. An Improved Model for Predicting Soil Thermal Conductivity from Water Content at Room Temperature. *Soil Science Society of America Journal*, 71(1), 8-14.

LU, Y., LU, S., HORTON, R. & REN, T. 2014. An Empirical Model for Estimating Soil Thermal Conductivity from Texture, Water Content, and Bulk Density. *Soil Science Society of America Journal*, 78, 1859-1868.

LUNNE, T., ROBERTSON, P. K. & POWELL, J. J. M. 1997. *Cone Penetration Testing in Geotechnical Practice*, Blackie Academic & Professional, London.

LURIE, M. V. 2008. *Modeling of Oil Product and Gas Pipeline Transportation*, Wiley-VCH Verlag GmbH & Co. KGaA, Weinheim, Germany.

MAHAJAN, V. & PETERSON, R. A. 1985. *Models for Innovation Diffusion*. Series: Quantitative Applications in the Social Sciences, Series/Number 07-048, Sage Publications, Newbury Park, CA.

MAKASIS, N., NARSILIO, G., BIDARMAGHZ, A. & JOHNSTON, I. W. 2018. The application of retaining walls and slabs as energy structures in underground train stations. *In: Energy Geotechnics – SEG 2018*. Springer Series in Geomechanics and Geoengineering, 43-50.

MAYNE, P. W. 2007. Cone penetration testing: A synthesis of highway practice. *NCHRP Synthesis 368*. Transportation Research Board, Washington, D.C.

MAYNE, P. W. 2014. Interpretation of geotechnical parameters from seismic piezocone tests. Third International Symposium on Cone Penetration Testing, Las Vegas, Nevada, ISSMGE Technical Committee TC 102, 47-73.

MAYNE, P. W. & BROWN, D. A. 2003. Site characterization of Piedmont residuum of North America. *In: Characterization and Engineering Properties of Natural Soils*, Singapore, Vol. 2, 1323-1339.

MAYNE, P. W., BROWN, D. A., VINSON, J., SCHNEIDER, J. A. & FINKE, K. A. 2000. Site Characterization of Piedmont Residual Soils at the NGES, Opelika, Alabama. National Geotechnical Experimentation Sites, GSP 93, American Society of Civil Engineers, Reston, VA, 160-185.

MAYNE, P. W., PEUCHEN, J. & BOUWMEESTER, D. 2010. Soil unit weight estimation from CPTs. Second International Symposium on Cone Penetration Testing, Huntington Beach, CA, Vol. 2, 169-176.

MCCARTNEY, J. S. & ROSENBERG, J. E. 2011. Impact of Heat Exchange on Side Shear in Thermo-Active Foundations. GeoFrontiers 2011, Dallas, TX, American Society of Civil Engineers, GSP 211, 488-498.

MCGILLIVRAY, A. V. 2007. *Enhanced Integration of Shear Wave Velocity Profiling in Direct-Push Site Characterization Systems*. PhD Dissertation, Georgia Institute of Technology.

MIMOUNI, T. & LALOUI, L. 2014. Towards a secure basis for the design of geothermal piles. *Acta Geotechnica*, 9, 355-366.

NASIRIAN, A., CORTES, D. D. & DAI, S. 2015. The physical nature of thermal conduction in dry granular media. *Géotechnique Letters*, 5, 1-5.

NGUYEN, V. T. 2017. *Comportement thermique et thermo-mécanique des pieux énergétiques*. PhD Dissertation, Université Paris-Est.

NIKOLAEV, I. V., LEONG, W. H. & ROSEN, M. A. 2013. Experimental Investigation of Soil Thermal Conductivity Over a Wide Temperature Range. *International Journal of Thermophysics*, 34, 1110-1129.

NOONAN, D., HSIEH, L. C. & MATISOFF, D. 2015. Economic, sociological, and neighbor dimensions of energy efficiency adoption behaviors: Evidence from the U.S residential heating and air conditioning market. *Energy Research & Social Science*, 10, 101-113.

OLGUN, C. G. & MCCARTNEY, J. S. 2014. Outcomes from International Workshop on Thermoactive Geotechnical Systems for Near-Surface Geothermal Energy: from research to practice. *DFI Journal: The Journal of the Deep Foundations Institute*, 8, 59-73.

OLGUN, C. G., OZUDOGRU, T. Y., ABDELAZIZ, S. L. & SENOL, A. 2015. Long-term performance of heat exchanger piles. *Acta Geotechnica*, 10(5), 553-569.

PAHUD, D. & HUBBUCH, M. 2007. Measured thermal performances of the energy pile system of the Dock Midfield at Zurich Airport. Proceedings European Geothermal Congress, Unterhaching, Germany, 1-7.

PAVICH, M. J., LEO, G. W., OBERMEIER, S. F. & ESTABROOK, J. R. 1989. Investigations of the Characteristics, Origin, and Residence Time of the Upland Mantle of the Piedmont of Fairfax County, Virginia. U.S. Geological Survey Professional Paper 1352, United States Geological Survey, Washington D.C.

PETERS-LIDARD, C. D., BLACKBURN, E., LIANG, X. & WOOD, E. F. 1998. The effect of soil thermal conductivity parameterization on surface energy fluxes and temperature. *Journal of Atmospheric Science*, 55, 1209-1224.

PHILIP, J. R. 1964. Similarity Hypothesis for Capillary Hysteresis in Porous Materials. *Journal of Geophysical Research*, 69(8), 1553-1562.

REES, S. W., ADJALI, M. H., ZHOU, Z., DAVIES, M. & THOMAS, H. R. 2000. Ground heat transfer effects on the thermal performance of earth-contact structures. *Renewable and Sustainable Energy Reviews*, 4, 213-265.

RHOADES, J. D., RAATS, P. A. C. & PRATHER, R. J. 1976. Effects of Liquid-phase Electrical Conductivity, Water Content, and Surface Conductivity on Bulk Soil Electrical Conductivity. *Soil Science Society of America Journal*, 40, 651-655.

RINALDI, V. A. & SANTAMARINA, J. C. 2008. Cemented soils: Small-strain stiffness. *In: Deformational Characteristics of Geomaterials*, Amsterdam, 267-273.

ROBERTSON, E. C. 1988. *Thermal Properties of Rocks*. Open File Report 88-441, U.S. Department of the Interior Geological Survey, Reston, VA.

ROBERTSON, P. K. 1990. Soil classification using the cone penetration test. *Canadian Geotechnical Journal*, 27, 151-158.

ROBERTSON, P. K. 2009. Interpretation of cone penetration tests - a unified approach. *Canadian Geotechnical Journal*, 46, 1337-1355.

ROBERTSON, P. K. 2010. Soil behaviour type from the CPT: an update. Second International Symposium on Cone Penetration Testing. Huntington Beach, CA, 1-8.

ROBERTSON, P. K. 2016. Cone penetration test (CPT)-based soil behaviour type (SBT) classification system — an update. *Canadian Geotechnical Journal*, 53, 1910-1927.

ROBERTSON, P. K. & CABAL, K. L. 2010. Estimating soil unit weight from CPT. Second International Symposium on Cone Penetration Testing. Huntington Beach, CA, 1-8.

ROBERTSON, P. K. & CABAL, K. L. 2015. Guide to Cone Penetration Testing for Geotechnical Engineering, Sixth Edition, Gregg Drilling & Testing, Inc., Available Online at www.greggdrilling.com.

ROBERTSON, P. K., CAMPANELLA, R. G., GILLESPIE, D. & GREIG, J. 1986. Use of Piezometer Cone Data. In Situ '86 – Use of In-Situ Testing in Geotechnical Engineering, GSP 6, American Society of Civil Engineers, Reston, VA, 1-18.

ROBERTSON, P. K. & WRIDE, C. E. 1998. Evaluating cyclic liquefaction potential using the cone penetration test. *Canadian Geotechnical Journal*, 35, 442-459.

ROSHANKHAH, S. 2015. *Thermal Properties of Geomaterials with Relevance to Energy Geo-Systems*. PhD Dissertation, Georgia Institute of Technology.

ROSSMAN, G. 2009. The Diffusion of the Legitimate and the Diffusion of Legitimacy. *In: California Center for Population Research On-Line Working Paper Series*, University of California, Los Angeles.

RUBIO, C. M., JOSA, R. & FERRER, F. 2011. Influence of the Hysteretic Behaviour on Silt Loam Soil Thermal Properties. *Open Journal of Soil Science*, 1, 77-85.

SALOMONE, L. A. & KOVACS, W. D. 1984. Thermal Resistivity of Soils. *Journal of Geotechnical Engineering*, 110(3), 375-389.

SALOMONE, L. A., KOVACS, W. D. & KUSUDA, T. 1984. Thermal Performance of Fine-Grained Soils. *Journal of Geotechnical Engineering*, 110(3), 359-374.

SALOMONE, L. A. & MARLOWE, J. I. 1989. Soil and Rock Classification According to Thermal Conductivity – Design of Ground Couple Heat Pump Systems. EPRI CU-6482, Project 2892-3, Final Report.

SANCHEZ, M., FALCAO, F., MACK, M., PEREIRA, J.-M., NARSILIO, G. A. & GUIMARAES, L. 2016. Salient comments from an expert panel on energy geotechnics. *Proceedings of the Institution of Civil Engineers*, 4(EG2), 135-142.

SCHNEIDER, J. A. & MOSS, R. E. S. 2011. Linking cyclic stress and cyclic strain based methods for assessment of cyclic liquefaction triggering in sands. *Géotechnique Letters*, 1, 31-36.

SCHNEIDER, J. A., RANDOLPH, M. F., MAYNE, P. W. & RAMSEY, N. R. 2008. Analysis of Factors Influencing Soil Classification Using Normalized Piezocone Tip Resistance and Pore Pressure Parameters. *Journal of Geotechnical and Geoenvironmental Engineering*, 134(11), 1569-1586.

SCHRAFFRIN, A., SEWERIN, S. & SEUBERT, S. 2015. Toward a Comparative Measure of Climate Policy Output. *Policy Studies Journal*, 43(2), 257-282.

SEXTON, S. E. & SEXTON, A. L. 2014. Conspicuous conservation: the Prius effect and willingness to pay for environmental bona fides. *Journal of Environmental and Economic Management*, 67(3), 303-317.

SEYBOTH, K., BEURKENS, L., LANGNISS, O. & SIMS, R. E. H. 2008. Recognizing the potential for renewable energy heating and cooling. *Energy Policy*, 36, 2460-2463.

SINGH, D. N., KURIYAN, S. J. & MANTHENA, K. C. 2001. A generalized relationship between soil electrical and thermal resistivities. *Experimental Thermal and Fluid Science*, 25, 175-181.

SINGH, G., DAS, B. M. & CHONG, M. K. 1997. Measurement of Moisture Content with a Penetrometer. *Geotechnical Testing Journal*, 20(3), 317-323.

SOWERS, G. F. & RICHARDSON, T. L. 1983. Residual Soils of the Piedmont and Blue Ridge. *Transportation Research Record No. 919*, 10-16.

SREEDEEP, S., RESHMA, A. C. & SINGH, D. N. 2005. Generalized relationship for determining soil electrical resistivity from its thermal resistivity. *Experimental Thermal and Fluid Science*, 29, 217-226.

STEWART, M. A. & MCCARTNEY, J. S. 2013. Centrifuge Modeling of Soil-Structure Interaction in Energy Foundations. *Journal of Geotechnical and Geoenvironmental Engineering*, 140(4), 04013044, 1-11.

SURYATRIYASTUTI, M. E., MROUEHA, H. & BURLON, S. 2012. Understanding the temperature-induced mechanical behaviour of energy pile foundations. *Renewable and Sustainable Energy Reviews*, 16, 3344-3354.

TARNAWSKI, V. R., LEONG, W. H., GORI, F., BUCHAN, G. D. & SUNDBERG, J. 2002. Inter-particle contact heat transfer in soil systems at moderate temperatures. *International Journal of Energy Research*, 26, 1345-1358.

TARNAWSKI, V. R., MCCOMBIE, M. L., LEONG, W. H., WAGNER, B., MOMOSE, T. & SCHONENBERGER, J. 2012. Canadian Field Soils II. Modeling of Quartz Occurrence. *International Journal of Thermophysics*, 33, 843-863.

TARNAWSKI, V. R., MOMOSE, T. & LEONG, W. H. 2009. Assessing the impact of quartz content on the prediction of soil thermal conductivity. *Géotechnique*, 59(4), 331-338.

TARNAWSKI, V. R., MOMOSE, T., LEONG, W. H. & PIPER, D. J. W. 2011. Estimation of Quartz Content in Mineral Soils. *In: Encyclopedia of Agrophysics*, GLIŃSKI, J., HORABIK, J. & LIPIEC, J. (eds.), Springer, 275-280.

VARDON, P. J., BALTOUKAS, D. & PEUCHEN, J. 2018. Interpreting and validating the thermal cone penetration test (T-CPT). *Géotechnique*, 0, 1-13.

VENULOE, S., LALOUI, L., TERZIS, D., HUECKEL, T. & HASSAN, M. 2016. Effect of microbially induced calcite precipitation on soil thermal conductivity. *Géotechnique Letters*, 6, 39-44.

WADSO, L. 2015. RE: Thermal properties of concrete with various aggregates. Email correspondence with F. Atalay, 08/04/2015.

WALLEN, B. M., SMITS, K. M., SAKAKI, T., HOWINGTON, S. E. & DEEPAGODA, C. 2016. Thermal Conductivity of Binary Sand Mixtures Evaluated through Full Water Content Range. *Soil Science Society of America Journal*, 80(3), 592-603.

WALSH, J. B. & DECKER, E. R. 1966. Effect of Pressure and Saturating Fluid on the Thermal Conductivity of Compact Rock. *Journal of Geophysical Research*, 71(12), 3053-3061.

WIRTH, X. & ATALAY, F. In Press. Mineralogical composition of soils and implications on soil thermal conductivity. Proceedings of the XVII ECSMGE-2019, Reykjavik.

WOODSIDE, W. & MESSMER, J. H. 1961. Thermal Conductivity of Porous Media. I. Unconsolidated Sands. *Journal of Applied Physics*, 32(9), 1688-1699.

YUN, T. S. & SANTAMARINA, J. C. 2008. Fundamental study of thermal conduction in dry soils. *Granular Matter*, 10, 197-207.

ZARRELLA, A., DE CARLI, M. & GALGARO, A. 2013. Thermal performance of two types of energy foundation pile: Helical pipe and triple U-tube. *Applied Thermal Engineering*, 61, 301-310.